Wave Sources and Structures in the Earth's Magnetosheath and Adjacent Regions

---

Von der Fakultät für Physik
der Technischen Universität Carolo-Wilhelmina
zu Braunschweig
zur Erlangung des Grades eines
Doktors der Naturwissenschaften
(Dr.rer.nat.)
genehmigte
Dissertation

von Ovidiu Dragoş Constantinescu
aus Bukarest / Rumänien

Bibliografische Information Der Deutschen Bibliothek

Die Deutsche Bibliothek verzeichnet diese Publikation in der Deutschen Nationalbibliografie; detaillierte bibliografische Daten sind im Internet über `http://dnb.ddb.de` abrufbar.

1. Referent: Karl-Heinz Glassmeier
2. Referent: Uwe Motschmann
eingereicht am: 11 · 12 · 2006
mündliche Prüfung (Disputation) am: 01 · 03 · 2007

Copyright © Copernicus GmbH 2007

ISBN xxxxyyyy

Copernicus GmbH, Katlenburg-Lindau
Druck: Schaltungsdienst Lange, Berlin

Printed in Germany

To my mother

Contents

Summary **1**

1 The magnetosphere **3**
1.1 Introduction 5
1.2 The solar wind 5
1.3 The shock and the foreshock 8
1.4 The magnetosheath and the cusp 9
1.5 The magnetosphere proper 10

2 Instrumentation **13**
2.1 Introduction 15
2.2 The fluxgate magnetometer 17
2.3 The Cluster ion spectroscopy experiment 19

3 Virtual interference techniques **23**
3.1 Introduction 25
3.2 Virtual interference and patterns 25
3.3 Beamformer 29
  3.3.1 Application to synthetic data: Plane waves 31
3.4 Capon technique 36
  3.4.1 Application to synthetic data: Plane waves 36
    On the invertibility of $\mathcal{M}$ 37
    Preparing the data 38
    Wave vector determination 39
    Wave length validity domain 45
    Plane wave telescope applied to non-planar waves 45

4 Source locator **53**
4.1 Introduction 55
4.2 Source locator 55
4.3 Spherical waves and dynamic effects 56
  4.3.1 Moving Observer: Doppler effect 58
  4.3.2 Medium flow: Wave length change 59
4.4 Application to synthetic data 64
  4.4.1 Single static source 65
  4.4.2 Multiple static sources 67

4.4.3 Sensor motion . . . 67
4.4.4 Subsonic flow . . . 70
4.4.5 Supersonic flow and sensor motion . . . 71
4.4.6 Extended Source . . . 72
4.5 Discussion . . . 73
4.6 Application to Cluster data . . . 75
4.6.1 Localized source . . . 76
4.6.2 Magnetosheath crossing: Sources distribution . . . 79
Experimental data . . . 80
Typical samples . . . 84
Statistical study . . . 87
Discussion . . . 91

5 Magnetic mirrors **95**
5.1 Introduction . . . 97
5.2 A model for mirror structures . . . 97
5.2.1 The anisotropy for bi-Maxwellian distribution . . . 98
5.2.2 The Magnetic Field . . . 99
5.2.3 The Instability Mechanism . . . 104
5.3 Particle kinetics and distribution function . . . 106
5.3.1 Single particle evolution . . . 107
Types of orbits . . . 107
Chaotic particles . . . 109
5.3.2 Distribution function evolution . . . 111
Preparation of the initial state . . . 111
The final state . . . 114
Particle populations . . . 117
5.4 Application to Cluster data . . . 120
5.4.1 Fit technique . . . 121
Single spacecraft fit . . . 121
Multiple spacecraft fit . . . 124
5.4.2 A case study . . . 126
5.5 Remarks . . . 130

Outlook **131**

Appendix **133**
A.1 Notation Conventions . . . 135
A.2 Array output for vector signals . . . 137
A.3 Source locator numerical implementation . . . 138
A.3.1 Code listings . . . 139
A.4 Equirectangular projection . . . 146

Acknowledgements **149**

Bibliography **159**

Curriculum Vitae **161**

Index **165**

List of Figures

1.1 The Earth's magnetosphere 6
1.2 The Parker spiral 7
1.3 Charged particle orbit in dipolar magnetic field 11

2.1 The Cluster spacecraft before launch 16
2.2 Sketch of a fluxgate magnetometer 18
2.3 Top-hat electrostatic analyzer 19

3.1 Example of patterns 27
3.2 Power spectrum for various time resolutions 31
3.3 Power spectrum for various interval lengths 32
3.4 String array beamformer for one plane wave 33
3.5 Tetrahedron array beamformer for one plane wave 34
3.6 Cube array beamformer for one plane wave 35
3.7 Model data for two plane waves 38
3.8 Tetrahedron array Capon power for one scalar plane wave 40
3.9 Tetrahedron array Capon power for two scalar plane waves 41
3.10 Cube array Capon power for four scalar plane waves 42
3.11 Tetrahedron array Capon power for three vectorial plane waves 44
3.12 Long wave length limit for the wave telescope 46
3.13 Spherical wave analyzed with the plane wave telescope 48
3.14 Effect of the wave front curvature on the plane wave telescope power 50

4.1 Moving sensor 57
4.2 Doppler effect 58
4.3 Subsonic plasma flow 60
4.4 Supersonic plasma flow 61
4.5 Diagram representing the ξ factors 62
4.6 Propagation rays for a point source in subsonic flow 63
4.7 Propagation rays for a point source in supersonic flow 64
4.8 Source location for a single static source at various distances 66
4.9 Source location for three static sources 68
4.10 Source location for moving source 69
4.11 Source location for single source in subsonic flow 70
4.12 Source location for moving source and supersonic flow 71
4.13 Source location for static extended source 72
4.14 Source location for moving extended source 73

4.15 Effect of grid resolution . . . 74
4.16 Cluster orbit on February 26 - 27 2002 . . . 76
4.17 Magnetic field observed by Cluster on February 26 2002 . . . 77
4.18 Elongated moving source from Cluster data on February 26 2002 . . . 78
4.19 Cluster orbit on February 18 2002 . . . 80
4.20 Foreshock configuration on February 18 2002 . . . 81
4.21 Field and plasma parameters on February 18 2002 . . . 82
4.22 The magnetic field measured by Cluster on February 18 2002 . . . 83
4.23 Sample results in the foreshock . . . 85
4.24 Sample results in the magnetosheath, magnetosphere, and cusp . . . 86
4.25 Wave number, close sources, and gyrotropy . . . 88
4.26 Propagation angle, B-n correlation, and anisotropy . . . 89
4.27 Statistics of the distance to source . . . 91

5.1 The α^2 parameter versus the unperturbed anisotropy . . . 101
5.2 The magnetic field perturbation for the main structure . . . 102
5.3 Three dimensional view of the mirror structure magnetic field . . . 103
5.4 The magnetic field lines of a mirror structure . . . 104
5.5 The ring current density inside a mirror structure . . . 105
5.6 The existence and instability domains in the $(A_0, \beta_{0\perp})$-plane. . . . 106
5.7 Trapped particle orbit . . . 108
5.8 Various particle orbits inside a mirror structure . . . 109
5.9 The magnetic moment of a particle inside a mirror structure . . . 110
5.10 Numerical generated Maxwellian distributions . . . 112
5.11 Initial phase-space density . . . 113
5.12 Final phase-space density . . . 114
5.13 Resulted velocity distributions versus ideal Maxwell distributions . . . 115
5.14 The final anisotropy . . . 116
5.15 Trapped and escaping particles distributions . . . 117
5.16 Chaotic and adiabatic particles distributions . . . 119
5.17 Effect of the perturbation strength on particles populations . . . 120
5.18 The normal coordinates . . . 122
5.19 Scan example . . . 123
5.20 Orbit of the reference and a regular s/c relative to a mirror structure 124
5.21 Cluster tetrahedron configuration on November 10 2000 . . . 127
5.22 Fit result . . . 128
5.23 Cluster orbits relative to the reconstructed structure . . . 129
5.24 Mirror structure reconstructed from Cluster data . . . 129

A.1 Flowchart for the source locator . . . 138
A.2 Flowchart of the main IDL code . . . 140
A.3 Sketch of a typical longitude-latitude representation . . . 146

List of Tables

3.1 Beamformer results. Single scalar plane wave, tetrahedron array . . . 36
3.2 Capon technique results. Single scalar plane wave, tetrahedron array. 40
3.3 Capon technique results. Two scalar plane waves, tetrahedron array. . 40
3.4 Capon technique results. Four scalar plane waves, cube array. 43
3.5 Capon technique results. Three vector plane waves, tetrahedron array 43
3.6 Capon technique results. Single scalar spherical wave, tetrahedron array 47

4.1 Source locator results. Single static source, various distances 65
4.2 Source locator results. Three static sources 67
4.3 Source locator results. Moving source 69
4.4 Source locator results. Plasma flow 70
4.5 Source locator results. Extended source 73
4.6 Source locator results. Cluster data, February 26 2002 79
4.7 Number of close sources and of gyrotropic samples 89

5.1 Particle simulation results 118
5.2 Fit results 127

Summary

The near-Earth space environment is a result of the violent interaction between the supersonic solar wind and the magnetic field generated in the Earth core. Among other physical phenomena, it abounds in a multitude of plasma waves which mediate the energy transfer from the solar wind towards the inner magnetosphere.

For many years, the study of the Earth magnetosphere has been limited to isolated measurements performed by rockets or spacecraft. Single point measurements do not allow to disentangle spatial from temporal variations unless strong assumptions are made. It is also very difficult to determine even elementary three dimensional quantities, such as wave vectors, with single point measurements.

With the launch of the four Cluster spacecraft, simultaneous multi-point measurements in space are routinely available. This work aims to develop the necessary tools, and to use the multi-point measurements provided by Cluster to their full potential in order to shed a bit of light on the magnetic structures and wave sources in the Earth magnetosphere.

CHAPTER 1 gives a brief overview of the near-Earth space environment and of the physical processes taking place here.

CHAPTER 2 introduces the Cluster spacecraft fleet and their payload. Special emphasis is put on the magnetic field and particle instruments which produce the data later used in this work.

CHAPTER 3 presents the general formalism of the mathematical techniques we use to analyze the multi-point measurements from Cluster. Using synthetic data and a plane wave representation, we investigate the capabilities and limitations of the simplest technique in this class, the beamformer. We conclude that, given the limited number of sensors offered by Cluster, the beamformer is of no practical use.

The Capon technique, which overcomes the limitations of the beamformer, is examined next. We apply the Capon technique to artificial data representing various number of plane waves detected by various sensor configurations. Here we also study the effect of the wave front curvature on the results given by the Capon technique when plane wave representation is used. The plane wave representation performs well as long as the source of the detected wave is far from the Cluster constellation but fails if the source is close.

CHAPTER 4 is devoted to the source locator – the Capon technique with spherical wave representation. While a plane wave representation provides the wave vector, a spherical wave representation provides the distance to the source as well. For sensor geometries similar to Cluster configuration, synthetic data is used again to study the performance of the method for different scenarios, such as single or multiple wave sources placed at various distances. Particular attention is paid to effects arousing

from the motion of the source and of the sensors relative to the background plasma. Such motions have an influence on both the observed frequency and on the local wave length.

Once the performances of the source locator are established, we perform two case studies with Cluster data. The first case study shows a close wave source with an elongated shape in the day-side magnetosheath. The second is a statistical study of waves nature and origin in the magnetosheath and adjacent regions.

Chapter 5 presents a magnetohydrostatic model for mirror structures. The model describes well many observed features and gives the three dimensional magnetic field geometry inside the mirror structure. By means of direct numerical integration, single particle orbits are investigated. They are categorized as trapped or escaping and regular or irregular. The evolution of a bi-Maxwellian ensemble shows a decrease in the pressure anisotropy and slight departures from the density - magnetic field anti-correlation.

The mirror magnetic field is too complex to allow for a virtual interference technique to be applied. Therefore, a method for fitting multi-spacecraft data is developed and applied to Cluster magnetic field measurements. This way, a magnetic mirror structure is identified in the dusk side magnetosheath.

1

The magnetosphere

1.1 Introduction 5
1.2 The solar wind 5
1.3 The shock and the foreshock 8
1.4 The magnetosheath and the cusp 9
1.5 The magnetosphere proper 10

1.1 Introduction

The first evidence of the geomagnetic field was the alignment of the magnetic needle with the local magnetic meridian observed by Chinese over one thousand years ago. In 1600, Sir William Gilbert, physician of Queen Elizabeth I of England, showed that this phenomenon could be explained if the Earth itself is a great magnet - “Magnus magnes ipse est globus terrestis” (*Gilbert* 1600). Later, in 1896, Birkeland created an artificial aurora by sending electrons against a magnetized sphere. This way he linked the auroral activity with the Earth magnetic field. The link between the Sun and the geomagnetic activity was suggested in 1931 by *Chapman and Ferraro* (1931). They showed that plasma flowing from the Sun would create a current sheet which would compress and confine the Earth magnetic field. But only after the beginning of the space age, in the 1950’s, in situ measurements from rockets and satellites were available and enabled a more detailed view of the magnetosphere (*Stern* 1996).

The Earth magnetosphere is a complex system generated by the interaction between the streaming plasma of the solar wind and the Earth magnetic field. It extends about 30 R_{E} transversal to the Sun-Earth line and up to thousands Earth radii in the Sun-Earth direction.

The speed of the solar wind when it encounters the Earth magnetosphere is highly supersonic. Therefore a standing shock wave is formed in front of the magnetosphere. Passing through the shock, the solar wind plasma is heated, compressed and slowed down to subsonic speed. This hot plasma (red in figure 1.1) encloses like a sheath the Earth magnetic field. The violent interaction between the solar wind and the Earth magnetosphere gives birth to a multitude of physical phenomena such as plasma waves, turbulence, and particle acceleration in the shocked plasma and even in front of the MHD shock.

The Earth magnetic field itself is highly deformed, compressed in the day-side and stretched in a long tail in the night side. Through the cusps (see figure 1.1) energetic plasma of solar origin finds its way into the ionosphere creating day-side diffuse aurorae, while during magnetic substorms, the energy stored into the tail lobes is transfered to the plasmasheet particles which are responsible for the night-side discrete aurorae.

1.2 The solar wind

The source of the solar wind is the outermost region of the Sun atmosphere, the hot, tenuous corona. The equilibrium relation between the pressure gradient and the gravitational force for a static, isothermal, spherical symmetric atmosphere leads to the barometric expression for the pressure p at the distance r from the center of the Sun:

$$p(r) = p_0 \exp\left\{ \frac{G M_{\odot} m}{2 k_{\mathrm{B}} T} \left(\frac{1}{r} - \frac{1}{R} \right) \right\} \tag{1.1}$$

where G is the gravitational constant, k_{B} is the Boltzmann constant, $M_{\odot}$ is the mass of the Sun, m is the particle mass, and p_0 is the pressure at the base of the corona (at the distance R from the center of the Sun).

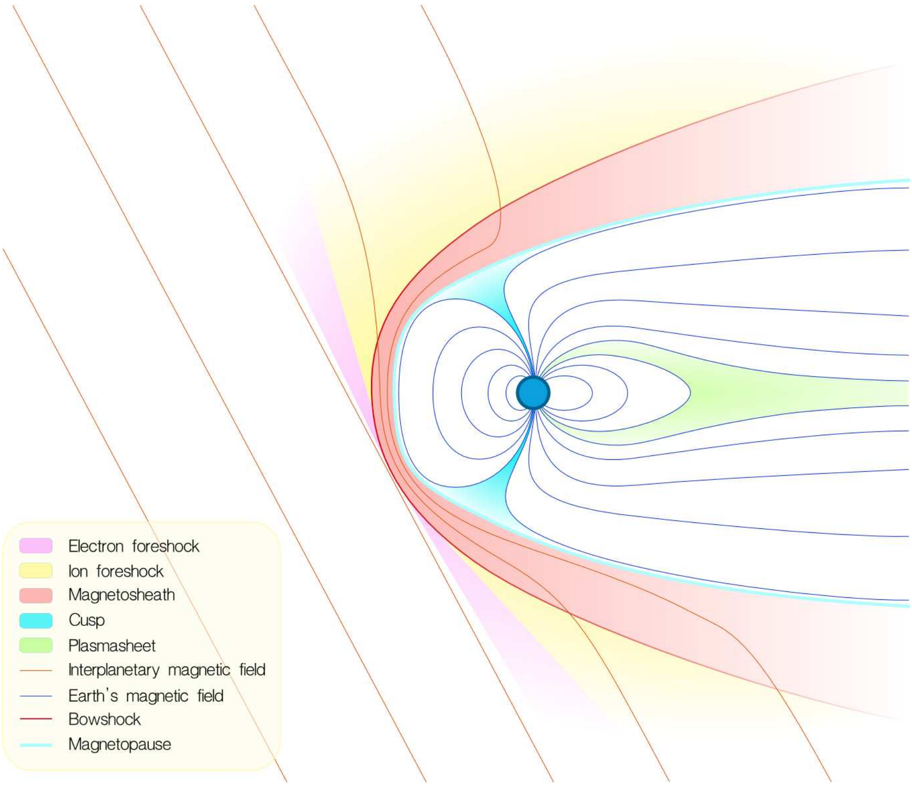

Figure 1.1: Meridional section through the Earth magnetosphere with the Sun on the left. The Earth magnetic field interacts with the solar wind to form the bowshock at a standoff distance of about 15 R_E. The magnetosheath formed by the shocked solar wind wraps the cavity which contains the deformed dipole field.

The asymptotic pressure at infinity, resulting from the equation (1.1), is about $e^{-8} \times p_0$, several orders of magnitude larger than the pressure of the interstellar medium. This indicate that the Sun atmosphere cannot be in static equilibrium. This fact, together with the observations of *Biermann* (1951) of cometary tails, suggesting that gas is streaming outward from the Sun, leaded *Parker* in 1958 to its famous solution of steady expansion of the solar corona. Solving the stationary continuity and the momentum conservation equations for non-null radial flow, he obtains the flow velocity as a function of the distance from the Sun:

$$u^2 - \frac{2k_\mathrm{B}T}{m} - \frac{2k_\mathrm{B}T}{m}\ln\frac{mu^2}{2k_\mathrm{B}T} = 8\frac{k_\mathrm{B}T}{m}\ln\frac{r}{r_\mathrm{c}} + 2GM_\odot\left(\frac{1}{r} - \frac{1}{r_\mathrm{c}}\right) \tag{1.2}$$

where $r_\mathrm{c} = GM_\odot m/(4k_\mathrm{B}T)$ is the distance from the Sun where the flow velocity becomes equal with the thermal velocity: $u^2 = 2k_\mathrm{B}T/m$. This flow speed becomes soon supersonic in the interplanetary medium. Unlike equation (1.1), the Parker solution gives a pressure which tends to zero at large distances. On this basis, before any direct interplanetary observations were available, *Parker* deduced the existence of a continuous, supersonic solar wind.

The rotation of the Sun combined with the steady radial flow bend the solar magnetic field (IMF) into an Archimedean spiral (known as the Parker spiral) as illustrated in the figure (1.2). By the time they reach the Earth orbit, the angle

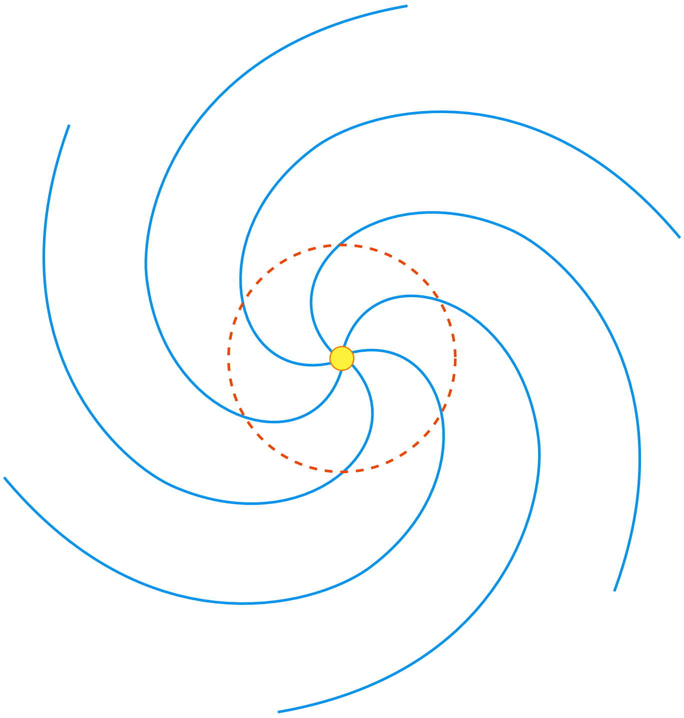

Figure 1.2: The effect of the Sun rotation on its magnetic field. The magnetic field is frozen into the radially expanding plasma. It follows an Archimedean spiral resembling the water spiraling out from a rotating sprinkler. The Earth orbit is represented by the red dashed line.

between the magnetic field lines and the solar wind direction is already close to 45° (*Parker* 1958, 1965).

As the solar wind expands, at some large distance, the interstellar plasma pressure will become comparable with the solar wind pressure (since the former now tends to zero) and the solar wind has to slow down. The interaction between the two plasmas results into a shock called *termination shock*. As the Sun moves relative to the interstellar medium, beyond the termination shock, there is a heliopause, a heliosheath and a bow shock. After 27 years from its launch, Voyager 1 reached the termination shock on December 16, 2004, at a distance of 94 AU from the Sun (*Stone et al.* 2005).

The solar wind consists largely of hydrogen plasma with less than 5% (number density) of ionized helium and traces of heavier elements. At 1 AU the solar wind flows with a typical velocity of 500 km/s although it can reach at times speeds as high as 1500 km/s. The typical sound speed here is only about 50 km/s which means the flow is highly supersonic. The particle density decreases from $10^4\,\mathrm{cm}^{-3}$ in the corona to $5\,\mathrm{cm}^{-3}$ close to the Earth orbit, while the plasma temperature decreases from 10^6 to 10^5 K. The magnetic field at 1 AU is about 5 nT. The magnetic pressure is comparable with the plasma pressure indicating that the magnetic effects will be as important as the pressure effects in the near-Earth solar wind plasma.

1.3 The shock and the foreshock

Shocks are very common phenomena. They appear whenever an object moves faster than the information can propagate through the unperturbed surrounding medium. The shock modifies the properties of the medium such that, through the shocked medium, the information can propagate faster than the moving object. The shock becomes in this way the information horizon for the moving object. Typically, the shocked medium downstream of the shock is hotter, denser, and flows slower than the medium upstream of the shock.

As the supersonic solar wind encounters the Earth magnetic field, a shock is formed. This shock is called *bowshock* because its shape, symmetrical about the Sun - Earth line, is close to a paraboloid of revolution. The standoff distance of the bowshock is about 14 R_{E}.

The thickness of a shock formed in an ordinary gas is of the order of the mean free path of the gas molecules. The mean free path in the solar wind plasma is about 1 AU. Since the bowshock thickness is between 100 and 1000 km, collisions cannot play a role in the bowshock physics. The place of collisions is taken by the magnetic fields which intermediate the interactions between particles. Another difference between ordinary gas shocks and astrophysical shocks is the richness of wave modes in magnetized plasma compared with only one isotropic, non-dispersive pressure wave mode (sound) present in ordinary gas.

It is often convenient to use a reference frame for which the shock is at rest. The electric field associated with the upstream flow is $\boldsymbol{E}_{\mathrm{u}} = -\boldsymbol{u}_{\mathrm{u}} \times \boldsymbol{B}_{\mathrm{u}}$, where the index “u” denotes the upstream value. If we locally approximate the shock surface with a plane, we can chose a reference system which moves parallel with the shock surface such way that the upstream flow velocity becomes parallel with the upstream magnetic field. In this reference frame, called *de Hoffman - Teller* frame (HTF), the electric field is null and the particles follow simple orbits described by a combination between uniform motion along the magnetic field and a gyrating motion around it. The HTF velocity is (*Kivelson and Russell* 1995):

$$\boldsymbol{v}_{\mathrm{HT}} = \frac{\hat{\boldsymbol{n}} \times (\boldsymbol{u}_{\mathrm{u}} \times \boldsymbol{B}_{\mathrm{u}})}{\hat{\boldsymbol{n}} \cdot \boldsymbol{B}_{\mathrm{u}}}, \tag{1.3}$$

$\hat{\boldsymbol{n}}$ being the shock normal.

In the simplest treatment, the shock is regarded as a MHD discontinuity. A conservation law, with the general form

$$\frac{\partial Q}{\partial t} + \nabla \cdot \boldsymbol{F} = 0, \tag{1.4}$$

reduces to a relation between the normal components of the upstream and downstream flux of the conserved quantity:

$$\boldsymbol{F}_{\mathrm{u}} \cdot \hat{\boldsymbol{n}} = \boldsymbol{F}_{\mathrm{d}} \cdot \hat{\boldsymbol{n}} \tag{1.5}$$

In this approximation, the conservation of mass, momentum, and energy, together with the Maxwell equations lead to a set of relations between the upstream and the downstream quantities, known as the *Rankine - Hugoniot relations* (see *Kivelson and Russell* 1995). They describe MHD discontinuities, including shocks.

A discontinuity is a shock if the normal flow component is finite and compression and dissipation occur. The change in the magnetic field strength determines different kinds of shocks. They correspond in the weak shock limit to small amplitude MHD waves. The fast MHD waves are associated with the *fast shock*, where the field strength increases together with the plasma pressure in the downstream region. The slow MHD waves are associated with the *slow shock*, where the plasma pressure increases while the strength of the magnetic field decreases. However, since the plasma density is not affected by Alfvén waves, no compression can occur, thus this type of waves are only associated with a rotational discontinuity, sometimes improper called *Alfvén shock*. The most common observed shocks in the Solar System are fast shocks.

An important parameter which determines the properties of the shock, is the propagation angle, or the angle between the upstream magnetic field and the normal to the shock, θ_{Bn}. The importance of the shock propagation direction becomes clear when we look at the particles orbits in the HTF. For a *quasi-parallel* shock (θ_{Bn} close to 0°), the particles escape upstream from the shock relatively easy, gyrating along the filed lines. The escaping particles bring the information horizon ahead of the MHD shock increasing the scale of the shock. This mechanism is responsible for the formation of the *foreshock* in collisionless plasma (*Tsurutani and Stone* 1985; *Stone and Tsurutani* 1985). On the contrary, for a *quasi-orthogonal* shock (θ_{Bn} close to 90°), the gyrating particles are quickly dragged together with the field lines into the shock.

The shock angle varies along the Earth bowshock, from quasi-orthogonal close to the point where the IMF is tangent to the shock (figure 1.1), to quasi-parallel. The upstream region region populated by reflected particles from the shock is called foreshock. The fast particles beams interact with the solar wind plasma and excite waves in the foreshock (*Tsurutani and Rodriguez* 1981).

Since the energetic electrons escape easier than the ions, there is a region in the foreshock where we can find back-streaming electrons but almost no reflected ions. This is the *electron foreshock*. The waves predominantly excited in the electron foreshock are Langmuir waves (*Kasaba et al.* 2000). The reflected ions form the *ion foreshock* for $\theta_{\mathrm{Bn}} > 70°$. Here they couple with the solar wind plasma through ion-cyclotron waves.

1.4 The magnetosheath and the cusp

Behind the bowshock, the compressed, heated, and turbulent solar wind plasma wraps around the deformed dipole of the Earth magnetic field. This region, bounded upstream by the bowshock and downstream by the *magnetopause* is known as the *magnetosheath*. The magnetosheath is an entirely open system with a tremendous influx of energy from the solar wind. This energy excites a large number of waves and is dissipated through turbulence and wave-particle interactions. At the lowest order, the overall properties of the magnetosheath are determined by gas dynamics.

However, the conditions at both boundaries control the magnetosheath.

One of the factors influencing the magnetosheath is the shock geometry. A quasi-orthogonal shock leads to a large temperature anisotropy due to the effect of field compression and plasma depletion along field lines (*Crooker and Siscoe* 1977). This provides free energy for mirror mode and for ion-cyclotron waves growth. A quasi-parallel shock generates more turbulence both upstream and downstream of the shock. Small changes in the upstream conditions are greatly amplified downstream.

The magnetosheath inner boundary, the magnetopause, was first proposed by *Chapman and Ferraro* (1931, 1932, 1933). It is formed where the pressure of the magnetosheath balances the magnetic pressure of the Earth dipole. At this location a large scale duskward thin current sheet develops. This current, called the *Chapman-Ferraro current*, cancels the Earth magnetic field outside the magnetopause. At the same time, close to the magnetopause, the inside dipole field is increased to about twice its nominal value. Similar currents flow around the tail to confine the Earth magnetic field. The magnetic field created by these currents have an important contribution to the total magnetic field at the Earth surface.

Inside the magnetosheath, the direction of the magnetic field changes from parallel with the IMF in the outer region to draped around the magnetopause in the inner region. The southward/northward character of the IMF reflects into the direction of the magnetic field close to the magnetopause. This determines if reconnection (*Treumann and Baumjohann* 1997) will take place or not in the day-side magnetopause. The reconnection has a great impact on the magnetosheath flow and structure. Southward IMF triggers reconnection at the magnetopause which increases the efficiency of plasma and magnetic field transport in the north-south direction. A northward orientation of the IMF inhibits the reconnection. As a consequence, magnetic field piles up in front of the sub-solar magnetopause. Pressure balance than requires that the thermal pressure in this region has to decrease. The result is a region of depleted density and increased magnetic field called *plasma depletion layer*.

The topological region separating the close from the open magnetic field lines of the Earth deformed dipole field determines the *plasma sheet boundary layer* on the tail side and the two *cusps* on the day-side magnetosphere. The cusps are funnel shaped regions which provide a direct entry of the magnetosheath plasma into the magnetosphere. The entry region extends only about three hours in local time and about one degree in latitude. The magnetosheath plasma penetrating into the low altitude cusp is responsible for the day-side auroral precipitation. Not only plasma, but also parallel propagating waves are focused by the converging field lines into the cusps up to the ionosphere increasing the coupling between the magnetosheath and the magnetosphere.

1.5 The magnetosphere proper

The Earth magnetic field standing against the solar wind is produced by a dynamo mechanism inside its fluid iron core (*Braginsky* 1964). Close to the dynamo region, the complex magnetic field topology is the result of the superposition of many mul-

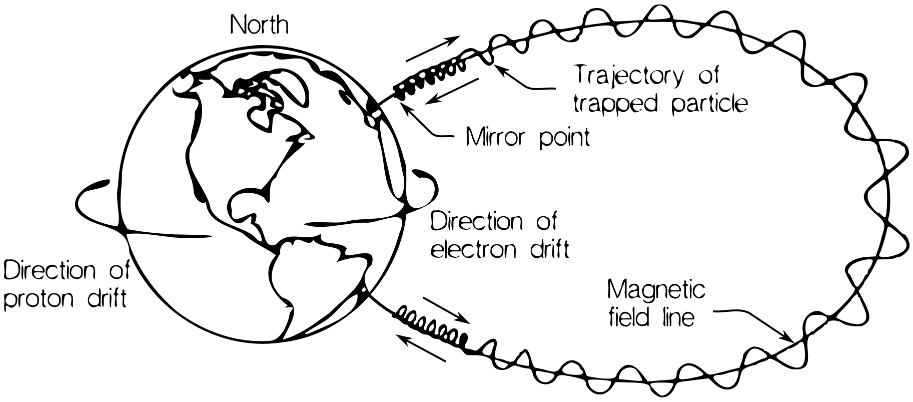
North
Trajectory of trapped particle
Mirror point
Direction of electron drift
Direction of proton drift
Magnetic field line

Figure 1.3: In the Earth dipolar field, the motion of a charged particle has three components: Gyration around the magnetic field line, bounce between the mirror points and drift around the Earth. The direction of the drift motion depends on the charge sign, therefore a ring current is produced. Figure adapted from Iver Cairns (`http://www.physics.usyd.edu.au`)

tipol orders with comparable magnitudes. As the distance to the core increases, the high order contributions fade out and the field becomes mostly dipolar at the Earth surface. The small scale departures from dipolar field at the Earth surface are mainly due to crust magnetization. At $2\,R_{\mathrm{E}}$ from the center of the Earth, the magnetic field is almost a perfect dipole.

The strength and the orientation of the dipole field varies with time. On geological time scales, the magnetic field reversals are well known phenomena. However, the variation of the Earth magnetic field also takes place for much shorter time scales. In the last 400 years, the strength has decreased by 20% and the north pole has drifted 45° westward and 7° southward (*Barton* 1989). Currently, the magnetic dipole axis is tilted with 11° from the Earth rotation axis and the dipole moment is $8 \cdot 10^{15}\,\mathrm{Tm}^3$.

The dipole configuration of the Earth magnetic field can trap charged particles. The trapped particles bounce between the mirror points and are subject to a drift induced by the gradient and the curvature of the magnetic field (see figure 1.3). Since opposite charges result in opposite drift directions, an electric current flows around the Earth. The intensity of this current depends on the number of trapped particles and can increase dramatically if new charged particles are injected into trapped orbits e.g. by the arrival of a CME or because of a solar flare. The increased ring current creates a magnetic field disturbance at the surface of the Earth, called *magnetic storm*.

While the ring current is carried mostly by hot particles with the energy of keV order, the same mechanism also traps particles with much higher energies (up to 10 MeV) into the *radiation belts* (*Van Allen et al.* 1958, 1959). The radiation belts overlap the lower part of the ring current domain, from an altitude of 1000 km up to $6\,R_{\mathrm{E}}$. Due to the very low density, the particle loss rate in the radiation belts is very low. Energetic particles from the Starfish nuclear bomb (*Brown et al.* 1963) detonated 400 km over the Pacific, remained trapped for over 5 years in the Earth radiation belts (*Hess* 1968).

The collisionless character of the magnetospheric plasma makes possible for the ring current and radiation belts particles to occupy the same space. Moreover, a cold neutral population of hydrogen atoms extending up to 4-5 R_{E} exists in the same space. Restricted towards the equatorial and mid latitudes, the *plasmasphere* also overlaps with the radiation belts. The plasmasphere co-rotates with the Earth, it contains cold (1 eV), dense ($100\,\mathrm{cm}^{-1}$) plasma of primarily ionospheric origin, and merges smoothly with the ionosphere.

The solar wind stretches the Earth dipole in the anti-solar direction creating a *magnetic tail* extending thousands Earth radii, far beyond Moon's orbit (64 R_{E}) (*Dungey* 1965; *Villante* 1977). The tail consists of two lobes with opposing magnetic fields, separated by a region with null magnetic field called the *neutral sheet*. Inside the lobes the plasma density is extremely low, much under $0.1\,\mathrm{cm}^{-1}$, and the magnetic pressure is much larger than the plasma pressure. The tail lobes store huge amounts of energy which is released during substorms.

To maintain the pressure balance, the region in between the tail lobes is filled with hot and relatively dense plasma (up to $1\,\mathrm{cm}^{-1}$) called *plasma sheet*. The plasma sheet is between 4 and 8 R_{E} thick and it maps to the auroral oval. During magnetic substorms plasma from this region is injected into the Earth ionosphere causing auroral activity.

2

Instrumentation

2.1 Introduction 15
2.2 The fluxgate magnetometer 17
2.3 The Cluster ion spectroscopy experiment 19

2.1 Introduction

The Cluster mission (*Escoubet et al.* 1997), consisting from four identical spacecraft flying in formation, is the first multi-spacecraft mission to study the Earth magnetosphere and the near Earth solar wind. Simultaneous multi-point measurements allow for the first time to separate spatial from temporal variations and to investigate the three-dimensional small scale structures in the Earth's plasma environment.

On 4-th of June 1996, in Kourou, French Guiana, the maiden flight of Ariane 5, loaded with the four Cluster spacecraft, ended in disaster due to an error in the Flight Control System software inherited from Ariane 4 (*Lions* 1996). A software exception was caused by the execution of a data conversion from 64-bit floating point to 16-bit signed integer value. The variable in question was the horizontal velocity which was considerably higher than for Ariane 4. The Flight Control System issued a diagnostic pattern interpreted as flight data by the On-Board Computer which erratically commanded full nozzle deflections of the solid boosters and the Vulcain main engine. As a consequence, 37 seconds after lift-off, the launcher started to disintegrate and the self-destruct system was triggered.

In April 1997, the ESA Science Programme Committee approved the recovery mission. The four re-builded Cluster spacecraft were launched in pairs on 16 July and 9 August 2000, with Soyuz rockets from the Baikonur Cosmodrome. After the orbital manoeuvres have been completed, the spacecraft were placed on close polar orbits with the perigee at $4\,R_\mathrm{E}$, the apogee at $20\,R_\mathrm{E}$, and the period equal to 57 hours. Due to the slightly different orbital parameters, the spacecraft form a tetrahedron with a characteristic size which can be varied during the mission time from 200 km to 20000 km. Different tetrahedron sizes allow the investigation of different scales.

The scientific payload consists from 11 instruments which can be grouped into three categories: magnetic and electric field investigation, plasma waves investigation, and charged particles investigation. These are, of course, not strict categories.

Two instruments belong to the first category: The FluxGate Magnetometer (FGM) (*Balogh et al.* 1997) for measuring the magnetic field, and the Electron Drift Instrument (EDI) which measures the electric field using an electron beam to probe the spacecraft surroundings (*Paschmann et al.* 1997). In contrast to the "wave" instruments, these instruments are capable to measure static and slowly variable electric and magnetic fields.

The Wave Experiment Consortium (WEC) (*Pedersen et al.* 1997) employs five experiments which investigate plasma waves: The Spatio-Temporal Analysis of Field Fluctuation experiment (STAFF) (*Cornilleau-Wehrlin et al.* 1997) measures high frequency magnetic waves using a search coil magnetometer. The Electric Field and Wave experiment (EFW) consists from four Langmuir probes deployed with 50 m cables in the spin plane to study electrostatic waves in plasma. Waves of HIgh frequency and Sounder for Probing of Electron density by Relaxation (WHISPER) (*Décréau et al.* 1997) is an active experiment which emits short pulses to detect plasma echoes. The Wide Band Data (WBD) receiver (*Gurnett et al.* 1997) provides high resolution electric field waveforms. The Digital Wave Processing (DWP) (*Woolliscroft et al.* 1997) does on-board data processing and coordinates the WEC instruments.

Figure 2.1: The second Cluster pair and the Fregat upper stage ready for integration into the Soyuz fairing. Location: The Upper Composite Integration Facility, Baikonur, Kazakhstan. Courtesy of ESA.

The charged particles are investigated by the remaining four instruments. The Cluster Ion Spectroscopy (CIS) experiment (*Rème et al.* 2001) provides the full three-dimensional distribution function for the major ion species. Two top-hat sensors are used to reach a compromise between the mass per charge resolution and the angular resolution. One sensor, the Composition and Distribution Function analyzer (CODIF) provides mass per charge plasma composition with relatively low angular resolution, while the second sensor, the Hot Ion Analyzer (HIA) has high angular resolution but no mass per charge resolution.

Based on the same principle as CIS-HIA, the Plasma Electron and Current Experiment (PEACE) (*Johnstone et al.* 1997) measures the full velocity distribution of the electrons every half spin period thanks to its two sensors, the Low Energy Electron Analyzer (LEEA), and the High Energy Electron Analyzer (HEEA).

The energetic particles are detected by the two sensors of the Research with Adaptative Particle Imaging Detectors (RAPID) instrument (*Wilken et al.* 1997). One sensor, the Imaging Ion Mass Spectrometer (IIMS) detects the different energetic ion species, while the other, the Imaging Electron Spectrometer (IES) detects the high energy electrons.

All measurements involving charged particles are extremely sensible to the spacecraft electrostatic potential. The control and stabilization of this is the duty of the Active Spacecraft Potential Control (ASPOC) experiment (*Riedler et al.* 1997). The control is exercised through emission of indium ions with a total current up to 50 μA.

Data from two experiments is extensively used in this work: the magnetic field measured by FGM, and the plasma density and bulk velocity provided by CIS. Therefore a more detailed description of these instruments is given in the following sections.

2.2 The fluxgate magnetometer

Many types of magnetometers measure the magnetic field by using the potential difference produced by a change in the magnetic flux (*Acuña* 2002):

$$U = -N\frac{\mathrm{d}\phi}{\mathrm{d}t} \tag{2.1}$$

where N is the number of windings of the measuring coil. If we associate the vector $\boldsymbol{A} = A\,\hat{\boldsymbol{n}}_A$ to the area enclosed by a winding, the flux can be written as

$$\phi = \boldsymbol{A}\cdot\boldsymbol{B} = \mu\boldsymbol{A}\cdot\boldsymbol{H} \tag{2.2}$$

and the potential difference is

$$U = -\underbrace{NB\frac{\mathrm{d}A_\perp}{\mathrm{d}t}}_{\text{rotating coil}} - \underbrace{N\mu A_\perp\frac{\mathrm{d}H}{\mathrm{d}t}}_{\text{searching coil}} - \underbrace{N\boldsymbol{A}\cdot\boldsymbol{H}\frac{\mathrm{d}\mu}{\mathrm{d}t}}_{\text{fluxgate}} \tag{2.3}$$

The first term in the above expression is due to the variation of the orientation of the sensing coil relative to the ambient magnetic field. Rotating coil magnetometers (*Nettleton and Llewellyn* 1930) are using this term to measure static magnetic fields.

The second term is due to the variation in time of the ambient magnetic field. Searching coil magnetometers (*Séran and Fergeau* 2005) are using this term to measure time variable magnetic fields. A triaxial search coil magnetometer is part of the STAFF experiment (*Cornilleau-Wehrlin et al.* 1997) on-board Cluster.

The third term is due to the variation of the relative permeability with the intensity of the magnetic field. Fluxgate magnetometers (*Primdahl* 1979) are using this effect to measure static or low frequency magnetic fields.

A sketch illustrating the construction of a fluxgate magnetometer is shown in figure (2.2). A pick-up coil is wounded around two parallel ferromagnetic cores made from high permeability material. The ferromagnetic cores are periodically driven deep in and out saturation by the drive windings. The strong nonlinear coupling due to core saturation results in harmonics of the driven frequency in the pick-up coil. The amplitude of the even harmonics is proportional to the component of the magnetic field parallel with the cores.

Aschenbrenner and Goubau (1936) constructed the first fluxgate magnetometer in 1928 using a bundle of soft iron florist wire for the core. Their theoretical treatment was based on a simple mathematical model which approximated the magnetization curve of the iron core, neglecting the hysteresis, with a third order polynomial:

$$B = aH + bH^3 \tag{2.4}$$

Inside each coil, the total magnetic field is the sum of the external and the driven magnetic field. Because the driven magnetic field directions in the two coils are anti-parallel, we can write:

$$H_\pm = H_\mathrm{e} \pm H_\mathrm{d} \tag{2.5}$$

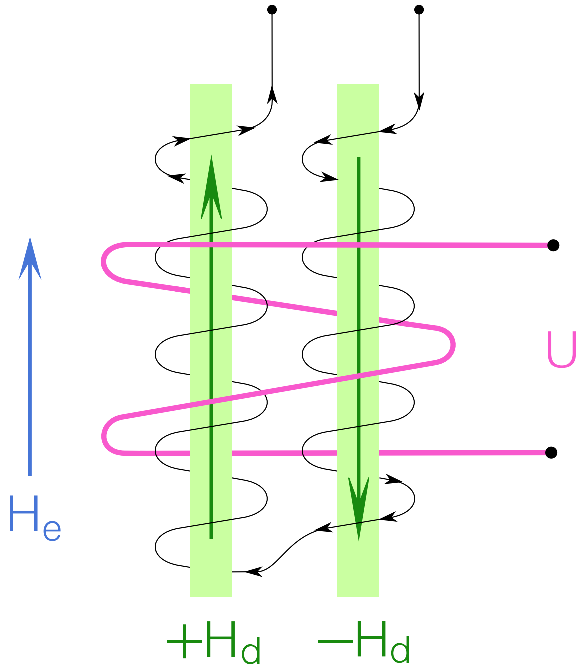

Figure 2.2: Sketch of a fluxgate magnetometer. The two high magnetic permeability cores are driven in and out saturation. The driven magnetic field ads to, respectively subtracts from the external magnetic field. This asymmetry reflects into the potential induced into the pick-up coil.

then the total magnetic field in each coil is made from a symmetric and an antisymmetric part:

$$B_{\pm} = H_\mathrm{e}(a + bH_\mathrm{e}^2 + 3bH_\mathrm{d}^2) \pm H_\mathrm{d}(a + bH_\mathrm{d}^2 + 3bH_\mathrm{e}^2) \tag{2.6}$$

Only the symmetric part contributes to the total flux through the pick-up coil:

$$\phi = \phi_+ + \phi_- = 2AH_\mathrm{e}(a + bH_\mathrm{e}^2 + 3bH_\mathrm{d}^2) \tag{2.7}$$

Assuming time independent external magnetic field, the potential difference in the sensing coil is proportional with the external field:

$$U = -12bNAH_\mathrm{e}H_\mathrm{d}\frac{\mathrm{d}H_\mathrm{d}}{\mathrm{d}t} \tag{2.8}$$

For a sinusoidal driver current

$$H_\mathrm{d} = c\sin(\omega t), \tag{2.9}$$

the signal in the pick-up coil is the first harmonic of the driver frequency:

$$U = -6bc^2\omega NAH_\mathrm{e}\sin(2\omega t) \tag{2.10}$$

The fluxgate magnetometers (*Balogh et al.* 1997) on-board Cluster use a variation of the geometry shown in figure (2.2). The two cores are connected to form a ring core sensor. This configuration results in a more stable and energy efficient sensor.

To minimize the effect of the magnetic field created by the other instruments and to help the in-flight calibration, each spacecraft is equipped with a pair of triaxial

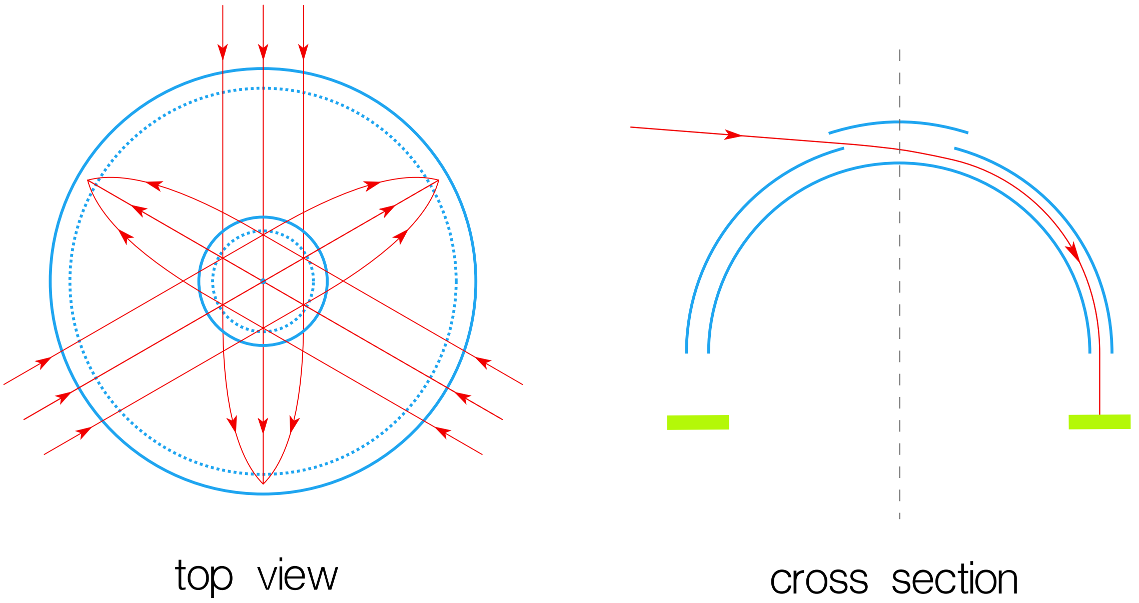

Figure 2.3: Top-hat electrostatic analyzer. The potential difference between the inner and the outer plate deflects and focuses the charged particles (red trajectories) on the position-sensitive detector (green). Only particles with selected energy per mass are transmitted.

fluxgate magnetometers, one at the end of a 5 m long radial boom, and the second 1.5 m inboard from the tip of the boom. The (inter)calibration of the magnetometers is very important since the essential phase information lies in the differences between spacecraft. All eight fluxgate magnetometers have been calibrated at the Magnetsrode facility (*Lühr* 1984) of the IGeP Braunschweig. The calibration was done for the sensitivity factors, the offsets, the orthogonality, and the alignment of the sensors.

The fluxgate magnetometers provide high sample rates (up to 67 vectors/s) at high resolution (up to 8 pT). They also provide the measured magnetic field to other instruments through the Inter-Experiment Link (IEL) to coordinate measurement sequences.

2.3 The Cluster ion spectroscopy experiment

The Cluster Ion Spectroscopy (CIS) experiment (*Rème et al.* 2001) is designed to obtain the full three-dimensional ion distributions with mass per charge composition determination with time resolution of one spacecraft spin. It covers a wide dynamical range using two top-hat electrostatic analyzers (*DeSerio* 1989): the Hot Ion Analyzer (HIA), and the Composition and Distribution Function (CODIF) analyzer. To minimize the telemetry rate, moments of the distribution functions are computed on-board by a sophisticated dual-processor instrument-control and Data Processing System (DPS).

Top-hat electrostatic analyzers are symmetric optics instruments which provide continuous and uniform phase space coverage. Figure (2.3) illustrates the principle of a top-hat electrostatic analyzer. It consists from a small circular top cap which defines the entrance aperture, an outer hemispherical or toroidal plate with a circular opening, and an inner hemispherical or toroidal plate. The potential difference applied between the inner and the outer plate selects only particles with a limited range of energy per mass ratio to be transmitted. A parallel beam of ions suffers a 90° deflection and is focused to a position-sensitive detector system (*Sablik et al.* 1988). The exit position reflects the incident polar angle. The spacecraft spin axis is orthogonal on the analyzer symmetry axis which results in scanning of the azimuth angle with the spacecraft twice the spin frequency. The rotational symmetry results in a 360° polar angle field of view with uniform focusing characteristics.

HIA uses the spherical variant of the top-hat electrostatic analyzer (*Carlson et al.* 1982) with micro-channel plate (MCP) electron multipliers and position encoding discrete anodes. It does not provide mass discrimination, instead it offers high angular resolution, appropriate for the investigation of cold ion beams such as the solar wind. To cope with highly variable plasma characteristics, it has two 180° field of view sections with different sensitivities. The low gain section uses $8 \times 5.626^\circ + 8 \times 11.25^\circ$ detecting sectors. Two sectors, each of 22.5°, positioned close to the rotation axis remain blank. The high gain section is equally divided into 8 sectors, each of 11.25°. For each sensitivity section, a full 4π steradian scan is completed every spacecraft spin. The azimuth resolution of 5.625° is determined by the 64 times per spin voltage sweep rate. The instrument is capable to detect particles with energies between $5\,\mathrm{eV/e^-}$ and $30\,\mathrm{keV/e^-}$.

The CODIF experiment is based on the toroidal variant (*Young et al.* 1988) of the top-hat electrostatic analyzer combined with a time-of-flight section in order to provide mass resolution for the major ion species (H^+, He^+, He^{++}, and O^+). The advantage of the toroidal design is the longer focal length needed to accommodate the time of flight section. Similarly with HIA, CODIF also has two 180° field of view sections with different sensitivities. This is accomplished by placing an attenuation grid at the exit of the toroidal section. Half of the grid has a 1% transmission factor while the other half has a 95% transmission factor. The polar range is equally divided into 16 sectors, each spanning over 22.5°. The energy sweep is performed 32 times per spin, thus the azimuth resolution is 11.25°. The energy range of the instrument is from $15\,\mathrm{eV/e^-}$ to $40\,\mathrm{keV/e^-}$, extended toward lower energies with the help of a retarding potential analyzer.

CODIF uses a time-of-flight spectrometer (*Möbius et al.* 1985) to resolve the different plasma species. This section lies between the exit from the deflection plates and the solid state detector. The timing information is obtained by inserting a thin ($3\,\mu\mathrm{g/cm^2}$) carbon foil 3 cm above the detecting micro channel plate. The start signal is provided by the secondary electrons emitted from the carbon foil during the passage of the ions. The detection of the ions at the MCP marks the stop time. Knowing the velocity and the energy per charge of the detected ions, their mass per charge can be deduced.

The full output from CIS exceeds by far the telemetry capabilities of Cluster. Therefore, the on-board Data Processing System (DPS) computes moments and reduced distributions from the full three dimensional distributions. The moments of the distribution function, up to the third (i.e., the particle density, the flow velocity, the pressure tensor, and the heat flux vector) are computed and transmitted with the spacecraft spin rate. To calculate the moments, the integrals over the velocity space are approximated by sums over the count rates. Additionally, reduced two dimensional pitch angle distributions and averaged snapshots of three dimensional distributions are computed and transmitted in certain telemetry modes.

3

Virtual interference techniques

3.1 Introduction 25
3.2 Virtual interference and patterns 25
3.3 Beamformer 29
3.4 Capon technique 36

3.1 Introduction

The use of sensor arrays is common in seismology and oceanography where powerful methods have been developed in order to take maximum advantage on the information provided. We are interested in a particular class of techniques which combine multi-sensor measurements using appropriate weights (patterns) to determine the properties of the wave field (*Capon et al.* 1967; *Booth and Mohnkern* 1994). We will refer to these techniques as *virtual interference techniques* (VIT). These methods have been mostly used for elastic waves in solids or fluids and for large number of sensors (up to thousands). Nevertheless, the four Cluster spacecraft form an array of sensors which provide us with measurements of plasma properties such as magnetic and electric field, hence adapting VIT for waves in space follows naturally (*Motschmann et al.* 1995; *Pinçon and Motschmann* 1998; *Glassmeier et al.* 2001).

The most direct VIT, *beamforming technique*, has the advantage of simplicity and is a good starting point for understanding how virtual interference works. However, due to its limited resolution it cannot be used for data processing for arrays with low number of sensors such as Cluster. *Capon* (1969) has optimized this method developing a tool with much better resolution than the beamformer. Under the assumption of plane waves, the *Capon technique* have been successfully applied to Cluster data for finding the propagation direction of waves (*Glassmeier et al.* 2001; *Sahraoui et al.* 2003) and in conjunction with a mode decomposition technique (*Motschmann et al.* 1998) have been used to find the first experimental dispersion relation in space (*Narita et al.* 2003).

In the general framework, no assumption is made about the wavefront geometry of independent sources. However, most applications in space physics are using the plane waves representation. There are situations in which more information can be extracted by selecting another representation. It is the purpose of this chapter to present the VIT in a general framework and to show how the methods are applied in the particular case of plane waves representation. This is preparing the ground for the next chapter, dedicated to the spherical waves representation.

3.2 Virtual interference and patterns

The central idea of VIT is to combine the measured values from an array of S sensors $\boldsymbol{X} = (X_1, \dots, X_S)^\mathsf{T}$ with a test pattern $\boldsymbol{w} = (w_1, \dots, w_S)^\mathsf{T}$ depending on the parameters $\boldsymbol{q} = (q_1, \dots, q_M)^\mathsf{T}$ in order to construct the output power $P = P(\boldsymbol{q})$ which should maximize when $\boldsymbol{q}$ coincides with the parameters of the wave field being measured. The measured values $\boldsymbol{X}$ can correspond to any physical quantity which obey a wave propagation law, such as displacement for seismic waves, pressure for acoustic waves, electromagnetic field for radar or spacecraft observations. The test pattern is chosen depending on the problem to study. It acts like a base for the observed wave field and have to be normalized, i.e. $\|\boldsymbol{w}\| = 1$. The way of constructing the power differentiates between different VIT methods (beamforming, Capon technique, etc)

With a proper choice of $\boldsymbol{w}$, the values measured by the sensor positioned at $\boldsymbol{r}_s$

in a wave field generated by N sources with the parameters $\boldsymbol{q}_1, \ldots, \boldsymbol{q}_N$ which we group under the notation $\boldsymbol{Q}$, can be written as:

$$X_s = X(\boldsymbol{Q}, \boldsymbol{r}_s, t) = \sum_{n=1}^{N} c_n w(\boldsymbol{q}_n, \boldsymbol{r}_s, t) \tag{3.1}$$

In other words, the measured wave field is a superposition of elementary waves w produced by N sources. We define the *array output* for the set of parameters $\boldsymbol{q}$ as the projection of the measured values vector $\boldsymbol{X}$ on the test pattern $\boldsymbol{w}$ corresponding to $\boldsymbol{q}$ [1]

$$X_A(\boldsymbol{q}) = \langle w(\boldsymbol{q}, \boldsymbol{r}, t) | X(\boldsymbol{Q}, \boldsymbol{r}, t) \rangle_{\boldsymbol{r},t} \tag{3.2}$$

If w form an orthogonal system, i.e.

$$\langle w(\boldsymbol{q}, \boldsymbol{r}, t) | w(\boldsymbol{q}', \boldsymbol{r}, t) \rangle_{\boldsymbol{r},t} = \delta(\boldsymbol{q} - \boldsymbol{q}') \tag{3.3}$$

then

$$X_A(\boldsymbol{q}) = \sum_{n=1}^{N} c_n \delta(\boldsymbol{q} - \boldsymbol{q}_n) \tag{3.4}$$

We define the *output power* as the square of the norm of the array output

$$P(\boldsymbol{q}) = \|X_A(\boldsymbol{q})\|^2 \tag{3.5}$$

The above defined power differs from zero only when the set of parameters $\boldsymbol{q}$ coincides with the parameters of one of the sources. Assuming that each elementary wave is associated with a source, the power corresponding to the source n, $P(\boldsymbol{q}_n) = |c_n|^2$, represents the contribution of that source to the wave field. In principle all we have to do is to scan the parameter space and look for peaks in in the power P. In practice the scanning procedure uses finite steps in parameter space. This corresponds to a reduction of the original set $\{w(\boldsymbol{q}, \boldsymbol{r}, t)\}$ which normally covers an infinite number of elementary waves to a finite set where only the scanned $\boldsymbol{q}$ values appear. This changes the δ function in the orthogonality relation (3.3) into a finite function with maxima at the sources parameter positions. For the definition of array power for vector signals see Appendix (A.2).

The simplest pattern we can think of is the *Fourier pattern* (*Glassmeier and Motschmann* 1995)

$$w(\omega, t) = \frac{1}{\sqrt{2\pi}} e^{-i\omega t} \tag{3.6}$$

Of course, this pattern leads us to the usual Fourier analysis:

$$\langle w(\omega, t) | X(\boldsymbol{\Omega}, t) \rangle_t = \tilde{X}(\omega) \tag{3.7}$$

$$P(\omega) = \|\tilde{X}(\omega)\|^2 \tag{3.8}$$

The tilde sign denotes the Fourier transformation. In this case our array consists from one single sensor and the parameter space $\{\boldsymbol{q}\} = \{\omega\}$ is the one dimensional

---

[1] The meaning of $\langle \cdot | \cdot \rangle$ is defined in Appendix (A.1)

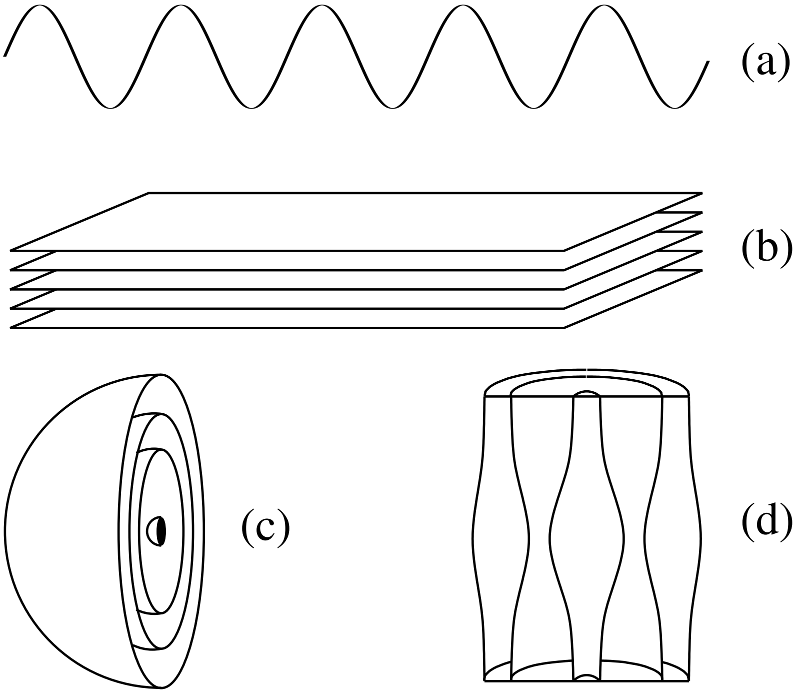

Figure 3.1: Example of patterns: (a) Fourier pattern, (b) Plane wave pattern, (c) Spherical wave pattern and (d) Cylindrical wave pattern

frequency space. Therefore using Fourier analysis we can determine the frequencies which are present in a wave field. The Fourier pattern satisfies the orthogonality condition (3.3) if the measurements are extended over an infinite time interval:

$$\langle w(\omega,t)|w(\omega',t)\rangle_t = \frac{1}{2\pi}\int_{-\infty}^{\infty} e^{i\omega t}e^{-i\omega' t}\mathrm{d}t = \delta(\omega-\omega') \tag{3.9}$$

However, Fourier analysis is used for finite time intervals. If the wave field is generated by several sources with different frequencies we will find local power maxima corresponding to those frequencies.

The next pattern in terms of complexity is the *plane wave pattern*

$$w(\boldsymbol{k},\omega,\boldsymbol{r}_s,t) = \frac{1}{4\pi^2}e^{i(\boldsymbol{k}\cdot\boldsymbol{r}_s-\omega t)} \tag{3.10}$$

which leads us again to Fourier analysis, this time in four dimensions. The orthogonality relation (3.3) is in this case

$$\langle w(\boldsymbol{k},\omega,\boldsymbol{r},t)|w(\boldsymbol{k}',\omega',\boldsymbol{r},t)\rangle_{\boldsymbol{r},t} = \delta(\boldsymbol{k}-\boldsymbol{k}')\delta(\omega-\omega') \tag{3.11}$$

We note that the above orthogonality relation implies measurements over an infinite period in time and with an infinite number of sensors. However, in practice the integral in time changes to a sum over time samples and the integral in position space changes to a sum over available sensor positions. To preserve the normalization for the discrete case, the pattern is changed to

$$w(\boldsymbol{k},\omega,\boldsymbol{r}_s,t_j) = \frac{1}{\sqrt{SN_T}}e^{i(\boldsymbol{k}\cdot\boldsymbol{r}_s-\omega t_j)} = w_{sj}(\boldsymbol{k},\omega) \tag{3.12}$$

where N_T is the number of time samples. Since (3.4) no longer holds for discrete samples, the power is no longer represented by delta functions. However, even for a small number of sensors we will still obtain local maxima. Plane wave representation is by far the most common used for array sensing. This representation allows for determining the frequency ω and the $\boldsymbol{k}$ vector.

Because spatial and temporal dependence of the pattern can be separated

$$w(\boldsymbol{k},\omega,\boldsymbol{r},t)=w(\boldsymbol{k},\boldsymbol{r})w(\omega,t), \tag{3.13}$$

the array output (3.2) becomes:

$$X_A(\boldsymbol{k},\omega)= \sum_{s=1}^{S} w^{\star}(\boldsymbol{k},\boldsymbol{r}_s)\left\langle w(\omega,t)|X(\boldsymbol{Q},\boldsymbol{r}_s,t)\right\rangle_t=\sum_{s=1}^{S} w_s^{\star}(\boldsymbol{k})\tilde{X}_s(\boldsymbol{Q},\omega)= \boldsymbol{w}^{\dagger}(\boldsymbol{k})\tilde{\boldsymbol{X}}(\boldsymbol{Q},\omega) \tag{3.14}$$

In practice this separation is very useful because allows us to treat differently the spatial variations (for which we often have a limited number of sensors) from the temporal variations (which can contain a fairly large number of measurements). An effective method is to apply a fast Fourier transform in order to obtain $\tilde{\boldsymbol{X}}(\boldsymbol{Q},\omega)$ for the dominant frequencies and then compute the power $P(\boldsymbol{k})$ over a $\boldsymbol{k}$-domain for these frequencies (*Glassmeier et al.* 2001).

Equation (3.14) gives us a direct way to find the dispersion relation for the measured wave field. We only have to integrate the array output over all arrival directions:

$$X_A(k,\omega)=\int X_A(\boldsymbol{k},\omega)\mathrm{d}\theta_{\boldsymbol{k}}\mathrm{d}\varphi_{\boldsymbol{k}}=\boldsymbol{w}^{\dagger}(k)\tilde{\boldsymbol{X}}(\boldsymbol{Q},\omega) \tag{3.15}$$

where

$$w_s(k)=\frac{2\pi}{\sqrt{S}}\int_{-\pi/2}^{\pi/2} e^{ikr_s\cos\theta}\mathrm{d}\theta \tag{3.16}$$

The resulting power $P(k,\omega)$ will map the dispersion relation.

For patterns that can be separated in two factors, one containing the spatial variables and the other the temporal ones $w(\boldsymbol{q}_r,q_t,\boldsymbol{r},t)=w(\boldsymbol{q}_r,\boldsymbol{r})w(q_t,t)$ we define the *pattern dimension* as the dimension of the vector $\boldsymbol{q}_r$. In this respect the Fourier pattern is zero dimensional and the plane wave pattern is three dimensional. The pattern dimension is a measure of the quantity of information we can extract by using it. The computing time needed for mapping the power in the pattern parameter space increases exponentially with the pattern dimension.

An example of a four dimensional pattern is the *spherical pattern* shown in the figure (3.1 c).

$$w(\boldsymbol{r}_{\text{source}},k,\omega,\boldsymbol{r},t)=w(\rho,k,\omega,\boldsymbol{r},t)=C\frac{1}{\rho}e^{i(k\rho-\omega t)} \tag{3.17}$$

where C is a normalization coefficient. The dependence on the source and sensor positions is hidden in $\rho=\|\boldsymbol{r}-\boldsymbol{r}_{\text{source}}\|$ which is the distance source-sensor. The parameters on which this pattern depends are the source position, wave number and frequency. Compared to the plane wave representation, the spherical wave representation allows for the determination of the distance to the source in addition to the propagation direction, wave number and frequency.

We can go further and define more complex patterns. For instance, for a mirror wave field we could try a pattern like the one in the figure (3.1 d) which illustrates the magnetic field configuration for a mirror structure in magnetohydrostatic equilibrium (*Constantinescu* 2002). However, we still have to concern ourselves with the orthogonality of the function set we choose to represent the pattern and to be aware that increasing complexity means increasing the dimensionality of the parameter space. The simplest cylindrical pattern is already six dimensional: three parameters for position, one for the wave length and two parameters for the symmetry axis orientation. Though it provides more information it also dramatically increase the computing time. Moreover, as we move towards more complex patterns we lose generality and we need do justify their use. For identifying such complex patterns a better approach might be to directly fit the model pattern on the measured data (*Constantinescu et al.* 2003). We apply this method to Cluster magnetic field data in section 5.4.

3.3 Beamformer

In this section we will discuss in detail the beamformer technique for plane waves which is nothing more than Fourier analysis in four dimensions. However, Fourier analysis assumes a sufficient number of samples for each dimension, providing a system of functions which acts like a basis. The small number of sensors is what makes our situation special. This discussion will serve as an introduction to the Capon technique for plane and spherical waves in Section (3.4).

Our goal is to study a wave field composed by a superposition of N plane waves:

$$X(\boldsymbol{K},\boldsymbol{\Omega},\boldsymbol{r},t)=\sum_{n=1}^{N}x_n e^{i(\boldsymbol{k}_n\cdot\boldsymbol{r}-\omega_n t)} \tag{3.18}$$

where $\boldsymbol{K}$ contains the wave vectors $\boldsymbol{k}_n$ of all sources and $\boldsymbol{\Omega}$ contains the frequencies ω_n.

We will use the plane wave pattern defined by the equation (3.12) which we can split into the position dependent part and the time dependent part:

$$w_{sj}(\boldsymbol{k},\omega)=w_s(\boldsymbol{k})w_j(\omega) \tag{3.19a}$$

$$w_s(\boldsymbol{k})=\frac{1}{\sqrt{S}}e^{i\boldsymbol{k}\cdot\boldsymbol{r}_s} \tag{3.19b}$$

$$w_j(\omega)=\frac{1}{\sqrt{N_{\mathrm{T}}}}e^{-i\omega t_j} \tag{3.19c}$$

Therefore we could express the array power in terms of the Fourier components of the measured field (equation 3.14). However, in order to illustrate the technique we prefer not to separate the spatial part from the temporal one yet.

These elementary waves are normalized but they do not form an complete orthogonal system because the time t and the components of the position vector $\boldsymbol{r}$ take now discrete values.

To investigate the properties of the the power (3.5) we consider a wave field composed only from one wave $X(\boldsymbol{k}', \omega', \boldsymbol{r}, t)$. The array output is

$$X_A(\boldsymbol{k}, \omega) = \frac{x}{\sqrt{S N_\mathrm{T}}} \sum_{s=1}^{S} \sum_{j=1}^{N_\mathrm{T}} e^{i[(\boldsymbol{k}'-\boldsymbol{k})\cdot\boldsymbol{r}_s - (\omega'-\omega)t_j]} \tag{3.20}$$

The power reaches indeed its maximum when the the wave vector $\boldsymbol{k}$ matches the wave vector $\boldsymbol{k}'$ and the frequency ω matches ω'. [2]

$$P(\boldsymbol{k}, \omega)\Big|_{\substack{\boldsymbol{k}=\boldsymbol{k}' \\ \omega=\omega'}} = \max = S N_\mathrm{T} x^2 \tag{3.21}$$

Unlike the power for the case when the pattern functions form an orthogonal system, it does not vanish for “wrong” arguments.

$$P(\boldsymbol{k}, \omega)\Big|_{\substack{\boldsymbol{k}\neq\boldsymbol{k}' \\ \omega\neq\omega'}} \neq 0 \tag{3.22}$$

To see how the number of sensors affects the output power, let us consider an one dimensional array of equally spaced sensors measuring a sine wave. The array extends over about two wave lengths. Figure (3.2 b) represents the signal and the sensor positions. The corresponding powers are shown in figure (3.2 a).

Indeed, the power spectrum is far from ideal. Moreover, it seems that apart from shifting the Nyquist threshold toward higher wave numbers, increasing the number of sensors alone does not improve the spectra around the frequency of interest. This is because the broadness of the maximum depends on the number of oscillations in the sample and we have only two oscillations in our example.

To illustrate the dependency of the Fourier power on number of oscillations contained in the data interval we measure a sine wave with a wavelength $\lambda = 1\,\mathrm{m}$ (k=6.28 m^{-1}) using 512 sensors equally distributed on intervals of lengths of 3, 10, 50 and 150 λ. The resulting power spectra are shown in figure (3.3). It can be seen that the less oscillations are contained in the measured interval, the larger is the deviation of the power from a delta function.

According to the Nyquist theorem the minimum wave length which can be measured is twice the distance between sensors. If we try to go under the Nyquist length, we begin to see maxima corresponding to multiples of the real wave number. This phenomenon is called aliasing and it limits drastically the k domain which can be measured by the array. These additional maxima can be seen in the figures (3.2 a) and (3.3) above the Nyquist thresholds. As a consequence of the Nyquist theorem the interval which can be covered by an array of S sensors for a given wave length λ cannot be larger than $S\lambda/2$. In other words, the signal sample should not contain more than $S/2$ oscillations. Hence the broadening of the main power maximum and the apparition of side lobes are indirect consequences of the Nyquist theorem.

---

[2] It could be convenient to redefine the power as $P = \|X_A\|^2/S N_\mathrm{T}$ so its maximum would depend only on the measured wave field

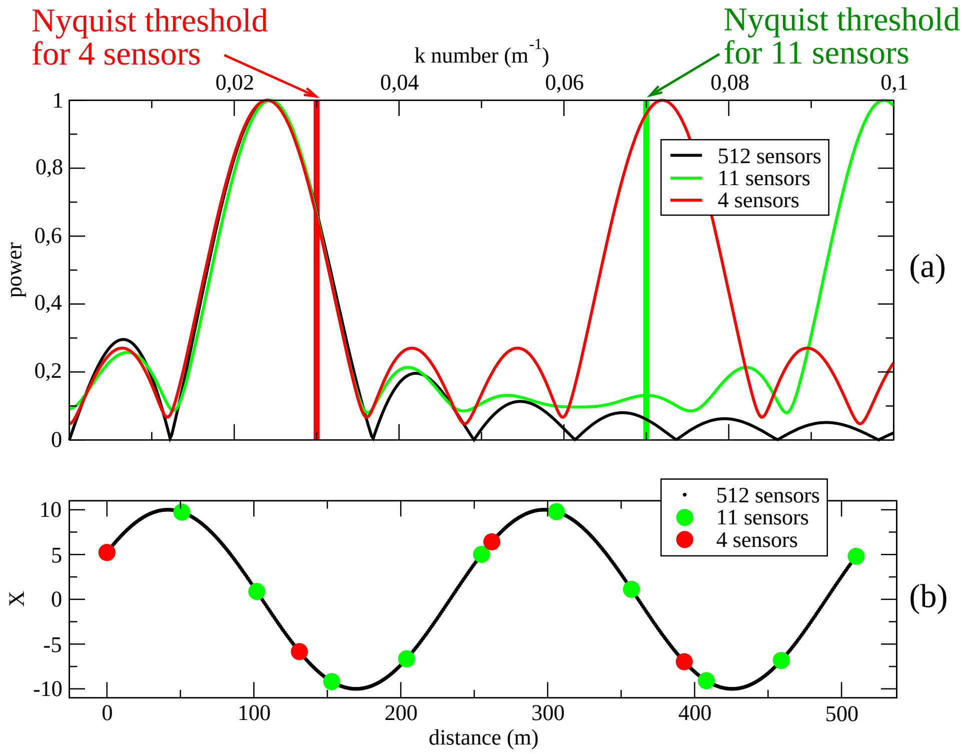

Figure 3.2: The power of the same signal computed using different number of sensors equally distributed over the same interval. The Nyquist thresholds for the arrays of 4 and 11 sensors are represented by vertical lines in (a). For the 512 sensors array the Nyquist threshold falls far outside the graph limits (3.14 m^{-1}).

When more waves come into play, the main peaks will merge and the the presence of side peaks will make the interpretation of the power spectrum very difficult if not impossible especially if we allow for waves of different powers (*Motschmann et al.* 1995) unless the number of sensors is large enough. The solution will be discussed in Section (3.4). For now we will limit ourselves to the one plane wave case.

3.3.1 Application to synthetic data: Plane waves

In what follows we will apply the beamformer technique for various sensor geometries to synthetic data set representing a plane wave of frequency ω' and wave vector $\boldsymbol{k}'$. For each sensor there are a number of 512 measurements taken with a frequency of 1 Hz. All results are expressed in the *array reference system* which has its origin in the center of mass of the sensor array. The z axis goes through the most distant sensor from the center of mass and the next distant sensor belongs to the (z, y) plane, $y \geq 0$. The advantage of using this reference system is that is unique for a given configuration (assuming that the sensors are not equally distanced from the center of mass). We compute the power on a grid of dimensions $30 \times 30 \times 30 \times 30$. The first dimension is for the longitude of the wave vector, ranging from $-180°$ to $180°$. The second dimension is for the latitude of $\boldsymbol{k}$, from $-90°$ to $90°$. The third dimension is for the frequency $\omega \in (0, \omega_{\text{Nyquist}})$. The fourth and last dimension is for

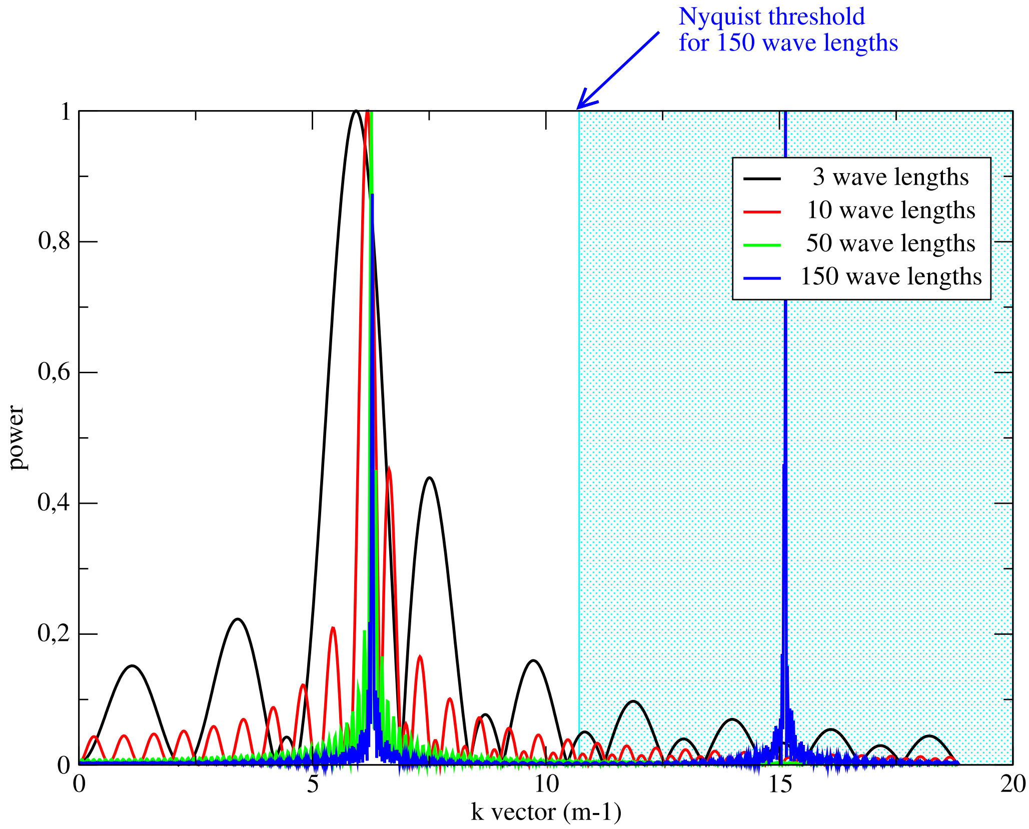

Figure 3.3: The power of the same signal computed using 512 sensors equally distributed over 3, 10, 50 and 150 λ. The Nyquist threshold for the longest interval is 10.71 m^{-1}

the wave number $k \in (0, k_{\mathrm{Nyquist}})$. The results for all array geometries used here are summarized in table (3.1).

The first array we are using consists of a string of 50 equally spaced sensors with a distance of 10 km between them. The z axis of the array reference system is along the string direction and its origin is in the middle of the string. The plane wave to be analyzed is launched at a latitude $\theta' = 60°$ and a longitude $\varphi' = 40°$ having a frequency $\nu' = 0.2\,\mathrm{Hz}$ and a wave length $\lambda' = 33\,\mathrm{km}$. This gives about 100 wave periods and 15 wave lengths included into the measured interval which should provide enough resolution both in space and in time for determining the wave parameters. We are also on the safe side concerning the Nyquist thresholds: $\nu' < \nu_{\mathrm{Nyquist}} = 0.5\,\mathrm{s}$, and $\lambda' > \lambda_{\mathrm{Nyquist}} = 20\,\mathrm{km}$. In figure (3.4) we show sections through the resulting output power. Each section contains the point of maximum power. One feature to be noticed is the independence of the power on longitude. This is due to the rotational symmetry of the sensor array. Obviously we cannot determine the longitude of an incoming wave using a string array. What is not so obvious is that we cannot determine neither the latitude nor the wave number.

The power maximizes when the exponent in eq. (3.20) becomes zero for all the sensors at all times. For a string array, the position dependent part of the exponent becomes $\big(k' \cos(\pi/2 - \theta') - k \cos(\pi/2 - \theta)\big) r_s$. That means that the output power

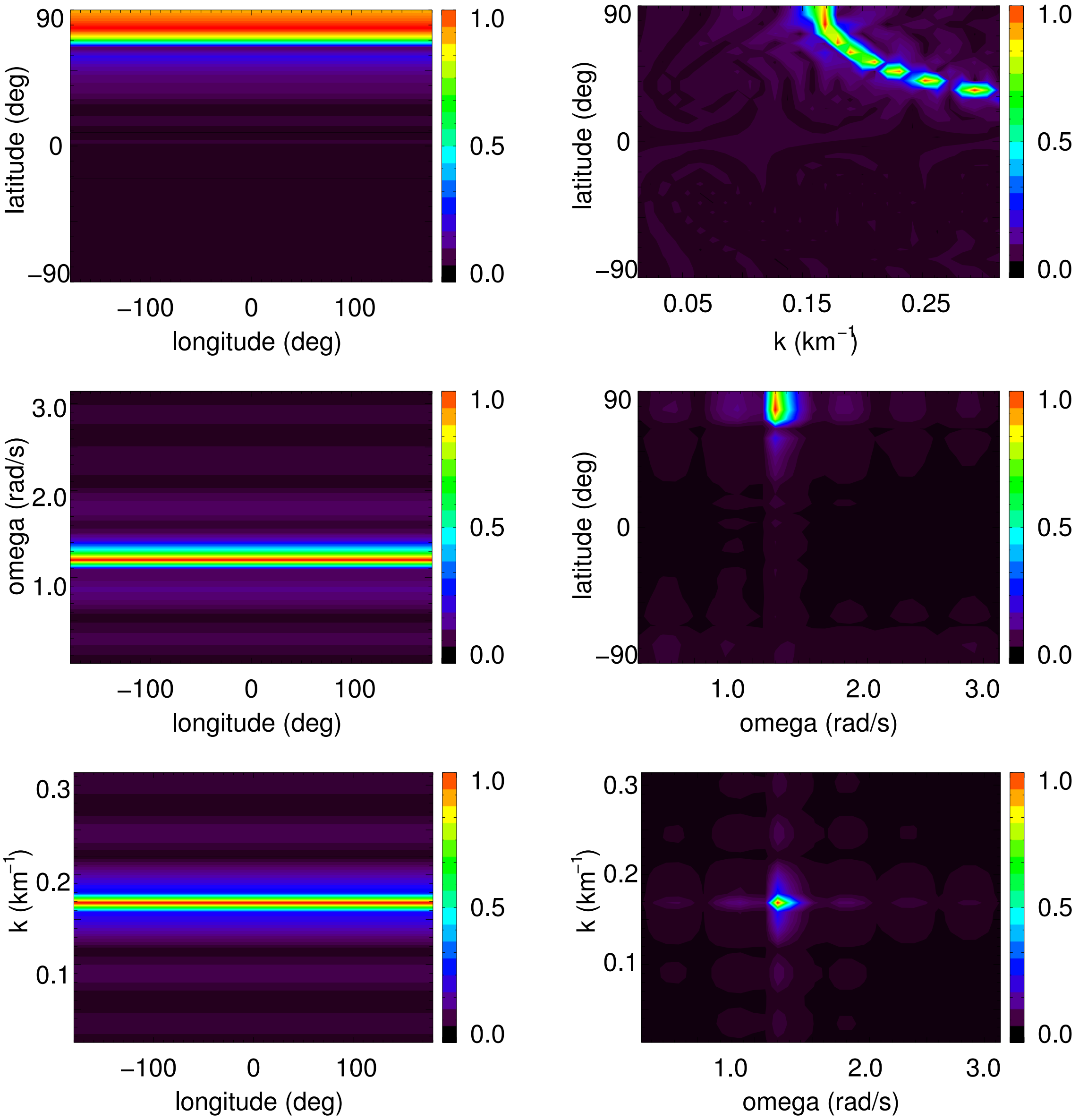

Figure 3.4: Beamformer output power for one plane wave detected with a string array consisting of 50 sensors aligned with z axis. Note that only the latitude of the incoming wave can be determined using this configuration.

maximizes for any combination (k, θ) which satisfies

$$k \sin \theta = k' \sin \theta' \tag{3.23}$$

This can be clearly seen in the (k, latitude) section in the figure (3.4) where the power reaches its maximum according to equation (3.23). We can still determine from which hemisphere the wave comes (North or South) and we can determine a minimum value for the wave number which is given by the power maximum at ±90° latitude.

$$k' \geq k \Big|_{\substack{\text{latitude}=\pm 90^\circ \\ P=\text{maximum}}} \tag{3.24}$$

The string array fails to give a complete description of the wave field because

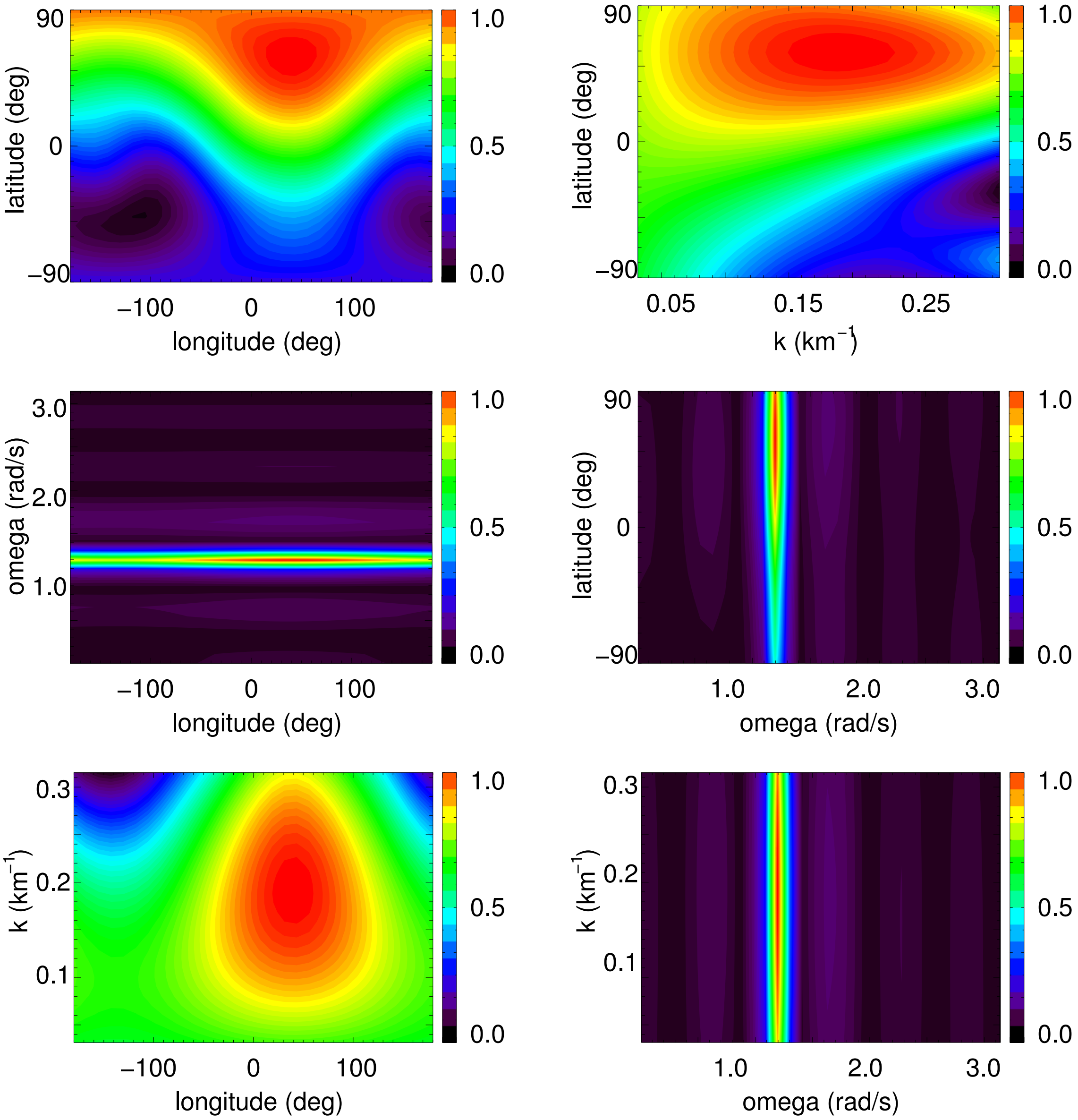

Figure 3.5: Beamformer output power for one plane wave detected with a tetrahedron array. While the resolution in frequency is good, the power maximum in the wave vector domain is very broad.

it covers only one dimension in a three dimensional space. Similarly, a sensor array with a planar configuration would be unable to provide an unambiguous image of the measured field. Therefore, in order to determine the wave vector we need the sensors arranged in a three dimensional configuration. The minimum number of sensors needed for this is four. The output power from a regular tetrahedron configuration with a distance of 10 km between sensors for a plane wave with same parameters as used before is shown in the figure (3.5). This time we can determine both the magnitude and the direction of the $\boldsymbol{k}$ vector with good accuracy. The power maximum is sharp for the frequency but very broad for the $\boldsymbol{k}$ vector. This is due to the small number of sensors we are using. The presence of an additional wave would rise difficulties in interpreting the power spectrum.

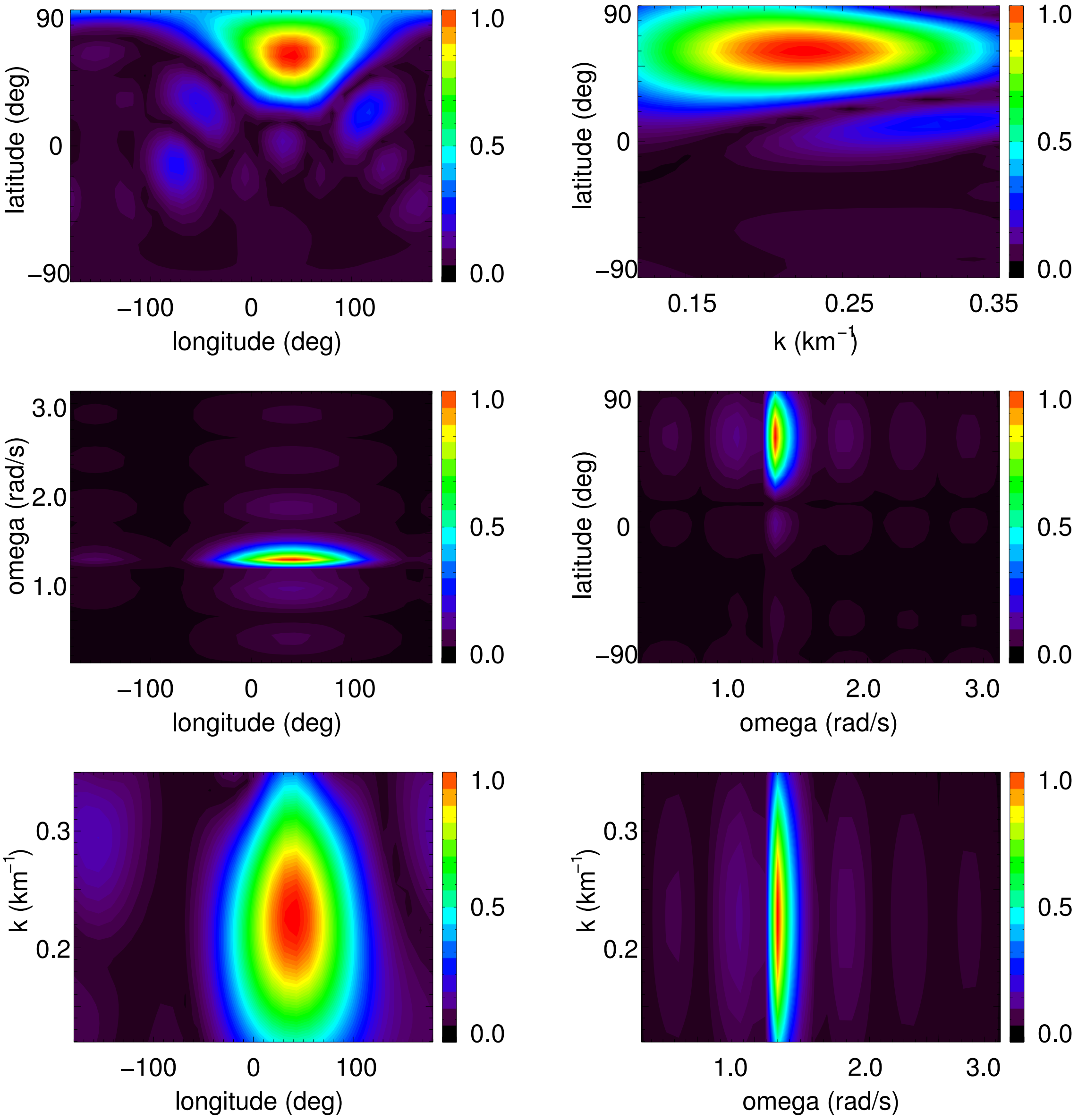

Figure 3.6: Beamformer output power for one plane wave detected with a cube cube array consisting of 64 sensors. The resolution in the wave vector space is improved by increasing the number of sensors. However, thousands of sensors are needed to resolve more than one wave using this technique.

One way to get around this problem is to increase the number of sensors. In the figure (3.6) we display the output power obtained using an array consisting of 64 sensors arranged in a cube with a distance of 10 km between two adjacent sensors. The parameters of the measured wave are the same as before except the wave length which is now 29 km. A comparison with the figure (3.5) shows that increasing the number of sensors sharpens the maxima in power which would make the investigation of real multi-wave fields possible. Since at this time in space physics the largest number of sensors which can be used as an array is four, we have to find a way to make the power maxima sharper without increasing the number of sensors.

	String		Tetrahedron		Cube	
	data	result	data	result	data	result
longitude (deg)	40	-	40	43	40	43
latitude (deg)	60	-	60	58	60	59
frequency (rad/s)	1.22	1.19	1.22	1.2	1.22	1.2
wave number (km^{-1})	0.19	>0.17	0.19	0.19	0.22	0.22

Table 3.1: Beamformer results for a single plane wave using various sensor array configurations. To uniquely determine the wave vector, a three dimensional configuration consisting of at least four sensors is required.

3.4 Capon technique

The weak point of the beamformer technique results from artificial contributions to the power at points in the parameter space which do not correspond to any real wave source. A remedy is to minimize these contributions while keeping the power corresponding to the real wave sources unmodified. This is accomplished by Capon's minimum variance estimator (*Capon et al.* 1967).

We have to find a new set of elementary waves $\{h(\boldsymbol{q})\}$ which satisfy the problem:

$$\min \|X_A\|^2 = \min_{|h\rangle} \langle h|X\rangle\langle X|h\rangle \quad \text{subject to} \quad \langle h|w\rangle = 1 \tag{3.25}$$

The new weights are found as

$$|h\rangle = \frac{(|X\rangle\langle X|)^{-1}}{\langle w|\,(|X\rangle\langle X|)^{-1}\,|w\rangle}\,|w\rangle \tag{3.26}$$

which gives the new expression for the power:

$$P = \left[\langle w|\,(|X\rangle\langle X|)^{-1}\,|w\rangle\right]^{-1} \tag{3.27}$$

For the sake of simplicity we have limited ourselves to scalar fields. Nevertheless, these considerations are easily extended to vector fields as well (see Appendix A.2).

3.4.1 Application to synthetic data: Plane waves

The expression (3.27) for the array power has been deduced independent on the choice of the system of elementary waves $\{\boldsymbol{w}\}$. Here we are going to show how the Capon technique is applied in the particular case when the system $\{\boldsymbol{w}\}$ consists of plane waves (equation 3.12).

For discrete position space the power can be written in a more familiar vector notation:

$$P(\omega, \boldsymbol{k}) = \left[\boldsymbol{w}^{\dagger}(\boldsymbol{k})\mathcal{M}^{-1}(\omega)\boldsymbol{w}(\boldsymbol{k})\right]^{-1} \tag{3.28}$$

where

$$[\mathcal{M}(\omega)]_{ij} = \tilde{X}_i^\star(\omega)\tilde{X}_j(\omega) \tag{3.29}$$

and

$$w_j(\boldsymbol{k}) = \frac{1}{\sqrt{S}}\, e^{i\boldsymbol{k}\cdot\boldsymbol{r}_j} \tag{3.30}$$

The indexes i and j run over the position space i.e. over the sensors.

The separation of space and time in (3.28) is accomplished by applying the time domain Fourier transformation (3.7) on the measured data. Our strategy is to find the frequency ω_0 of the dominant wave by analyzing the Fourier power spectrum (3.8) for each sensor and then to compute the array power (3.28) for ω_0 fixed for each point of a grid in the three dimensional wave vector space. The position in the k-space for which the resulting array power maximizes is giving the wave vector $\boldsymbol{k}_0$ corresponding to the wave with frequency ω_0. Of course, if there are multiple waves with different frequencies discernible in the time domain Fourier transformation, the procedure can be repeated for each of them since the wave vector corresponding to a frequency ω_1 will not influence in any way the array power computed for a different frequency ω_2. On the other hand, two waves having frequencies closer than the resolution of the time domain Fourier transformation will both appear in the computed array power, resulting in local maxima corresponding to their wave vectors. Depending on the number of sensors in the array and on their spatial configuration these maxima will or will be not resolved. Note that the previous scenario does not include coherent waves. The resulting interference pattern would render the method unusable.

On the invertibility of $\mathcal{M}$

As can easily be seen from (3.29), the matrix $\mathcal{M}$ has elements of the form $v_i v_j^\star$ being therefore singular. Nevertheless, we need to compute the array power (3.28). One way to do this is to apply a regularization procedure.

Assume that we are interested in the frequency ω_0. The time resolution of our measured data is Δt which gives a frequency resolution of $\Delta\omega(N) = 2\pi/(N\Delta t)$ where N is the number of samples in the data interval. We use the notation $\tilde{X}|_{t_1}^{t_2}(\omega)$ for the result of the Fourier transformation applied to the data subinterval between t_1 and t_2. The Fourier transform of one data interval, measured by the s sensor, containing $N' < N$ data points, shifted with pl data points from the moment t_0 and corresponding to a frequency shifted with $m\Delta\omega(N')$ from the frequency of interest ω_0, is:

$$\tilde{X}_s^{lm}(\omega_0) = \tilde{X}_s\Big|_{t_0+pl\Delta t}^{t_0+(pl+N')\Delta t}\big(\omega_0 + m\Delta\omega(N')\big) \tag{3.31}$$

Then we construct the $\mathcal{M}$ matrix by averaging both in the time and in the frequency domain:

$$[\mathcal{M}(\omega_0)]_{ij} = \frac{1}{L(2M+1)} \sum_{\substack{l=0\\ \text{time}}}^{L-1} \sum_{\substack{m=-M\\ \text{frequency}}}^{M} \left[\tilde{X}_i^{lm}(\omega_0)\right]^\star \tilde{X}_j^{lm}(\omega_0) \tag{3.32}$$

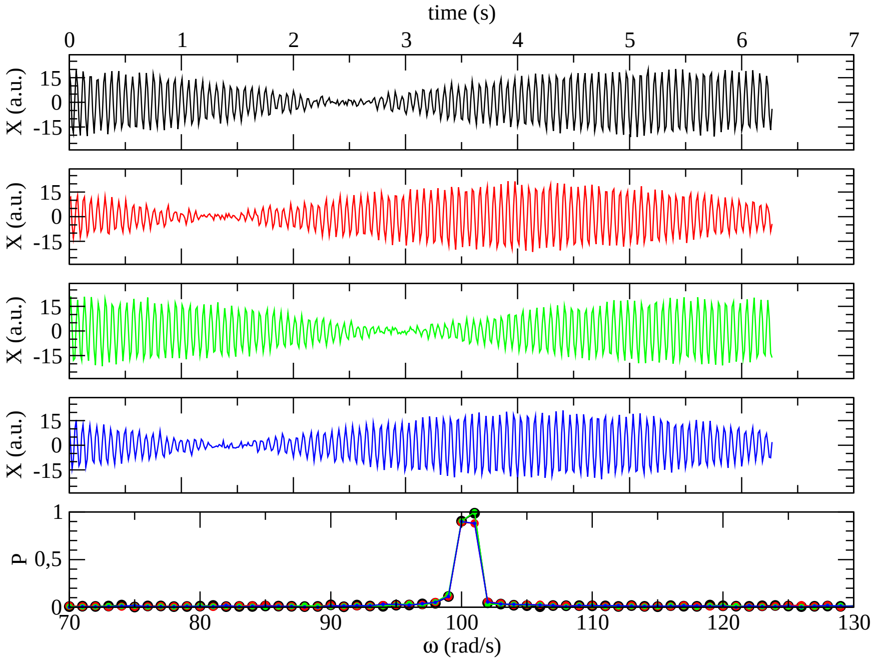

Figure 3.7: Model data for two plane waves. The first four panels illustrate the measured data, the fifth shows the corresponding Fourier power spectra. The frequencies (ω') of the waves are 100.2 rad/s, respectively 99.6 rad/s. Note that the two waves cannot be resolved by Fourier analysis even without averaging.

The $\mathcal{M}$ matrix obtained this way is no longer singular and can be inverted. The price to be paid is a decreased frequency resolution. We loose resolution once by mixing frequencies when we do the frequency averaging and second by applying the Fourier transformation on a shorter interval (the number of samples is reduced from N to N').

The scheme we use in practice to achieve good results with minimum of frequency resolution loss is the following: We start with an interval containing $N = 2^n$, $n > 7$ data samples. For the time averaging we use 16 overlapping intervals, each half the dimension of the original interval i.e. $N' = 2^{n-1}$ and $L = 16$. In order to use the whole data available we have to choose $p = 2^{n-5}$. This strategy also provides the fast Fourier transformation algorithm used for processing the data with a power of two number samples which is needed for maximum efficiency. For the frequency averaging we choose M between 1 and 3 which adds between 2 and 6 neighboring frequencies to the one for which the analysis is done.

Preparing the data

We are going to apply the Capon technique on synthetic data representing various wave fields measured with various sensor array configurations. Since we are interested to find out how the method behaves when more waves with very close frequencies (indiscernible by the Fourier transformation but still not identical) are simultaneously measured we simulate a random deviation from the given frequency ω_0:

$$\omega' = \omega_0 \big[1 + \epsilon_\omega \, \mathrm{rnd}(-1, 1)\big] \tag{3.33}$$

where $\mathrm{rnd}(x, y)$ is a random number between x and y, and ϵ_ω represents the amount of deviation from the given value. In what follows we usually analyze data intervals with length of 100 wave periods. In an ideal case this would provide a frequency resolution $\Delta\omega = \omega/100$ but since we use the regularization technique previously described the resolution in frequency domain is reduced under $\omega/50$ due to time averaging and even more due to frequency averaging. This is the value we choose for ϵ_ω to assure the waves will not be resolved by Fourier filtering. The frequency ω_0 is chosen to be 100 rad/s and the data interval for one sensor consists of 512 time samples.

The model field corresponding to one plane wave is

$$X(\boldsymbol{k}', \omega', \boldsymbol{r}, t) = X_0 \left[\Re\big(\exp\{i(\boldsymbol{k}' \cdot \boldsymbol{r} - \omega' t + \varphi)\}\big) + \epsilon_X \, \mathrm{rnd}(-1, 1) \right] \tag{3.34}$$

The second term in the above expression represents the random noise with the level specified by ϵ_X. We typically choose a value of 1/10 for this parameter.

The phase φ is also randomly chosen. To take into account errors in in positioning of the sensors, $\boldsymbol{r}_s$ is transformed into $\boldsymbol{r}'_s$:

$$\boldsymbol{r}'_s = \boldsymbol{r}_s + \epsilon_{\boldsymbol{r}} \mathbf{rnd}(-1, 1) \min_{i,j}(|\boldsymbol{r}_i - \boldsymbol{r}_j|) \tag{3.35}$$

The error magnitude is given by $\epsilon_{\boldsymbol{r}}$ and for our model data is equal to 1/100. The final model data is obtained by summing over the desired number of waves. An example of such synthetic data representing two plane waves measured by four sensors arranged in a regular tetrahedron configuration is shown in figure (3.7).

Wave vector determination

The first case we are going to investigate is one plane wave detected with a regular tetrahedron sensor array. As shown in section (3.3.1) the tetrahedron configuration requires the minimum number of sensors to uniquely determine the wave vector. The distance between sensors is 10 km. As we did for the beamformer technique, we use the array reference system. The model data was produced with a frequency $\omega' = 98.37$ rad/s and a wave length $\lambda' = 26$ km. The model wave propagates along a direction given by 40° longitude and 60° latitude. We first Fourier analyze the whole 512 s model data to determine the wave frequency. The result is $\omega = 98$ rad/s which will be used as analysis frequency for the Capon technique. Following the procedure described on page 37 we compute the $\mathcal{M}$ matrix averaged in time and frequency domain. The matrix $\mathcal{M}$ now contains all the information about the measured data which will be used in our analysis and no assumption yet about the wave field. Only when we calculate the array power (3.28) using the plane waves (3.30) as elementary waves do we treat the measured field as a superposition of plane waves.

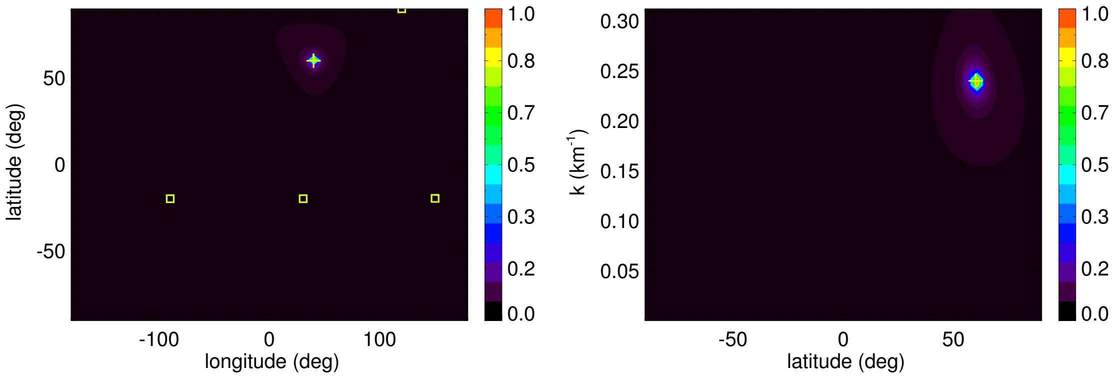

Figure 3.8: Array power for one wave detected with a regular tetrahedron array sensor. The real location of the wave vector is represented by the plus sign. In the longitude – latitude plot the sensor locations are represented by squares.

	ω (rad/s)	k (km^{-1})	longitude (deg)	latitude (deg)
data	98.4	0.240	40.0	60.0
result	98.0	0.242	40.4	60.6

Table 3.2: Capon technique results for one plane wave detected with a regular tetrahedron sensor array. Both the frequency and the wave vector are well determined.

The array power computed on a grid of $50 \times 50 \times 50$ points in a sphere with radius k_{Nyquist} in the wave vector space is shown in figure (3.8). The power maximum lies at the correct position and is not only much sharper than the maximum for the beamformer using the same array configuration but is even much sharper than the maximum for the beamformer using 64 sensors in figure (3.6). The wave vector deduced from the position of the maximum array power and the input values used for generating the model data are given in table (3.2).

We have seen in section (3.3.1) that the beamformer technique is unable to analyze a wave field consisting from more than one wave when using a tetrahedron sensor array. To find out if the Capon technique can deal with multiple waves with close frequencies detected with a tetrahedron sensor array we analyze simulated data which consists from two plane waves with the frequencies of 99.6 rad/s and

	Wave 1		Wave 2	
	data	result	data	result
longitude (deg)	40	40.4	-30	-33.1
latitude (deg)	60	60.6	20	16.5
frequency (rad/s)	99.6	100	100.2	100
wave number (km^{-1})	0.242	0.244	0.134	0.135

Table 3.3: Capon technique results for two plane waves detected with a regular tetrahedron sensor array. Both waves are well recovered from the data.

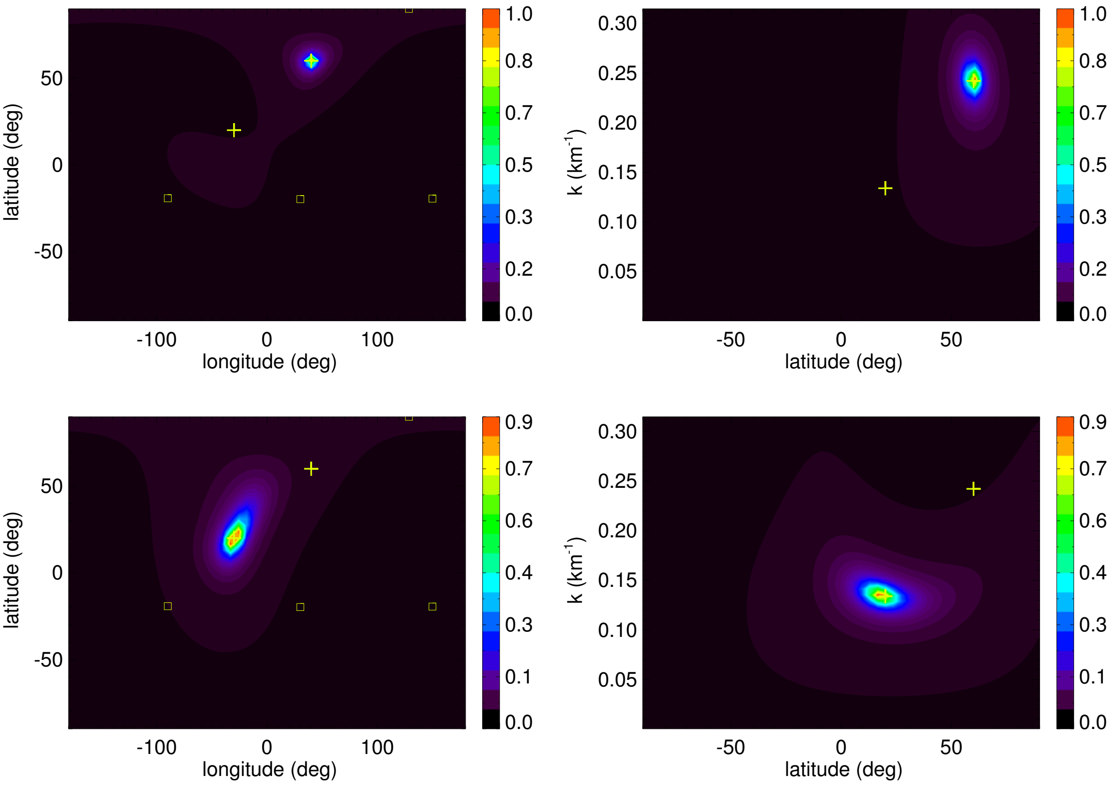

Figure 3.9: Array power for two waves detected with a regular tetrahedron array sensor. The symbols have the same meaning as in figure (3.8). The power maxima become wider than for the single wave case but they are still well defined.

100.2 rad/s. The 99.6 rad/s wave has the same wave vector as for the single wave case (wave length: 26 km, longitude: 40°, latitude: 60°) while the 100.2 rad/s wave has a wave length of 47 km and its propagation direction is given by a longitude of $-30°$ and a latitude of 20°. Both waves have the same amplitude. We use the same array configuration as we did for the single wave. The simulated data is shown in the figure (3.7). The slightly different frequencies give rise to the beats visible in the data panels but they are not resolved in the power spectra.

We compute the output power the same way as for the single wave and we are able to identify two local maxima corresponding to the two waves modeled. The figure (3.9) shows slices through the resulted output power. The wave vectors for the both waves are accurately determined by the position of the power maxima, the results being given in the table (3.3). This demonstrates that the Capon technique can be used for wave vector determination with a tetrahedron array configuration in real situations when more than one wave is detected.

If we simulate three or more waves having the same amplitude, the power maxima become wider and begin to shift from the correct positions and to merge. Note that this problem only occurs when the waves can not be resolved by Fourier analysis. Nevertheless, if one of the waves dominates the others, its wave vector is still correctly determined by the absolute maximum in the output power.

To resolve many waves with frequencies closer than Fourier analysis resolution

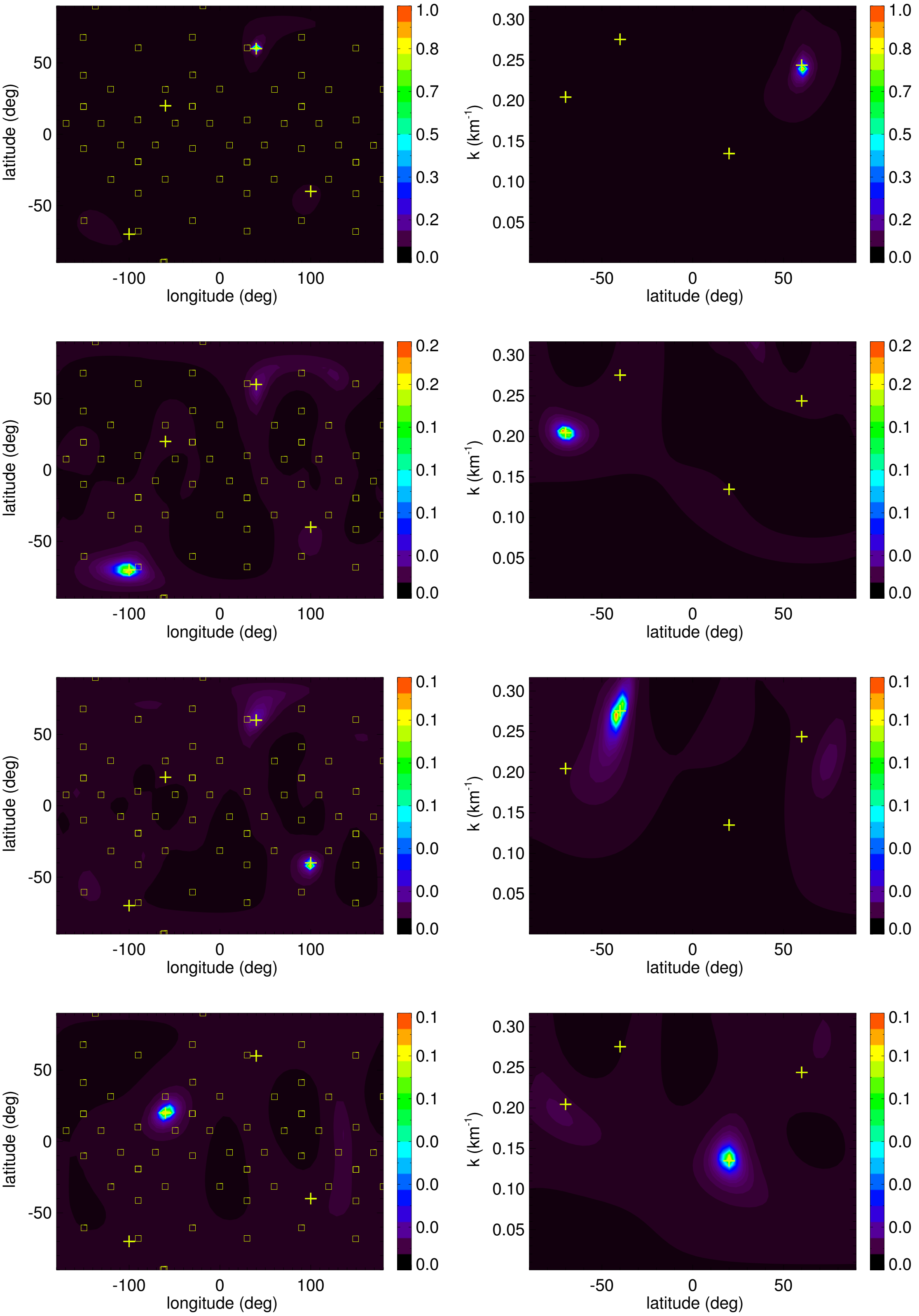

Figure 3.10: Array power for four waves detected with a cube array consisting of 64 sensors. The symbols have the same meaning as in figure (3.8).

	Wave 1		Wave 2		Wave 3		Wave 4	
	data	result	data	result	data	result	data	result
long (deg)	40	40.4	-60	-62.4	100	99.2	-100	-99.2
lat (deg)	60	60.6	20	20.2	-40	-42.2	-70	-71.6
ω (rad/s)	100.9	100	99.8	100	100.2	100	101.5	100
k (km^{-1})	0.243	0.239	0.135	0.136	0.275	0.272	0.204	0.207

Table 3.4: Capon technique results for four plane waves detected with a cube array consisting of 64 sensors. All the wave vectors are recovered with high accuracy.

	Wave 1		Wave 2		Wave 3	
	data	result	data	result	data	result
long (deg)	40	40.4	-60	-62.4	100	99.18
lat (deg)	60	60.6	20	20.2	-40	-38.57
ω (rad/s)	98.7	100	100	100	101.6	100
k (km^{-1})	0.253	0.252	0.275	0.271	0.234	0.232

Table 3.5: Capon technique results for three three dimensional vector waves detected with a tetrahedron sensor array.

power we can increase the number of sensors in the array. As for an example, a 64 sensor array can easily resolve four waves as shown in the figure (3.10). The simulated wave vectors and the recovered ones as well as the frequencies are given in table (3.4).

If increasing the number of sensors is not possible there are other possibilities to resolve more than two waves with close frequencies simultaneously detected. Remember, up to now we considered only scalar fields in our simulations. However, this tool is intended to be used for analyzing Cluster data. Cluster provides vectorial measurements for the magnetic and electric field and by analyzing only their magnitudes we lose precious information. We can use all three components of either magnetic or electric field measurements or we can combine both in a six component vector. The array output power (3.28) computed as described in the appendix (A.2) becomes

$$P(\omega, \boldsymbol{k}) = \mathrm{trace}\left(\left[\mathcal{W}^{\dagger}(\boldsymbol{k})\mathcal{M}^{-1}(\omega)\mathcal{W}(\boldsymbol{k})\right]^{-1}\right) \tag{3.36}$$

To illustrate how using the whole information contained in a vectorial field measurement influences the resolution of the method we analyze a vector field consisting of three components obeying the plane wave propagation law, each component being described by equation (3.34). The resulted array output power is presented in figure (3.11). From the figure is clear not only that the technique can now successfully deal with multiple waves but it also have improved accuracy. The parameters of the model waves, together with their recovered values are given in the table (3.5).

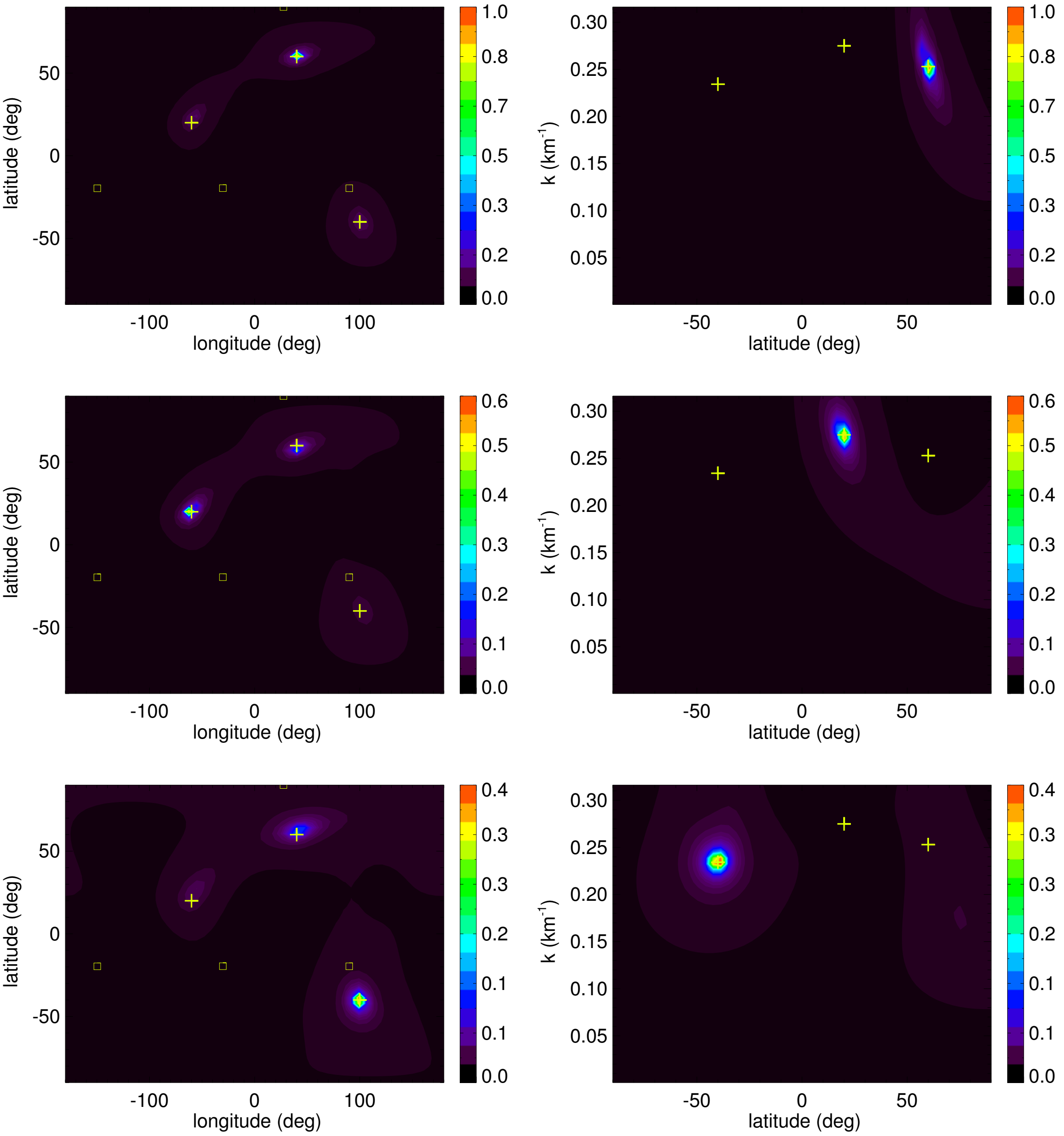

Figure 3.11: Array power for three three dimensional vector waves detected with a tetrahedron sensor array. Using all the three vector components increases the resolution of the method. The symbols have the same meaning as in figure (3.8).

Physical constrains can be directly included into the expression of the output power (*Motschmann et al.* 1998). Examples are relations between the electric and the magnetic field (*Tjulin et al.* 2005), or properties of the measured field itself. Imposing constrains helps to filter the measured signal which eliminates part of the background power and further improves the resolution. The *wave telescope* technique referred also as *k-filtering* analyzes the vectorial magnetic field signal and uses its divergence free nature as a constrain.

For plane waves, i.e. $\boldsymbol{B} = \boldsymbol{B}_0 \exp\{i(\boldsymbol{k} \cdot \boldsymbol{r} - \omega t)\}$, the divergence of the magnetic field is proportional to the projection of the magnetic field on the wave vector:

$$\boldsymbol{\nabla} \cdot \boldsymbol{B} = i\boldsymbol{k} \cdot \boldsymbol{B} = 0 \tag{3.37}$$

This means that the magnetic $\boldsymbol{B}$ field can be replaced with $\boldsymbol{B} + (\boldsymbol{B} \cdot \hat{\boldsymbol{k}})\hat{\boldsymbol{k}}$ which is equivalent with replacing it with $\mathcal{V}(\hat{\boldsymbol{k}})\boldsymbol{B}$, where

$$\mathcal{V}(\hat{\boldsymbol{k}}) = \mathcal{I} + \hat{\boldsymbol{k}}\hat{\boldsymbol{k}}^{\mathsf{T}} \tag{3.38}$$

The effect on the output power (3.36) is to replace $\mathcal{W}(\boldsymbol{k})$ with $\mathcal{W}(\boldsymbol{k})\mathcal{V}(\hat{\boldsymbol{k}})$ yielding

$$P(\omega, \boldsymbol{k}) = \operatorname{trace}\left(\left[\mathcal{V}^{\dagger}(\hat{\boldsymbol{k}})\mathcal{W}^{\dagger}(\boldsymbol{k})\mathcal{M}^{-1}(\omega)\mathcal{W}(\boldsymbol{k})\mathcal{V}(\hat{\boldsymbol{k}})\right]^{-1} \right) \tag{3.39}$$

Motschmann et al. (1995) show that the wave telescope is able to resolve up to seven distinct plane waves using a tetrahedron configuration of the sensors.

Wave length validity domain

We have seen in section (3.3) that a sensor array can be used to determine the k vector for waves with wave lengths only within a limited range. While the low limit is clearly stated by Nyquist theorem, there is no upper limit in principle for the wave length to be determined with a given sensor array. However, due to the finite dimension of the sensor array, in practice we cannot determine arbitrary long wave lengths.

Increasing the wave length decreases the resolution of the tool resulting in broader power maxima. To investigate this phenomenon we use a regular tetrahedron sensor array configuration to analyze artificial data representing two three-component plane waves. The ratio between their wave lengths is 1.5 and the shortest wave length takes increasing values: 10, 40, and 80 spacecraft separations. The results are shown in figure (3.12).

Even for the least favorable case ($\lambda_1 = 800\,\text{km}$) both input waves are recovered. However, the resolution decreases very much, and the power maxima become very broad and begin to merge with each other. A safe limit for the upper wave length value to be used in practice for a regular tetrahedron configuration seems to be around 50 spacecraft separation distances. This limit might be different for different array configurations. A possible working value for the validity domain for an arbitrary configuration is $\lambda \in (2d_{\max}, 50d_{\min})$.

The finite wave length domain for a given sensor array configuration has implications in the design of multi spacecraft missions which investigate different scales at the same time. If for each scale a group of minimum four spacecraft with separations characterizing the scale to be investigate is used, then it makes sense to combine measurements from two different groups only if their validity domains are overlapping and only for the wave lengths within the domain intersection.

Plane wave telescope applied to non-planar waves

The expression (3.27) is general but the choice (3.30) for the elementary waves $\{\boldsymbol{w}\}$ implies a plane waves representation of the detected wave field. The system of plane

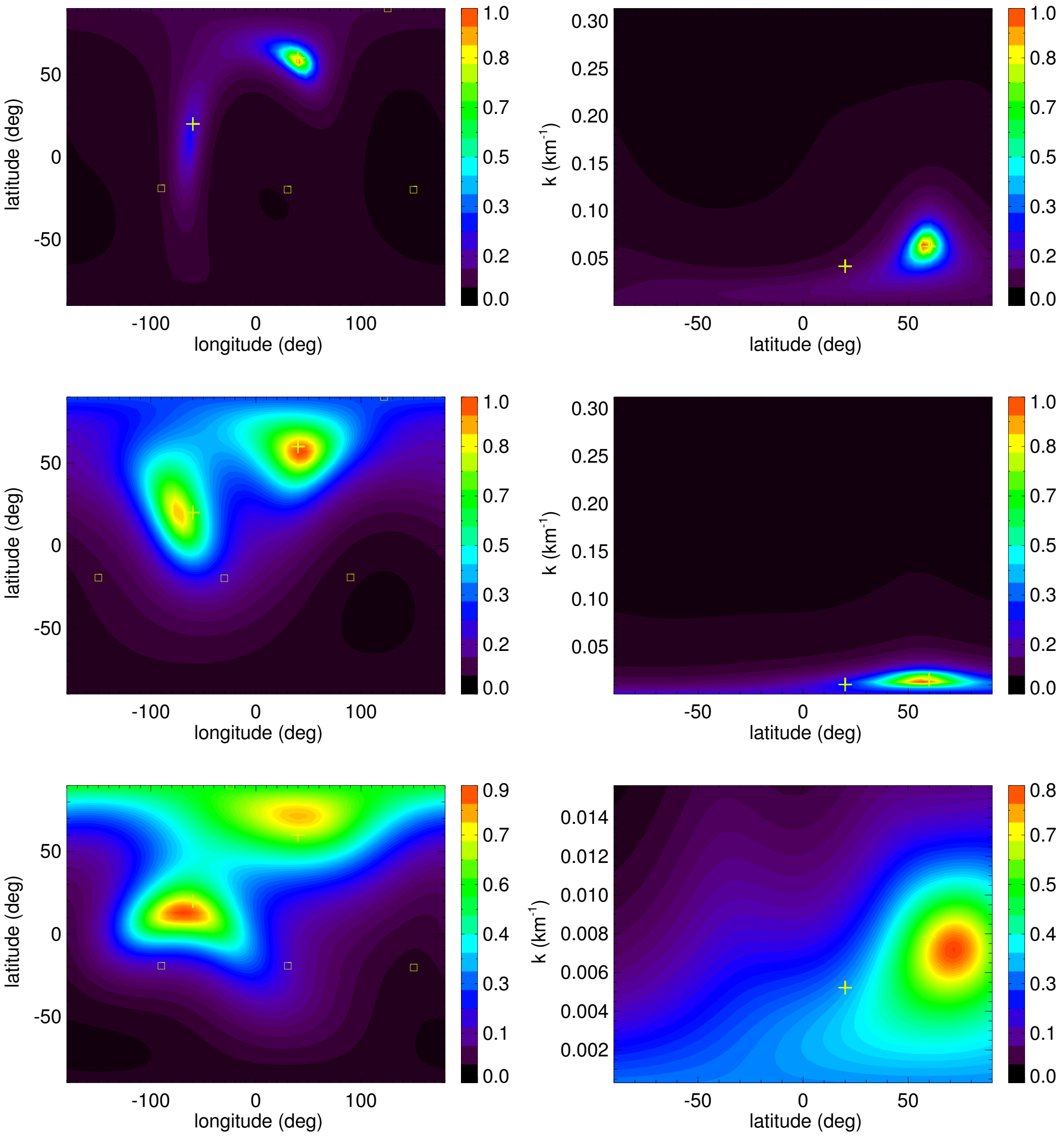

Figure 3.12: Wave telescope applied to a two plane waves wave field at the long wave length limit. The wave lengths in spacecraft separation units are from top to bottom: 10 and 15, 40 and 60, and 80 and 120. Only the power slices corresponding to the shortest wave length are shown.

waves ($\exp\{i(\boldsymbol{k}\cdot\boldsymbol{r}-\omega t)\}$) is indeed a basis for the wave field space, i.e. any wave field can be uniquely represented by a superposition of plane waves provided the wave field is known at all points in space and all moments in time. As discussed in section (3.3), since we have access only to a limited number of measurements in space and time, the plane waves representation is no longer unique.

The wave telescope can at best represent the wave field for a given frequency by several plane waves with different propagation directions and different wave lengths and most of the times by only *one* plane wave. What happens when the measured wave field truly consists from an infinite number of superposed plane waves with

distance (km)	200	150	100	50	40	30	20	10	2
$\Delta\varphi$ (deg)	0.41	0.41	7.75	0.41	6.94	7.75	37.1	21.6	51.0
$\Delta\theta$ (deg)	0.61	0.61	3.06	0.61	0.61	3.06	0.61	36.1	25.1
$\Delta k \times 10^3$ (km^{-1})	0.75	0.75	0.75	0.75	5.64	7.22	0.75	13.7	65.2

Table 3.6: The deviation of determined wave vectors from the given ones for various distances between the wave source and the center of a tetrahedron array with an average separation of 10 km. The grid resolution is 7.2° for the longitude (φ), 3.6° for the latitude (θ) and 6×10^{-3} km^{-1} for the wave number.

comparable amplitudes? An example of such a wave field is the wave field produced by a point source which is generating spherical waves. In this section we are going to study the results of the wave telescope when applied to a wave field consisting from spherical waves.

We generate synthetic data in a similar fashion as shown in the section (3.4.1). The difference is that equation (3.34) is changed to represent now the component j of a spherical wave coming from a point source located at the position $\boldsymbol{r}'$ and detected by the sensor s at position $\boldsymbol{r}_s$:

$$X_j(\boldsymbol{r}', k', \omega', \boldsymbol{r}_s, t) = \frac{X_{0j}}{|\boldsymbol{r}_s - \boldsymbol{r}'|}\left[\Re\big(\exp\{i(k'|\boldsymbol{r}_s - \boldsymbol{r}'| - \omega' t + \varphi_j)\}\big) + \epsilon_X \,\mathrm{rnd}_j(-1,1)\right] \tag{3.40}$$

Let us begin by investigating the dependence of the array power on the curvature of the detected wave fronts. In order to do so, we analyze the wave field produced by a point source situated at a latitude of $-60°$ and a longitude of $-140°$ producing a wave having a frequency of 100 Hz and a wave length of 5.4 average spacecraft distances. When the distance to the source tends to infinity the perturbation reaching the sensor array tends a plane wave with the direction of propagation given by 40° longitude and 60° latitude. Different distances to the wave source give different local curvatures of the wave fronts.

The array power computed using a tetrahedron sensor array with a separation of 10 km detecting a wave generated by a source at distances of 200, 30, 10, and 2 km from the center of mass of the configuration is shown in the figure (3.13). Results for more distances are listed in the table (3.6). We see that spherical waves with reasonable curvatures are interpreted by the wave telescope as plane waves propagating in a direction opposite to the direction to the wave source. The error caused by the wave front curvature is under the grid resolution even for sources as close as three average spacecraft separations. However, under this distance the tool is not anymore able to give accurate results and of course it gets totally confused when the source emits from inside the configuration.

The inability of the wave telescope to give accurate results when the wave source is very close to the spacecraft configuration could raise difficulties in justifying its application when the array is going through an active region where waves are generated at random places. To investigate the wave telescope behavior when crossing

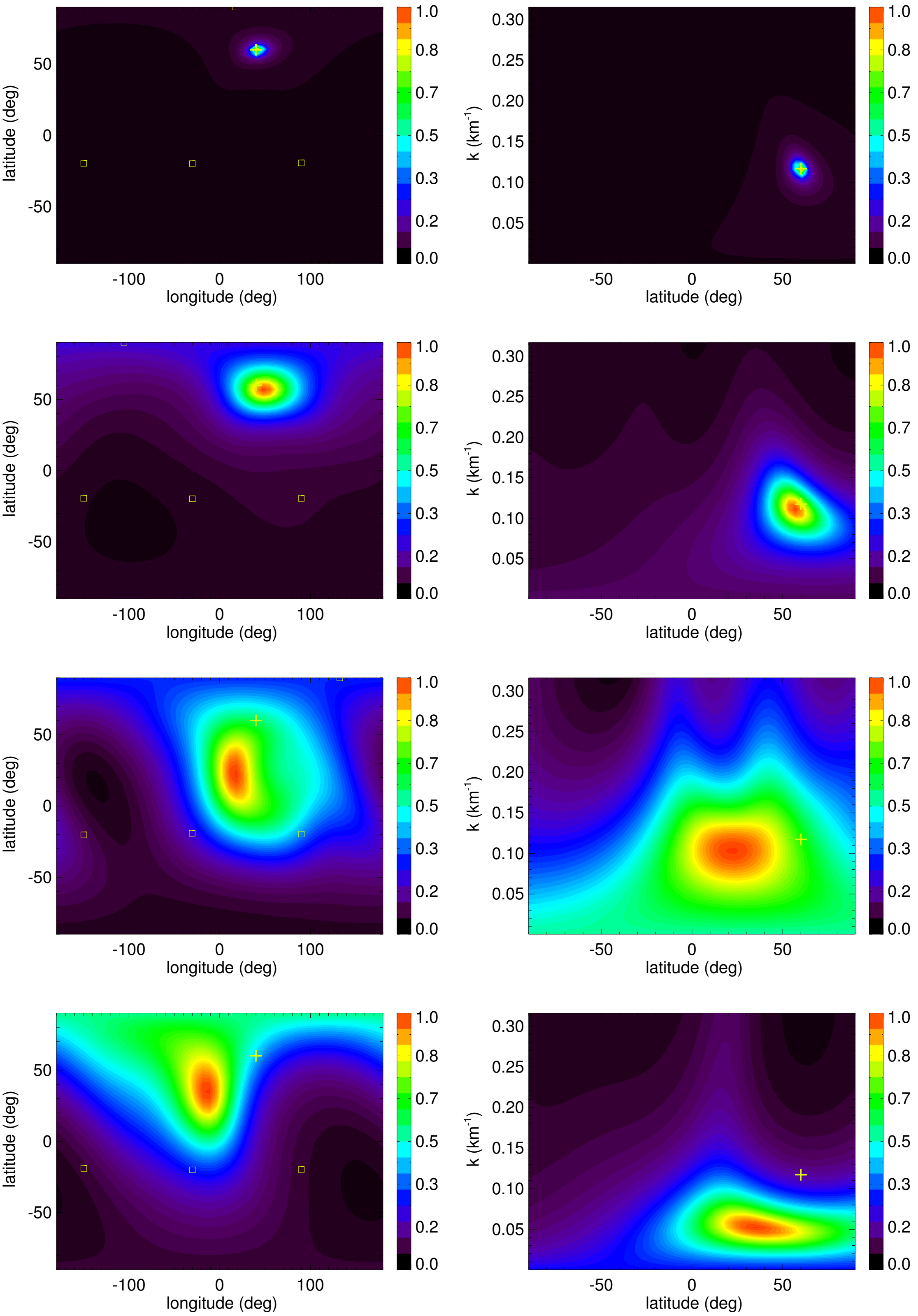

Figure 3.13: Results for a spherical wave detected with a tetrahedron sensor array. The distances between the wave source and the center of mass of the sensor configuration are from top to bottom: 20, 3, 1, and 0.2 (source inside the array) average s/c distances.

such a region we analyze synthetic data simulating a wave field generated by two point sources, one at a fixed distance of five average spacecraft separations from the configuration center and the other placed at various distances beginning from inside the configuration up to 80 average spacecraft separations. We are interested to see which wave is associated to the global array power maximum and how accurate its wave vector is determined.

From the study of single source wave field we know that if alone, the fixed distance source would be easily found by the wave telescope. Now it competes with the variable distance source. We distinguish four different regimes depending on the distance d to the variable distance source:

I. $d < 40\,\mathrm{km}$:
The array power maximum corresponds to the fixed distance source (remotest).

II. $40\,\mathrm{km} < d < 60\,\mathrm{km}$:
The array power maximum is randomly associated with one of the sources.

III. $60\,\mathrm{km} < d < 700\,\mathrm{km}$:
The array power maximum corresponds to the variable distance source (remotest).

IV. $d > 700\,\mathrm{km}$:
The array power maximum corresponds to the fixed distance source (closest).

Every time the wave vector is accurately recovered.

In the first interval the wave fronts from the variable distance source are very curved and the wave amplitude is very different between sensors. This prevents the wave telescope to recognize it as a plane wave. The array power maximum corresponds to the fixed distance source. In the second interval the curvatures of both wave fronts are comparable. The maximum array power has no definite preference for either source. In the third interval the variable distance source gets far enough to significantly lower the wave front curvature at the array location. The wave associated with is is now closer to a plane wave than the wave generated by the fixed distance source. As a consequence the maximum array power corresponds now to the variable distance source. This remains true up to very large distances even if the radial decay greatly diminish the wave energy density compared to the fixed distance source. Finally, in the fourth interval the variable distance source reaches distances for which the planarity of the wave front is no longer sufficient to balance the radial decay and the wave telescope switches back to the closer fixed distance wave source.

The conclusion is that the wave telescope is extremely selective when wave fronts with different curvatures are simultaneously detected. It strongly favors the wave which is closest to a plane wave even when the energy density corresponding to the plane wave is orders of magnitude lower then the energy density corresponding to the non-planar wave. It follows that in fact the wave telescope can be safely used even when waves are generated very close or even inside the sensor array with the condition that reasonably distant sources participate as well to the generation of the detected wave field.

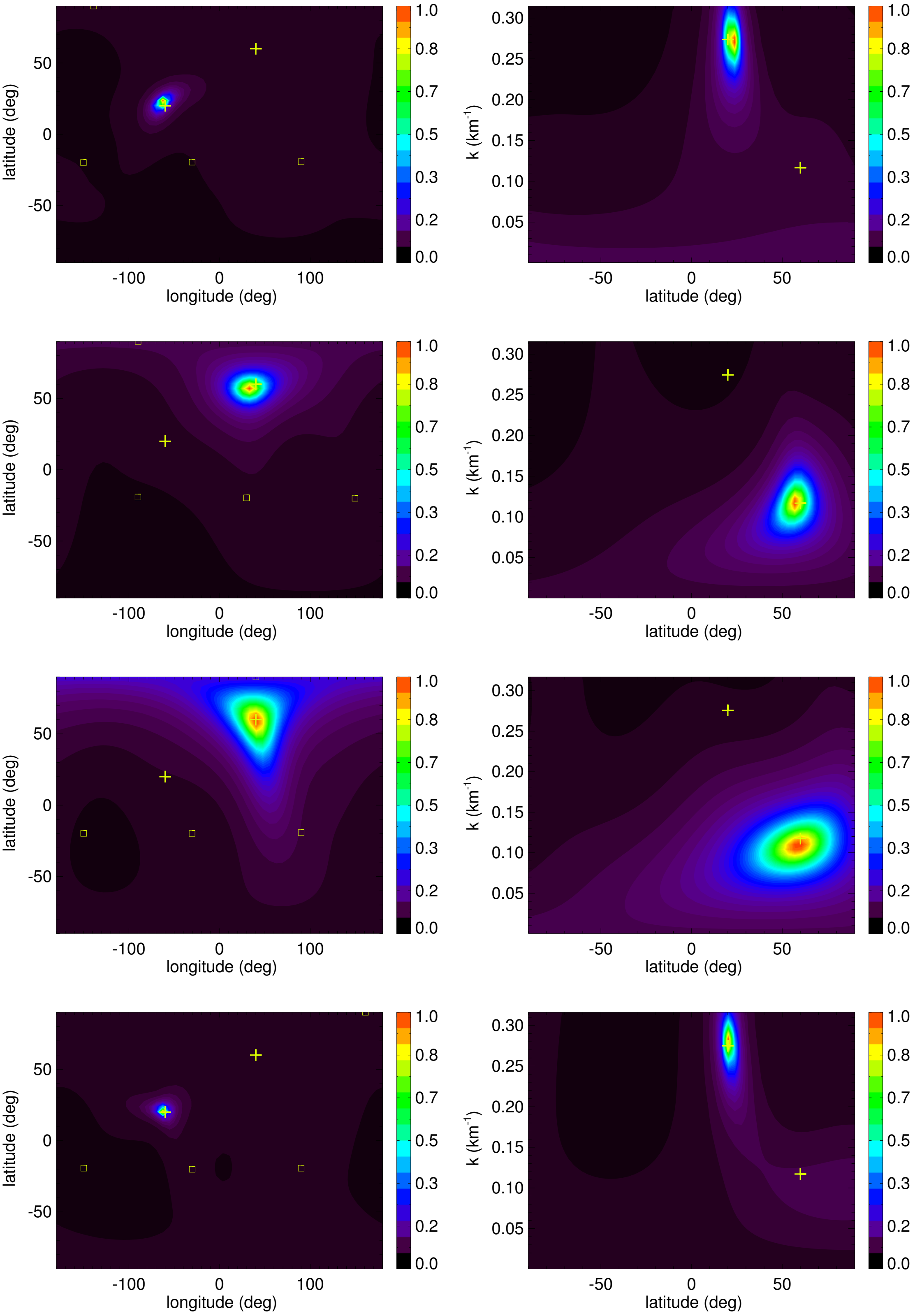

Figure 3.14: Array power for a wave field produced by two point sources detected with a tetrahedron array with an average separation of 10 km. The source producing the wave propagating in the direction (long=−60°, lat=40°) is at a fixed distance of 50 km, from the configuration center. The second source (long=20°, lat=60°) is placed at 2, 40, 60, and 70 km (top to bottom).

The wave telescope is giving the far field view of the detected waves. The information contained in the curvature of the wave fronts is disregarded. This is why the wave telescope can say nothing about the distance to the wave sources. If we are to use this information we have to give up the plane waves representation.

4

Source locator

4.1 Introduction 55
4.2 Source locator 55
4.3 Spherical waves and dynamic effects 56
4.4 Application to synthetic data 64
4.5 Discussion 73
4.6 Application to Cluster data 75

4.1 Introduction

We have seen in the previous chapter that using sensor arrays providing multi-point measurements in space we can successfully determine the wave vectors of the dominant waves of a measured wave field. This is achieved by expanding the measured wave field into its plane wave components using the technique given by *Capon et al.* (1967). The method works well even with as few as four sensors which represent the minimum number of space samples required to recover a three dimensional quantity. When applied to magnetic field using its divergence free nature as a constraint, the method is known as the wave telescope technique. Using Cluster magnetic field data, the wave telescope provided the first direct measurement of plasma wave vectors in an extraterrestrial environment (*Glassmeier et al.* 2001).

While the plane waves representation has multiple advantages, it also limits the applicability of the wave telescope to the far field case. As a result, this method cannot directly answer fundamental questions related to the sources of the measured field. Examples are finding the positions of the wave sources, their motion or their geometrical characteristics. If these questions are to be answered, we have to give up the plane waves representation in favor of a representation which takes into account the distance to the wave source, such as the spherical waves representation.

In what follows, we discuss in detail the Capon technique using the spherical waves representation, hereafter called *source locator*.

4.2 Source locator

In order to determine the sources locations we have to choose a system of elementary waves which contains information about the distance to the source. The most natural (and simple) choice is the spherical waves representation where the elementary waves are characterized by $\boldsymbol{q} = (\boldsymbol{r}_{\text{source}}, k, \omega) = (\boldsymbol{r}, k, \omega)$ representing the position, wave number, and frequency of the source. Thus for the sensor s at the position $\boldsymbol{r}_s$ one gets

$$w(\boldsymbol{r}, k, \omega, \boldsymbol{r}_s, t) = C \frac{1}{\rho_s} e^{i(k\rho_s - \omega t)} \tag{4.1}$$

where $\rho_s = \rho(\boldsymbol{r}_s, \boldsymbol{r}) = |\boldsymbol{r}_s - \boldsymbol{r}|$ is the distance between the source and the sensor s. The elementary wave associated to the sensor s becomes after separation of the time dependent part

$$w_s(\boldsymbol{r}, k) = C \frac{1}{\rho_s} e^{ik\rho_s} \tag{4.2}$$

The normalization coefficient is:

$$C = \left(\sum_{\substack{s=1 \\ \text{sensors}}}^{S} \frac{1}{\rho_s^2} \right)^{-1/2} \tag{4.3}$$

Even if the single-sensor elementary wave w_s depends only on the distance ρ_s between source and sensor, the vector $\boldsymbol{w} = (w_1, \ldots, w_S)^{\mathsf{T}}$ depends on $\boldsymbol{R} = (\rho_1, \ldots, \rho_S)^{\mathsf{T}}$

which is a function of the source position. As a consequence, the array power, which has the same formal expression as for the wave telescope (equation 3.36), will also depend on the source position.

$$P(\omega, \boldsymbol{r}, k) = \mathrm{trace}\left(\left[\mathcal{W}^{\dagger}(\boldsymbol{r}, k)\mathcal{M}^{-1}(\omega)\mathcal{W}(\boldsymbol{r}, k)\right]^{-1}\right) \tag{4.4}$$

In contrast to the three dimensional parameter space of the wave telescope $\{\boldsymbol{q}\} = \{\boldsymbol{k}\}$, the parameter space of the source locator $\{\boldsymbol{q}\} = \{\boldsymbol{r}_{\text{source}}, k\}$ is four dimensional. As for the wave telescope, in order to find the source parameters we have to scan the parameter space in order to determine the array power at each point of a grid and identify the power maxima.

The scan domain in the position space can formally be extended to $0 < \rho < \infty$, but the more distant the source is, the more the observed wave will approach a plane wave and the uncertainty in determining the distance will increase. For the wavelength (k-number) space we shall take into consideration the Nyquist theorem otherwise aliasing occurs. It is possible to define the maximum wave number as a function of propagation direction (e.g. *Neubauer and Glassmeier* 1990; *Pinçon and Motschmann* 1998; *Glassmeier et al.* 2001) but we chose the simple approach $k \leq k_{\text{Nyquist}} = \pi/d_{\max}$, $d_{\max}$ being the maximum spacecraft separation.

The resulting array power is a local representation of the wave field. The position $\boldsymbol{r}$ derived from the array power maximum represents the center of spherical shells determined by the source locator by analyzing the local curvature of the wave fronts and the spatial decay of the field. This position is associated with a *virtual source* which generally differs from the real source. The two coincide only when the wave isotropically propagates in an homogeneous medium. In order to relate the position of the virtual source to the position of the real source we have to extrapolate our local knowledge of the propagation medium and to take into account the mode in which the waves propagate. This differs from case to case and no general recipe can be given. As for an example for fast magnetosonic waves the position of the virtual source is a good approximation of the position of the real source but this is not true for an Alfvén wave. It follows that a complete source location analysis would consist of two steps. First, determine the virtual source position using a general procedure, second, link this position to the real wave source using wave mode analysis and medium related considerations. Since it is already far from trivial, we only consider in this chapter the case of isotropic propagation through an homogeneous medium.

4.3 Spherical waves and dynamic effects

By introducing the source point from which the wave originates, the spherical waves representation loses the symmetry to spatial translations characterizing the plane waves representation. While for the plane waves representation only the motion of the Observer relative to the propagation medium was influencing the measurements output through the Doppler effect, for the spherical waves representation the motion of the source comes also into play. It is the interplay between these three key ingredients which determines the final outcome of the measurements. Before we go

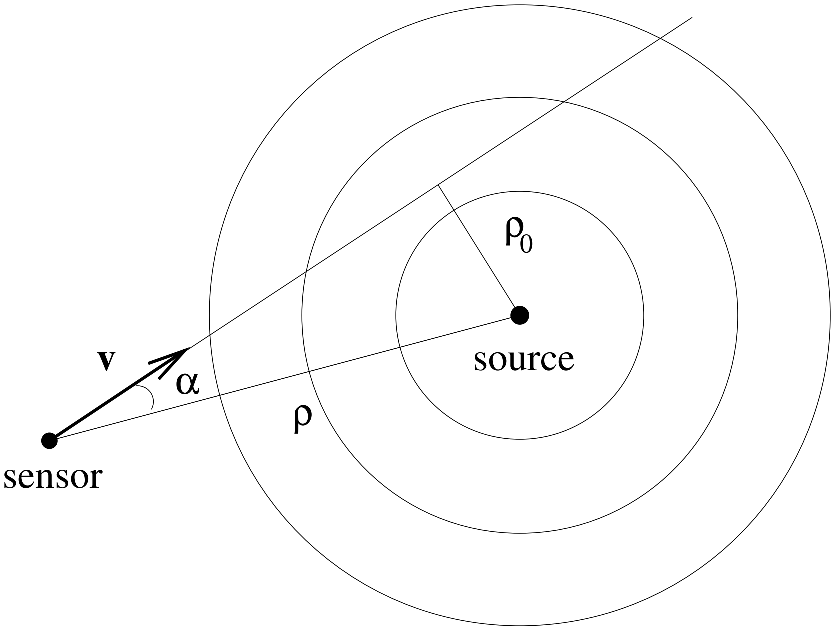

Figure 4.1: The sensor is moving with the velocity v. The measured frequency depends on the angle α between the velocity and the direction to the source.

further with more detailed discussions on the source locator and its applications we need to understand the effect of these motions.

The raw result of the source locator consists of the frequency ω, the local wave length λ, and the position of the local wave front curvature center (virtual source), $\boldsymbol{r}$. This is equivalent with the set $(\omega, \boldsymbol{k}, \rho)$ where $\boldsymbol{k}$ is the *local* wave vector and ρ is the *local* curvature radius, i.e. the distance to the virtual source. We wish to see how these quantities depend on the motions mentioned above. In what follows we place ourselves into the wave source reference system. The Observer moves with the velocity $\boldsymbol{v}$ and the medium moves with the velocity $\boldsymbol{u}$ relative to the source.

For a wave field described by the general expression

$$X(\boldsymbol{r}, t, \boldsymbol{u}) = X_0 e^{i\varphi(\boldsymbol{r}, t, \boldsymbol{u})} \tag{4.5}$$

the local wave vector is given by the gradient of the phase φ

$$\boldsymbol{k}(\boldsymbol{r}, t, \boldsymbol{u}) = \nabla\varphi(\boldsymbol{r}, t, \boldsymbol{u}) \tag{4.6}$$

which is determined by the phase spatial pattern at the moment t and does not depend on the relative motion of the Observer, $\boldsymbol{v}$. Since the wave front is defined by constant phase, the wave vector is always orthogonal to the wave front and it points to the local propagation direction. Note that the wave vector can depend on the medium flow $\boldsymbol{u}$ due to the distortion of the wave fronts by the flow.

For the particular case of plane waves with $\varphi(\boldsymbol{r}, t) = \boldsymbol{k}_0 \cdot \boldsymbol{r} - \omega_0 t$, the wave vector is simply $\boldsymbol{k}_0$. For spherical waves (point source, $\boldsymbol{u} = 0$) with $\varphi(\boldsymbol{r}, t) = k_0\rho - \omega_0 t$, the wave vector points in the opposite direction to the wave source: $\boldsymbol{k}(\boldsymbol{r}) = k_0 \hat{\boldsymbol{e}}_\rho$.

The measured frequency is given by the total time derivative of the phase φ

$$\omega(t) = -\frac{\mathrm{d}\varphi}{\mathrm{d}t} = -\frac{\partial\varphi}{\partial t} - \boldsymbol{v} \cdot \nabla\varphi = \omega_0 - \boldsymbol{v} \cdot \boldsymbol{k} \tag{4.7}$$

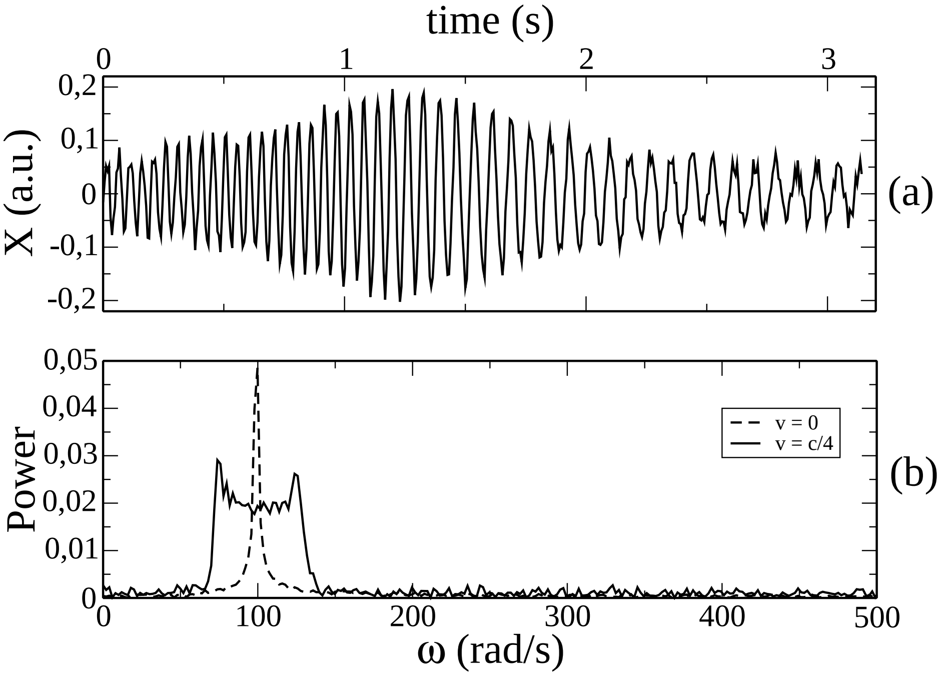

Figure 4.2: Doppler effect. The source frequency is 100 radians per second, the Observer speed is one quarter of the wave phase speed. The top panel illustrates the measurements made by the moving Observer. Note the visible change in both wave amplitude and frequency. The bottom panel shows how the frequency shift appears in the Fourier analysis. The solid line represents the measurements of the moving Observer in contrast with the measurements made by an Observer at rest represented with the dashed line.

The term $\omega_0 = -\partial\varphi/\partial t$ above represents the intrinsic time variation of the wave field and the second term represents the variation seen by the Observer due to its motion through the spatial structure of the phase. In the general case it depends on both the Observer motion and on the propagation medium flow. Equation (4.7) represents the Doppler effect. For plane waves it becomes $\omega = \omega_0 - (\boldsymbol{v} - \boldsymbol{u}) \cdot \boldsymbol{k}_0$.

It is important to realize that the two types of motion lead to fundamentally different effects. The Observer motion has a *relative* effect, only affecting the frequency measured by him. By contrast, the medium flow has an *absolute* effect, distorting the wave fronts and causing global changes to the wave vector field.

4.3.1 Moving Observer: Doppler effect

Let us concentrate on the simple case of a spherical wave detected by a moving Observer as shown in figure (4.1). The wave source is at rest with respect to the propagation medium.

The measured field becomes

$$X = \frac{X_0}{\rho(t)} e^{i[k_0\rho(t) - \omega_0 t]}. \tag{4.8}$$

which leads to a time dependent Doppler shifted frequency given by

$$\omega(t) = \omega_0 \left[1 - \frac{v}{c} \cos \alpha(t)\right] \tag{4.9}$$

In the above relations $\rho(t)$ is the distance between the sensor and the source, $\boldsymbol{v}$ is the sensor velocity, α is the angle between the velocity and the sensor−source direction and $c = \omega_0/k$ is the wave phase velocity.

Figure (4.2) shows both the measurements made by a moving Observer and the corresponding Fourier spectrum. Note that because the frequency depends on time, a given frequency range corresponds to a certain time subinterval which in turn corresponds to a certain position range of the Observer. For instance, the low frequency peak centered around 75 radians per second corresponds to the last part of the data interval measured while the Observer was already moving away from the wave source. It follows that frequency filtering is equivalent with Observer position filtering.

4.3.2 Medium flow: Wave length change

As we have seen in the previous section, when the Observer is moving with respect to the wave source, the measured frequency is no longer fixed but the measured wave length is the same as for the static situation. When the propagation medium is flowing and the source is at rest in the Observer reference frame, the opposite happens. The Observer will measure the same frequency as for the static case but the wave length differs from the original one. In this section we concentrate on the case of a point source emitting waves detected by an Observer at rest in a streaming medium.

Figure (4.3) schematically represents the case for subsonic flow velocities. The wave front emitted at the moment $t = 0$ by the source is drifting with the plasma flow. By the time $t = \tau$ when the wave front reaches the Observer it will be a sphere with a radius $c\tau$ and the center shifted at a distance $u\tau$ from the source in the flow direction. The presence of the flow introduces a preferred direction in the medium. The situation is equivalent with a change of the the wave phase velocity which now depends on the angle with the preferred direction, i.e. is equivalent with anisotropic propagation through the medium.

We call the center of the wave front tangent to the sensor, *ghost source* to differentiate it from a virtual source which has a shifted position from the real source due to "real" anisotropy of the medium. Note that the position of the ghost source is not absolute. It depends on the position of the Observer. If the Observer assumes that he detects a spherical wave isotropically propagating from a point source then he will identify the ghost source as the originating place of the detected wave. In particular, the source locator will give not the position of the real wave source but the position of the ghost source. Therefore it is important to bring the position of the ghost source into relation with the position of the real wave source. From Figure (4.3) we have the following relation:

$$(c\tau)^2 = \rho_{\mathrm{g}}^2 = (u\tau)^2 + \rho^2 - 2u\tau\rho\cos\alpha \tag{4.10}$$

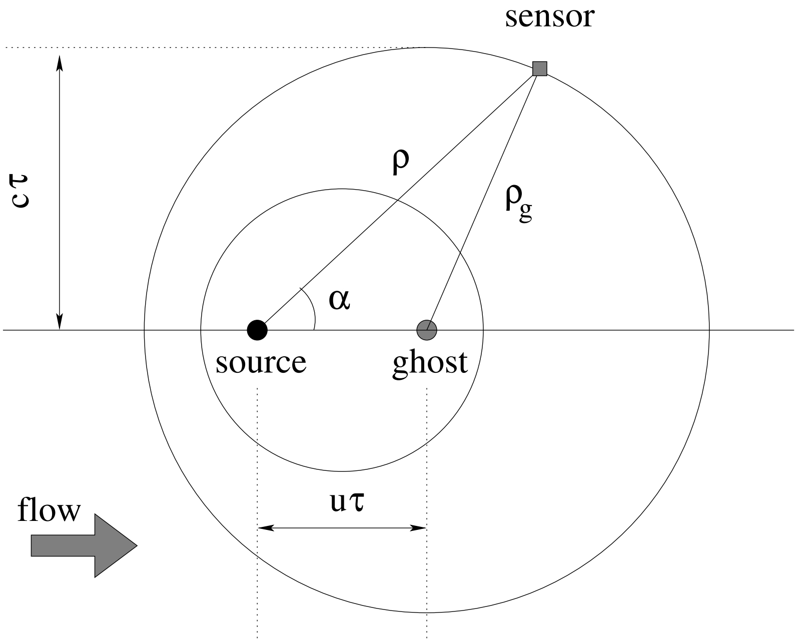

Figure 4.3: Subsonic plasma flow. The sensor is measuring a spherical wave apparently originating from the ghost source position. The measured frequency is the same as for the static case but the measured wave length depends on the angle α between the flow velocity and the source - sensor direction.

from which we can express the distance between the ghost source and the Observer

$$\rho_{\mathrm{g}\pm}(\rho, \alpha, M) = \frac{\rho}{\xi_\pm(M, \alpha)} \tag{4.11}$$

with the notation

$$\xi_\pm(M, \alpha) = M \cos\alpha \pm \sqrt{1 - M^2 \sin^2\alpha}, \tag{4.12}$$

where $M = u/c$ is the Mach number. Consequently, the *arrival time* defined as the time needed for the wave to travel from the source to the Observer is

$$\tau_\pm(\rho, \alpha, M) = \frac{\rho}{c\xi_\pm(M, \alpha)} \tag{4.13}$$

Once we know the arrival time, we can determine the position of the ghost source as:

$$\boldsymbol{r}_{\mathrm{ghost}\pm} = \boldsymbol{r}_{\mathrm{source}} + \boldsymbol{u}\tau_\pm \tag{4.14}$$

The factor $\xi_\pm$ has a number of remarkable properties. One first aspect is that $\xi_\pm$ is not always a real number. Indeed, for $\xi_\pm$ to be a real number, $\sin\alpha$ has to be smaller than $1/M$. This is always true for subsonic flows ($M < 1$) but it gives a limit angle $\alpha_M = \mathrm{asin}(1/M)$ for supersonic flows. The angle α_M defines the *Mach cone* outside which the wave never propagates.

The condition of reality for $\xi_\pm$ is not sufficient to assure that the distance ρ_g in equation (4.10) represents a physical solution. It also has to be positive defined. For subsonic flows only ξ_+ is positive independent on the position of the Observer.

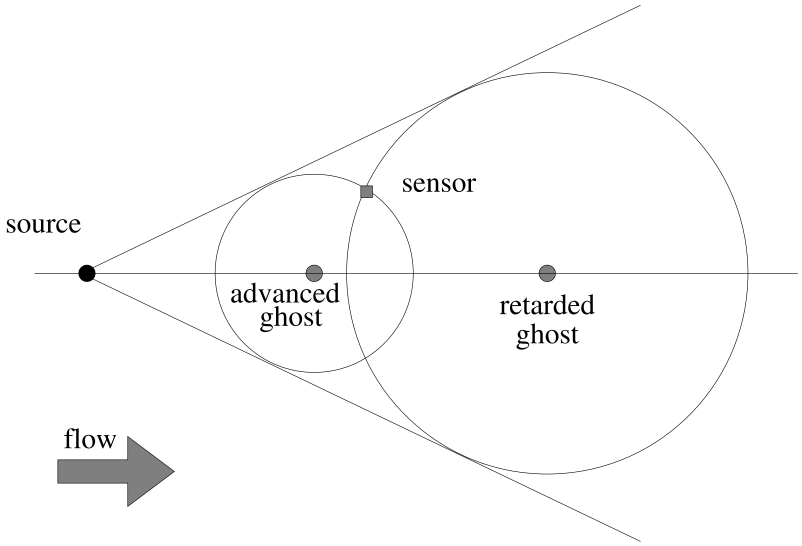

Figure 4.4: Supersonic flow. Both the advanced and retarded waves are measured by the sensor. The ghost sources locations depend on the Mach number and on the position of the sensor, therefore they are different from sensor to sensor.

For supersonic flows both ξ_+ and ξ_- are positively defined inside the Mach cone. Two simultaneously valid solutions mean that the Observer sees two different ghost sources which correspond to one and the same real source. This is sketched in figure (4.4). The wave corresponding to the "+" sign arrives after a short time from the moment of emission, traveling in the flow direction. We call this wave, *advanced wave*. The wave corresponding to the "−" sign travels against the flow and arrives after a longer time from its moment of emission (which is further in the past than the moment of emission of the advanced wave – both waves arrive simultaneously at the Observer). We call this wave *retarded wave*.

Other useful properties of $\xi_\pm$ are expressed by the following relations:

$$\xi_\pm(M,\alpha)\big|_{M=0} = \pm 1 \tag{4.15a}$$

$$\xi_\pm(M,\alpha)\big|_{M=1} = (1 \pm 1)\cos\alpha \tag{4.15b}$$

$$\xi_\pm(M,\alpha)\big|_{\alpha=0} = M \pm 1 \tag{4.15c}$$

$$\xi_\pm(M,\alpha)\big|_{\alpha=\alpha_M} = \sqrt{M^2-1} \tag{4.15d}$$

$$\xi_\pm(M,\alpha)\xi_\mp(M,\alpha) = M^2 - 1 \tag{4.15e}$$

Some of these relations have direct physical interpretations. For instance, equation (4.15a) means that the advanced ghost has the same position with the real wave source in the absence of the flow. The retarded ghost is unphysical. Equation (4.15b) describes the Mach equal one case: The advanced ghost is at finite distance inside the Mach cone but as the Observer approaches the Mach cone surface, the advanced ghost moves towards infinity. The retarded ghost is at infinite distance for any Observer position. Equation (4.15c) gives the ghosts positions when the Observer is on the flow line going through the wave source. Finally, equation (4.15d) corresponds to the Observer being on the Mach cone surface. In this case, $\xi_+ = \xi_-$ and the retarded ghost has the same position as the advanced ghost.

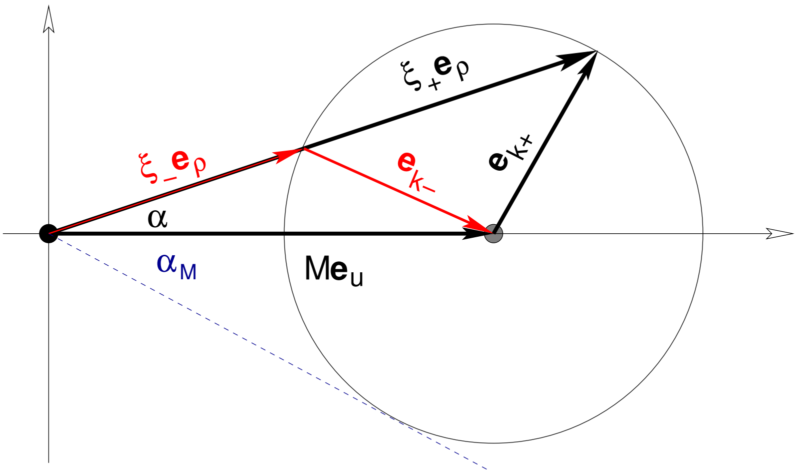

Figure 4.5: Diagram representing the ξ factors and the propagation directions of the advanced and retarded waves. The circle has the radius equal to one and its center has the coordinates (M, 0).

The wave field distorted by the flow takes the form:

$$X(\rho,\alpha,M,t) = \frac{X_0}{\rho_{\mathrm{g}}(\rho,\alpha,M)} e^{i[k_0\rho_{\mathrm{g}}(\rho,\alpha,M)-\omega_0 t]} \tag{4.16}$$

where k_0 and ω_0 are the wave number and the frequency in the absence of the flow.

Using equation (4.6) it is possible to derive the wave vector at the Observer's position:

$$\boldsymbol{k}_\pm(M,\alpha) = \frac{k_0}{\xi_\pm\sqrt{1-M^2\sin^2\alpha}}\,\hat{\boldsymbol{e}}_{k_\pm} \tag{4.17}$$

with the versor of the wave vector given by

$$\hat{\boldsymbol{e}}_{k_\pm} = \pm(\xi_\pm\hat{\boldsymbol{e}}_\rho - M\hat{\boldsymbol{e}}_u) \tag{4.18}$$

The diagram (4.5) conveniently illustrates relations between the ξ factors and the wave propagation directions. Equations (4.15) have a geometrical correspondent here. The unit circle in the diagram has the center situated at the coordinate x equal to the Mach number and $y = 0$. The Mach cone angle α_M is given by tangent through the origin to the unit circle. For a given angle α between the flow direction and the line of sight to the source the two ξ factors are equal to the distances from the origin to the intersection points between the unit circle and the line corresponding to the angle α. The propagation directions of the advanced and of the retarded waves are defined by the directions from the intersection points to the center of the unit circle.

The wave vector (4.17) is orthogonal to the local wave front and it defines the local wave length as $\lambda_\pm = 2\pi/k_\pm$. Note that the definition of the wave length as the distance between two consecutive wave fronts is meaningful only for plane or undisturbed spherical waves.

An interesting property of the wave vector is it's independence on the distance to the wave source at fixed α:

$$\left.\frac{\partial\boldsymbol{k}_\pm}{\partial\rho}\right|_\alpha = 0 \tag{4.19}$$

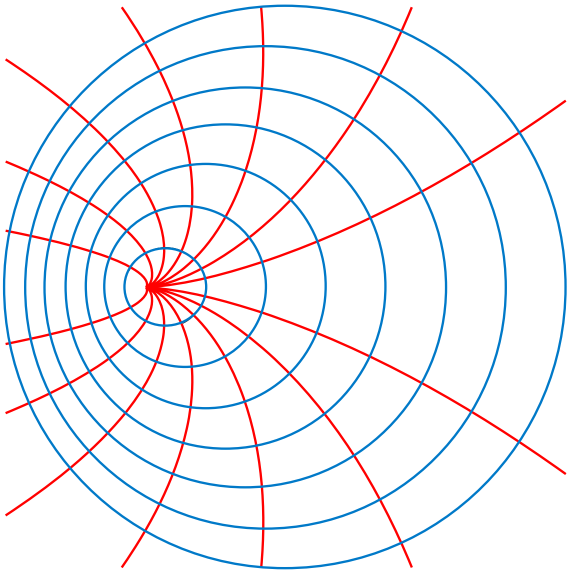

Figure 4.6: Wave fronts (blue) and propagation rays (red) for a point source emitting in a medium flowing with half the wave phase velocity. The rays are curved and tend to bundle up anti-parallel to the flow in the upstream region

Hence the wave vector is the same along any straight line going through the wave source.

The rays are defined as the curve family orthogonal to the wave fronts, or equivalent, the field lines of the wave vector field – everywhere tangent to the wave propagation direction. They are parallel lines for plane waves and strait lines originating from the wave source for undisturbed spherical waves. We wish to find the wave rays in the presence of the flow. To achieve our goal we first rewrite the wave vector in polar coordinates:

$$\boldsymbol{k}_\pm(M,\alpha) = \frac{k_0}{\xi_\pm}\left(\hat{\boldsymbol{e}}_\rho \pm \frac{M\sin\alpha}{\sqrt{1-M^2\sin^2\alpha}}\,\hat{\boldsymbol{e}}_\alpha\right) \tag{4.20}$$

Because the rays are always tangent to the direction of the local wave vector, their equation in polar coordinates is given by

$$\frac{1}{\rho}\frac{\mathrm{d}\rho}{\mathrm{d}\alpha} = \frac{k_\rho}{k_\alpha} \tag{4.21}$$

Solving this differential equation yields the parametric set of ray equations:

$$\rho_\pm^{\pm 1}(C,M,\alpha) = \frac{C\xi_+}{\sqrt{2|1-M|}}\left|\frac{\xi_+ - (M+1)\cos\alpha}{\xi_+ - (M-1)\cos\alpha}\right|^{\frac{1}{2M}} \tag{4.22}$$

The integration constant $C \in (0,\infty)$ distinguishes between different rays.

In figures (4.6) and (4.7) we plotted both the wave fronts and the propagation rays for subsonic and respectively supersonic flows. For subsonic flow they are curved such way that they always point against the flow when the length along the ray is

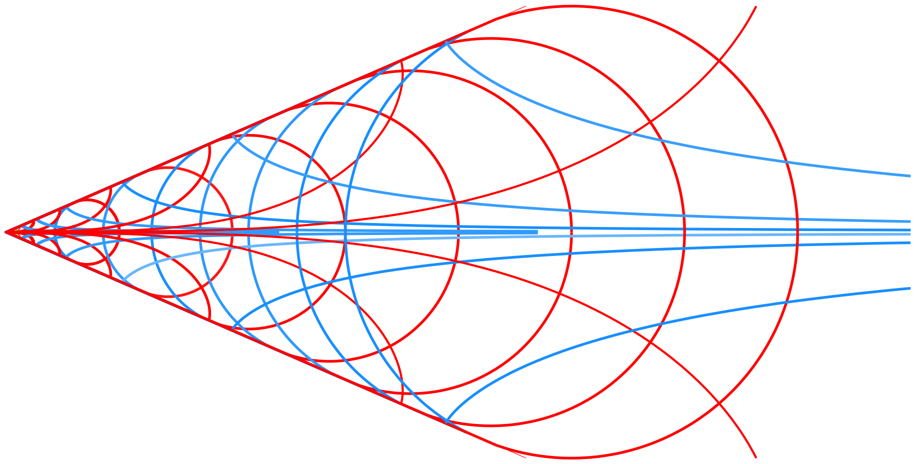

Figure 4.7: Advanced (red) and retarded (blue) wave fronts and propagation rays for a point source emitting in a medium flowing supersonically with M = 2.5. The rays are orthogonal to their respective wave fronts and both families are orthogonal too the Mach cone surface.

long enough. In the case of supersonic flow there are two families of propagation rays: One corresponds to the advanced wave fronts (red in figure (4.7)), originates from the wave source and divergently travels towards the Mach cone surface. The second corresponds to the retarded wave fronts (blue in figure (4.7)), originates from the Mach cone surface and converges in the flow direction.

4.4 Application to synthetic data

Despite being the simplest case after the plane waves, the case of spherical waves proves to be fairly complex once dynamical effects are taken into consideration. The source locator technique assumes that the measured wave field is a superposition of undisturbed spherical waves with determined frequencies as expressed by equation (4.1). As soon as the dynamic effects discussed above intervene, these assumptions cease to be true. Nevertheless, locally in time and space, the wave field is approximated by a spherical wave with a fixed frequency, fact that allows us to use the source locator even in these situations. Here, using synthetic data, we investigate a number of possible scenarios. First we ask ourselves how far can a source be to still be correctly identified as a spherical wave and not as a plane wave. Next we concentrate on the maximum number of sources that can be simultaneously recovered. The effects of the sensor motion and of the propagation medium flow on the source locator results are studied in detail. Finally we apply the source locator to a wave field generated not by a point source but by a source which is extended in space.

The synthetic data are generated taking into account the noise and the random variations of the frequency, phase, and the sensor positions in the same way as for the wave telescope in section (3.4.1). Instead of representing plane waves, now the artificial data have to model the measurements made by moving sensors of waves produced by point sources in a flowing medium.

For a source at position $\boldsymbol{r}'$ and for a sensor s at $\boldsymbol{r}_s(t) = \boldsymbol{r}_{s0} + \boldsymbol{v}t$, the measurements

distance (km)	200	150	100	50	40	30	20	10	2
$\Delta\varphi$ (deg)	2.76	2.76	2.76	2.76	2.76	2.76	2.76	2.76	2.76
$\Delta\theta$ (deg)	1.03	1.03	1.03	1.03	1.03	1.03	1.03	1.03	1.03
$\Delta k \times 10^3$ (km^{-1})	2.08	1.85	2.38	1.56	2.61	2.59	2.02	0.99	14.2
$\Delta\rho$ (km)	10.1	20.1	13.1	2.50	4.06	3.21	1.83	0.41	0.07

Table 4.1: The deviation of determined source parameters from the given ones for various distances between the wave source and the center of a tetrahedron array with an average separation of 10 km. The grid resolution is 7.2° for the longitude (φ), 3.6° for the latitude (θ) and 6×10^{-3} km^{-1} for the wave number. The ρ resolution is 17 km for the distance d = 200 km, 8 km for d between 150 and 10 km and 0.5 km for d = 2 km.

are given by:

$$\boldsymbol{X}(\boldsymbol{r}', k', \omega', \boldsymbol{r}_s, t) = \begin{cases} \boldsymbol{X}_+(\boldsymbol{r}', k', \omega', \boldsymbol{r}_s, t) & \text{for } M < 1 \\ \boldsymbol{X}_+(\boldsymbol{r}', k', \omega', \boldsymbol{r}_s, t) + \boldsymbol{X}_-(\boldsymbol{r}', k', \omega', \boldsymbol{r}_s, t) & \text{for } M > 1 \end{cases} \tag{4.23}$$

where the subscripts + and − represent the advanced, respectively the retarded component of the wave.

The component j of the vectorial wave field is

$$X_{j\pm}(\boldsymbol{r}', k', \omega', \boldsymbol{r}_s, t) = \frac{X_{0j}}{\rho_{\mathrm{g}\pm}(|\boldsymbol{r}_s(t) - \boldsymbol{r}'|, \alpha, M)} \cdot \left[\Re\big(\exp\{i(k'\rho_{\mathrm{g}\pm}(|\boldsymbol{r}_s(t) - \boldsymbol{r}'|, \alpha, M) - \omega' t + \varphi_j)\}\big) + \epsilon_X \,\mathrm{rnd}_j(-1, 1)\right] \tag{4.24}$$

with the distance $\rho_{\mathrm{g}\pm}$ to the advanced/retarded ghost given by the equation (4.11). As before, the final wave field is the sum over the considered wave sources. A brief description of the numerical code is given in the appendix (A.3).

4.4.1 Single static source

We start by applying the source locator to the very same data we use in section (3.4.1) for the single spherical wave case (see figure 3.13). Both the wave source and the sensor are at rest with respect to the propagation medium ($\boldsymbol{v} = 0 = \boldsymbol{u}$). In this case the components of the wave field (4.23) reduce to the expression (3.40).

The source locator results are shown in figure (4.8). The complete set of results is listed in the table (4.1). For any of the distances to the source considered here (from 20 to 0.2 average spacecraft distances from the configuration center) the source parameters are very well recovered by the source locator.

Comparing with the wave telescope results in figure (3.13) is easy to see that the array power has much sharper maxima, resulting in much better precision for both close and remote sources. However, while the precision of the recovered direction to the wave source seems to be independent on the source distance, the precision for the wave length slightly decreases when the source is inside the sensor array.

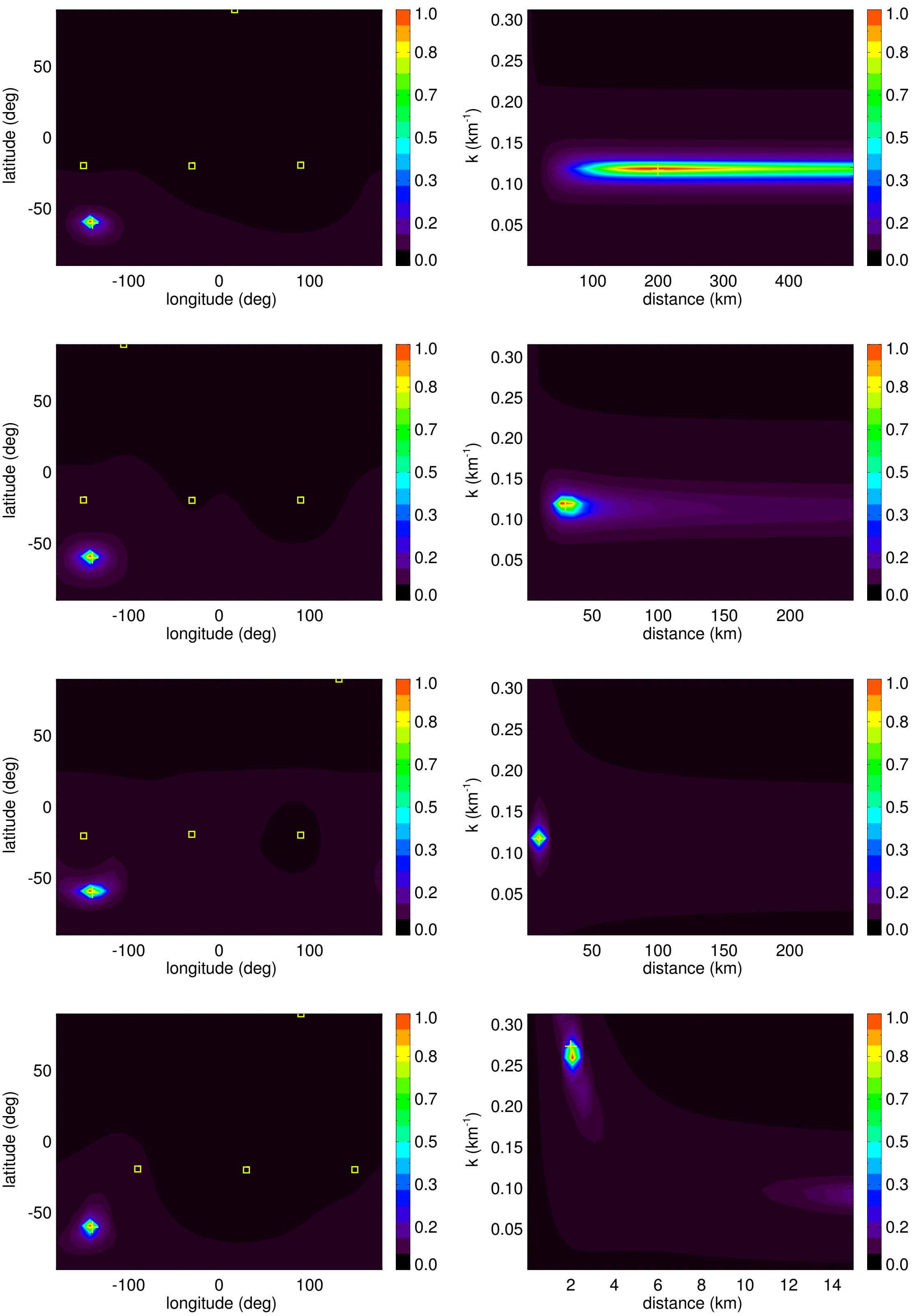

Figure 4.8: The results of the source locator applied to the same data used with the wave telescope in figure (3.13). The distances between the wave source and the center of mass of the sensor configuration are from top to bottom: 20, 3, 1, and 0.2 (source inside the array) average s/c distances.

	Source 1		Source 2		Source 3	
	data	result	data	result	data	result
long (deg)	40	43.4	-60	-55.9	100	105
lat (deg)	60	59.0	20	21.7	-40	-40.3
ω (rad/s)	99.0	99.0	101.6	99.0	100.8	99.0
k (km^{-1})	0.275	0.281	0.181	0.173	0.234	0.238
ρ (km)	29.8	26.5	59.6	67.4	79.5	67.4

Table 4.2: Source locator results for three wave sources detected with a tetrahedron sensor array.

Looking at the distance-k plot for $d = 200\,\mathrm{km}$ we note that, even if the maximum power lies at the right position, it has an elongated shape in the distance dimension direction. This is due to the limited extent of the sensor array in the position space compared to the distance to the source. Above this distance it becomes problematic to distinguish between a spherical and a plane wave. The closer the source is, the more localized the peak is.

4.4.2 Multiple static sources

As for the plane waves case, it is important that the source locator technique is able to to provide the wave sources parameters when more waves with frequencies indiscernible by the tool are simultaneously detected. To investigate this aspect we model a wave field produced by three equal power sources at rest with respect to the propagation medium. The sensors, also at rest, are placed into a regular tetrahedron formation with 10 km side. The parameters of the wave sources as well as the values recovered by the source locator are presented in table (4.2).

Figure (4.9) shows sections through the array power for the maxima corresponding to each source. Most of the signal power comes from the closest source whose parameters are best recovered. The weaker contribution of the more distant two sources is enough to recover well the wave lengths and the respective propagation directions but the effect of elongation in the radial direction is more evident than for single sources at similar distances. Therefore, while the source associated with the global maximum in the array power is well recovered and we can safely trust the source locator, the resulted distances to the wave sources associated with the second, third, and higher order maxima should be regarded with caution.

4.4.3 Sensor motion

We now allow for relative motion between the sensor array and the wave source as discussed in section (4.3.1). The sensor motion introduces differences compared to the static case. Not only the relative source position is changing over time but also the apparent frequency is now depending on time. Moreover, each sensor will measure slightly different frequencies. The sensors will record snapshots of the source

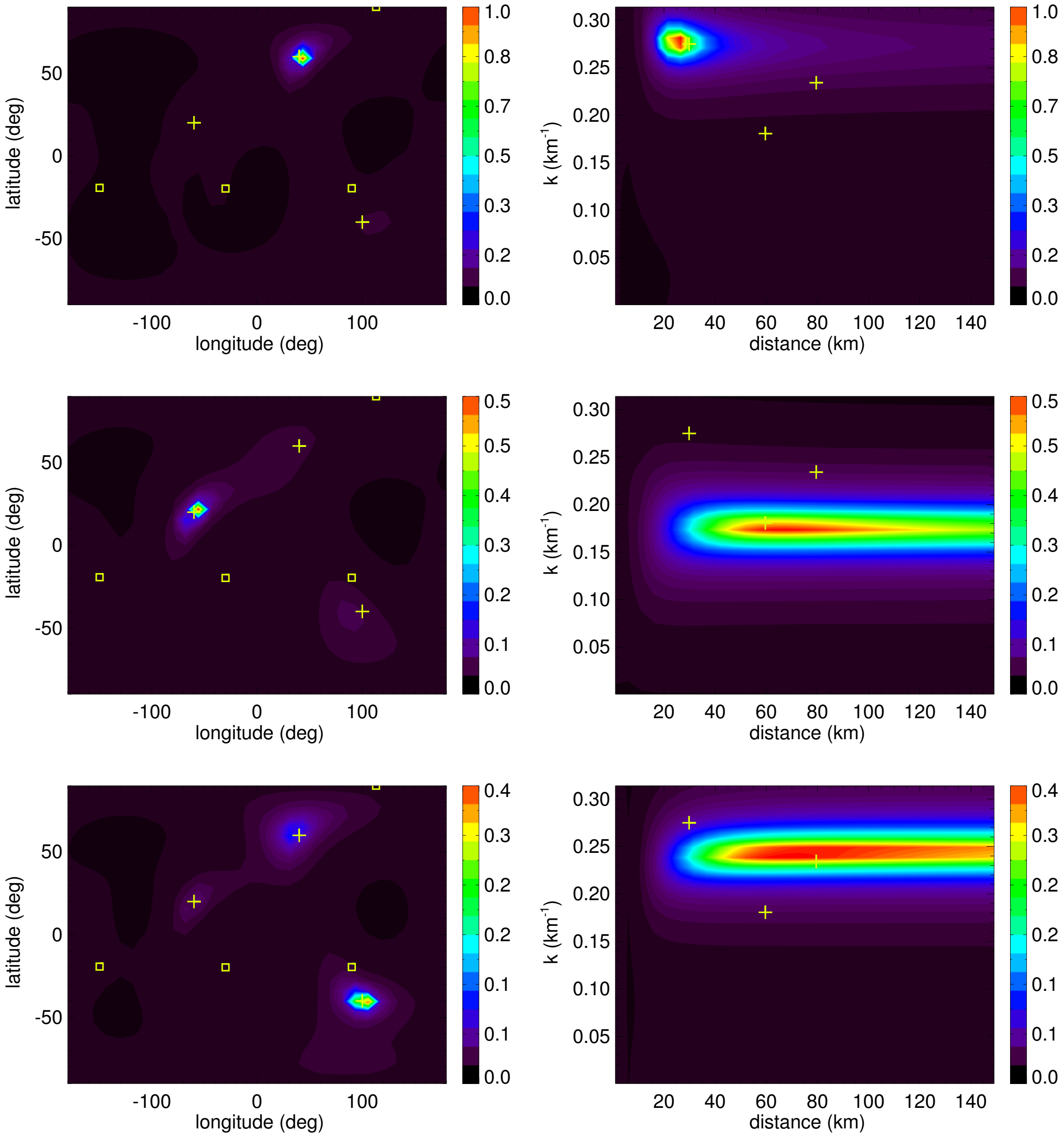

Figure 4.9: Array power for three wave sources detected with a tetrahedron sensor array. The maxima associated to the more distant sources are strongly elongated in the distance dimension.

position at the corresponding frequencies and the relative source motion will leave a trace in the array power.

As an example we apply location analysis to synthetic data representing a source with a frequency of 100 rad/s and a k-number of 0.11 km^{-1}, initially positioned at a distance of 70 km from the spacecraft configuration center, a latitude of 60° and a longitude of 40°. The sensors are moving with a velocity of 171 km/s (roughly half of the wave phase velocity) in the direction (latitude $= 55°$, longitude $= 44°$). For this velocity the maximum Doppler shift is ±19% of the source frequency. Because of the Doppler effect, the Fourier power maximizes for a frequency of 110 rad/s which corresponds to an angle α of about 122° between the direction of motion of the

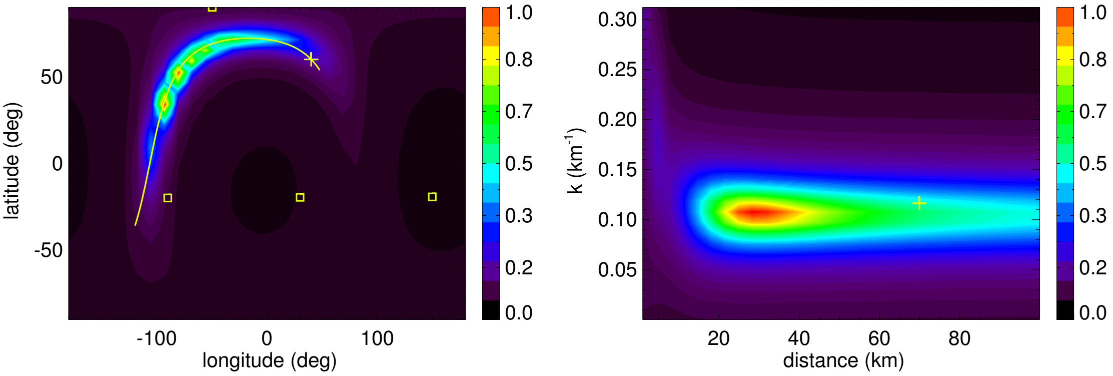

Figure 4.10: Array power when the sensors are moving with respect to the source. The array power maximizes in the vicinity of the closest approach rather than at the initial source location. The cross in the longitude-latitude plot represents the relative initial position of the wave source and the line, the apparent source trajectory projection.

	initial location	found	closest approach
distance	70 km	28 km	21 km
longitude	40°	$-93°$	$-91°$
latitude	60°	34°	39°
k	0.11 km^{-1}	0.10 km^{-1}	0.11 km^{-1}

Table 4.3: Results of source location analysis when the sensors are moving with respect to the source.

source and the sensor to source direction. We use this frequency for our analysis. The closest approach is at a distance of 21 km at a longitude of $-91°$ and a latitude of 39°. The distance-k and longitude-latitude cuts through the resulting array power are shown in figure (4.10) and the results are summarized in table (4.3).

The symbols in figure (4.10) have the same meaning as the ones explained in section (3.4), in addition we have represented with a continuous line the projection of the apparent motion of the source in the longitude-latitude plot. For more details of how a straight line trajectory is mapped on the longitude – latitude plot see the appendix (A.4). Unlike for the static case, the maximum array power is not localized but is now stretched along the source trajectory. This is due to frequency mixing involved in computing the $\mathcal{M}$ matrix. Since a given frequency corresponds to a definite position of the source relative to the sensor, a range of frequencies is equivalent with a range of positions. In this case it corresponds to an angle between the direction of motion of the sensor and the relative direction to the source ranging from 48° to 132°. We also note that the array power reaches its maximum in the vicinity of the closest approach point and not near the initial position of the source (see table 4.3). The characteristic signature of a moving source in the longitude-latitude plot can be identified in order to distinguish between static and moving sources. Together with equation (4.9), the source trace can in principle be used to determine the source velocity vector.

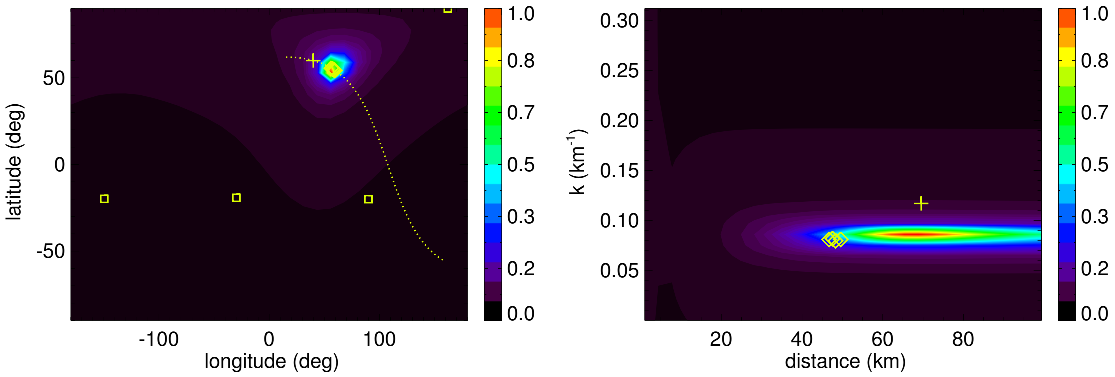

Figure 4.11: Array power when the plasma is flowing with 0.5 M with respect to the source. There is no relative motion between source and sensor array. The plus sign represents the source location, the diamonds the ghosts and the squares the sensors. The dotted line in the longitude-latitude plot represents the flow line through the source.

	real source	found	ghost
distance	70 km	68 km	48 km
longitude	40°	56°	58°
latitude	60°	53°	55°
k	0.11 km^{-1}	0.08 km^{-1}	0.08 km^{-1}

Table 4.4: Results of source location analysis for flowing plasma. The sensors are not moving. The ghost column shows averaged values over the sensors.

4.4.4 Subsonic flow

We apply the location analysis to synthetic data representing a source with the same position and frequency as the static source detected by moving sensors in section (4.4.3), with the difference that the propagation medium is now flowing with a velocity of 0.5 M with respect to both the source and the sensor array. The flow direction longitude is 175° and the latitude is $-60°$.

We show the array power in figure (4.11) and the analysis results in table (4.4). The dotted line in the longitude-latitude plot is representing the flow line going through the source and the diamonds are representing the ghost sources.

As expected, the source locator is now detecting the ghost sources instead of the real wave source. Because the arrival time (4.13) is different from sensor to sensor, each sensor is linked to a different ghost. The real wave source and the ghosts are all along the same flow line. As the flow velocity increases, the ghosts are sliding away from the wave source and from each other. Nevertheless, for subsonic flows, they remain grouped enough for the source locator to correctly identify them. If the flow velocity is known, equation (4.14) allows us to recover the direction to the real source.

The direction to the ghosts as well as the distorted wave length are accurately determined. However, the distance delivered by the source locator does not fit either the distance to the wave source nor the distance to the ghosts, most of the times it falls somewhere between the two. The explanation for this phenomenon lies in the

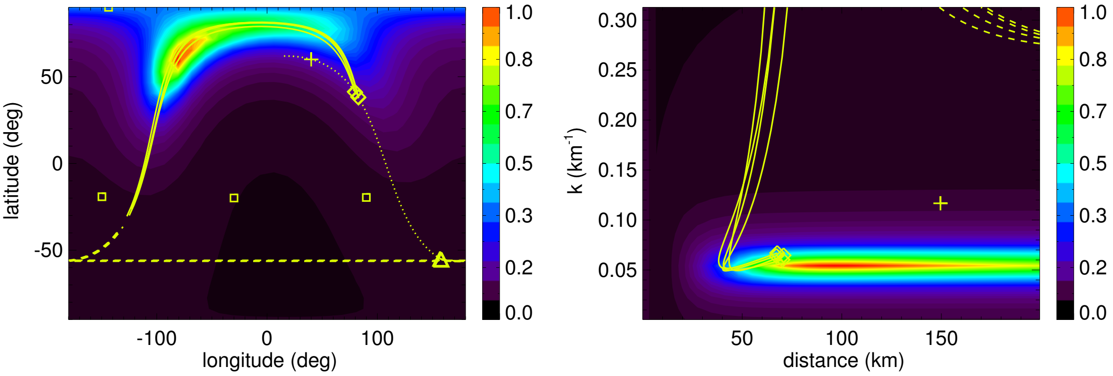

Figure 4.12: Array power when the plasma is flowing with 1.4 M with respect to the source and the sensor array is moving with a speed of 0.1 phase velocity. The plus sign represents the initial source location, the diamonds the advanced ghosts, and the triangles the retarded ghosts. The dotted line in the longitude-latitude plot represents the flow line through the source, the solid lines are the apparent advanced ghosts trajectories and the dashed lines are the apparent retarded ghosts trajectories.

expression (4.24) of the distorted wave field. To find the distance, the source locator has to find the spherical wave which best fits locally the measured distorted wave. The distance to the source determines two main quantities for a spherical wave: the curvature of the wave fronts and the radial decay of the wave amplitude. The source locator solves the inverse problem: the detected curvature and spatial decay are used to determine the distance o the source. The curvature corresponds to the distance to the ghost source, $\rho_{g\pm}$, but the wave amplitude has a totally different spatial distribution. The distance corresponding to the local spatial decay is given by the gradient of the amplitude of the detected wave:

$$\frac{1}{\rho^2_{\mathrm{decay}\pm}} = \left|\nabla \frac{1}{\rho_{g\pm}}\right| = \frac{\xi_\pm(M,\alpha)}{\rho^2}\sqrt{\frac{1+M^2\cos^2\alpha}{1-M^2\sin^2\alpha}} \tag{4.25}$$

The array power produced by the source locator reflects this mix by maximizing somewhere in between these two values.

4.4.5 Supersonic flow and sensor motion

When the flow becomes supersonic the sensor array will detect waves apparently coming from two different sources: the advanced ghost and the retarded ghost. If the array is at rest with respect to the wave source, the measured frequency of the two ghost sources will be the same. The two ghost sources will behave as coherent sources and the performance of the source locator is much degraded. However, as soon as the sensor array begins to move, thanks to the Doppler effect, the measured frequency of the retarded ghost becomes different from the measured frequency of the advanced ghost, allowing the source locator to discern between them.

Figure (4.12) shows the array power determined from data simulating the measurements made by a regular tetrahedron formation of sensors moving through a

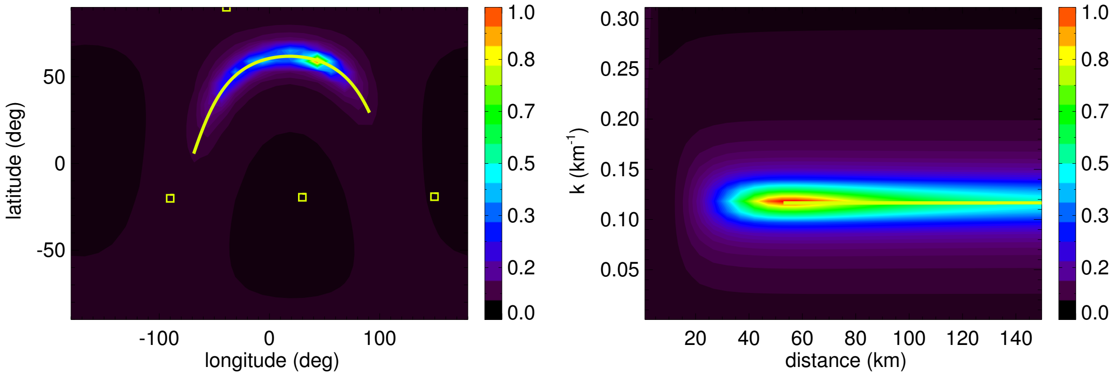

Figure 4.13: Array power for a static linear extended source. The source represented by the line in the longitude-latitude plot has a length of 30 km and is placed at 60 km away from the sensor array center.

wave field produced by a point source in a supersonically flowing medium. The sensor velocity is one tenth of the wave phase speed and the Mach number for the flowing medium is 1.4. The advanced ghosts are taking the place of the real source in section (4.4.3) leaving their trail in the array power. The retarded ghosts do not influence the array power because their Doppler shifted frequency is different from the advanced ghosts frequency. The dependence of the k number on the source position (4.17) is illustrated in the distance – k number plot. The solid lines are for the advanced ghosts and the dashed lines are for the retarded ghosts.

4.4.6 Extended Source

Assume now the wave field is produced by a source having spatial extension and not being a point source. According to Huygens principle, the wave field produced by an extended source is the same as the wave field produced by a collection of point sources uniformly distributed over the space occupied by the original source. This means that we should be able to identify an extended source and to gain information about its location and geometrical characteristics with the help of the source locator.

In order to check this hypothesis we apply location analysis to synthetic data representing a wave field generated by a standing linear source with a length of 30 average spacecraft separation distances, oriented along a longitude of 100° and a latitude of 15° and placed at a distance of 6 average spacecraft separation distances. The emitted power is uniformly distributed along the source.

As it can be seen in figure (4.13) the source locator is indeed able to recover the original source. The position of the array power maximum as well as the position of the source center are given for comparison in table (4.5).

When the sensor array is moving, the array output might not represent anymore the source geometry if the source is moving fast and close to the array. If we apply location analysis to the same extended source as in the previous example but with a non zero sensor velocity, instead of recovering the source geometry we get an array power maximum which is elongated in the direction of motion. As a matter of fact, we see a trace of the source point closest to the sensor array. We show the

	source center	found
distance	60 km	57 km
longitude	40°	43°
latitude	60°	59°
k	$0.11\ \mathrm{km}^{-1}$	$0.11\ \mathrm{km}^{-1}$

Table 4.5: Results of source location analysis for a static linear extended source.

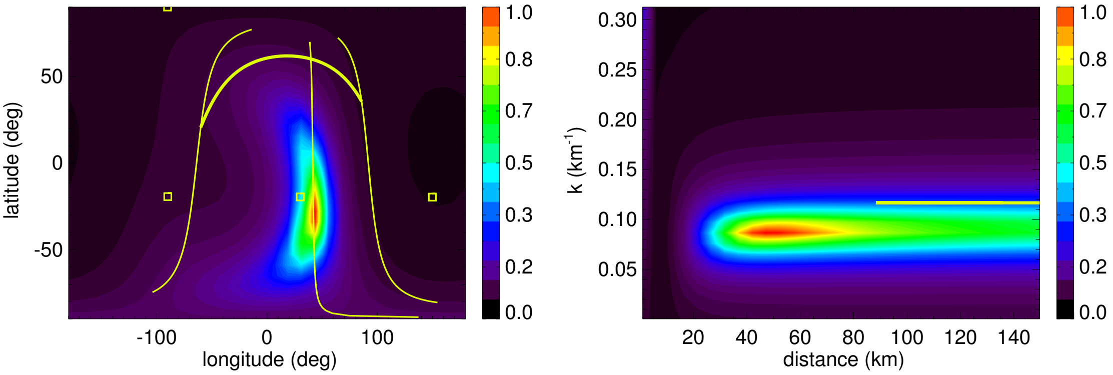

Figure 4.14: Array power for a linear extended source. The sensors are moving with a velocity of 171 km/s in the direction of 35° longitude and 79° latitude. The apparent motion of the middle and end points of the source are represented by the thin lines while the source itself is represented by the thick line in the longitude-latitude plot.

corresponding array power in figure (4.14). The thick line represents the source, the thin lines represent the motion of the middle and end points of the extended source.

If plasma flow is present, the source locator will recover in a similar fashion the position of the ghost source but if the sensor array is also moving, the results cannot unambiguously be interpreted.

4.5 Discussion

We have seen that the source locator can give us information about the sources which are generating the measured wave field for various scenarios. However, when we have to analyze real data, the difficulty lies in differentiating between these situations.

Physical insight and a priori assumptions can be used to rule out some scenarios. As for an example, if we assume we are measuring a field produced by a magnetic structure frozen into the plasma we can rule out the scenario in section (4.3.2) describing the plasma flow in respect to the source.

On the other hand, the signatures of the array power in the section plots can give us a hint about which situation we are in. The shape of the power maximum in the k-angle plots is a measure of the dependence of the wave number on the direction. In other words, a symmetrical shape of the power maximum in the k-angle plots means that the wave isotropically propagates through the medium and it probably comes from a source at rest with respect to the plasma frame. An asymmetrical shape in a k-angle plot tells us that either the propagation pattern of the wave is not isotropic,

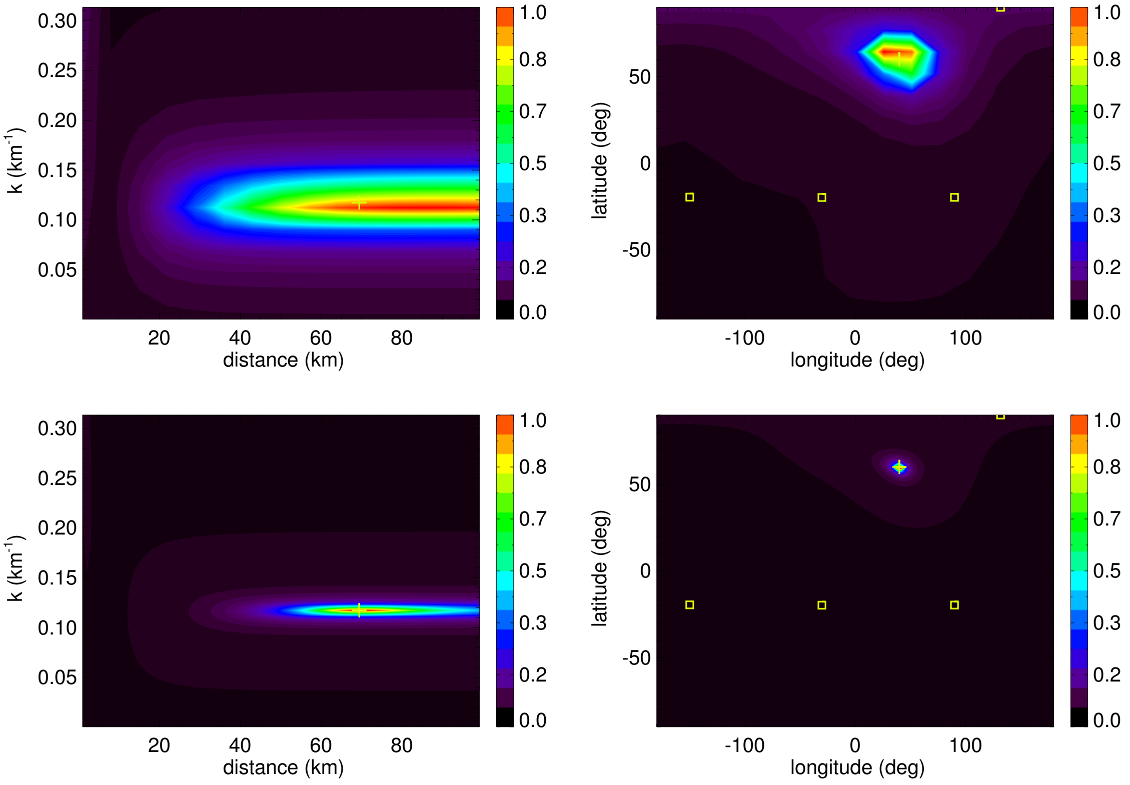

Figure 4.15: Source location results for the same data representing a single static source using different grid resolutions. The upper panels show the 15 × 15 × 15 × 15 and lower ones the 100 × 100 × 100 × 100 grid resolution results. The results in section 4.4 are obtained with a 30 × 30 × 30 × 30 grid resolution.

the source is moving with respect to plasma background, or we are dealing with an extended source.

The array power for moving sensors or for linear sources have very distinctive signatures in the latitude-longitude plots. These signatures resemble a sine-function and are the projection of a straight line on the longitude-latitude map (see appendix A.4). The ambiguity appears because we are dealing with an inverse problem, i.e. an unique set of measurements can correspond to several physical situations. For instance, the sine-function signature might also be produced by an homogeneous distribution of wave sources if the waves are only propagating orthogonal to a given direction. This is why the interpretation of the source locator results needs a careful analysis. To differentiate between a linear and a moving point source we can for example apply the source locator to the same data interval for different frequencies. If the field is produced by a moving source, because of the Doppler effect, different frequencies will represent the source on different positions on its trajectory. Also, comparing the orientation of the longitude-latitude trace with relevant directions like the local flow velocity or the background magnetic field direction can prove to be useful.

We should also keep in mind that the output of the source locator represents a virtual source, which still has to be related to the real source by analyzing the wave propagation mode.

The accuracy of the source locator is affected by the same factors affecting the accuracy of the wave telescope. One source of errors is the violation of the stationarity and homogeneity conditions. Statistical errors in the field measurements also affect the accuracy of the tool, leading to a decreased resolution but are not affecting the positions of the maxima. The scales to be investigated (wave lengths, source distance) have to be of the same order as the characteristic spacecraft separation. Otherwise spatial aliasing occurs for scales smaller than the configuration scale or the resolution decreases substantially for larger scales. One important factor is the array geometry. Large deviations from a three dimensional configuration – measured by the configuration quality index (*von Stein et al.* 1992, 1993; *Robert et al.* 1998) – such as a very elongated or very flat array configurations affect the quality of the results. *Pinçon and Lefeuvre* (1992) discussed in detail the effects of the array geometry as well as of the errors in time synchronization and spacecraft position on the reliability of the wave telescope.

Of course, the resolution of the tool cannot be higher than the scanning grid resolution. If the grid is too loose and the source is very localized (i.e. the wave energy is concentrated in a very small domain in the $(k, \boldsymbol{r})$ space) the tool will not accurately locate the wave source. This is illustrated in figure 4.15 where we show the results of a location analysis performed with different grid resolutions on the same synthetic data data modeling a single stationary source .

The grid resolution $15 \times 15 \times 15 \times 15$ is too small and the error in locating the source is even larger than the grid resolution. However, the high resolution $100 \times 100 \times 100 \times 100$ gives basically the same results as the $30 \times 30 \times 30 \times 30$. Both the shape and location of the maximum are only minimally affected by increasing the grid resolution over $30 \times 30 \times 30 \times 30$.

The grid resolution strongly affects the CPU time and computer memory needed for the analysis. These are proportional to the number of grid points used which have a power law dependence on the parameter space dimension (3 for the wave telescope, 4 for the source locator).

4.6 Application to Cluster data

This section illustrates two applications of the source locator to Cluster magnetic field data. The first application is a case study of a localized wave source. The shape of the power maximum at different frequencies and its alignment with the plasma flow direction and with the magnetic field direction gives important clues about the nature of the wave source. The second application is a statistical study of the waves detected during one magnetosheath crossing. Particular attention is paid to the ratio between close and remote sources and to the angle of propagation with respect to the background magnetic field. For details of how the Cluster data is numerically handled see the appendix (A.3).

As discussed above, the source locator determines a virtual source defined as the local curvature center of the measured wave fronts. To derive the position of the real source from the position of the virtual one, a wave mode analysis is necessary.

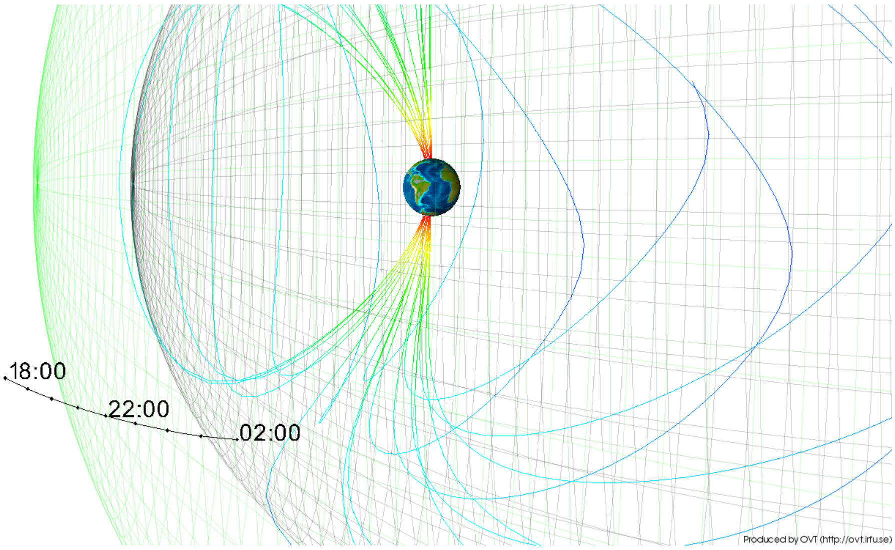

Figure 4.16: Cluster orbit between February 26 2002 18:00 and February 27 2002 02:00. The formation was moving from the solar wind into the magnetosphere, crossing the bow-shock around 22 hrs. Plot produced with OVT (`http://ovt.irfu.se`).

However, despite the fact that it generally has different position in space, the virtual source is an image of the real source and properties like close – remote, static – moving, point source – extended source region are common for the two. Therefore, when we refer to these properties we identify the virtual source with the real source.

4.6.1 Localized source

To illustrate the potential of the source locator we analyze the magnetic field magnitude measured by the FluxGate Magnetometer (FGM) instrument (*Balogh et al.* 1997) on-board Cluster during a 512 seconds interval just after an inbound shock crossing on February 26 2002 between 22:03 and 22:11 UT (see figure 4.17). The Fourier spectrum reveals multiple peaks offering the opportunity to apply the location analysis tool for different frequencies.

During this time the shock regime was quasi-parallel and the spacecraft formation was close to a regular tetrahedron with a minimum spacecraft separation of 87 km and a maximum separation of 135 km. The average plasma flow velocity inferred from the proton bulk velocity measured by the Cluster Ion Spectrometry (CIS) instrument (*Rème et al.* 1997) was 140 km/s having an orientation of $-45°$ in latitude and $-171°$ in longitude. The average magnetic field was 21 nT, with a direction given by 31° latitude and $-89°$ longitude (when not otherwise specified, we use the GSE coordinate system). The maximum variance direction of the magnetic field was closely aligned with the mean magnetic field direction which implies large compressional fluctuations during the selected interval. This justifies the use of the magnetic field magnitude instead of its components for this case study.

The results of location analysis for five different frequencies are listed in table (4.6). The array power spectra for $\omega = 181$, 91, and 66 mHz are shown in figure (4.18). We have represented the projections of the flow line and of the magnetic

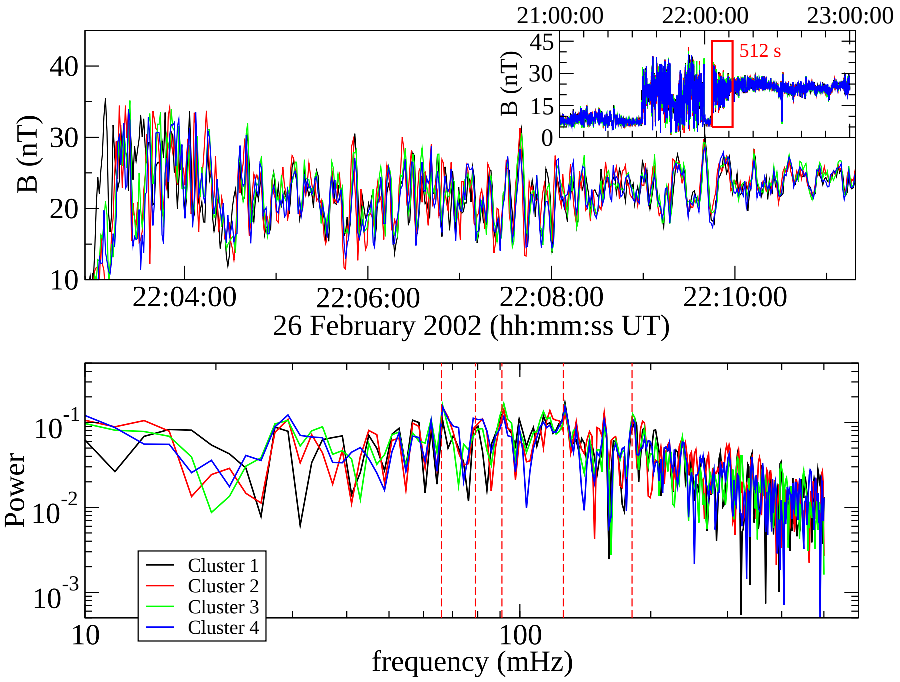

Figure 4.17: Upper panel: Magnetic field magnitude observed by Cluster in the magnetosheath shortly after an inbound shock crossing on 26 February 2002 between 22:03 and 22:11 UT. An overview plot with the interest interval marked with a red box is shown in the cassette. Lower panel: Frequency power spectrum for the analyzed data interval. The vertical dashed lines indicate the frequencies for which location analysis was performed.

field line passing through the identified virtual source position by the dashed, respectively continuous lines in the longitude-latitude plots. The triangles in these plots represent the point of minimum distance between the center of the spacecraft formation and the flow line, respectively the magnetic field line. The squares represent the spacecraft positions. As it can be seen from the k-distance plots, the source is close for the frequency of 66 mHz but is distant – in other words seen as a plane wave by the source locator – for the higher frequencies of 91 mHz and 181 mHz. The grid on which the array power was computed has the same dimensions as for synthetic data, i.e. $30 \times 30 \times 30 \times 30$ for the dimensions distance, latitude, longitude, wave number.

Because of the Doppler effect (equation 4.9) the measured source frequency is changing as the source moves on its trajectory. If the source comes toward the sensor array, the measured frequency is highest when the source is at the maximum distance and is continuously moving towards lower frequencies as the source is approaching. This means that location analysis performed for different frequencies on the same data interval will reveal different locations of the source corresponding to its motion, allowing us to trace the evolution of the source in time.

In figure (4.18) the plot for $\omega = 181\,\mathrm{mHz}$, the highest frequency in the sequence, shows the power maximum clearly aligned with the magnetic field. The wave source could be a point source moving along the magnetic field but the results from the other frequencies suggest that the measured wave comes rather from a source strongly

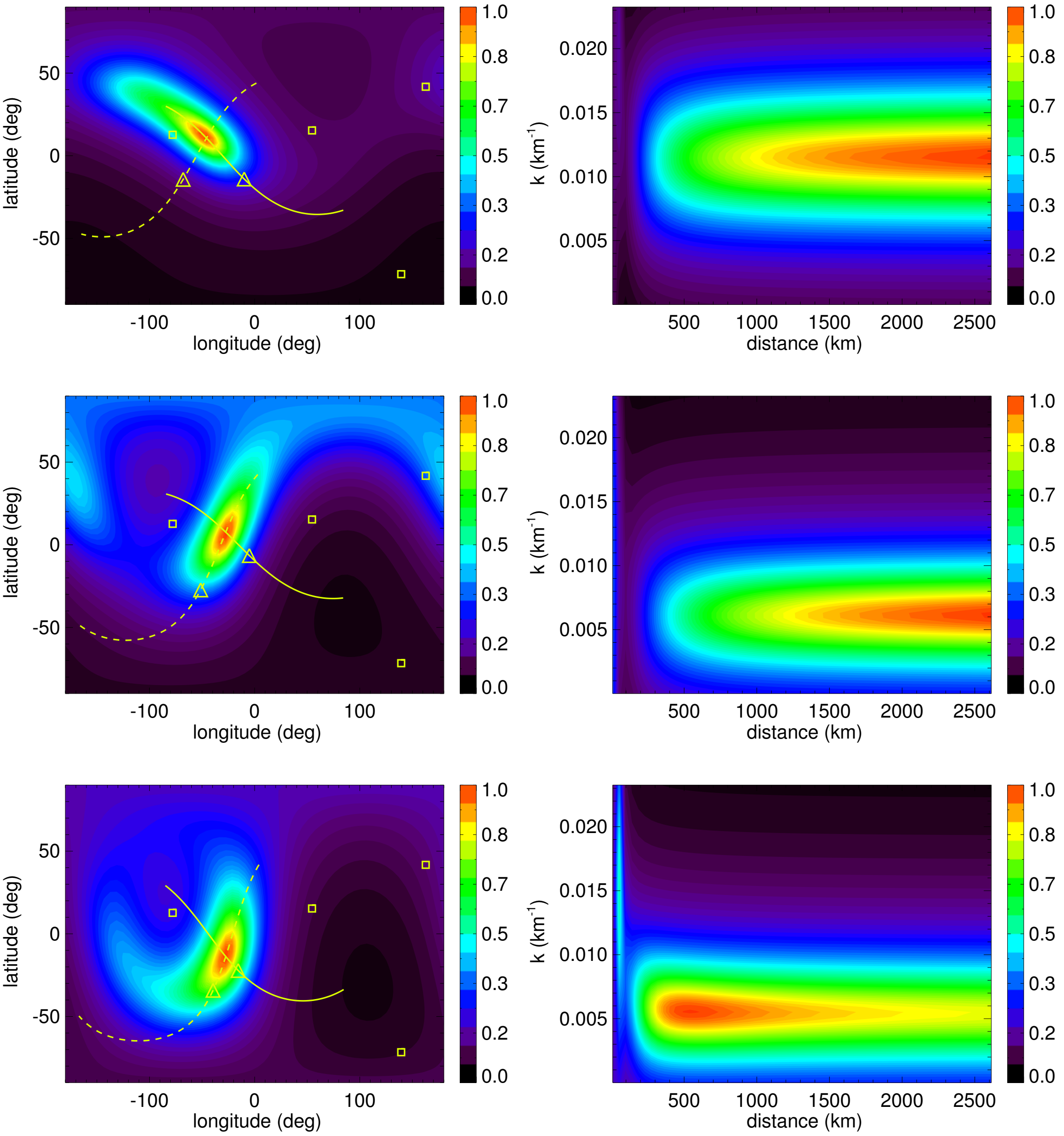

Figure 4.18: Array power for the magnetic field magnitude measured by Cluster. Location analysis is applied to the same 512 seconds data interval for the frequencies (from top to bottom) 181, 91, and 66 mHz. The squares in the longitude-latitude plot represent the spacecraft positions, the continuous lines are the projections of the magnetic field lines passing through the maximum power point. Similarly, the dashed lines represent the plasma flow lines. The triangles on the lines are the points where the distance from the configuration center to the respective line reaches minimum.

elongated in the magnetic field direction.

When we move towards lower frequencies, the power maximum changes its shape and aligns itself with the plasma flow direction. At the same time the distance to the virtual source decreases from more than 2000 km to about 500 km. The source seems to move with the plasma flow, approaching the spacecraft formation. This is also consistent with the change in the angle α between the line of sight to the virtual

ω (mHz)	distance (km)	$k \times 10^3$ (km^{-1})	longitude (deg)	latitude (deg)	α (deg)
181	> 2000	11.4	-45	10	57
126	> 2000	11.0	-39	4	59
91	> 2000	6.3	-27	7	49
79	759	6.3	-27	-10	65
66	538	5.5	-27	-13	68

Table 4.6: Results of source location analysis for different frequencies. α is the angle between the line of sight and the plasma flow direction.

source and the plasma flow direction.

A possible explanation for the change in the alignment of the power maximum is the change in the apparent angular velocity of the source. When the source is far away, its angular velocity is small and it has more time to emit energy from an apparently fixed position. This makes the source to behave more like the static source in figure (4.13) and we can resolve its shape. As the source approaches, its angular velocity increases and the source locator will register just the trace of the "brightest" point of the source like in figure (4.14).

Quantitatively, the ratio between the angular velocity corresponding to the angles between line of sight and direction of motion α_1 and α_2 is:

$$\frac{v_{\mathrm{ang}}(\alpha_1)}{v_{\mathrm{ang}}(\alpha_2)} = \frac{1 + \tan^2 \alpha_2}{1 + \tan^2 \alpha_1} \qquad (4.26)$$

Applying the above relation we find that the angular velocity corresponding to $\omega = 66\,\mathrm{mHz}$ is more than twice larger than for $\omega = 181\,\mathrm{mHz}$.

We draw the conclusion that we are tracing one and the same source during its evolution. The measurements are consistent with a source elongated in the magnetic field direction and moving with the plasma flow at close distance to the spacecraft formation.

4.6.2 Magnetosheath crossing: Sources distribution

Numerous studies had been dedicated to the origin and nature of the plasma waves in the magnetosheath and its adjacent regions. *Song et al.* (1990, 1992a,b) showed evidence of a standing slow mode wave in front of the magnetopause, over which higher frequency mirror modes convected with the magnetosheath flow are superposed. *Schwartz et al.* (1996) gave a comprehensive overview of low frequency waves in the magnetosheath, pointing out the difficulties and complications faced by wave mode identification. Their conclusion is that Alfvén/ion-cyclotron (AIC) and mirror modes are dominant throughout the magnetosheath. They are rarely pure modes but most of the times mixed between them and with other wave modes. *Hubert et al.* (1998) suggests that the depth of the magnetosheath is a key parameter determining the plasma waves nature. During a crossing of the Earth's magnetosheath

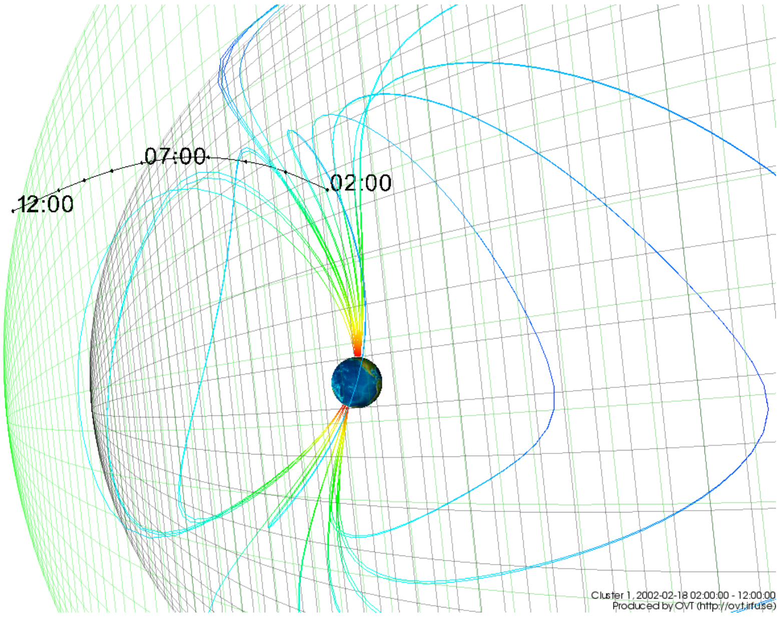
12:00
07:00
02:00
Cluster 1, 2002-02-18 02:00:00 - 12:00:00
Produced by OVT (http://ovt.irfu.se)

Figure 4.19: View from the GSE y axis of the Cluster orbit between 02:00 and 12:00 on February 18, 2002. The spacecraft formation was moving from the cusp region, through the outer magnetosphere and the day side magnetosheath, into the solar wind. Plot produced with OVT (`http://ovt.irfu.se`).

they found compressive and AIC modes in the oblique foreshock, pure AIC waves in the outer magnetosheath, a mixture of AIC and mirror modes in the middle magnetosheath and pure mirror modes in the inner magnetosheath. *Narita and Glassmeier* (2005) used magnetic field data from Cluster to determine the wave vectors across the magnetosheath. The multi-point measurements allowed for Doppler correction and for the determination of the dispersion relation, facilitating the wave mode identification. They found a mixture of ion-cyclotron and mirror modes close to the shock, then a region where mirror modes were dominating and finally, close to the magnetopause they found distorted mirror modes.

The source locator is an ideal tool to investigate the distribution of wave sources across the magnetosheath.

Experimental data

We analyze a ten hours data interval in which Cluster goes from within the cusp region into the solar wind, crossing the outer day side magnetosphere and the magnetosheath (see figure 4.19). During the magnetosheath crossing, the interplanetary magnetic field pointed northward and the average shock angle was around 17° (*Narita and Glassmeier* 2005). The tetrahedron configuration changes during this time interval but remains reasonably close to a regular tetrahedron with a characteristic separation distance of about 100 km.

An overview of the plasma and field parameters over this time can be seen in figure (4.21) adapted from the Cluster Active Archive. The different regions crossed by the Cluster constellation are marked by the colored rectangles. They are as follows:

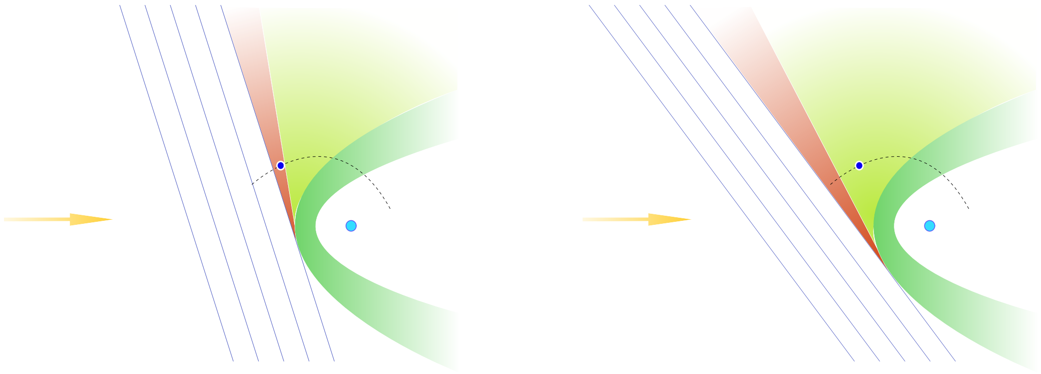

Figure 4.20: Sketch of two foreshock configurations encountered by Cluster during the February 18 2002 foreshock crossing. The drawing on the left illustrates the configuration between 08 and 10 UT when Cluster came out of the magnetosphere, traversed the ion foreshock (labeled (I) in the text) and entered the electron foreshock. Then, a change in the IMF direction occurred, producing the foreshock configuration drown on the right. In the new configuration, the spacecraft are again in the ion foreshock (labeled (II) in the text).

02:00 – 02:10	Magnetosphere
02:10 – 03:30	Cusp
03:30 – 05:00	Magnetosphere
05:00 – 07:45	Magnetosheath
07:45 – 09:00	Ion foreshock (I)
09:00 – 10:15	Electron foreshock
10:15 – 12:00	Ion foreshock (II)

The enhancement of the high energy electrons density seen in the PEACE (*Johnstone et al.* 1997) data as well as the small decrease in the magnetic field amplitude visible in the FGM data around 03:10 indicate the cusp traversal. The high level of continuum noise below 30 kHz in the WHISPER (*Décréau et al.* 1997) spectrogram from 03:30 to 05:00 UT is likely due to trapped particles in the magnetosphere between cusp and magnetosheath. The transition between the magnetosphere and the magnetosheath and between the magnetosheath and the foreshock can easily be seen both in the ion CIS (*Rème et al.* 2001) data and in the electron PEACE data. In the WHISPER data we identify electrostatic Langmuir waves through almost the whole interval. Their frequency is proportional to the square root of the electron density: between 15 and 30 kHz in the cusp and magnetosphere regions, around 60 kHz in the magnetosheath and around 40 kHz in the foreshock.

The electron foreshock is indicated by the increase in the Langmuir wave activity and by the presence of waves with twice the electron plasma frequency, the so-called $2f_\mathrm{p}$ emissions (see *Tsurutani and Rodriguez* 1981; *Kasaba et al.* 2000).

The incursion into the electron foreshock and back to the ion foreshock is due to changes in the interplanetary magnetic field direction (see figure 4.20). During the ion foreshock (I) interval, the presence of weak Langmuir and $2f_\mathrm{p}$ waves suggests that the constellation was already close to the electron foreshock. Between the ion

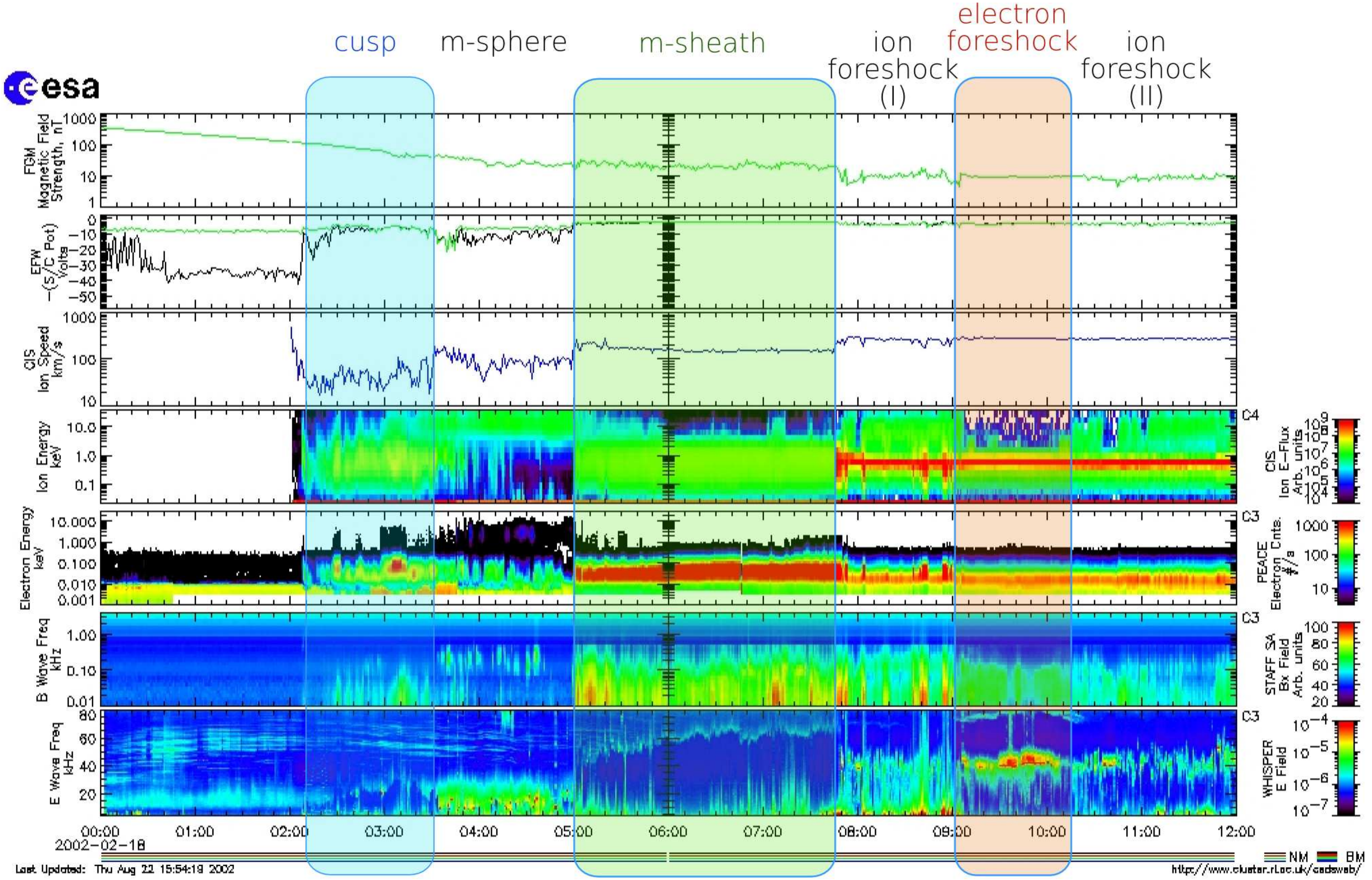

Figure 4.21: Overview of field and plasma parameters measured by Cluster 3 on February 18, 2002. From top to bottom: The magnetic field magnitude (FGM), the spacecraft potential (ASPOC), the ion speed (CIS/HIA), the ions energy (CIS/HIA), the electrons energy (PEACE), the magnetic field waves power (STAFF), and the electric field waves power (WHISPER). Courtesy ESA, adapted from the Cluster Active Archive (`http://caa.estec.esa.int/caa/`).

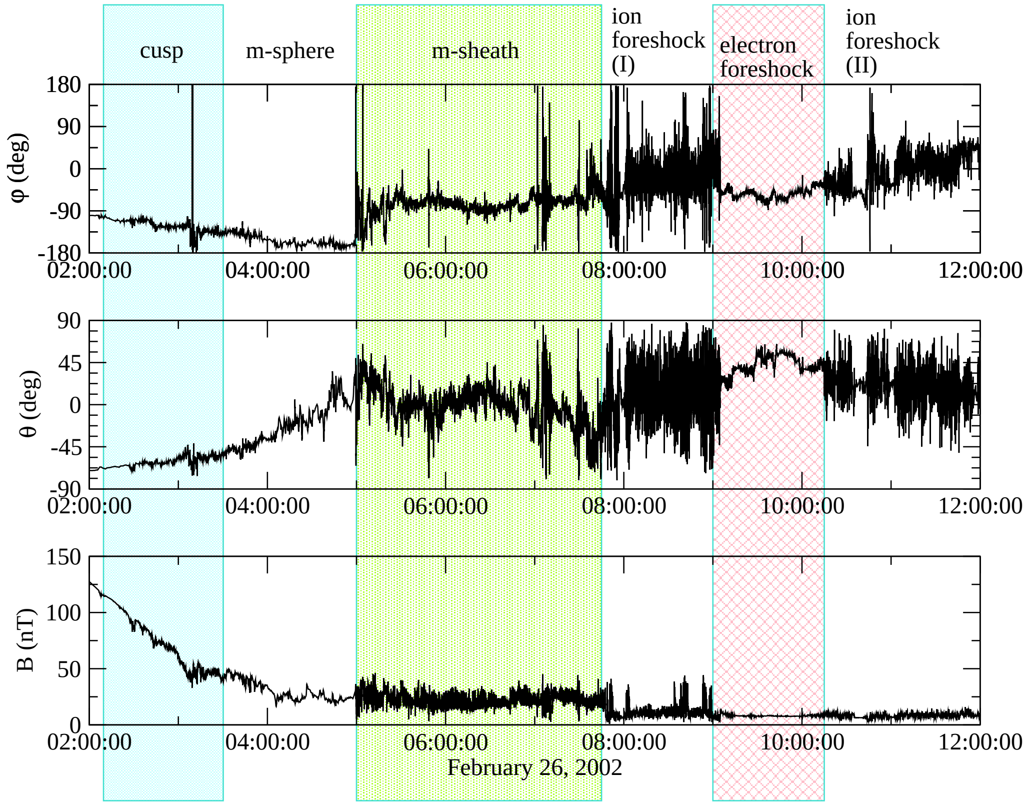

Figure 4.22: The magnetic field in spherical GSE coordinates measured by Cluster 1 on February 18, 2002. Different regions are marked by colored rectangles.

foreshock (I) and the electron foreshock interval, the angle between the mean magnetic field and the x_{GSE} axis changes only with 10°, from 50° to 60°. It is not clear if this slight change in the magnetic field direction determined the electron foreshock to move over the spacecraft or if the spacecraft entered the electron foreshock due to its own motion. However, about one hour later, a more dramatic change from 60° to 20° alters the foreshock configuration in such way that the spacecraft is once again immersed in the ion foreshock plasma, this time further away from the foreshock boundary. As we will see later, the larger distance to the foreshock boundary makes the two ion foreshock intervals to have different properties.

We have chosen this time interval because parts of it already have been analyzed in several papers giving us an opportunity for comparison. Using the k-filtering technique *Sahraoui et al.* (2003) investigates a magnetic field data interval of 164 seconds in lengths, in the inner magnetosheath, starting from from 05:34 UT. The power spectrum for frequencies between 350 and 12500 mHz suggests a turbulence cascade and more wave modes are found for each given frequency. They find that mirror mode propagating at an angle around 60° to the background magnetic field dominates, but there are also contributions from Alfvén, slow, and cyclotron wave modes. For the same data interval but for lower frequencies *Sahraoui et al.* (2004) find similar results, with the mirror modes propagating closer to the orthogonal direction at 80°. *Tjulin et al.* (2005) confirm the presence of mirror modes for the same interval by analyzing the electric field fluctuations after using both magnetic and electric field as input for the k-filtering. *Walker et al.* (2004) compare the results obtained via k-filtering with those obtained via phase differencing method (*Balikhin et al.* 1997) applied to the same 164 seconds data interval. They find a mixture of slow, Alfvén, and mirror waves with their wave vectors close to the orthogonal direction to the average magnetic field. They stress the "highly changeable" nature of the waves present in this interval. At low frequencies, the mirror mode is found to be dominating. Finally, *Narita and Glassmeier* (2005) analyze four different intervals for this crossing: one in the inner magnetosheath, one in the middle magnetosheath, one in the outer magnetosheath and one in the ion foreshock (I) region. They use the wave telescope technique to determine the wave vectors which are then used to find the experimental dispersion relation. In the foreshock they find waves propagating slightly oblique ($20° - 30°$) to the background magnetic field and a minority population of orthogonal propagating waves. From the interpretation of the dispersion relation they suggest the detected waves in the foreshock are ion-whistler and beam-resonant mode. The waves in the outer magnetosheath have various propagation angles from oblique to orthogonal and it is suggested that they are mirror modes with small contribution from other modes, perhaps ion-cyclotron. In the middle magnetosheath they find orthogonal propagating, linear polarized waves interpreted as mirror modes which are convected with the plasma flow into the inner magnetosheath region where they coexist with the slow mode (MIAOW waves).

Typical samples

Before we discuss the statistics of waves detected during the selected time interval, we shall have a look at typical array power plots for each of the magnetospheric regions crossed. Figure (4.23) shows the array power as derived by the source locator for sample intervals in the ion foreshock (II), electron foreshock and ion foreshock (I). Figure (4.24) completes the picture with power plots from the magnetosheath, magnetosphere, and cusp samples. Besides the guiding elements already introduced in section 4.6.1 (the magnetic field line through the source is represented by the solid line, the plasma flow line through the source is represented by the dashed line, the closest approach points of these lines to the configuration center are represented by the triangles, and the spacecraft positions are represented by the squares), in the latitude-longitude plots are displayed some new guiding elements: the red cross represents the background magnetic field direction, the yellow cross represents the direction anti-parallel with the background magnetic field and the dotted line represents all directions making the same angle with the background magnetic field as the line of sight to the source. For more details see appendix A.4.

In the ion foreshock (II) sample the source locator detects a plane wave (remote source) with a frequency of 83 mHz in the spacecraft frame, a wave length around 3000 km and an angle of 148° with the background magnetic field. The frequency in the plasma rest frame is found using equation (4.9) to be -20 mHz. The negative frequency means that in the plasma rest frame the wave propagates in the opposite direction as detected in the spacecraft frame ($\boldsymbol{k} \rightarrow -\boldsymbol{k}$). The wave propagates against the solar wind but because of the relatively low phase speed (around 60 km/s) it is

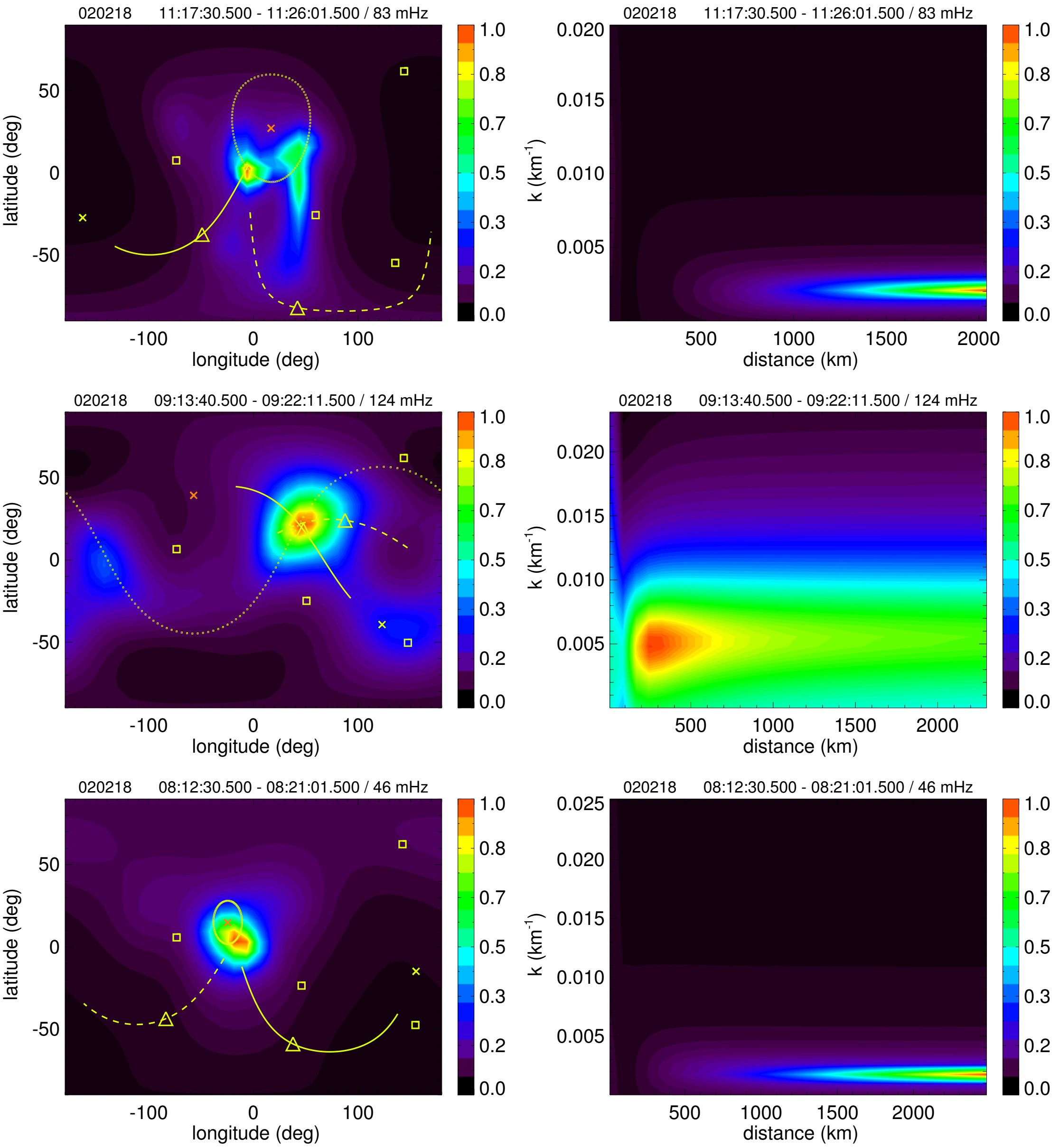

Figure 4.23: Array power for data samples in different magnetospheric regions. From top to bottom: ion foreshock (II), electron foreshock, ion foreshock (I). For a detailed explanation of the plot elements see appendix A.4. The ion foreshock (II) wave propagates oblique from a remote source. The local generated electron foreshock wave propagates orthogonal to the mean magnetic field. In the ion foreshock (I) a parallel propagating plane wave is detected.

convected by the flow.

As opposed to the ion foreshock (II) sample, the electron foreshock sample reveals a a close source positioned at only 244 km from the array center. This suggest that waves are locally generated in this region. The wave propagates orthogonal to the magnetic field ($\theta = 96°$) with a spacecraft frame frequency of 124 mHz. If we assume the wave source is convected with the plasma flow, after the Doppler correction the frequency becomes -46 mHz. The phase speed is the same as for the ion foreshock (II) sample, 60 km/s.

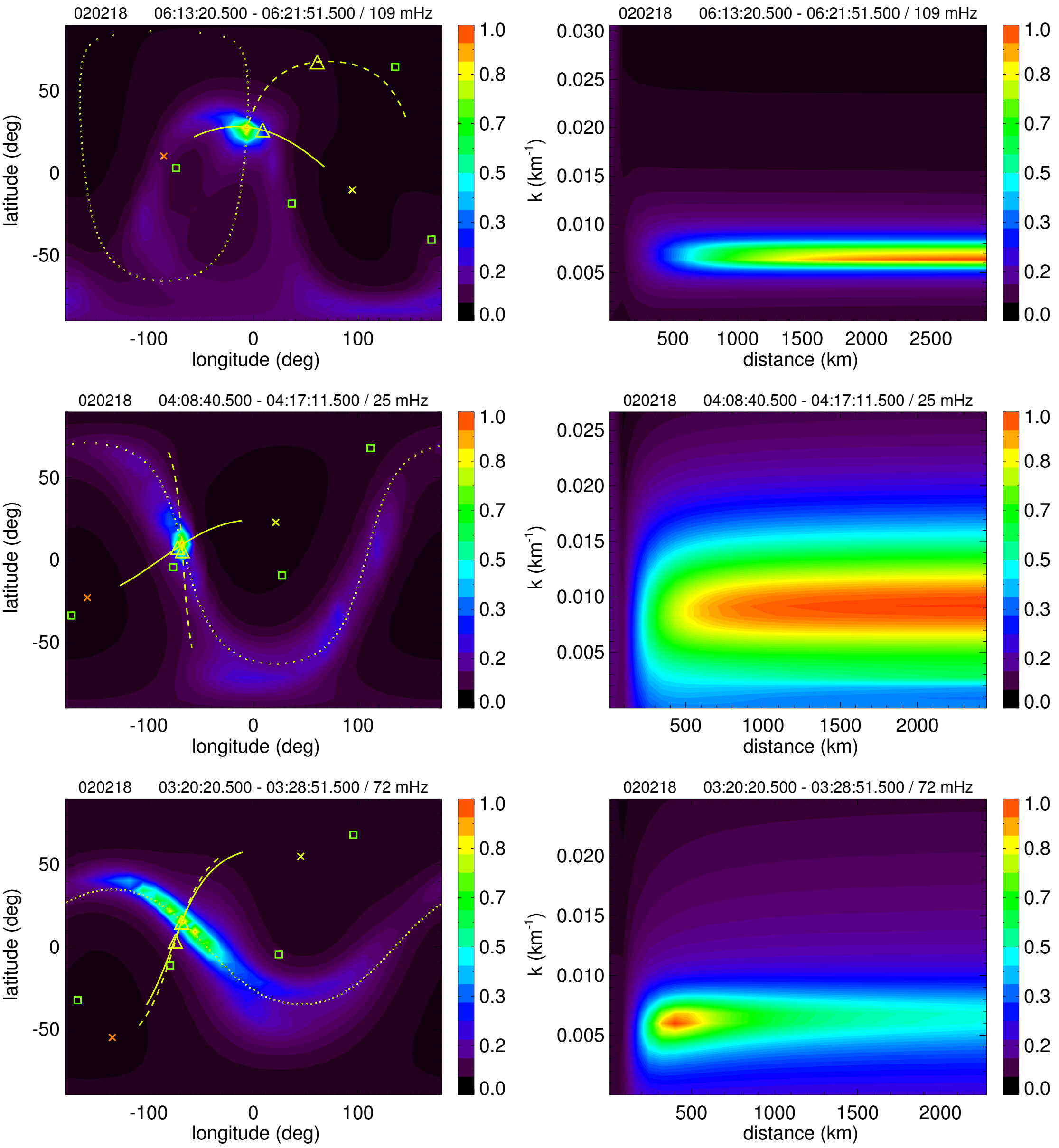

Figure 4.24: Array power for data samples in different magnetospheric regions: From top to bottom: magnetosheath, magnetosphere, and cusp region. The magnetosheath wave propagates almost orthogonal to the mean magnetic field. This wave comes from a remote source. A remote source of orthogonal propagating waves is detected in the magnetosphere. Note the increased power along the “90 degrees line”. The cusp wave also propagates along the orthogonal direction to the mean magnetic field. Most of the power comes from a close source. However, there is an important contribution from an orthogonal propagating waves background.

With an angle of 167° to the background magnetic field, the ion foreshock (I) wave is propagating almost parallel to the ambient magnetic field. The source is remote and the latitude-longitude plot is very clean, indicating a wave with a well defined propagation direction. The Doppler correction changes the detected frequency of 48 mHz to a negative rest frame frequency of -20 mHz. Taking into account the wave length of about 3500 km, the phase speed is 70 km/s.

The wave detected in the magnetosheath sample propagates with an angle of 105° to the average magnetic field. It is also a plane wave, the distance to the source being larger than 30 times the inter-spacecraft distance. The detected frequency of 109 mHz becomes -13 mHz in the plasma rest frame. With a wave length of about 1000 km this yields a phase speed of just 12 km/s.

After the crossing of the magnetopause we detect a remote source emitting a wave with a wave length of around 700 km, a frequency of 25 mHz in the spacecraft frame, propagating at an angle of 93° with the mean magnetic field. The plasma flows almost orthogonal to the line of sight to the source, minimizing the Doppler effect. The plasma rest frame frequency of this wave is 12 mHz. The phase speed is as low as 8 km/s.

In the cusp sample, the source locator detects once more a close wave source about 400 km away from the configuration center, emitting a wave which propagates orthogonal to the background magnetic field ($\theta = 91°$). The wave length is around 1000 km and the frequency in the spacecraft frame is 72 mHz. Because the plasma flows with lower velocities in the cusp and the wave propagation direction is almost orthogonal to the plasma flow, the Doppler corrected frequency remains positive, taking a value of 45 mHz. The corresponding phase speed is 47 km/s.

A striking feature of the latitude-longitude plot for both the cusp and the magnetosphere sample is the almost perfect alignment of the array power maximum with the line marking all directions orthogonal to the background magnetic field. This means the source locator detects waves propagating in all directions in a plane orthogonal to the mean magnetic field. The wave field consists of a dominating wave coming from the identified close source, superposed on a more or less isotropic background field of orthogonal propagating waves. Such wave field suggests that the Cluster constellation is immersed in an active region of homogeneously distributed sources generating orthogonal propagating waves. In our statistical analysis we have encountered many similar situations especially in the cusp and the outer magnetosphere regions. We call the wave field *gyrotropic* when the array power maximizes for all directions making a certain angle with the background magnetic field.

Statistical study

We now apply the source locator to 52 data intervals, each 512 seconds in length, with a time resolution of 1 s, distributed over the time period 02:00 – 12:00 UT on February 18, 2002. Each interval is Fourier analyzed and the source locator is applied for several frequencies for which the wave power maximizes. In total there are 264 samples for various time intervals and frequencies, giving an average of five frequency samples for each data interval.

In the figure (4.25 a) we show the wave lengths as determined by the source locator. The colored boxes mark the different magnetospheric regions in the same way as in figure (4.22). For each data interval, the percent of the sources detected close to the spacecraft array is shown in figure (4.25 b). The percent of samples exhibiting gyrotropic wave fields is shown in figure (4.25 c). Averages over each region are given in table (4.7).

Figure (4.26) displays the wave propagation angle with respect to the background

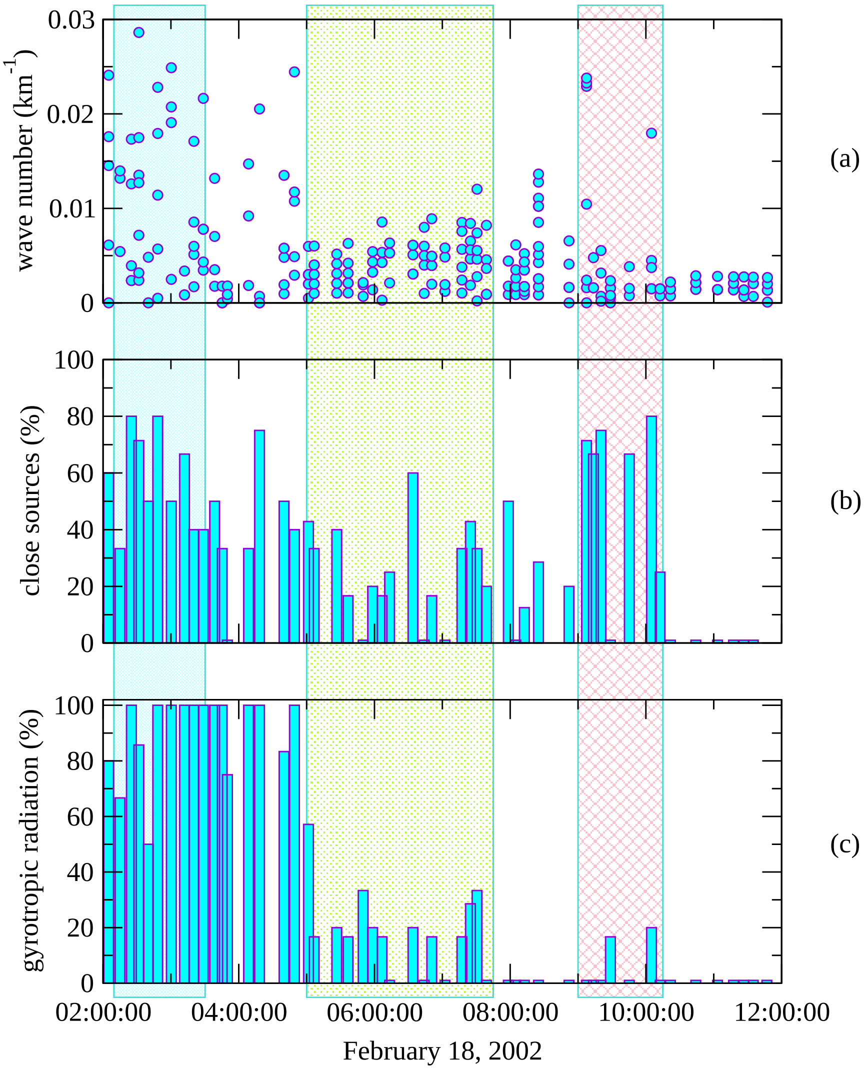

Figure 4.25: The wave number (a), the percent of close sources (b), and the percent of samples showing gyrotropic wave fields (c). The statistics are based on a total number of 264 samples distributed over 52 time intervals.

magnetic field for the 264 considered samples, the correlation between the magnetic field and the plasma density, and the temperature anisotropy ($A = T_{\perp}/T_{||}$).

We detect distinct (as opposed to gyrotropic wave field) long wave length plane waves in the ion foreshock (II). Most waves propagate oblique, at an angle around 30° to the average magnetic field. A minority of orthogonal propagating waves is also present. The magnetic field variations are in phase with the plasma density and the anisotropy is variable showing values both above and below one. These waves might be fast mode waves.

The character of the waves changes dramatically in the electron foreshock. Now a few waves with short wave lengths are mixed with the long wave lengths waves and more than half of the waves comes from close sources. A slight indication of gyrotropy suggest an increased spatial density of the wave sources. The waves have scattered propagation directions with a majority of orthogonal propagating waves.

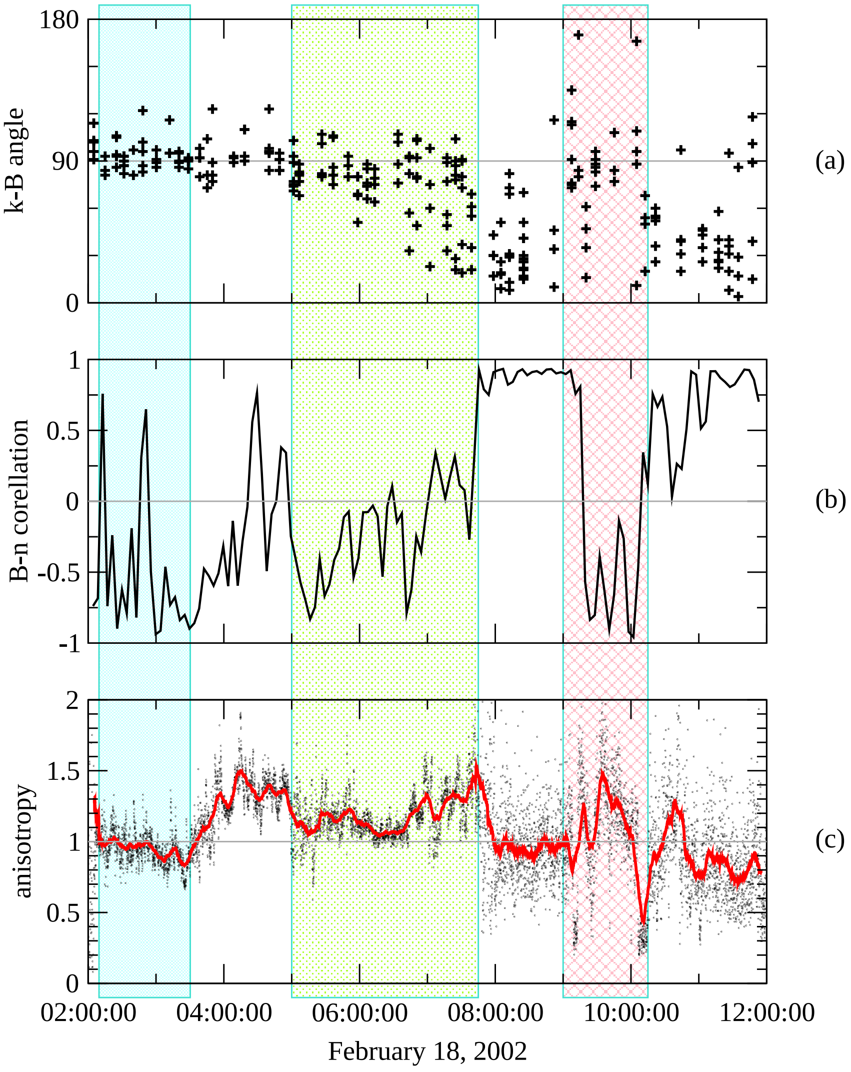

Figure 4.26: The propagation angle with respect to the background magnetic field (a), the correlation between the magnetic field magnitude and the plasma density (b), and the proton temperature anisotropy (c). The anisotropy plot shows both the 4 seconds resolution anisotropy (scattered black dots) and the 10 minutes running average (red line).

	close sources (%)	gyrotropic waves (%)
ion foreshock (II)	0	0
electron foreshock	55	5
ion foreshock (I)	22	0
magnetosheath	25	18
magnetosphere	40	94
cusp	57	89

Table 4.7: The average number of close sources and the average number of gyrotropic samples for each magnetospheric interval.

The magnetic field becomes anti-correlated with the plasma density and the temperature anisotropy rises up to a value of 1.5 from a low of 0.5. The waves here might be slow or mirror modes mixed with a minority of AIC waves.

In the ion foreshock (I) we encounter different wave characteristics again. Even though there are fewer close sources than in the electron foreshock, their contribution is still significant. Waves are generated near to, as well as remote from the spacecraft configuration. The propagation is once again oblique, with an average angle of 20° to the mean magnetic field. The magnetic field is now highly correlated with the particle density and the plasma temperature is almost isotropic. The AIC and fast mode are compatible with these wave properties.

About one quarter of the magnetosheath waves are generated within a distance of 2000 km from the spacecraft configuration center. More samples show gyrotropic fields, indicating more stable waves than in the foreshock. The average wave length increases as we move from the shock towards the magnetopause. A transition is also observed in the waves propagation direction. Close to the shock we detect waves propagating at various angles to the background magnetic field. This angle distribution smoothly changes to orthogonal propagation in the vicinity of the magnetopause. The correlation between the magnetic field and the plasma density has a descending trend, from values indicating no significant correlation in the outer magnetosheath, to negative values indicating anti-correlation in the inner magnetosheath. The plasma temperature anisotropy is variable during the magnetosheath crossing. First it fluctuates around 1.3 in the outer magnetosheath, it decreases close to unity in the middle magnetosheath, and fluctuates around a value of 1.1 in the inner magnetosheath. These properties are consistent with mirror mode growing while being convected by the plasma flow. The waves close to the shock might be a mixture of AIC and mirror modes, gradually changing to a mixture of mirror and slow modes close to the magnetopause.

The waves in the outer magnetosphere have a broader distribution of the wave lengths and propagate orthogonal to the mean magnetic field. Almost half of them originate from close sources and over 90 % of the wave fields measured here are gyrotropic. No clear correlation between the plasma density and the magnetic field is observed close to the magnetopause. Toward the cusp, the magnetic field tends to be anti-correlated with the plasma density. The temperature anisotropy indicates possible mirror mode activity.

The cusp waves are highly gyrotropic and more than half of them come from close sources. Both features are consistent with a region where waves are locally produced by a homogeneous distribution of point sources. The waves propagation directions remain orthogonal to the mean magnetic field while the correlation between the magnetic field and the plasma density is mostly negative with occasional positive values. The plasma temperature in the cusp region is nearly isotropic with a slight decreasing tendency towards the end of the time subinterval. These facts suggest that slow mode waves are generated in, and populating the cusp.

The distribution of the distances to the sources for a magnetospheric region carries information about the spatial distribution of the wave sources within that region. For instance, if we assume the sources are uniformly distributed in space, then the distribution of the distances to the sources given by the source locator will reflect

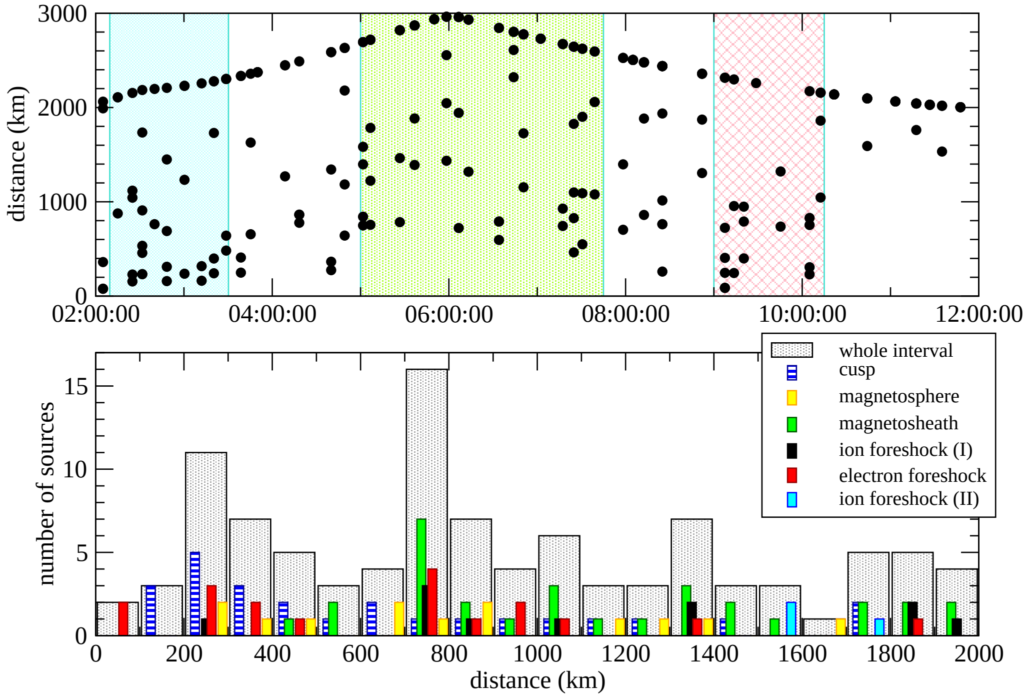

Figure 4.27: Distances to the sources. Top panel: distances to the wave sources for all detected waves during the interval. Only the sources closer than 2000 km are considered in the bottom panel. Bottom panel: Histogram of the distances to the sources for the entire data interval and for specific regions.

the distribution of the distance between a wave source and its first order neighbor. The top panel in figure (4.27) shows the distance to each source detected by the source locator. The points gathered at large distances aligned at the top of this figure are remote sources. For these sources the array power maximized at the maximum distance in the scan domain, indicating that the distance to these sources is too large to be determined by the source locator. The bottom panel of the figure (4.27) shows a histogram of the distribution of the distances to sources. Gray colour is for the whole data interval while coloured bars are for different magnetospheric regions. If we assume uniform distribution of wave sources across each magnetospheric region, from the cusp histogram we find the source characteristic distance (defined as the most probable distance between two sources) in the cusp to be 250 km. Similarly, the source characteristic distance in the magnetosheath is 750 km. The electron foreshock histogram seems to be splitted between the cusp and the magnetosheath characteristic distances, suggesting two different regimes in the electron foreshock. The other magnetospheric regions histograms are not concludent.

Discussion

The interpretation of the statistical results presented above is not always straightforward. For instance, it would be tempting to interpret the ratio between close and remote sources in the figure (4.25 b) as representing the wave sources density. It does, but not in an absolute way. A strong damping of the waves would increase this ratio because the remote sources would simply become “lost in the fog” and the source locator would only detect close sources. The same is valid for the gyrotropy. High gyrotropy can be achieved either through high density of wave sources or through low damping of the waves. The transition of waves from one mode to another would decrease the wave field gyrotropy. However, combining the statistical information about the close-remote ratio, the gyrotropy, and the source characteristic distance gives us sufficient confidence in our interpretation.

The highly changeable nature of the waves for this particular interval was noticed by *Walker et al.* (2004). The nature of the waves differs from interval to interval and from frequency to frequency for a given interval. Though we did not investigate the secondary power maxima, there is evidence (*Sahraoui et al.* 2003) that even for a given interval and given frequency there is a significant mixing of wave modes. As pointed out by *Sahraoui et al.*, this results in a mix of polarizations creating difficulties in wave mode identification.

The spatial distribution of the wave sources allows one to differentiate between active regions where waves are locally generated and passive ones where the detected waves are just propagating through. All the magnetospheric regions covered here show a certain degree of activity. The cusp and the outer magnetosphere seem to be particularly active regions with high spatial density of wave sources. The magnetosheath is as well very active but the characteristic distance between wave sources is larger here. The characteristic distance for the foreshock is uncertain. Nevertheless, the high percentage of close sources found in the electron foreshock suggest that the electron foreshock is as well very active. Interestingly, we find only few close sources of low frequency waves in the ion foreshock and only close to the electron foreshock. This is contrary to what we expect. The counter-streaming ions should locally generate waves through the beam instability. Are there quiet regions in the ion foreshock? Is this a temporal effect indicating intermittence in the wave generation? Is this an isolated case which occurred just for this particular crossing? Or maybe the ion beam instability only determines mode conversion and further grow of the already present small amplitude waves propagating from the electron foreshock. We favor the last possibility but we cannot exclude any of the above cases.

A possible scenario of the solar wind - magnetosphere interaction for the considered interval is: The solar wind flow encounters the counter-streaming reflected electrons in the electron foreshock region as a first sign of the shock ahead. The resulting interaction excites small amplitude mirror mode and AIC waves. When the electron foreshock waves penetrate into the ion foreshock, mode conversions triggered by the ion beam instability occur. High amplitude AIC and fast magnetosonic waves populate this region. Most of them originate in and close to the electron foreshock. They continuously gain energy from the reflected ions as they travel across the ion foreshock. After the solar wind crosses the bowshock, the wave lengths become gradually larger, waves are locally generated, and the AIC population extinguishes in favor of the mirror structures. Behind the magnetopause, mirror waves fill the more homogeneous region of the magnetosphere between the magnetosheath and the cusp. Slow mode waves are generated close to each other in the cusp region.

The above scenario is in good agreement with previous studies (*Song et al.* 1990; *Schwartz et al.* 1996; *Hubert et al.* 1998) which describe the magnetosheath waves as a mixture of AIC and mirror modes evolving in favor of the mirror modes as they are convected with the flow toward the magnetopause.

The study of *Narita and Glassmeier* (2005) focused on the ion foreshock (I) - magnetosheath part of the interval presented in this work, mostly agrees with our findings. It is only the inner magnetosheath region where slightly different conclusions are reached. While our analysis suggests a steady evolution to more mirror-like waves toward the magnetopause, *Narita and Glassmeier* (2005) find that the waves in the middle magnetosheath are closer to mirror modes than the waves in the inner magnetosheath. They regard this as a consequence of the interaction with the magnetopause which is distorting the mirror structures. There are two possible reasons for this minor discrepancy we can think of. First, the way of sample selection differs. *Narita and Glassmeier* (2005) are treating the power spectrum as a turbulent-like spectrum. Consequently, they do not select the frequencies based on their relative contribution to the wave field. On the contrary, we always select frequencies for which the power presents local peaks. Since indeed, most of the time there are not outstanding local maxima in the Fourier spectrum, but rather small local maxima (an exception being the foreshock region), this difference in samples selection should not influence much the statistical results. However, there is a fundamental difference between the plane waves representation of the wave telescope used by *Narita and Glassmeier* (2005) and the spherical waves representation of the source locator. We have seen in section 3.4.1 that the plane wave telescope filters out the close sources giving the far field view of the wave field. This means that instead of detecting young waves from close sources, the plane wave telescope is detecting the evolved mirror structures convected from upstream regions of the magnetosheath. These structures might have indeed reach a nonlinear regime and be distorted. In conclusion, the discrepancy is only apparent, the two tools are detecting different sets of waves.

An issue which can raise questions is the different interpretation of the maximum power shape in section 4.6.1 where for 91 and 66 mHz could be as well interpreted as an indication of gyrotropy and not of source motion. This is true, but since the array power has completely different alignment for 181 mHz and since the five different frequency samples which were considered are consistent with a moving source, we believe the interpretation given in the section 4.6.1 is the correct one.

5

Magnetic mirrors

5.1 Introduction 97
5.2 A model for mirror structures 97
5.3 Particle kinetics and distribution function 106
5.4 Application to Cluster data 120
5.5 Remarks 130

5.1 Introduction

In section 4.6.2 mirror modes have been detected almost in every magnetospheric region covered by the crossing we analyzed. Indeed, they frequently occur in space plasmas. The mirror instability requires increased orthogonal plasma temperature ($T_\perp > T_{||}$) which builds up in regions where magnetized plasma interacts with an obstacle (*Crooker and Siscoe* 1977). Such regions are common in the Universe, from cometary environments to supernovae shocks. Evidence of mirror structures have been provided by a multitude of spacecraft observations in the solar wind (see, e.g. *Winterhalter et al.* 1994; *Fränz et al.* 2003), the terrestrial magnetosheath (e.g., *Tsurutani et al.* 1982; *Hubert et al.* 1998; *Lucek et al.* 1999; *Lucek et al.* 2001) and magnetosphere (e.g., *Treumann et al.* 1990), cometary environments (e.g., *Glassmeier et al.* 1993; *Tsurutani et al.* 1999) and other planetary magnetospheres (e.g., *Russell et al.* 1999; *Huddleston et al.* 1999).

As the lowest frequency mode and typically having large amplitudes, mirror modes serve as one of the dominant energy inputs into plasma. Moreover, low parallel energy particles can be trapped in mirror modes and redistribute energy (cf. for instance, *Chisham et al.* 1998). Such trapped electrons excite banded whistler wave emission known under the name of lion roars and indicating that the mirror modes contain a trapped particle component while leading to the splitting of particle distributions (*Southwood and Kivelson* 1993; *Kivelson and Southwood* 1996; *Baumjohann et al.* 1999) into trapped and passing particles.

Since the mirror modes play such an important role, they deserve a detailed study. The geometry of the magnetic field inside the mirror structures determine their features. Assuming magnetohydrostatic equilibrium a model for mirror structures can be inferred (*Constantinescu* 2002). Besides the features directly derivable from the model, such as the magnetic field or the plasma temperature and density, once the magnetic field geometry is known, various other aspects can be investigated. For instance the particle distribution function inside magnetic mirrors can be studied via computer simulations or the magnetic field geometry can be used to identify the magnetic mirrors in spacecraft data.

In the light of chapter 3, the magnetic field provided by the model can be used to construct a set of elementary waves $\{\boldsymbol{w}\}$ for a minimum variance technique similar with the wave telescope or to the source locator. We have seen in chapter 4 how much the complexity of the tool increases when the simple system of plane waves is replaced by a system of spherical waves. The step toward the cylindrical waves describing the mirror structures proves to be impractical. However, a direct fit of the model magnetic field on the measured data can both help to identify the mirror structures and to determine their geometrical parameters such as size, shape and orientation.

5.2 A model for mirror structures

In this section we present a self-consistent model of mirror structures based on a perturbative magnetohydrostatic approach (*Constantinescu* 2002). Such treatment is justified by the vanishing phase velocity which turns the mirror modes in non-propagating structures in the plasma frame.

In the absence of the perturbation the magnetic field will be considered uniform and parallel with the z axis. The magnetic field perturbation will be chosen to be symmetrical in respect to the z axis in the meridian plane. For our simple model the plasma will be a mixture of electrons and protons at equilibrium: $n^{(e)} = n^{(p)} = 1/2n; T^{(e)} = T^{(p)} = T$.

The pressure equilibrium in the plasma reference frame is written

$$\nabla\left(p_\perp + \frac{B^2}{2\mu_0}\right) + \nabla\left[\left(p_\parallel - p_\perp - \frac{B^2}{\mu_0}\right)\frac{\mathcal{B}}{B^2}\right] = 0 \tag{5.1}$$

where μ_0 is susceptibility, B magnetic field strength, $\mathcal{B}$ is a tensor with elements $(\mathcal{B})_{ij} = B_i B_j$, and $p_\parallel$ and $p_\perp$ are plasma pressure components.

We assume bi-Maxwellian distribution function of the plasma. For two dimensions the anisotropy in a bi-Maxwellian plasma is (see, *Lee et al.* 1987)

$$A(\mathbf{r}) = \frac{T_\perp(\mathbf{r})}{T_\parallel(\mathbf{r})} = \left[1 - \left(1 - \frac{1}{A_0}\right)\frac{B_0}{B(\mathbf{r})}\right]^{-1} \tag{5.2}$$

where $A(\mathbf{r})$ and $B(\mathbf{r})$ are the final anisotropy and magnetic field, and A_0 and B_0 are unperturbed anisotropy and magnetic field.

We need to derive the temperature anisotropy for three dimensions. We do so in the following section and show that equation (5.2) holds both for two and for three dimensions.

5.2.1 The anisotropy for bi-Maxwellian distribution

We consider the plasma obeying a bi-Maxwellian distribution both before and after the perturbation is applied. The unperturbed distribution function for electrons and protons is:

$$\mathfrak{F}_0^{(s)}(v_{\perp 0}, v_{\parallel 0}) = \frac{n_0^{(s)}}{T_{\perp 0} T_{\parallel 0}^{\frac{1}{2}}}\left(\frac{m^{(s)}}{2\pi k_\mathrm{B}}\right)^{\frac{3}{2}} \exp\left\{-\frac{m^{(s)} v_{\perp 0}^2}{2k_\mathrm{B} T_{\perp 0}} - \frac{m^{(s)} v_{\parallel 0}^2}{2k_\mathrm{B} T_{\parallel 0}}\right\} \tag{5.3}$$

The superscript $^{(s)}$ distinguishes between electrons and protons. The kinetic energy and the magnetic moment of each particle are invariants:

$$W^{(s)} = \frac{m^{(s)}}{2}(v_\parallel^2 + v_\perp^2) \tag{5.4}$$

$$\mu^{(s)} = \frac{m^{(s)}}{2}\frac{v_\perp^2}{B} \tag{5.5}$$

The argument of the exponential factor in the distribution function can be expressed in terms of these invariants:

$$-\frac{W^{(s)}}{k_\mathrm{B} T_{\parallel 0}} - \frac{\mu^{(s)} B}{\alpha_0 k_\mathrm{B} T_{\parallel 0}} \tag{5.6}$$

In the previous relation we have denoted $\alpha_0 = \frac{1}{\frac{T_{\parallel 0}}{T_{\perp 0}} - 1}$.

Owing to the invariance of $W^{(s)}$ and $\mu^{(s)}$ (the number of particles with certain energy and magnetic moment must remain the same), the distribution function expressed in cylindrical coordinates (ρ, φ, z) after applying the perturbation is:

$$\mathfrak{F}^{(s)}(v_\perp, v_\parallel, \rho, z) =$$
$$\frac{n_0^{(s)}}{T_{\perp 0} T_{\parallel 0}^{\frac{1}{2}}} \left(\frac{m^{(s)}}{2\pi k_\mathrm{B}}\right)^{\frac{3}{2}} \exp\left\{-\frac{W^{(s)}(v_\perp, v_\parallel, \rho, z)}{k_\mathrm{B} T_{\parallel 0}} - \frac{B_0 \mu^{(s)}(v_\perp, v_\parallel, \rho, z)}{\alpha_0 k_\mathrm{B} T_{\parallel 0}}\right\} =$$
$$\frac{n_0^{(s)}}{T_{\perp 0} T_{\parallel 0}^{\frac{1}{2}}} \left(\frac{m^{(s)}}{2\pi k_\mathrm{B}}\right)^{\frac{3}{2}} \exp\left\{-\frac{m^{(s)}}{2\pi k_\mathrm{B} T_{\parallel 0}} \left[v_\parallel^2 + v_\perp^2 \left(1 + \frac{1}{\alpha_0}\frac{B_0}{B(\rho, z)}\right)\right]\right\} \tag{5.7}$$

The final number density can be fond through the integration of the distribution function:

$$\begin{aligned} n^{(s)}(\rho, z) &= \int_0^{2\pi} \mathrm{d}\varphi \int_{-\infty}^{\infty} \mathrm{d}v_\parallel \int_0^{\infty} v_\perp \mathrm{d}v_\perp \mathfrak{F}^{(s)}(v_\perp, v_\parallel, \rho, z) \\ &= n_0^{(s)} \left(1 + \frac{1}{\alpha_0}\right) \left(1 + \frac{1}{\alpha_0}\frac{B_0}{B(\rho, z)}\right)^{-1} \end{aligned} \tag{5.8}$$

We can now express the distribution function in terms of the final number density:

$$\mathfrak{F}^{(s)}(v_\perp, v_\parallel, \rho, z) = \frac{n^{(s)}(\rho, z)}{T_{\parallel 0}^{\frac{1}{2}} \tau} \left(\frac{m^{(s)}}{2\pi k_\mathrm{B}}\right)^{\frac{3}{2}} \exp\left\{-\frac{m^{(s)} v_\parallel^2}{2 k_\mathrm{B} T_{\parallel 0}} - \frac{m^{(s)} v_\perp^2}{2 k_\mathrm{B} \tau}\right\} \tag{5.9}$$

Above we have denoted by τ the following quantity:

$$\tau = T_{\parallel 0} \left(1 + \frac{1}{\alpha_0}\frac{B_0}{B(\rho, z)}\right)^{-1} \tag{5.10}$$

Because we ask the distribution function to remain bi-Maxwellian after the perturbation is applied, from equation (5.9) we find the final orthogonal and parallel temperatures:

$$T_\parallel(\rho, z) = T_{\parallel 0} \tag{5.11a}$$
$$T_\perp(\rho, z) = \tau(\rho, z) \tag{5.11b}$$

These relations lead us to the temperature anisotropy equation (5.2) of the perturbed plasma.

5.2.2 The Magnetic Field

The magnetic field in the first order of the perturbation theory is:

$$\boldsymbol{B}(\rho, z) = B_0 \hat{\boldsymbol{e}}_z + \delta \boldsymbol{B}(\rho, z) \tag{5.12}$$
$$B_\varphi = 0 \tag{5.13}$$

and the pressure is:

$$\mathcal{P} = p_\perp \mathcal{I} + (p_\parallel - p_\perp)\mathcal{E}_B \tag{5.14}$$

where $\mathcal{I}$ is the unity tensor and $(\mathcal{E}_B)_{ij} = (\hat{\boldsymbol{e}}_B)_i(\hat{\boldsymbol{e}}_B)_j$. In a local field aligned coordinate system the pressure becomes:

$$\mathcal{P} = \begin{pmatrix} p_\perp & 0 & 0 \\ 0 & p_\perp & 0 \\ 0 & 0 & p_\parallel \end{pmatrix} \tag{5.15}$$

The parallel and the orthogonal components of the pressure are:

$$p_\perp(\rho, z) = p_{0\perp} + \delta p_\perp(\rho, z) \tag{5.16a}$$

$$p_\parallel(\rho, z) = p_{0\parallel} + \delta p_\parallel(\rho, z) \tag{5.16b}$$

From equation (5.2) the pressure perturbation in the parallel direction is:

$$\delta p_\parallel(\rho, z) = (p_{0\perp} - p_{0\parallel})\frac{\delta B_z(\rho, z)}{B_0} + p_{0\parallel}\frac{\delta p_\perp(\rho, z)}{p_{0\perp}} \tag{5.17}$$

Substituting the first order expressions of the magnetic field (equations 5.12 and 5.13) and of the pressure (equations 5.16 and 5.17) in the equation (5.1) of the magnetohydrostatic equilibrium and taking into account the divergence-less condition for the magnetic field ($\nabla \boldsymbol{B} = 0$) we obtain the following system of coupled differential equations:

$$\frac{\partial}{\partial \rho}\delta p_\perp + \frac{B_0}{\mu_0}\frac{\partial}{\partial \rho}\delta B_z + \frac{1}{B_0}\left(p_{0\parallel} - p_{0\perp} - \frac{B_0^2}{\mu_0}\right)\frac{\partial}{\partial z}\delta B_\rho = 0 \tag{5.18a}$$

$$\frac{p_{0\parallel}}{p_{0\perp}}\frac{\partial}{\partial z}\delta p_\perp + \frac{2}{B_0}\left(p_{0\perp} - p_{0\parallel}\right)\frac{\partial}{\partial z}\delta B_z = 0 \tag{5.18b}$$

$$\frac{1}{\rho}\frac{\partial}{\partial \rho}\left(\rho \delta B_\rho\right) + \frac{\partial}{\partial z}\delta B_z = 0 \tag{5.18c}$$

The magnetic field and the plasma pressure are periodical in respect to z coordinate ($\boldsymbol{B}(\rho, z + 2L) = \boldsymbol{B}(\rho, z)$ and $\mathcal{P}(\rho, z + 2L) = \mathcal{P}(\rho, z)$) therefore we can expand them in Fourier series:

$$\delta B_\rho(\rho, z) = \sum_{n=-\infty}^{\infty} \delta B_\rho^n(\rho) e^{-in\frac{\pi z}{L}} \tag{5.19a}$$

$$\delta B_z(\rho, z) = \sum_{n=-\infty}^{\infty} \delta B_z^n(\rho) e^{-in\frac{\pi z}{L}} \tag{5.19b}$$

$$\delta p_\perp(\rho, z) = \sum_{n=-\infty}^{\infty} \delta p_\perp^n(\rho) e^{-in\frac{\pi z}{L}} \tag{5.19c}$$

Substituting these Fourier expansions into the system (5.18) we get a set of Bessel equations, one for each Fourier order of the ρ-component of the magnetic field perturbation:

$$\rho^2\frac{\mathrm{d}^2}{\mathrm{d}\rho^2}\delta B_\rho^n + \rho\frac{\mathrm{d}}{\mathrm{d}\rho}\delta B_\rho^n + \left[\left(\frac{n\alpha\rho}{L}\right)^2 - 1\right]\delta B_\rho^n = 0 \tag{5.20}$$

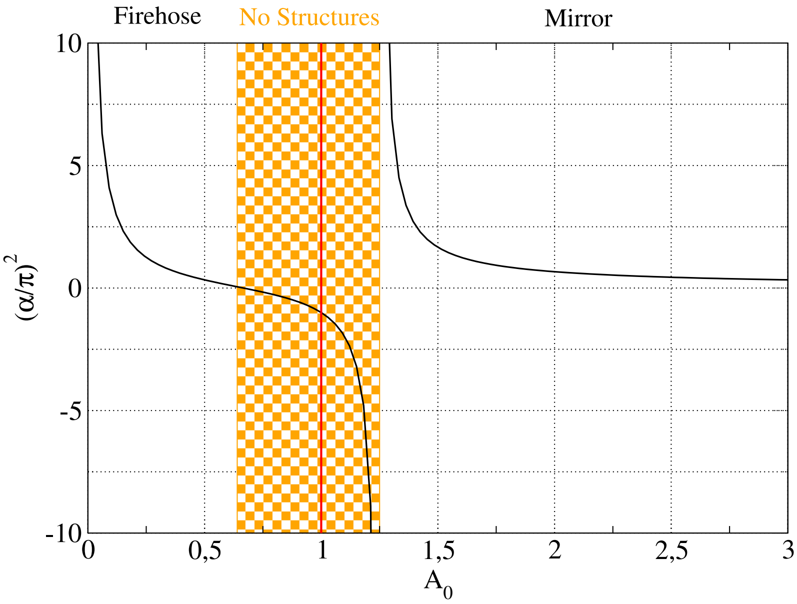

Figure 5.1: The α^2 parameter versus the unperturbed anisotropy for $\beta_{0\perp} = 3.47$. For anisotropies less than unity the perturbation is firehose type, while for anisotropies grater than unity a mirror structure develops. In the highlighted region ($\alpha^2 < 0$) no axi-symmetrical magnetic perturbation can be in equilibrium with the plasma pressure.

where α is a dimensionless parameter:

$$\alpha = \pi \sqrt{\frac{\frac{1}{2}\left(1 - \frac{1}{A_0}\right) + \frac{1}{\beta_{0\perp}}}{A_0 - 1 - \frac{1}{\beta_{0\perp}}}} \tag{5.21}$$

and $\beta_{0\perp}$ is the plasma parameter, i.e. the ratio between the orthogonal plasma pressure, $p_{0\perp}$ and the magnetic pressure, $\frac{B_0^2}{2\mu_0}$.

The non-divergent solution of equation (5.20) is:

$$\delta B_\rho^n(\rho) = \frac{i\pi}{\alpha} C_n J_1\left(\frac{n\alpha\rho}{L}\right) \tag{5.22}$$

This solution is non-divergent only if the argument of the Bessel function J_1 is a real number. Hence, $\alpha^2 > 0$ is an existence condition. In terms of the initial anisotropy and plasma β this is equivalent to:

$$A_0 > 1 + \frac{1}{\beta_{0\perp}} \tag{5.23a}$$

or

$$A_0 < \frac{\beta_{0\perp}}{\beta_{0\perp} + 2} \tag{5.23b}$$

The first inequality is the same as the mirror instability condition derived from the kinetic theory while the second one is the instability condition for the firehose mode (*Treumann and Baumjohann* 1997). The properties of the magnetic structure depend on which of the above conditions are satisfied. If inequation (5.23a) is satisfied, then the structure will be a classical magnetic mirror and the magnetic field will

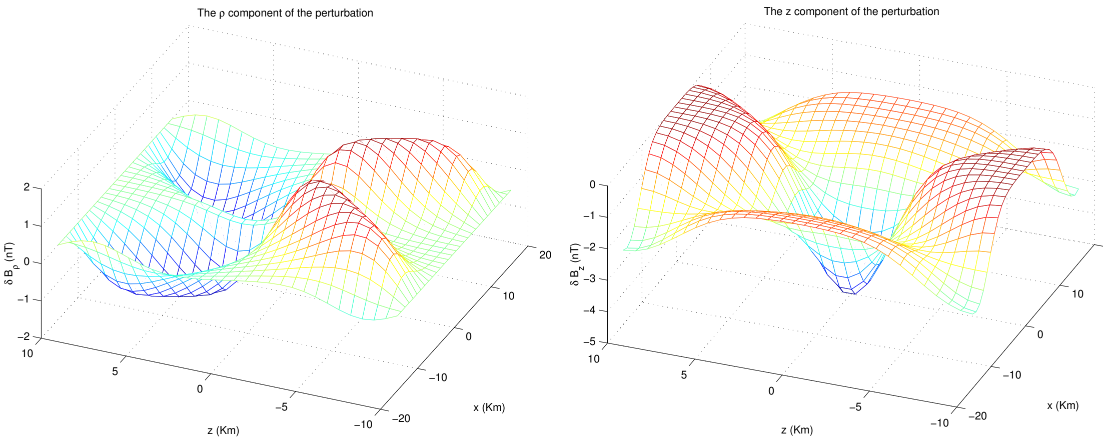

Figure 5.2: The magnetic field perturbation for the main structure. The perturbation on the axis has been chosen to be Gaussian: $\delta B_z(0,z) = \delta B_z(0,0)\exp(-z^2/a^2)$, $a = L/3$, the initial anisotropy is $A_0 = 1.3$, the unperturbed magnetic field is $B_0 = 20\,\mathrm{nT}$, the perturbation in the middle of the bottle is $\delta B_z(0,0) = -2\,\mathrm{nT}$, the unperturbed density of the electrons is $n_0 = 40e^-/\mathrm{cm}^3$, the length of the bottle is $2L = 20\,\mathrm{km}$ and the initial orthogonal temperature is $T_{0\perp} = 10^6\,\mathrm{K}$. With these parameters the radius of the main structure is $R = 2.09\,\mathrm{km}$, $\beta_{0\perp} = 3.47$ and $\alpha = 18.35$.

be anti-correlated with the plasma density. On the other hand, if inequation (5.23b) is satisfied then the magnetic field will be correlated with the plasma density.

The Fourier components of the z-component of the magnetic field perturbation are:

$$\delta B_z^n(\rho) = C_n J_0\left(\frac{n\alpha\rho}{L}\right) \tag{5.24}$$

and the Fourier components of the orthogonal pressure are:

$$\delta p_\perp^n(\rho,z) = -2p_{0\perp}(A_0-1)\frac{\delta B_z^n(\rho)}{B_0} \tag{5.25}$$

The magnetic field has to be real. In order to ensure this, the coefficients C_n must satisfy the relation:

$$C_{-n} = C_n^\star \tag{5.26}$$

The boundary condition used to establish the C_n coefficients is the perturbation of the magnetic field on the z-axis. Taking into consideration the orthogonality of the system $\{exp(in)\}$ and equation (5.26) we find:

$$C_n = \frac{1}{2L}\int_{-L}^{L} \mathrm{d}z\delta B_z(0,z)\exp\left(i\frac{n\pi z}{L}\right) \tag{5.27}$$

The components of the magnetic field perturbation become:

$$\delta B_\rho(\rho,z) \;=\; \frac{2\pi}{\alpha}\sum_{n=1}^{\infty} J_1\left(\frac{n\alpha\rho}{L}\right)\left[a_n\sin\left(\frac{n\pi z}{L}\right) - b_n\cos\left(\frac{n\pi z}{L}\right)\right] \tag{5.28a}$$

$$\delta B_z(\rho,z) \;=\; 2\sum_{n=1}^{\infty} J_0\left(\frac{n\alpha\rho}{L}\right)\left[a_n\cos\left(\frac{n\pi z}{L}\right) + b_n\sin\left(\frac{n\pi z}{L}\right)\right] \tag{5.28b}$$

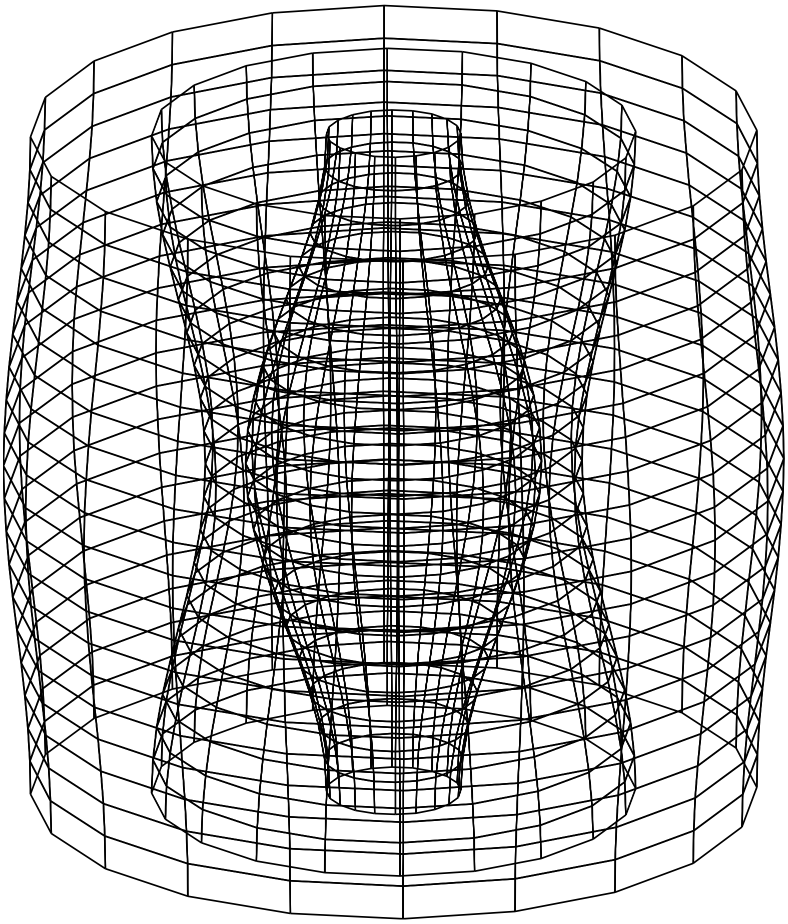

Figure 5.3: The surfaces defined by the field lines for the first Fourier component of the magnetic field perturbation. The main structure has the well known bottle shape. As we move away from the axis, we encounter other structures with similar symmetry, wrapping up each other.

The quantities a_n and b_n are the real and the imaginary part of the coefficients C_n. The components of the magnetic field perturbation for a Gaussian boundary condition are shown in the figure (5.2).

A closer look at the Fourier components in equations (5.28) reveals for each of them a complex geometry that is depicted in figure (5.3). The main structure (closest to the symmetry axis) has the well known bottle shape. As we move away from the axis, we encounter other structures with similar symmetry, wrapping up each other. For values of ρ for which $J_1(\rho) = 0$, the field lines become straight lines on the surface of the cylinder, defining the border between two layers of opposite curvature. The position of the first border, which defines the main structure is given by the ratio of radius to length of the central bubble

$$\frac{n\alpha R}{L} = 3.832 \tag{5.29}$$

and α thus determines the elongation of the bubble.

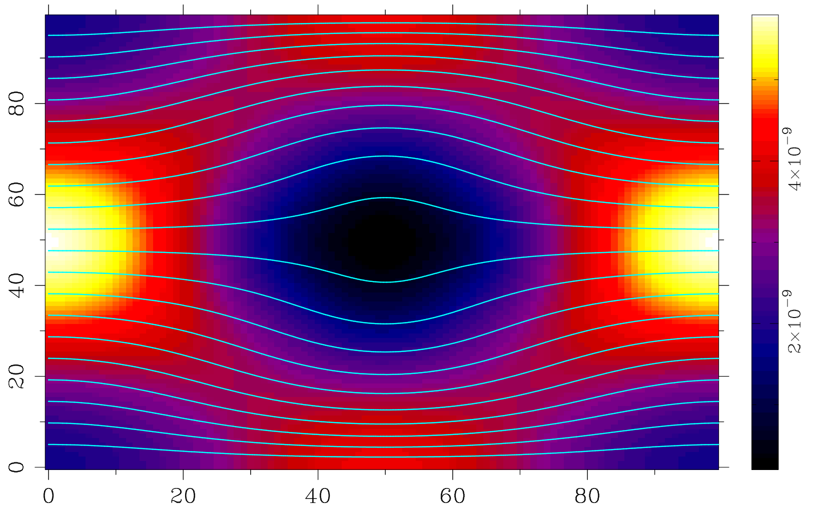

Figure 5.4: The magnetic field lines for the central structure in the first Fourier order. The distance units are arbitrary. The magnetic field intensity is color coded. Note the magnetic field depression in the center surrounded by increased magnetic field. The field intensity is especially high in the neck region of the bottle.

The first order perturbations of the anisotropy and plasma pressure are:

$$\delta p_\perp(\rho, z) = -2p_{0\perp}(A_0 - 1)\frac{\delta B_z(\rho, z)}{B_0} \tag{5.30a}$$

$$\delta p_\|(\rho, z) = -p_{0\|}(A_0 - 1)\frac{\delta B_z(\rho, z)}{B_0} \tag{5.30b}$$

$$\delta A(\rho, z) = -A_0(A_0 - 1)\frac{\delta B_z(\rho, z)}{B_0} \tag{5.30c}$$

These last three relations have also been obtained from the kinetic theory (*Hasegawa* 1969). Note that the in phase – out of phase with the magnetic field character of the pressure and anisotropy variations changes between mirror like ($A_0 > 1$) and firehose like ($A_0 < 1$) structures.

5.2.3 The Instability Mechanism

Both the internal energy perturbation of the plasma and the field energy perturbation are proportional with δB_z. Because of the symmetry of δB_z the global energy perturbation is zero

$$\int_{V_{\text{bottle}}} \mathrm{d}\boldsymbol{r}\delta B_z(\rho, z) = 0 \tag{5.31}$$

This would suggest that the magnetic structure given by the model is always in indifferent equilibrium. However, the electrical currents inside the magnetic mirror can influence its stability.

From the Ampère's law we can find the electric current density that should exist

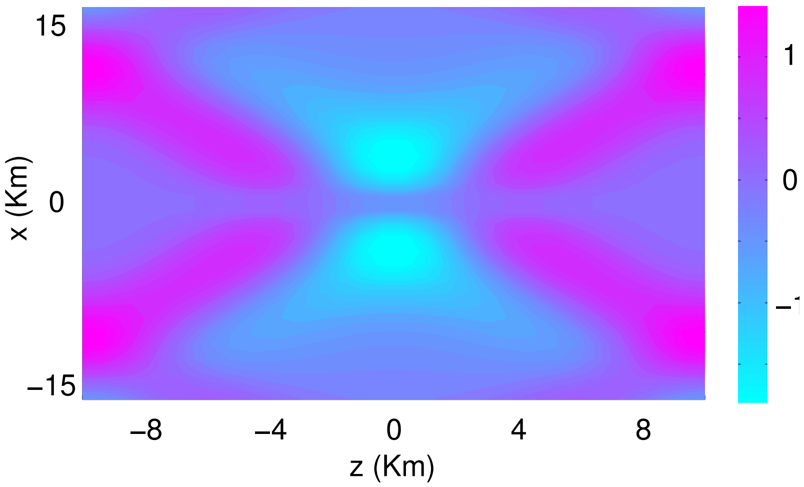

Figure 5.5: The ring current density j_B in μA/m^2. All currents inside the mirror structure flow around the symmetry axis and form current rings with alternate flow directions. Here it can be seen a central ring current bordered upon opposite sense ring currents.

inside the mirror structure:

$$\boldsymbol{j}_{\mathrm{A}}(\rho, z) = \frac{1}{\mu_0}\nabla \times \boldsymbol{B} =$$
$$\frac{2\pi^2}{\mu_0 \alpha L}\left[1+\left(\frac{\alpha}{\pi}\right)^2\right]\sum_{n=1}^{\infty} n J_1\left(\frac{n\alpha\rho}{L}\right)\left[a_n \cos\left(\frac{n\pi z}{L}\right) + b_n \sin\left(\frac{n\pi z}{L}\right)\right]\hat{\boldsymbol{e}}_{\varphi} \quad (5.32)$$

This ring current is illustrated in figure (5.5).

The actual current density $\boldsymbol{j}_{\mathrm{d}}$ existing into the mirror structure can be calculated from the gradient-curvature drift. The drift velocity a particle will gain because of the magnetic field gradient is:

$$\boldsymbol{v}_{\mathrm{G}}^{(s)} = -\frac{\mu^{(s)}}{q^{(s)}}\frac{(\nabla B)\times \boldsymbol{B}}{B^2} = \frac{m^{(s)} {v_{0\perp}^{(s)}}^2}{2B_0}\frac{1}{q^{(s)}}\frac{\mu_0}{2B_0}\frac{\left(\frac{\alpha}{\pi}\right)^2}{1+\left(\frac{\alpha}{\pi}\right)^2}\boldsymbol{j}_{\mathrm{A}} \quad (5.33)$$

The drift current density for species s associated with the magnetic field gradient is obtained from the average of $\boldsymbol{v}_{\mathrm{G}}^{(s)}$. The average of ${v_{0\perp}^{(s)}}^2$ will be expressed using the unperturbed temperature $T_{0\perp}$.

$$\boldsymbol{j}_{\mathrm{G}}^{(s)} = n^{(s)}(\rho, z) q^{(s)} \langle \boldsymbol{v}_{\mathrm{G}}^{(s)} \rangle = \frac{\beta_{0\perp}^{(s)}}{4}\frac{\left(\frac{\alpha}{\pi}\right)^2}{1+\left(\frac{\alpha}{\pi}\right)^2}\boldsymbol{j}_{\mathrm{A}} \quad (5.34)$$

The curvature drift velocity is:

$$\boldsymbol{v}_{\mathrm{C}}^{(s)} = -\frac{2W_{\parallel}^{(s)}}{q^{(s)}B^4}\left[(\boldsymbol{B}\nabla)\boldsymbol{B}\right]\times \boldsymbol{B} = \frac{m^{(s)} {v_{0\parallel}^{(s)}}^2}{2}\frac{\mu_0}{q^{(s)}B_0^2}\frac{1}{1+\left(\frac{\alpha}{\pi}\right)^2}\boldsymbol{j}_{\mathrm{A}} \quad (5.35)$$

The drift current density associated with the magnetic field curvature is found in the same way as $\boldsymbol{j}_{\mathrm{G}}^{(s)}$.

$$\boldsymbol{j}_{\mathrm{C}}^{(s)} = n^{(s)}(\rho, z) q^{(s)} \langle \boldsymbol{v}_{\mathrm{C}}^{(s)} \rangle = \frac{\beta_{0\parallel}^{(s)}}{4}\frac{1}{1+\left(\frac{\alpha}{\pi}\right)^2}\boldsymbol{j}_{\mathrm{A}} \quad (5.36)$$

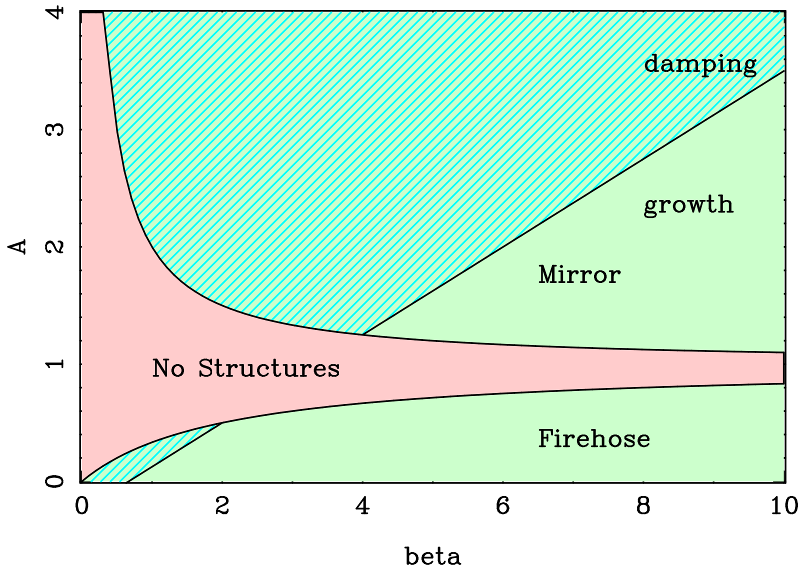

Figure 5.6: The existence and instability domains in the $(A_0, \beta_{0\perp})$-plane. In the pink region the existence condition is not fulfilled. Below the straight line the perturbation grows, above the straight line the perturbation is damped. The structures are mirror like in the upper green area and firehose like in the lower green area.

The combined gradient-curvature current density is:

$$\boldsymbol{j}_{\mathrm{d}} = \frac{1}{4}\frac{3\beta_{0\perp}+2}{2A_0+1}\boldsymbol{j}_{\mathrm{A}} \tag{5.37}$$

At equilibrium $\boldsymbol{j}_{\mathrm{d}} = \boldsymbol{j}_{\mathrm{A}}$. In this case the magnetic field perturbation produces a drift current which in turn sustains the perturbation. Depending on A_0 and $\beta_{0\perp}$ the drift current might be larger or smaller then the current $\boldsymbol{j}_{\mathrm{A}}$ required to sustain the magnetic field perturbation. If $\boldsymbol{j}_{\mathrm{d}} > \boldsymbol{j}_{\mathrm{A}}$ then the perturbation induced by the drift current will be larger then the original perturbation, consequently the drift current intensity will increase. In this situation the mirror structure is unstable. Similarly, if $\boldsymbol{j}_{\mathrm{d}} < \boldsymbol{j}_{\mathrm{A}}$ the magnetic field perturbation will decrease. Therefore the instability condition for the magnetic mirrors in the linear and magnetohydrostatic approximation is:

$$A_0 < \frac{1}{4}\left(\frac{3}{2}\beta_{0\perp} - 1\right) \tag{5.38}$$

Making use of equation (5.38) and of the inequations (5.23) we have plotted the existence and instability domains for the magnetic mirrors in figure (5.6).

5.3 Particle kinetics and distribution function

In section 5.2.3 we have seen that the drift motion of the charged particles gives rise to a pattern of ring currents which are essential for the stability of the magnetic mirror structure. However, to compute these currents we used the gyro-center motion assuming the particle gyro-radius is much smaller than the scale of the magnetic field spatial variations. Of course, when we deal with a statistical ensemble of particles, this approximation is valid only for a subset of the particles in the ensemble.

We wish to investigate in detail the motion of charged particles inside the magnetic mirror structures. We do this by numerically integrating the equation of motion. Depending on the particle initial velocity and on the magnetic field configuration, the particle motion can be either *regular* or *chaotic*. The regular (also called *adiabatic*) motion is well described in the gyro-center approximation and itself can be subdivided into *trapped* motion (the particle is reflected at the mirror points and always remains inside one "bottle") and *escaping* motion (the particle migrates along the magnetic field lines). Both trapped and escaping particles contribute to the ring current system. The chaotic motion obeys to deterministic chaos, the particle gyro-radius significantly changes within one orbit and the particle randomly jumps between neighboring bottles. The chaotic particles do not contribute to the ring current.

After single particle motion has been studied, the next logical step is to investigate how a statistical ensemble of particles described by a distribution function evolves in time and what is its final equilibrium state. We will see that each particle population has its own specific behaviour and equilibrium distribution function.

5.3.1 Single particle evolution

We analyze single particle motion inside a mirror structure given by the model in section 5.2 by direct numeric integration of the equation of motion:

$$m\frac{\partial^2 \boldsymbol{r}}{\partial t^2} = q\left(\frac{\partial \boldsymbol{r}}{\partial t} \times \boldsymbol{B}\right) \tag{5.39}$$

The mass of the particle is m, the charge is q, $\boldsymbol{r}$ is the position vector, t is the time, and $\boldsymbol{B}$ is the magnetic field. We do not take into account any electrostatic field.

Equation (5.39) is solved using the fifth order Runge-Kutta method with adaptive step size control (see *Press et al.* 2002, Ch. 16.2.). This integration method has the advantage of being very fast and accurate. The maximum acceptable error is given as an input parameter and the algorithm makes frequent changes in its step-size such as is most efficient for the requested accuracy. A way to check the overall accuracy is to verify the energy conservation which for our case is the conservation of the velocity magnitude. Most of the cases, even for long integration times, the difference between the initial and final energy is well below one percent.

Types of orbits

A typical example of trapped particle orbit is given in figure (5.7). The magnetic field obeys the first order equations (5.28) for the length $L = 1000\,\mathrm{km}$, $a_1 = -14\,\mathrm{nT}$, $b_1 = 0\,\mathrm{nT}$, an unperturbed field $B_0 = 15\,\mathrm{nT}$ and plasma characterized by $\alpha = 3$. The resulted radius of the main structure is $R = 1277\,\mathrm{km}$. The particle whose track is followed for $1.2\,\mathrm{s}$ is an electron launched with an initial velocity $\boldsymbol{v}_0 = (20, 0, 4) \times 10^3\,\mathrm{km/s}$ from an initial position $\boldsymbol{r}_0 = (200, 0, -100)\,\mathrm{km}$. The particle gyrates around the magnetic field and moves along the line until it reaches the mirror point where

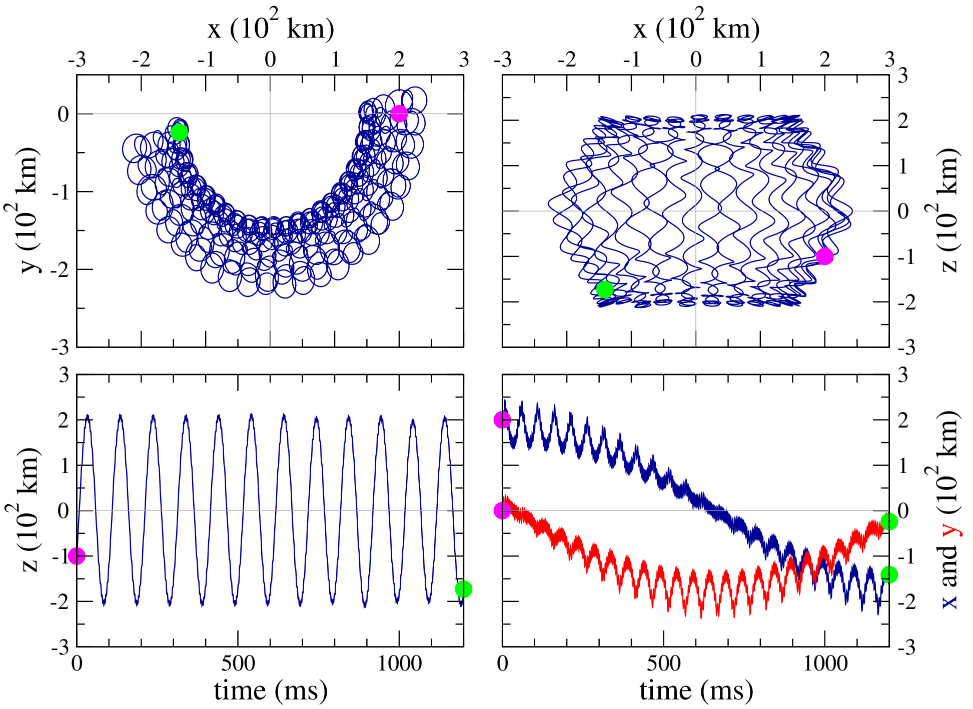

Figure 5.7: A typical orbit for an electron trapped into a magnetic mirror with the magnetic field configuration given by equations (5.28) in the first order with the parameters $L = 1000\,\mathrm{km}$, $a_1 = -14\,\mathrm{nT}$, $b_1 = 0\,\mathrm{nT}$, $B_0 = 15\,\mathrm{nT}$, and $\alpha = 3$. The electron initial position is marked by the magenta points and the final position by the green points.

it suffers a reflection (*Baumjohann and Treumann* 1996). Because of the magnetic field gradient and of the curvature of the magnetic field lines a drift around the structure axis is induced. The gyro motion, the bounce motion and the drift around the symmetry axis are well decoupled and clearly visible.

If we increase the z-component of the initial velocity, the particle will eventually penetrate into the the neighboring structure. The bounce motion disappears being replaced by a forward (*or* backward) motion along z-axis. However, the gyro motion and the drift around the mirror axis remain and are still decoupled.

Both trapped and escaping particles have regular motions for which the gyrocenter motion approximation makes sense. But not all charged particles follow regular motions within the mirror magnetic field. If the particle encounters weak magnetic field, its gyro-radius increases and if it becomes comparable with the magnetic field spatial variation scale, the motion of the particle can become chaotic.

To illustrate the different kinds of orbits we follow the motion of 18 particles with random initial velocities and random initial positions inside the main mirror structure. The model parameters are the same as for the trapped particle above. The result is shown in figure (5.8). Unlike figure (5.7) where we concentrate on the central part of the main structure, here we “zoom out” to encompass the periodicity of the mirror structure along its symmetry axis. Even if in reality the mirror structures cannot be strictly periodic, it is important to realize that particles flow in and out of the mirror structure along the magnetic field lines. Because the particles do not diffuse in the radial direction we did not include the outer shells of the structure.

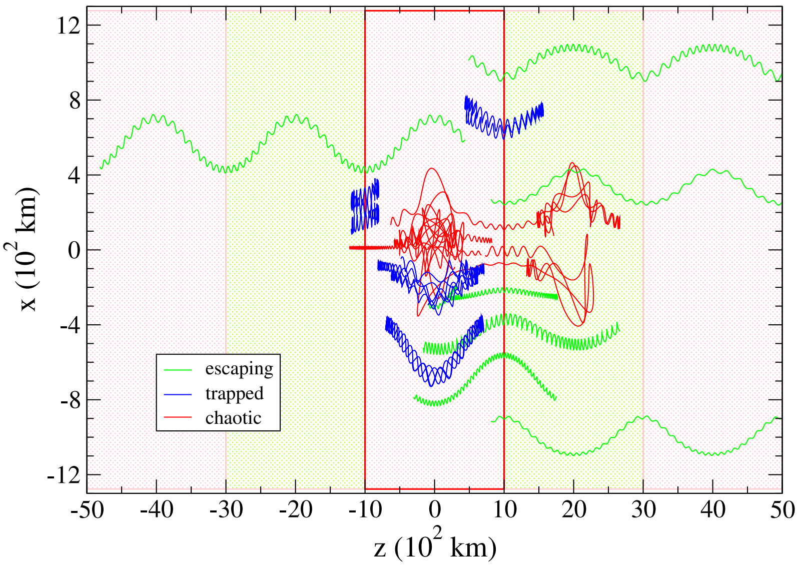

Figure 5.8: Various particle orbits inside a mirror structure. The magnetic field is the same as in figure (5.7) but the simulation time is shorter. The different coloured areas represent the periodicity along the z-axis. At the simulation start the particles are randomly placed inside the main structure (bordered with red) and they are given random speeds.

In order not to overload the plot, the simulation time is much shorter than the simulation time for the particle in figure (5.7). Because of this, the drift around the symmetry axis is much less visible.

The particles distribute themselves more or less equally between the three types. There are seven escaping particles with green orbits in the figure (5.8), they travel along the magnetic field without being reflected. At equilibrium there should be an equal number of particles leaving and entering the structure in this manner.

The five trapped particles with blue orbits reveal that it is possible for particles to be trapped not only inside the main mirror bottle but also in other regions where a weak magnetic field is surrounded by strong magnetic field. In this particular case is the toroidal region around the neck of the bottle. These particles have opposite drift direction with the particles trapped inside the main bottle.

Finally, there are six particles with chaotic orbits drawn in red in figure (5.8). Their trajectories are irregular and they seem to linger around the weak field regions occasionally passing through strong field regions. The chaotic character of the motion of these particles emerge from nonlinear resonances between the bounce and the gyro-motion.

Chaotic particles

Buechner and Zelenyi (1989) had shown that the particle dynamics is controlled by the *curvature parameter* determined by the ratio between the minimum curvature radius of the magnetic field lines and the maximum curvature radius of the particle orbit: $\kappa^2 = R_{\text{field-minimum}}/\rho_{\text{particle-maximum}}$. For κ much larger than one, the magnetic moment (equation 5.5) is a first order invariant of motion and the particles follow regular trajectories. When κ decreases, the magnetic moment ceases to be an

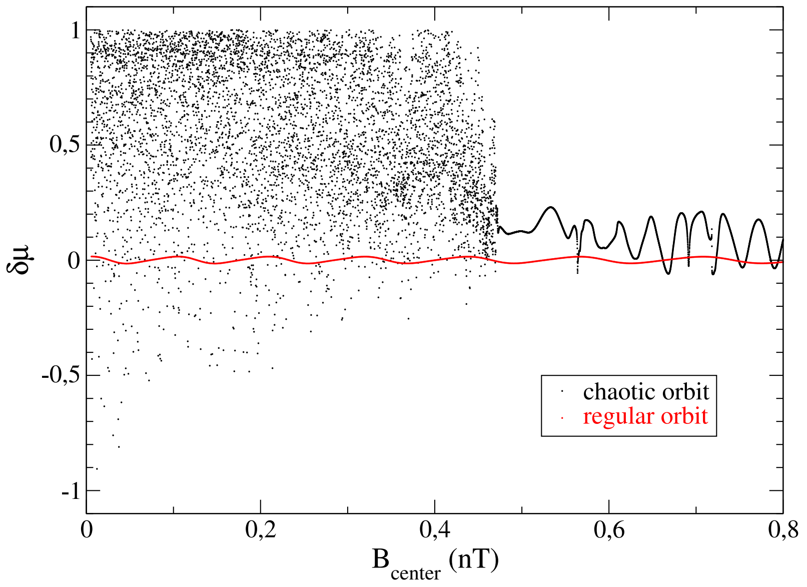

Figure 5.9: Magnetic moment conservation as a function of the magnetic field in the center of the mirror structure. $\delta\mu = (\mu_i - \mu_f)/\mu_i$ remains close to 0 for the adiabatic particle but it wildly oscillates for the chaotic particle.

invariant and the motion become chaotic.

To illustrate the relation between the conservation of the particle magnetic moment and the field curvature we compare the magnetic moment at the initial moment with the magnetic moment after about one hundred gyro-periods in different field configurations for a chaotic as well as for an adiabatic particle. The magnetic field models a structure with $L = 1000\,\mathrm{km}$ within a plasma with $\alpha = 3$. The unperturbed magnetic field B_0 is $5\,\mathrm{nT}$ and the perturbation a_1 takes 10000 values between $-5\,\mathrm{nT}$ and $-4\,\mathrm{nT}$ (corresponding to a magnetic field in the center of the structure between 0 and $1\,\mathrm{nT}$). All other a_j and b_j coefficients are zero. For each value of a_1 two particles are launched and let to evolve for 0.714 seconds corresponding to 100 gyrations in the unperturbed field.

The first particle is launched from the position $\boldsymbol{r} = (236, 624, -257)\,\mathrm{km}$ with a velocity $\boldsymbol{v} = (-5045, -24421, 2037)\,\mathrm{km/s}$. In the figure (5.9) we plot with red colour the quantity $\delta\mu = (\mu_{\mathrm{initial}} - \mu_{\mathrm{final}})/\mu_{\mathrm{initial}}$ as a function of the magnetic field intensity in the center of the bottle which is a measure of the maximum curvature of the magnetic field. The lower the magnetic field in the center, the higher the curvature. $\delta\mu$ remains close to 0 showing that the magnetic moment of this particle is conserved for all values of the perturbation. In fact, if we look at this particle orbit (not shown) we see that it is a trapped particle.

Not the same is true for the second particle launched from $\boldsymbol{r} = (-122, 171, 41)\,\mathrm{km}$ with a velocity $\boldsymbol{v} = (18436, -3334, 6497)\,\mathrm{km/s}$. The black dots in figure (5.9) represent $\delta\mu$ for this particle. If we read the plot from left to right, we observe oscillations in the magnetic moment as the intensity of the magnetic field decreases (curvature increases). Suddenly, as the magnetic field intensity in the center reaches the critical value of $0.47\,\mathrm{nT}$, the oscillations become erratic. This second particle exhibits a chaotic orbit.

When the magnetic mirror structure is filled with plasma, the collective behaviour of each type of particle (trapped, escaping, chaotic) will be different and will have different effects. The particle distribution function at equilibrium offers the richest information available to investigate these effects.

5.3.2 Distribution function evolution

In this section we study a statistical ensemble of charged particles under the influence of the mirror structure magnetic field. We use the *test particles* approximation, meaning that we only consider the action of the magnetic field on the particles and ignore the action of the charged particles motion on the magnetic field and their mutual interaction. In other words, we assume a given magnetic field configuration sustained by some external means in which charged particles are free to move independently from each other.

To simulate the natural evolution of a mirror structure we start with an uniform magnetic field immersed into an uniform density bi-Maxwellian plasma. We let the particles evolve and gradually deform the magnetic field toward its final mirror configuration. The magnetic field change is slow enough so it can be considered static at any time, i.e. no induced electric fields alter the particles motion. After the final magnetic field configuration has been reached, the particles are still let to evolve for a short time to allow for equilibrium.

A direct approach would be to freeze the system and examine the final phase-space density of the particle ensemble by dividing the phase-space into a grid and counting the particles in each cell. However, better statistics are obtained by letting the system to further evolve and assign to each cell a density obtained by the average number of particles which had cross the cell, weighted by the time each particle has spent inside the cell.

Preparation of the initial state

We have to generate the initial state of the particle set. There are numerical algorithms capable to produce pseudo-random numbers uniformly distributed over a given interval. The resulted sequence can be directly used for the generation of the initial particles positions in the simulation box but not for their initial velocities. The initial velocities should follow a given initial distribution function, in our case the bi-Maxwellian distribution (5.3) which is a product of three one dimensional Maxwell distributions:

$$\mathfrak{f}(v) = \left(\frac{m}{2\pi k_{\mathrm{B}}T}\right)^{1/2} \exp\left\{-\frac{m(v-u)^2}{2k_{\mathrm{B}}T}\right\} \tag{5.40}$$

We need a function v, which when applied to an uniform distributed set of numbers $\{s \in (0,1)\}$ to give a set of numbers following the Maxwell distribution $\mathfrak{f}$ in equation (5.40). For a Maxwellian ensemble of N particles, the number of particles with the component j of the velocity between v and $(v + \mathrm{d}v)$ is

$$\mathrm{d}n(v) = N\mathfrak{f}(v)\mathrm{d}v \tag{5.41}$$

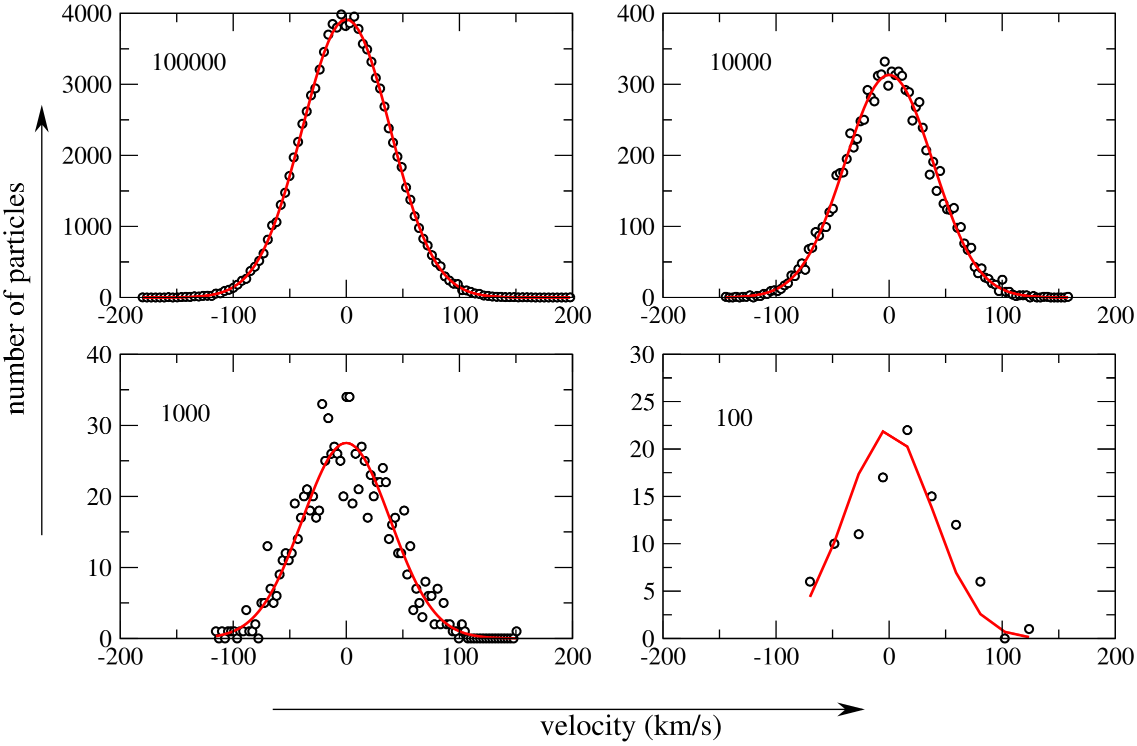

Figure 5.10: Numerical generated (dots) versus theoretical (red line) Maxwellian distribution for ensembles of $\mathrm{N} = 10^2, 10^3, 10^4$ and 10^5 electrons at a temperature $\mathrm{T} = 100\,\mathrm{K}$. To represent the generated velocity distributions we divided the resulted velocity interval into 10 bins for the $\mathrm{N} = 100$ set and into 100 bins for the other sets and counted the particles for each bin.

This number has to be the same when expressed in terms of the new, uniformly distributed, variable s.

$$\mathrm{d}n\big(v(s)\big) = N\mathfrak{g}(s)\mathrm{d}s = N\mathrm{d}s \tag{5.42}$$

It follows that

$$\mathfrak{f}(v)\mathrm{d}v = \mathrm{d}s \tag{5.43}$$

We integrate this equation from $-\infty$ to the velocity v to obtain the function v:

$$v(s) = u + \left(\frac{2k_\mathrm{B}T}{m}\right)^{1/2} \mathrm{erf}^{-1}(1-2s) \tag{5.44}$$

Here $\mathrm{erf}(z)$ is the inverse error function (*Abramowitz and Stegun* 1972) defined as

$$\mathrm{erf}(z) = \frac{2}{\pi}\int_0^z e^{-t^2}\mathrm{d}t \tag{5.45}$$

The initial velocity distribution for N test particles is numerically generated by applying the function v on a set of N pseudo-random numbers uniformly distributed over the interval $(0, 1)$.

Figure (5.10) illustrates the resulted velocity distribution compared with the theoretical Maxwellian distribution for sets with different numbers N of particles. The statistical deviations are large for the ensembles with low number of particles ($N = 100$ and $N = 1000$). Thermodynamic concepts like temperature and pressure

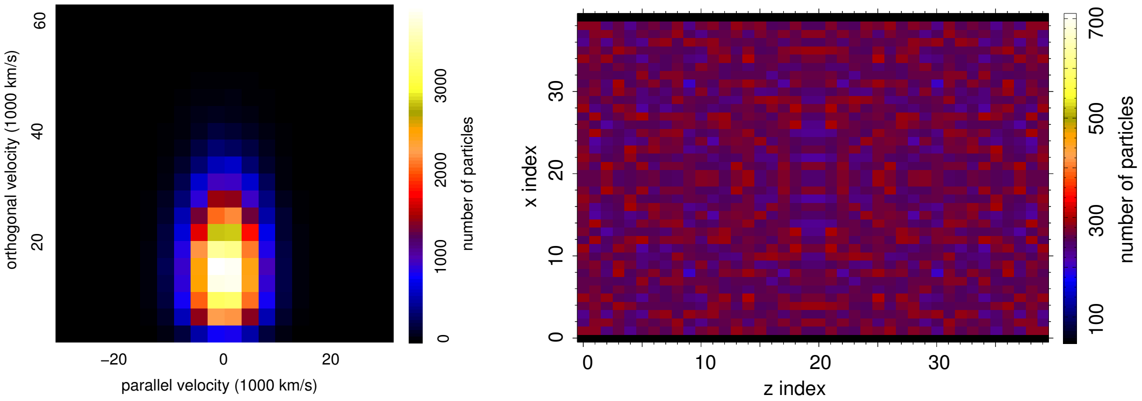

Figure 5.11: Initial phase-space density expressed in number of particles per cell. Left: bi-Maxwellian ($v_\perp = 2v_{||}$) velocity-space density, Right: uniform position-space density. The z coordinate runs from −1000 to 1000 km and the x coordinate from −1277 to 1277 km.

have questionable meanings for such small ensembles. To investigate the evolution of the distribution function we have to use statistical ensembles at least of $N = 10^4$ particles.

We generate an initial bi-Maxwellian set of 10^5 electrons using equation (5.44) with $T_\perp^{\text{input}} = 10$ million degrees Kelvin and $T_{||}^{\text{input}} = 5$ million degrees Kelvin. Because this is a relatively small statistical ensemble, a difference between the above input temperatures and the true kinetic temperatures occurs.

The kinetic temperature is a measure of the particles mean kinetic energy. The equipartition theorem allows us to write the parallel and the orthogonal temperatures as

$$T_{||} = \frac{m}{Nk_\text{B}} \sum_{j=1}^{N} v_{j||}^2 \tag{5.46a}$$

$$T_\perp = \frac{m}{2Nk_\text{B}} \sum_{j=1}^{N} v_{j\perp}^2 \tag{5.46b}$$

If we use the above relations to determine the temperature of our statistical ensemble for the initial state we find $T_\perp^{\text{initial}} = 10.99\,\text{MK}$ and $T_{||}^{\text{initial}} = 5.20\,\text{MK}$. The corresponding anisotropy is $A^{\text{initial}} = 2.11$. These are the reference values to be compared with the final state.

The particles cannot escape in the radial direction across the magnetic field but they will move along the magnetic field outside the initial space domain. At the simulation end a modulo $2L$ operation is applied to their z coordinate to bring them back into the initial domain. The simulated system is three-dimensional with a corresponding six-dimensional phase-space. However, owing to the symmetry of the system, we can reduce the phase-space dimension to four without losing any statistical information. The new dimensions correspond to the spatial coordinates ρ and z and to velocity-space coordinates $v_{||}$ and $v_\perp$. We construct the grid by dividing each dimension into 20 equal intervals. The magnetic structure is symmetrical in the z dimension allowing us to further compress the final phase-space domain by taking

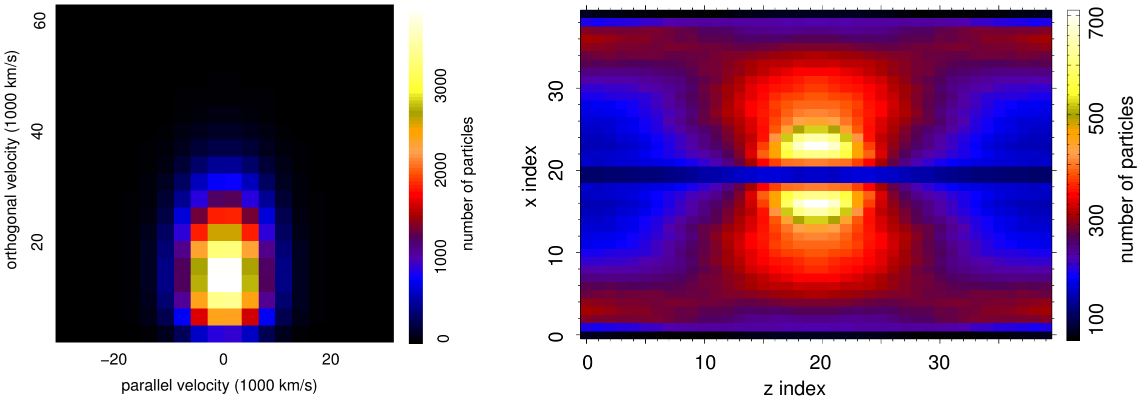

Figure 5.12: Final phase-space density. The velocity distribution remains bi-Maxwellian with an anisotropy reduced to 1.5. The particles density indicates a trapped population and shows kinetic effects such as particle depletion near the symmetry axis.

the absolute value of the z coordinate. Consequently the grid spans in position-space between 0 and L on the axial dimension and between 0 and R on the radial dimension. The limits in the velocity-space are given by the extreme orthogonal and parallel velocities.

The initial phase-space density is represented in figure (5.11). On the left is the two-dimensional velocity-space density obtained through integration over the whole position-space. The anisotropic bi-Maxwellian distribution yields a velocity-space density elongated in the orthogonal velocity dimension. On the right is the two-dimensional position-space density obtained through integration over the whole velocity-space. The small fluctuations are due to the random position assignment to the particles inside the simulation domain.

The final state

The initial uniform magnetic field $B_0 = 1.5\,\mathrm{nT}$ is perturbed to a final mirror structure with a semi-length $L = 1000\,\mathrm{km}$, a radius $R = 1277\,\mathrm{km}$ and a magnetic field intensity in the center $B_0 - a_1 = 0.1\,\mathrm{nT}$. The time elapsed from the simulation start to the moment the final magnetic configuration is attained is 20 unperturbed field gyro-periods. The particle set continue to evolve for another 10 gyro-periods. The ratio between the particles total kinetic energy at the initial and final moment $E^{\mathrm{kinetic}}_{\mathrm{initial}}/E^{\mathrm{kinetic}}_{\mathrm{final}}$ is 0.996 showing a good energy conservation. The last 10 gyro-periods are used for averaging.

The final phase space density is shown in figure (5.12). The velocity distribution is less elongated indicating a more isotropic distribution. Indeed, the final orthogonal temperature slightly decreases to 10.16 MK while the parallel temperature increases to 6.77 MK giving a reduced anisotropy $A^{\mathrm{final}} = 1.5$. These values can be used to cross-check the energy conservation. From the equations (5.46), the weight of the orthogonal temperature is twice the weight of the parallel temperature in the energy balance. This lead us to the very same ratio of 0.997 between the total final and initial kinetic energy of the particles.

To visualize the deviation of the final velocity distribution from an ideal Max-

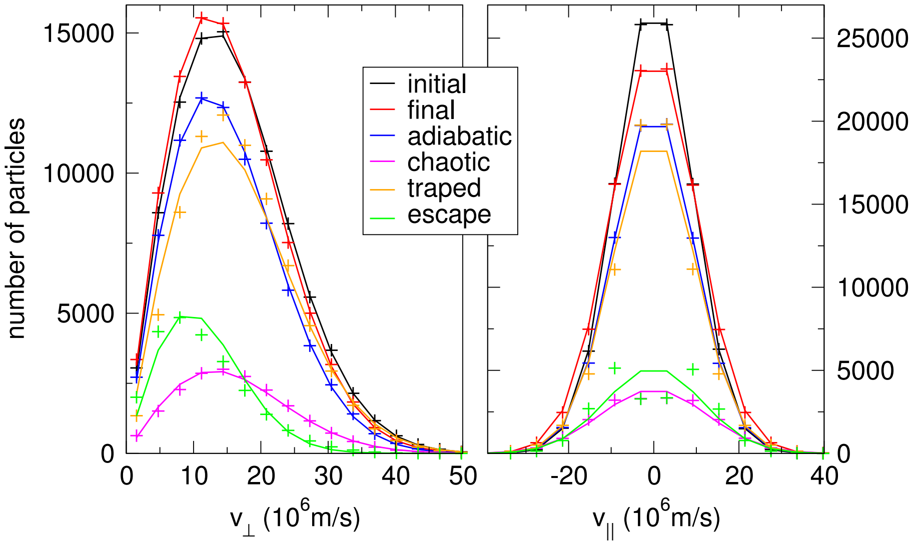

Figure 5.13: Orthogonal and parallel velocity distributions for initial state, final state and subsets of the simulated particle ensemble (plus signs) compared with ideal Maxwell distributions (solid lines). While the initial and the final states are well represented by bi-Maxwellians, in general the subsets are not. This is especially true for the adiabatic and for the chaotic subsets which develop a splitting in their parallel velocities distributions.

wellian distribution we plot in figure (5.13) the one-dimensional velocity densities obtained as the sum over all other dimensions of the phase space density of our particle ensemble versus the same velocity densities of ideal Maxwell ensembles. The plus signs represent our ensemble while the lines represent Maxwell distributions corresponding to the kinetic temperature of our ensemble. Both the initial and final state of our ensemble are well represented by bi-Maxwellian distributions. To be more exact we can compute the deviation as

$$\zeta = \frac{1}{2N} \int |n(\boldsymbol{v}) - n^{\mathrm{Maxwell}}(\boldsymbol{v})| \mathrm{d}\boldsymbol{v} \tag{5.47}$$

For the discrete case this becomes the normalized sum of the differences between the actual number of particles in each velocity space cell and the ideal Maxwellian number of particles

$$\zeta = \frac{1}{2N} \sum_{j=1}^{N^{\mathrm{cells}}} |n_j - n_j^{\mathrm{Maxwell}}| \tag{5.48}$$

This gives deviations of about only one percent for both initial and final state and for both parallel and orthogonal velocities distributions. The virtually no deviation of the final state from a bi-Maxwellian distribution is an a posteriori justification for the anisotropy calculation in section 5.2.

Coming back to figure (5.12) we concentrate on the final position-space density. As expected, the particles density is roughly anti-correlated with the magnetic field intensity, the particles being trapped in the middle o the magnetic bottle and being expelled from the necks where the field magnitude is high. However, a quick visual comparison with the magnetic field magnitude in figure (5.4) shows that the anti-

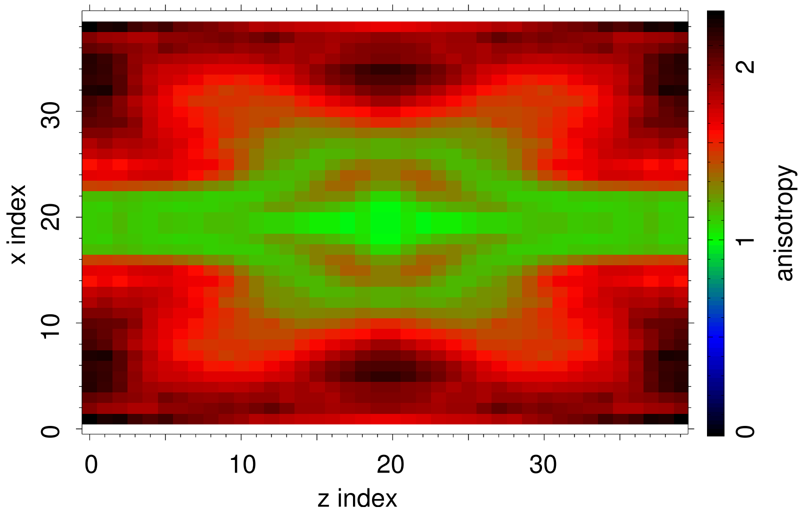

Figure 5.14: The final anisotropy is mostly correlated with the magnetic field magnitude. However, the correlation turns into anti-correlation close to z = ±L. A relatively wide region around the symmetry axis is populated by isotropic particles.

correlation is not perfect, not to mention the particle depletion along the structure axis seen in figure (5.12).

The anti-correlation between the field intensity and the particle density for the mirror structure is a MHD approximation, the deviation we found is a kinetic effect. The magnetic field variation seen by a particle gyrating along a field line is largest close to the structure axis. This makes the particle to be reflected sooner than if it would have if it would have gyrate further from the axis. The consequence is the characteristic erythrocyte shaped density in figure (5.12). If the particle gyrates *very* close to the axis, it will eventually encounter the very weak field in the center. The gyration radius will increase and the particle will start a chaotic motion spending most of the time away from the axis. This mechanism takes place only when the magnetic field perturbation is close to the unperturbed field magnitude and is responsible for the particles depletion along the structure axis. Of course, for a real structure the void of particles will determine an increase in the magnetic field magnitude, this makes the neighboring field lines to move in together with the particles gyrating around them and fill the void.

Equation (5.30c) derived from the mirror structure model shows that the anisotropy is correlated with the magnetic field intensity in the MHD approximation. Even though the number of particles per positions-space cell does not exceed 700 and can be as low as 100, we still can find the temperature anisotropy for each cell by computing the corresponding kinetic temperatures. The result is displayed in the figure (5.14). As for the particles density, the model only approximates the anisotropy. The anisotropy decreases indeed with the magnetic field in the central region of the structure and increases in the high intensity field at the edge of the bottle close to $z = 0$ plane. However, it has a behaviour opposite to the predicted one close to $z = \pm L$. The anisotropy along and in the vicinity of the symmetry axis is close to one. This might be caused by the mainly isotropic chaotic part of the population which has its highest density in the vicinity of the axis (see figure 5.16).

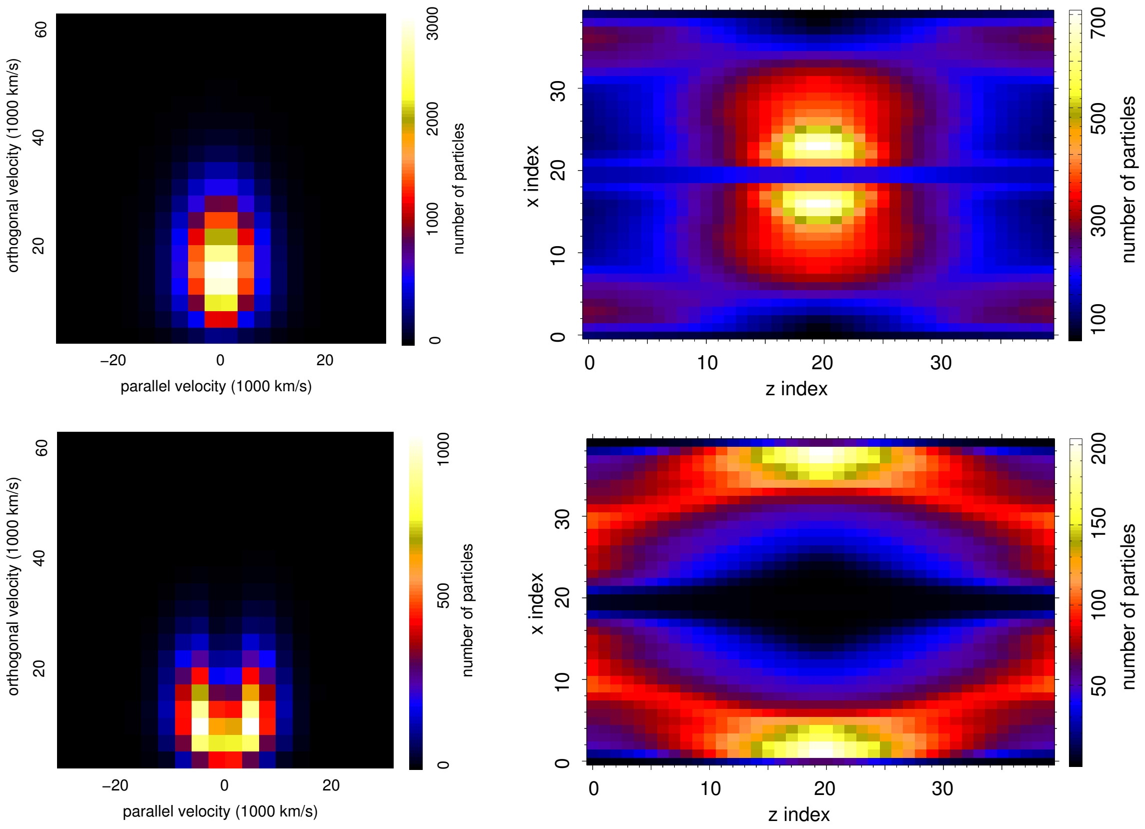

Figure 5.15: Trapped (top) and escaping (bottom) populations. Both velocity distributions deviate from bi-Maxwellians. The effect is stronger for the escaping part where a two beam splitting can be seen. Most of particles are trapped in the center of the bottle, surrounded by a shell of counter-streaming escaping particles.

Particle populations

We can differentiate between trapped and escaping particles by looking for changes in the sign of the velocity component along the magnetic field. If such changes occur, then the particle has suffered a reflection, if in addition, the particle has a regular motion than it will be trapped indefinitely in the low field region, otherwise it will be trapped only for a finite time interval. If the component along the magnetic field of the particle velocity does not change sign than chances are that the particle is an escaping particle. Because of the finite simulation time this definition is not completely accurate but is good enough for our purposes.

About three quarters of the total number of particles are trapped, the rest of one quarter escaping along the field lines. They form two statistical ensembles with different kinetic temperatures and distribution functions illustrated in figure (5.15). Most particles are trapped in the central bottle but an increase in the trapped particles density can also be seen in the toroidal regions around the bottle necks. The trapped population is hotter than the total population in both the orthogonal and the parallel direction. The anisotropy reaching a value close to 2 shows only a slight decrease from the initial value. The velocity distribution of the trapped particles deviates about 10 percent from a Maxwellian distribution for both the parallel and the orthogonal components. A look at figure (5.13) shows that the

	N	$T_\perp$ (MK)	$T_{\|\|}$ (MK)	A	$\zeta_\perp \times 100$	$\zeta_{\|\|} \times 100$
initial	100000	10.99	5.20	2.11	0.9	0.6
trapped	75967	11.5	6.20	1.86	8.5	9.8
escaping	24033	5.76	8.57	0.67	14.4	32.7
chaotic	19743	11.2	10.4	1.08	4.4	9.8
adiabatic	80257	9.99	5.88	1.68	1.9	1.0
total	100000	10.16	7.77	1.5	1.1	1.5

Table 5.1: Simulation results for an initial bi-Maxwellian ensemble of 10^5 particles. Particles are grouped into trapped and escaping, and into chaotic and adiabatic. The final distribution is also bi-Maxwellian but it has reduced anisotropy. The distribution function for the individual particle groups generally differs from bi-Maxwellian.

distribution of parallel velocities is narrower than the Maxwellian correspondent and the distribution of orthogonal velocities is both narrower and shifted toward higher velocities. This translates in an excess of slow particles for the parallel part and an excess of fast particles for the orthogonal part of the distribution.

The escaping population seems to be concentrated in a shell inside the mirror structure. The magnitude variation along the field lines decreases with the distance to the structure axis until it reaches a minimum value and then increases again. The minimum variance field line corresponds to the shell of high density escaping particles. Particles gyrating in this region see little variation in the field magnitude and have a large probability to penetrate into the neighboring structure.

There can be seen a density increase in the high field magnitude regions close to the $z = 0$ plane. There are two causes leading to effect: Firstly, the escaping particles have smaller orthogonal velocities, consequently smaller gyro radii so they follow closer the field lines. Because the field lines become closer in the high field regions, the particles following them are pushed together. Secondly, as the particle advances into the high intensity region, its gyration center moves slower along the line so the particle spends more time in these regions, also leading to an increase of the density.

The orthogonal temperature of the escaping particles ensemble is close to half the orthogonal temperature of the total ensemble. In contrast, the parallel temperature is about one third higher. The resulted anisotropy is about $2/3$.

The subset of particles disturbing the Maxwellian character of the trapped particles has to be taken from the escaping particles ensemble. Since the number of escaping particles is only one third of the number of trapped particles, the deviations from Maxwellian distribution are more serious here. They are about 15 percent for the orthogonal velocities and 30 percent for the parallel velocities. The orthogonal velocity distribution is shifted towards lower speeds while the parallel velocity distribution splits into two counter-streaming beams with speeds around $10000\,\mathrm{km/s}$. This is visible both in the figure (5.13) (the green plus signs) and in the velocity distribution illustrated in figure (5.15). The last shows that the splitting in the parallel velocities is more pronounced for particles with high orthogonal speeds.

We use the conservation of the magnetic moment as a selection criterion for the chaotic particles. This way we split the final state particle set into a set of about

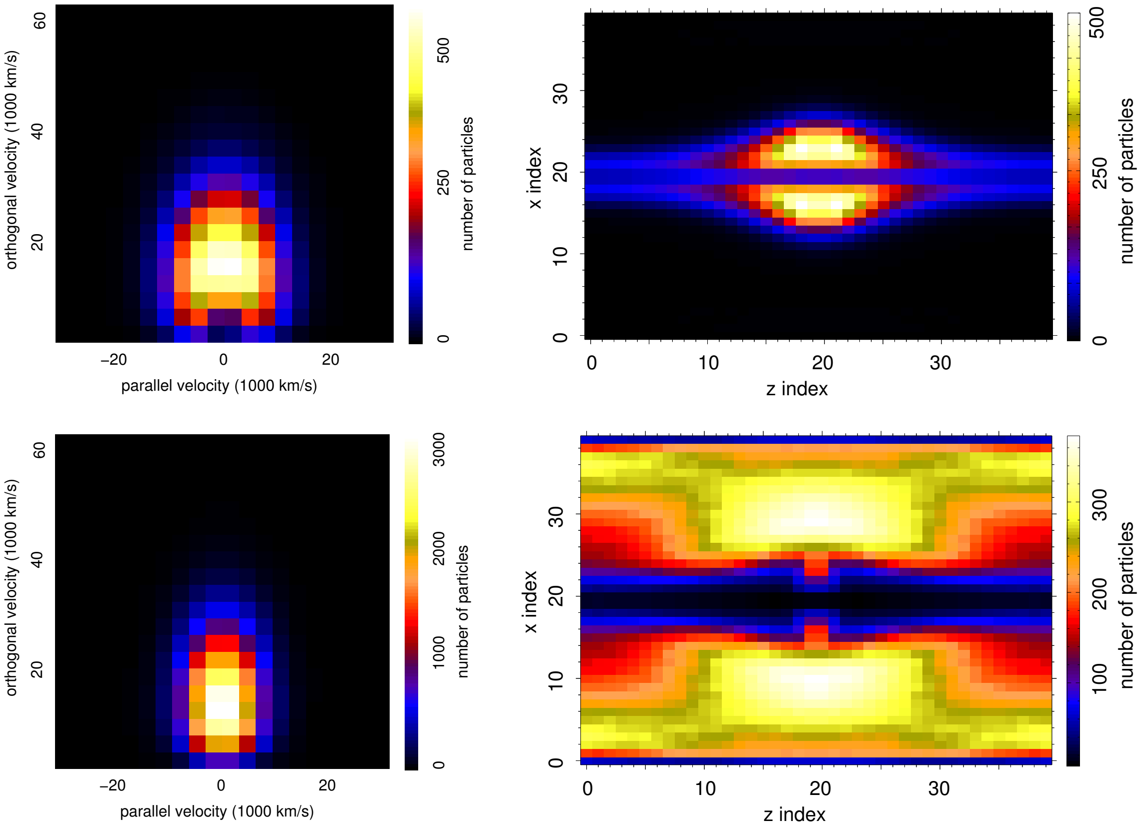

Figure 5.16: Chaotic (top) and adiabatic (bottom) populations. While the velocity distribution of the adiabatic particles is close to bi-Maxwellian, the distribution of chaotic particles deviates from am bi-Maxwellian, especially for the parallel velocities. The chaotic particles spend most of their time in the central region of the bottle. Most of the adiabatic particles are inside a torus surrounding the chaotic particles .

20000 chaotic particles and a set of about 80000 adiabatic particles. Their phase-space densities are shown in figure (5.16).

The deviations of the adiabatic set from a bi-Maxwellian ensemble are around only two percent for the orthogonal velocities and one percent for the parallel velocities. However, the chaotic component exhibits larger deviations. A slight narrowing of the orthogonal velocity distribution of the chaotic particles seen in figure (5.13) is responsible for about 4 percent deviation from the ideal Maxwellian distribution. More important is the 10 percent deviation caused by a splitting of the parallel velocity distribution. Unlike the splitting observed in the parallel velocity distribution of the escaping particles, for the chaotic particles the splitting is more apparent at low orthogonal velocities (see figure 5.16).

While the temperatures and the anisotropies of the adiabatic particles are close to those of the total final ensemble, the chaotic particles are hotter and almost isotropic with a temperature around 10 MK. The principal characteristics of the different ensembles are summarized in table (5.1).

From the spatial distribution of the chaotic and adiabatic particles we can see that there are virtually no adiabatic particles in the vicinity of the symmetry axis, most of the particles populating this area being chaotic. This is in accord with the

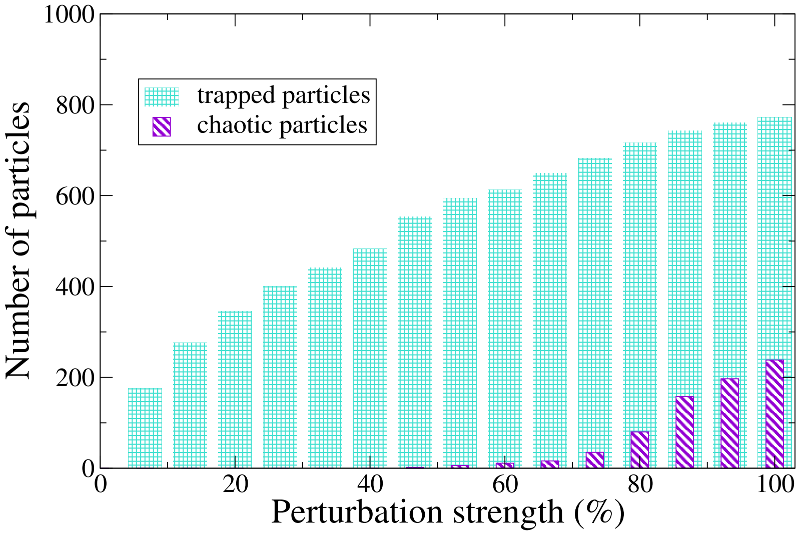

Figure 5.17: The dependence of the ratio of different particles populations on the strength of the magnetic field perturbation. The total number of particles is 1000, the orthogonal temperature is 10 MK, the parallel temperature is 5 MK and the unperturbed magnetic field is 1.5 nT.

above proposed mechanism to explain the particle depletion along the symmetry axis.

For given initial temperatures and unperturbed magnetic field, the ratio between the different particle populations depends on the perturbation strength. When the perturbation is zero, all particles are adiabatic and escaping. As soon as the field is perturbed some particles will be trapped. Much fewer particles will become chaotic for small perturbation of the magnetic field. They need to have high velocities in the distant tail of the distribution in order to have gyro-radii comparable with the field curvature radius. Increasing the perturbation increases both the trapped and the chaotic particles number. This is illustrated in figure (5.17). When the perturbation is half the initial field, about half of the particles are trapped and still no significant number of chaotic particles. One quarter of the total number of particles become chaotic when the perturbation becomes equal to the initial field.

5.4 Application to Cluster data

The model of mirror modes presented in section 5.2 provides the large scale geometry of the magnetic field inside these structures under the assumption of magnetohydrostatic equilibrium. Fitting the model field to measured mirror magnetic field allows for the determination of the dimensions of a mirror bubble in equilibrium and the determination of the bubble structure. For two reasons the measured mirror field signature is unlikely to contain a significant contribution from more distant layers. Firstly, the amplitude of the Bessel functions decays rapidly with increasing radial distance; and secondly the magnetic field at larger distances from the core of the structure is likely to be affected by the interaction of neighboring mirror modes. A mirror structure is identified when the fit is successful. Once the parameters characterizing the mirror structure are known, the magnetic field configuration for the entire structure can be reconstructed.

Because the magnetic field given by the equations (5.28) exhibits a complex three dimensional structure, single point measurements are not enough for unambiguously identify mirror structures. To eliminate the ambiguity, multi point measurements have to be used. The additional measurements can be exploited by different strategies. For instance we can compare the model field resulted from single point measurements with the magnetic field detected by the other (witness) spacecraft. If the correlation is high than we have increased confidence in the fit results. Of course, a better solution is to simultaneously fit multi point data. This has also the advantage of increasing the numerical stability of the fit procedure which can easily become unstable due to the many parameters involved.

This section is presenting the details of the fitting procedure and an application to Cluster magnetic field data.

5.4.1 Fit technique

Fitting the model magnetic field on the measured data is not a trivial task. Even if single spacecraft fit produces questionable results, the fit algorithm is the same as for multiple spacecraft. Therefore, for sake of clarity, we begin by presenting the single spacecraft fit procedure followed the next subsection by the multi spacecraft fit procedure actually used in our case study.

Single spacecraft fit

Application of the method requires the introduction of a normal coordinate system $\{h, d, \gamma, s\}$ (see figure 5.18) in which the spacecraft track is parallel to the (y, z)-plane. In these coordinates the spacecraft trajectory can be defined by three parameters: the angle $\gamma \in [0, \pi/2]$ between spacecraft path and the axis of the mirror structure; the distance $d \in [0, \infty)$ between spacecraft path and the structure axis; and the distance $h \in (-L, L]$ between the center of the structure and point A in figure (5.18). The position of the spacecraft relative to the mirror structure is then specified by one additional coordinate: $s \in (-\infty, +\infty)$, which is the distance between the point B in figure (5.18) and the spacecraft. The usual cylindrical coordinates can be expressed straightforward in terms of normal coordinates:

$$\rho = \sqrt{d^2 + s^2 \sin\gamma} \tag{5.49}$$

$$z = h + s\cos\gamma \tag{5.50}$$

The parameters used for fitting a data set are:

- **(1-3)** the trajectory normal coordinates (h, d, γ)
- **(4)** the initial position of the spacecraft on his path (s_0)
- **(5)** the length of the magnetic mirror (L)
- **(6)** the unperturbed magnetic field intensity (B_0)

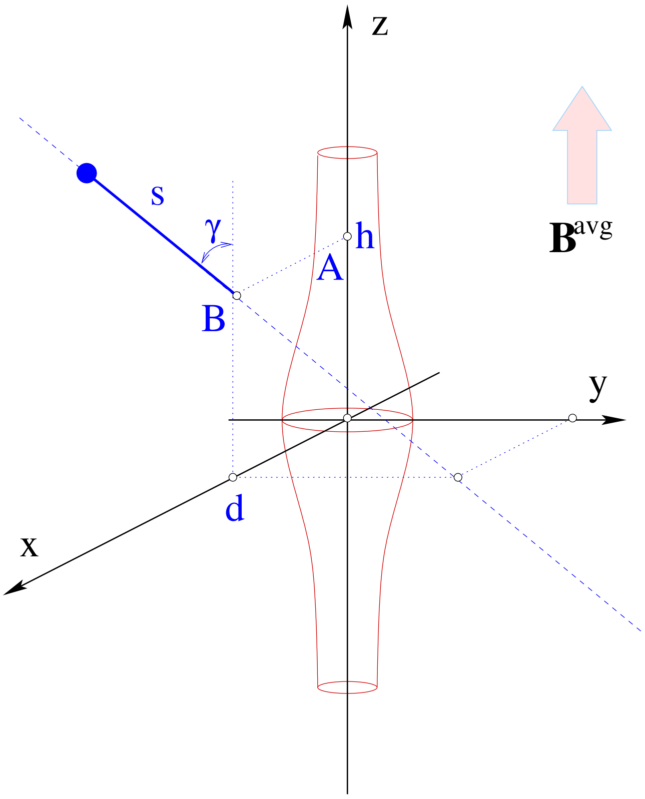

Figure 5.18: The normal coordinates. The dashed line is the spacecraft path which intersects the (x, z) plane of the magnetic mirror system in the point B (d, 0, h) and is parallel with the (y, z) plane. The angle between the trajectory and the z axis is γ and the distance between the spacecraft and the point B is s.

(7) the α plasma parameter

(8-n) the Fourier coefficients a_j and b_j

In order to identify the mirror structures and to determine if the minimization procedure is stable, we scan the magnetic field data using overlapping intervals. From an interval of about 6000 data points (corresponding to about 5 minutes of measurements) we subtract a subinterval $[i, i{+}200]$ corresponding to about 9 seconds or 7000 km. Depending on L and α values (equation 5.29) this corresponds to several layers of the mirror structure. For $L = 1500$ km the spacecraft will pass through 1-2 layers for $\alpha = 1$ and through 6-7 layer for $\alpha = 5$.

On the selected subinterval we perform the minimization of the chi-square function:

$$\chi^2(f, \boldsymbol{p}) = \sum_{k=1}^{n} \frac{\left[f^k_{\rm model}(\boldsymbol{p}) - f^k_{\rm data}\right]^2}{\sigma_k^2} \tag{5.51}$$

where $\boldsymbol{p}$ is the vector of free parameters, $f^k_{\rm model}(\boldsymbol{p})$ is the value derived from the model, $f^k_{\rm data}$ represents the value derived from the measurements and σ_k are the uncertainties. Depending on the stage of the minimization, f will either be the magnitude of the magnetic field or the angle between the spacecraft path and the magnetic field.

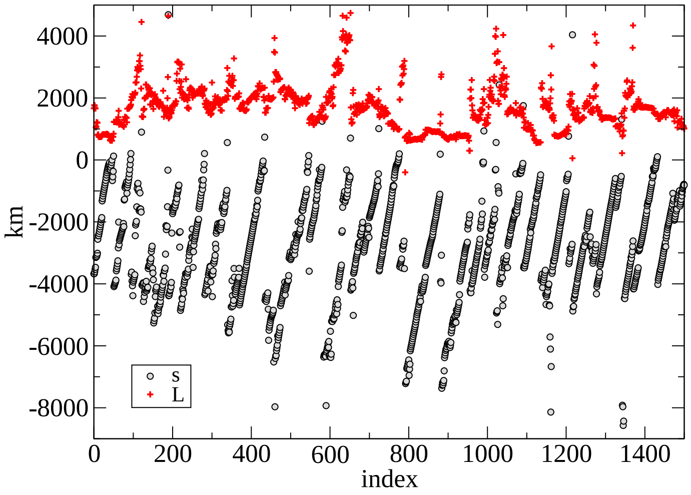

Figure 5.19: Scan example for 1500 200-points 99% overlapping intervals. L is represented by red crosses and s by black circles. The grouping of the parameters is evident. Even if L groups are not horizontal lines, the motion of the spacecraft transpare very clear from the s groups.

Because the magnetic field magnitude along the spacecraft path presents a very strong dependence on the angle γ, the minimization for the magnetic field magnitude with γ being a free parameter does not converge. To avoid this problem we perform a minimization for both magnetic field magnitude and angle, i.e $\chi^2 = \chi^2(B, \boldsymbol{p}) + \chi^2(u, \boldsymbol{p})$, where $u = \cos^{-1}(\boldsymbol{B} \cdot \boldsymbol{v}/Bv)$, $\boldsymbol{v}$ is the spacecraft velocity. Now we have a reasonable value for γ and we can perform the minimization for the magnetic field magnitude using the previous found parameters and keeping γ constant.

We expect that only the central structure and 2-3 layers around it will survive due to the decay of Bessel function and to the presence of other structures in the vicinity. Depending on the thickness of the layers, there could be the case that the data subinterval includes too many layers which no longer obey the model. To circumvent this problem and obtain more reliable parameters we modify the uncertainties:

$$\sigma_k = 1 + 4\left[1 - \exp\left(-\frac{s_k}{\frac{R_J(n)L}{\alpha}}\right)^8\right] \approx \begin{cases} 1 & \text{if } s_k \text{ is inside the first n layers} \\ 5 & \text{if } s_k \text{ is outside} \end{cases} \tag{5.52}$$

$R_J(n)$ is the n-th zero of the first Bessel function. Using these uncertainties the contribution from the outside layers will be very small.

The minimization procedure will produce a set of parameters for the data subinterval $[i, i + 200]$. If the minimization have converged and the parameters have reasonable (physical) values they will be used as start parameters for the next data subinterval $[i + n, i + n + 200]$, otherwise the default values will be used. We usually take $n = 2$ (99% overlapping intervals).

After scanning the whole data interval we will have about 3000 sets of parameters

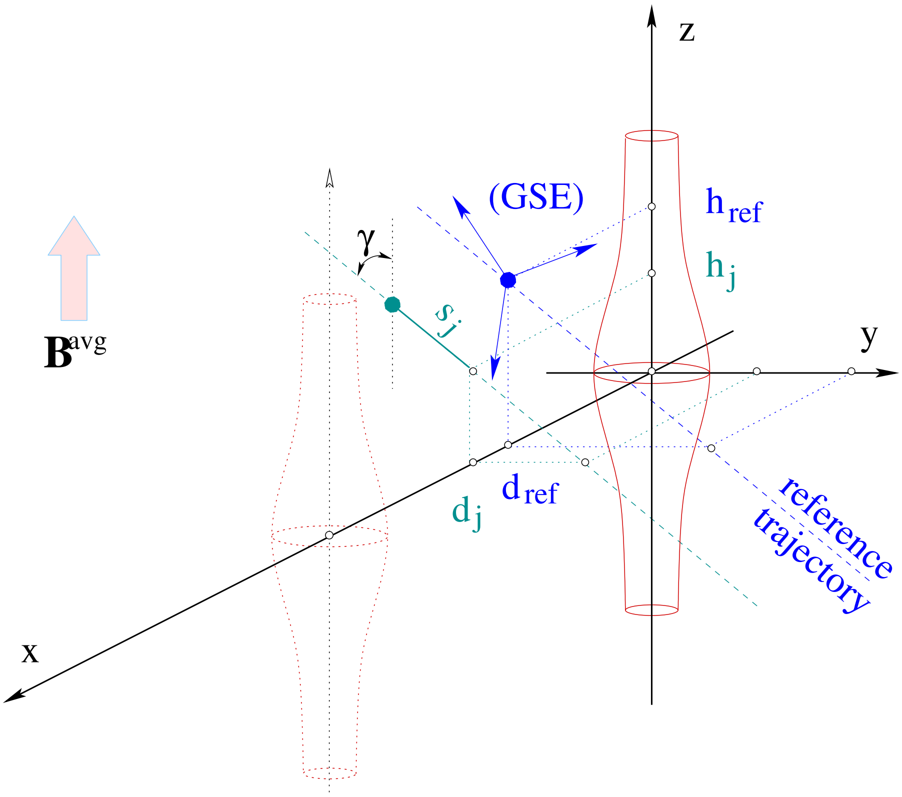

Figure 5.20: The reference spacecraft (blue) and one of the others spacecrafts (green) at the moment t=0. Dotted is represented the second possible position of the mirror structure.

(one set for each subinterval). These can be visually inspected representing the parameters versus the number (i) of the data subinterval which have produced them.

If the scan was successful we expect to see the parameters grouped close to each other for each region where a magnetic mirror was present in the data. All parameters but s should be grouped around constant values corresponding to their average values so the shapes of their groups should suggest horizontal lines. The s groups should also be linear but with the same positive slope, reflecting the motion of the spacecraft (see figure 5.19). These characteristics have been observed when the above procedure was applied to Cluster data.

However, single point measurements cannot unambiguously determine a three dimensional structure. We have to use multi point measurements.

Multiple spacecraft fit

To be able to express the model magnetic field at the other three spacecraft locations we need the transformation matrix from the local GSE system (GSE translated at point B in (figure 5.18)) to the magnetic mirror system.

A vector in the local GSE reference system can be expressed in the mirror system using the transformation:

$$\boldsymbol{w}^{(\mathrm{mirror})} = \boldsymbol{T} + \mathcal{R}^{z}(\theta)\mathcal{R}^{y}(a)\mathcal{R}^{x}(b)\boldsymbol{w}^{(\mathrm{GSE})} \tag{5.53}$$

By $\boldsymbol{T}$ we have denoted the translation vector and by $\mathcal{R}^{x_j}(\varphi)$ the rotation matrix with angle φ around the versor $\hat{\boldsymbol{x}}_j$.

The rotation $\mathcal{R}^y(a)\mathcal{R}^x(b)$ aligns the z axis with the average magnetic field:

$$\begin{aligned} \boldsymbol{w}' &= \mathcal{R}^y(a)\mathcal{R}^x(b)\boldsymbol{w}^{(\mathrm{GSE})} && (5.54) \\ \begin{pmatrix} 0 \\ 0 \\ B \end{pmatrix} &= \mathcal{R}^y(a)\mathcal{R}^x(b)\boldsymbol{B}^{(\mathrm{GSE})} && (5.55) \end{aligned}$$

The a and b angles are given by:

$$\begin{aligned} \tan b &= -\frac{B_y}{B_z} && (5.56) \\ \tan a &= \frac{B_x}{B_z \cos b + B_y \sin b} && (5.57) \end{aligned}$$

The last rotation, $\mathcal{R}^z(\theta)$ brings the (y, z) plane parallel with the spacecraft trajectories:

$$\begin{aligned} \boldsymbol{w}'' &= \mathcal{R}^z(\theta)\boldsymbol{w}' && (5.58) \\ \begin{pmatrix} 0 \\ v''_y \\ v''_z \end{pmatrix} &= \mathcal{R}^z(\theta)\boldsymbol{v}' && (5.59) \end{aligned}$$

The angle θ is given by:

$$\tan\theta = -\frac{v'_x}{v'_y} \qquad (5.60)$$

and the translation vector is:

$$\boldsymbol{T} = \begin{pmatrix} d^{\mathrm{ref}} \\ 0 \\ h^{\mathrm{ref}} \end{pmatrix} \qquad (5.61)$$

Knowing the normal coordinates for the *reference spacecraft* we have to find the normal coordinates for the other spacecraft. Let us define the origin of time as the moment when the reference spacecraft intersects the (x, z) plane of the MM system: $s^{\mathrm{ref}}(t = 0) = 0$. There are different time lags for the other spacecrafts:

$$s^j(\tau^j) = 0 \qquad (5.62)$$

Using the above coordinate transformations we can find these time lags:

$$\begin{pmatrix} x^{j\prime\prime}(\tau^j) \\ 0 \\ z^{j\prime\prime}(\tau^j) \end{pmatrix} = \begin{pmatrix} x^{j\prime\prime}(0) \\ y^{j\prime\prime}(0) \\ z^{j\prime\prime}(0) \end{pmatrix} + \begin{pmatrix} 0 \\ v''_y \\ v''_z \end{pmatrix} \tau^j \qquad (5.63)$$

$$\tau^j = -\frac{y^{j\prime\prime}(0)}{v''_y} \qquad (5.64)$$

The s coordinate for each spacecraft is:

$$s^j(t) = v(t - \tau^j) \qquad (5.65)$$

For our time scale, the trajectories are parallel with each other therefore the angle γ is the same for all spacecrafts. The other two normal coordinates are the x and z coordinates in the mirror system at $t = \tau^j$:

$$\begin{pmatrix} d^j \\ 0 \\ h^j \end{pmatrix} = \boldsymbol{T} + \boldsymbol{r}^{j\prime\prime}(0) + \boldsymbol{v}''\tau^j \tag{5.66}$$

Because of the symmetry there are two possible positions of the mirror structure once we know the normal coordinates for the reference spacecraft (figure 5.20). This implies two sets of normal coordinates for each non-reference spacecraft: $\{d^j, h^j, s^j, \gamma\}$ and $\{2d^{\text{ref}} - d^j, h^j, s^j, \gamma\}$.

Given a mirror structure characterized by the set of parameters $\{h^{\text{reference}}$, $d^{\text{reference}}$, γ, $s^{\text{reference}}$, L, B_0, α, a_j, $b_j\}$, we are now in position to compute the model magnetic field along all spacecraft tracks (model propagation).

The simplest application of model propagation is to use it as a quality indicator for single spacecraft fit. Once a mirror structure is found by fitting the data from one spacecraft selected as reference spacecraft, we calculate the normal coordinates for the other (witness) spacecraft and propagate the model magnetic field to their locations. By comparing the predicted magnetic field with the magnetic field measured by the witness spacecraft the quality of the fit can be tested. However, even if by comparing the propagated magnetic field with the measured data we gain more confidence in the fit results, due to the large number of parameters involved, the numerical code is still unstable to small changes in the initial parameters.

To really take advantage of the multi point measurements we have to simultaneously fit the data from all spacecraft. For the reference spacecraft we choose some starting guess parameters and we calculate the starting guess normal coordinates for the other three spacecraft. Having the normal coordinates we simultaneously fit the data from all spacecraft by minimizing the sum of χ^2 (equation 5.51) over all spacecraft. A scanning procedure similar with the one described in (sec.5.4.1) can be implemented.

It is also possible to combine these approaches: Simultaneously fit the data from $1 < n \leq 4$ spacecraft. With the resulted parameters calculate the model magnetic field for the remaining $4-n$ witness spacecraft and compute the correlations between the measured magnetic field and the fit/propagation model magnetic field.

5.4.2 A case study

In the way described above, we analyzed an interval of strong mirror wave activity (*Lucek et al.* 2001) from November 10, 2000 (Day 315) 08:20-08:25 UT. Cluster was in the dusk side magnetosheath with a typical spacecraft separation of 1000 km, moving with a velocity in the GSE frame of about 1 km/s. Using correlation analysis, corroborated with Wind observations, *Lucek et al.* (2001) concluded that the plasma flow velocity was of 815 km/s in the direction C1 – C3 (see figure 5.21).

Magnetic field data at a resolution of 22 vectors per second were analyzed using a fitting window with a width of 200 data points, corresponding to about 9 s or 7000 km. Depending on the values of L and α (equation 5.29) this corresponded to

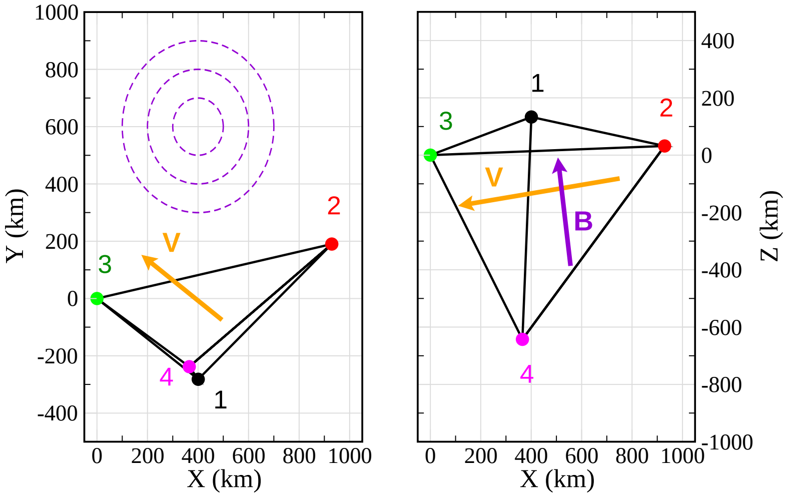

Figure 5.21: Cluster tetrahedron configuration on November 10, 2000, 08:20:00. The formation was close to a regular tetrahedron with 1000 km separation between spacecraft. The C1 – C3 direction was aligned with the plasma flow.

d^{ref}	=	1490 km	a_1	=	4.5	b_1	=	16.7
h^{ref}	=	383 km	a_2	=	11.3	b_2	=	33.3
γ	=	73.9^o	a_3	=	-24.8	b_3	=	-0.7
L	=	6186 km	a_4	=	-19.8	b_4	=	-13.4
B_0	=	52.2 nT						
α	=	11.5						

Table 5.2: Normal coordinates and model parameters as resulted from the fit for the identified mirror structure.

several layers of the mirror structure. Assuming that $L = 5000\,\text{km}$, the spacecraft would have passed through 1-2 layers for $\alpha = 5$, and through 3-4 layers for $\alpha = 10$. In order to identify subintervals where the fit procedure was stable with respect to small changes in the data selected for analysis, a sliding window technique was applied and the variability in the resulting parameters examined.

The subinterval [08:20:00, 08:20:10] is shown in detail. Here agreement between the model and the witness spacecraft was very good. The reference spacecraft C1 and spacecraft C2 were chosen to participate in the fit. C3 and C4 were chosen as witness spacecraft. C1 and C2 had a large separation in the direction orthogonal to the average magnetic field, and were expected to sample different mirror structure layers. The velocity vector was aligned with the C1 – C3 separation vector (*Lucek et al.* 2001), and so the magnetic field measured by C3 was very similar to the magnetic field measured by C1. As a consequence, the magnetic field measured by

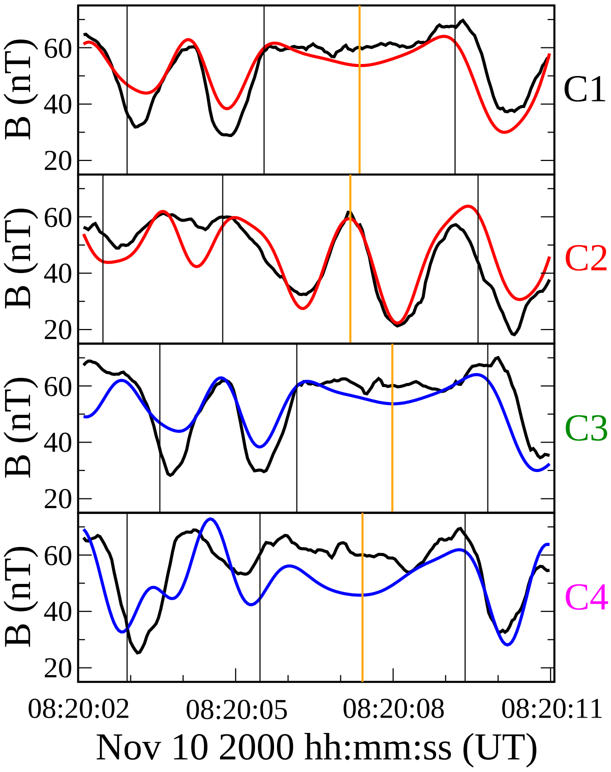

Figure 5.22: Measured (black lines) and model (colored lines) magnetic field intensity for the four Cluster spacecraft. C1 and C2 were participating in the fit, C3 and C4 were witness spacecraft. The vertical orange lines represent the intersection with (x, z) plane (i.e. s = 0) and the vertical black lines separates different layers of the mirror structure.

C3 did not contribute any additional information to the fit. A comparison between the measured and model magnetic field intensity for each spacecraft produced the following cross correlation coefficients: $C_1 = 0.81$, $C_2 = 0.83$, $C_3 = 0.78$, $C_4 = 0.64$. The fitting parameters are given in table (5.2). The radius of the main structure was found to be $R = 2061\,\mathrm{km}$.

Figure (5.22) shows the measured and model magnetic field intensities. The vertical orange lines mark the intersection with the (x, z) plane, i.e. the time when the distance (d) between spacecraft and the axis of the mirror structure was minimum. The vertical black lines mark the boundaries between different layers. Multiple minima result from passing through different regions of the same magnetic mirror structure. This can also be seen from figure (5.23), which shows the way in which the spacecraft passes through the layers of the structure.

Figure (5.24) shows the reconstructed magnetic field $(x - z)$ plane. This figure reveals that C1, C3 and C4 passed through a central uniform field region of the structure yielding plateaus in figure (5.22). C2 was much closer to the axis measuring large changes in the magnetic field inside the central structure.

Generally, the quality of the parameters can be improved by performing new fits,

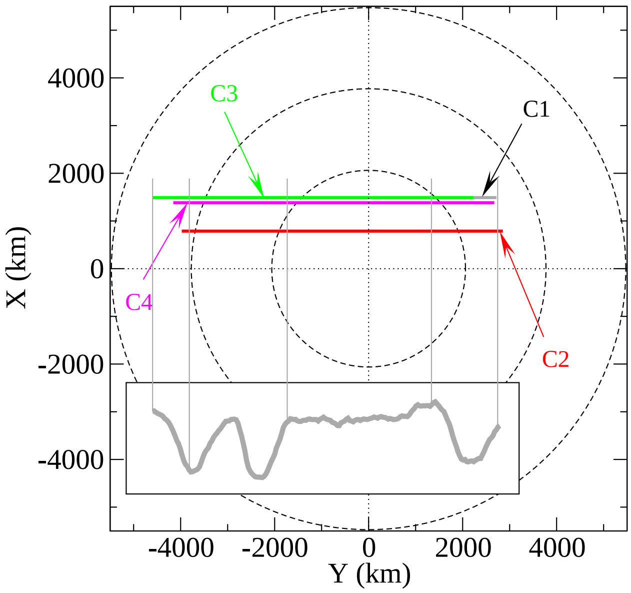

Figure 5.23: The projections of the spacecraft trajectories in the (x-y) plane (horizontal straight lines) and the magnetic field measured by C1 (gray curve). The circles represent the boundaries between different layers.

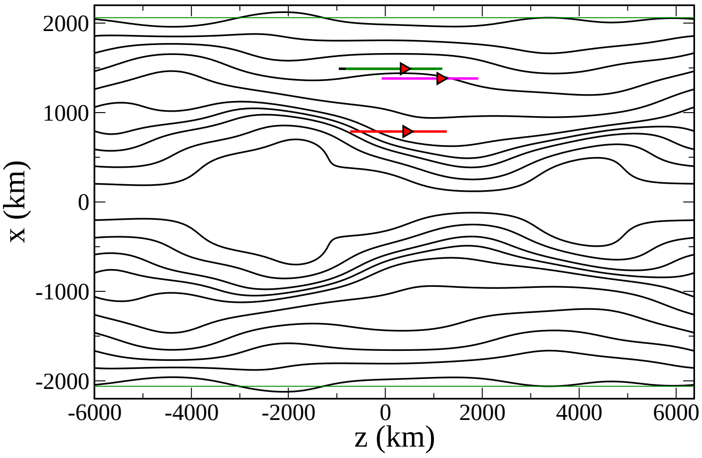

Figure 5.24: The magnetic field lines derived from the model. The straight lines are the projections of the spacecraft trajectories on the (x-z) plane. The triangles are the points where the spacecraft paths intersect the (x-z) plane.

using data from all four spacecraft and the previous parameters as start parameters. For this particular event, however, we found that no improvement could be achieved.

5.5 Remarks

The applications in this chapter are based on the mirror structure model presented in section 5.2. We have to be aware that this is a perturbative (first order) magnetohydrostatic model and it is only an approximation. Because of the interaction with other magnetic structures in the vicinity, and of the radial decay of the perturbation we expect the outer layers of the mirror structures measured *in situ* to deviate from our model. Rotational symmetry and periodicity are, of course, only approximations. Nonlinear (*Kivelson and Southwood* 1996) as well as kinetic effects can be significant and they can lead to large deviations from our model. Some kinetic effects were pointed out in section 5.3.2. A much more detailed discussion of kinetic effects is given by *Pokhotelov et al.* (2001a,b, 2003, 2004).

However, the model presented here describes well many observed properties of the mirror structures. It gives an insight into the physics of the mirror structures and can be used for simulations and for better understanding *in situ* magnetometric and particle data. To our knowledge, the model presented in section 5.2 is the first model which provides a three-dimensional geometry of the mirror structures magnetic field. It is also the first to give an estimation for the electrical current density distribution inside the mirror structures.

Outlook

Waves are ubiquitous in space plasmas. In particular they play a central role in the transfer of energy and momentum from the solar wind to the Earth's magnetosphere. The advent of the Cluster constellation opened up for the first time the possibility to determine three dimensional characteristics of these waves.

This thesis presents several techniques which take full advantage on the simultaneous multi-point measurements in space offered by Cluster. These techniques are applied to study the plasma waves in the near Earth space environment.

The beamformer technique requests too large number of sensors to have practical application in the foreseeable future in space science. The solution is the Capon technique which has been successfully applied to Cluster data. We investigated its limits in the wave length domain and showed that for a tetrahedron configuration it can be safely applied from the Nyquist wave length up to tens of average spacecraft separations. We also showed that it can accurately detect non-planar waves as long as the local curvature radius of the wave front is at least several times larger than the average spacecraft distance. An interesting finding is that the wave telescope is very selective regarding the planarity of the wave fronts. If two waves with different curvatures are simultaneously detected, the wave telescope strongly favors the wave closer to a plane wave. A consequence is that the waves detected by the wave telescope in Cluster data represent most probably the far field view, even if stronger, local generated waves are present.

By giving up the plane wave representation and adopting a spherical wave representation, the source locator is able to investigate waves generated in the immediate vicinity of the sensor array. Making use of synthetic data we showed that up to three waves with close frequencies can be simultaneously detected by the source locator. It has been demonstrated that the source locator is able to distinguish between plane and spherical waves for sources up to tens of inter-spacecraft separations. We have carefully examined the effects caused by the motion of the source and of the observer relative to the propagation medium. They can be very complex as they not only change the observed frequency but they also deform the wave fronts. The deformed wave fronts do not have any longer neither unique curvature center, nor unique wave length. These become local quantities. Nevertheless, we showed how to manage these cases and how useful information can still be extracted from the source locator output.

A case study on Cluster magnetic field data, revealing an apparently elongated source region drifting with the plasma flow has been presented. A longer data interval has been used to statistically investigate plasma wave sources across the foreshock, magnetosheath, outer magnetosphere, and cusp region. The source locator allowed the determination of the propagation directions and of the average distance between sources for each magnetospheric region. The electron foreshock and the cusp seem to be very active regions where waves are continuously generated at close distances.

A perturbative model, based on the equilibrium between the magnetic field and the plasma pressure has been developed to describe the static mirror structures. To our knowledge it is the first model able to give the three dimensional magnetic field configuration of mirror structures. The orbits of charged particles inside the magnetic field given by the model can follow regular trapped or escaping paths, or can follow irregular motions. The motion becomes irregular when the curvature radius of the orbit becomes comparable or larger than the curvature radius of the magnetic field lines. The evolution of an entire particles ensemble, from an initial uniform density bi-Maxwellian state to the equilibrium state, shows a decrease in the pressure anisotropy and slight departures from the density - magnetic field strength anti-correlation. Even if the total distribution function remains bi-Maxwellian, the different particle populations can largely deviate from bi-Maxwellian distributions.

A scan and fit procedure has been developed to identify magnetic mirror structures using multi-point magnetic field measurements. A case study, showing a mirror structure identified in the dusk side magnetosheath has been presented.

Appendix

A.1 Notation Conventions 135
A.2 Array output for vector signals 137
A.3 Source locator numerical implementation 138
A.4 Equirectangular projection 146

A.1 Notation Conventions

The conventions used in this thesis are as follows:

- Complex conjugation is denoted by a star superscript: $z^\star$
- The real part of a complex number is denoted by $\Re(z)$
- The imaginary part of a complex number is denoted by $\Im(z)$
- Vectors are represented with boldface symbols such as $\boldsymbol{V} = \begin{pmatrix} V_1 \\ \vdots \\ V_n \end{pmatrix}$
  - the corresponding raw vectors are $\boldsymbol{V}^\mathsf{T} = \big(V_1, \dots, V_n\big)$
  - The hermitian conjugates are $\boldsymbol{V}^\dagger = \big(\boldsymbol{V}^\mathsf{T}\big)^\star$
  - The scalar product of two column vectors is $\boldsymbol{V} \cdot \boldsymbol{W}$or $\boldsymbol{V}^\mathsf{T}\boldsymbol{W}$
  - The result of $\boldsymbol{V}\boldsymbol{W}^\mathsf{T}$is a matrix with elements $V_i W_j$
  - The vector product is $\boldsymbol{V} \times \boldsymbol{W}$
  - The Euclidean norm of a vector is $\|\boldsymbol{V}\| = \big(\sum_j V_j^2\big)^{1/2}$
  - Unit vectors are written as $\hat{\boldsymbol{n}}$.
- Matrices and tensors are indicated by calligraphic characters such as $\mathcal{M}$. As for the vectors, the transpose is $\mathcal{M}^\mathsf{T}$ and the hermitian conjugate is $\mathcal{M}^\dagger$.
- The inner product of two functions $f(\alpha)$ and $g(\alpha)$ is

  $$\langle f(\alpha) | g(\alpha) \rangle_\alpha = \begin{cases} \int f^\star(\alpha) g(\alpha) d\alpha & \text{if } \alpha \text{ takes continuous values,} \\ \sum_j f^\star(\alpha_j) g(\alpha_j) & \text{if } \alpha \text{ takes discrete values.} \end{cases}$$

  The integral or sum are taken over all possible values of α.
- The Fourier transform of a function $g(t)$ is

  $$\tilde{g}(\omega) = \frac{1}{2\pi} \left\langle e^{i\omega t} | g(t) \right\rangle_t$$

List of symbols

symbol	description	page
α	– line of sight angle	(59)
	– α parameter	(101)
β	plasma β parameter	(101)
$\delta(\cdot)$	Dirac function	(26)
$\chi(\cdot)$	χ function	(122)
ϵ	random deviation	(39)
φ	– wave phase	(39)
	– spherical coordinate	(28)
	– cylindrical coordinate	(99)
ϕ	magnetic flux	(17)
κ	curvature parameter	(109)
λ	wave length	(30)

μ	– magnetic moment	(98)
	– magnetic permittivity	(98)
ν	frequency (s^{-1})	(32)
ω	pulsation (rad/s)	(26)
ρ	distance source - sensor	(55)
$\tau_\pm$	arrival time	(60)
$\xi_\pm$	ξ factor	(60)
ζ	statistical deviation	(115)
A	- temperature anisotropy	(98)
	- area	(17)
a_j, b_j	Fourier coefficients	(103)
c	wave phase speed	(59)
d	– distance to wave source	(49)
	– normal coordinate	(121)
$\mathfrak{F}(\cdot)$	bi-Maxwellian distribution function	(98)
$\mathfrak{f}(\cdot)$	one-dimensional Maxwell distribution function	(111)
G	gravitational constant	(5)
$J_n(\cdot)$	Bessel function	(101)
k_B	Boltzmann constant	(98)
L	mirror structure length	(100)
M	Mach number	(60)
$M_\odot$	mass of the Sun	(5)
m	mass	(98)
N	– number of wave sources	(26)
	– number of particles	(111)
N_T	number of time samples	(28)
$n^{(s)}$	number density	(98)
$P(\boldsymbol{q})$	array output power	(25)
p	pressure	(98)
$q^{(s)}$	electric charge	(105)
R	mirror structure radius	(103)
S	number of sensors	(25)
T	temperature	(98)
t	time	(26)
U	potential difference	(17)
W	kinetic energy	(98)
w, h	elementary waves	(25, 36)
$X_\mathrm{A}(\boldsymbol{q})$	array output	(26)
(ρ, θ, φ)	spherical coordinates	(28)
(ρ, φ, z)	cylindrical coordinates	(99)
(x, y, z)	chartesian coordinates	(107)
(h, d, γ, s)	normal coordinates	(121)
$\boldsymbol{B}$	magnetic field vector	(44)
$\boldsymbol{E}$	electric field vector	(8)
$\boldsymbol{j}$	electric current density	(105)
$\boldsymbol{k}$	wave vector	(27)
$\hat{\boldsymbol{n}}$	normal vector	(17)
$\boldsymbol{Q}$	wave field parameters	(26)
$\boldsymbol{q}$	elementary wave parameters	(25)
$\boldsymbol{r}$	position vector	(26)
$\boldsymbol{u}$	flow velocity	(57)
$\boldsymbol{v}$	– sensor velocity	(57)
	– particle velocity	(98)
$\boldsymbol{X}$	array measured values	(25)
$\mathcal{I}$	unit matrix	(45)
$\mathcal{M}$	measurements matrix	(37)
$\mathcal{P}$	pressure dyad	(100)
$\mathcal{R}$	rotation matrix	(124)
$\mathcal{W}$	elementary wave matrix	(43)

Acronyms

AIC	Alfvén – Ion-Cyclotron wave
ASPOC	Active Spacecraft Potential Control (Cluster)
AU	Astronomical Unit
CAA	Cluster Active Archive
CIS	Cluster Ion Spectrometry experiment (Cluster)
CODIF	Composition and Distribution Function analyzer (CIS component)
CSDS	Cluster Science Data Center
CME	Coronal Mass Ejection
DPS	Data Processing System (CIS component)

DWP	Digital Wave Processing experiment (Cluster)
EDI	Electron Drift Instrument (Cluster)
EFW	Electric Field and Wave experiment (Cluster)
FFT	Fast Fourier Transform
FGM	FluxGate Magnetometer (Cluster)
GSE	Geocentric Solar Ecliptic reference system
HEEA	High Energy Electron Analyzer (PEACE component)
HIA	Hot Ion Analyzer (CIS component)
HTF	de Hoffman – Teller Frame
IEL	Inter-Experiment Link (Cluster)
IES	Imaging Electron Spectrometer (RAPID component)
IGeP	Institut für Geophysik und extraterrestrische Physik
IIMS	Imaging Ion Mass Spectrometer (RAPID component)
IMF	Interplanetary Magnetic Field
LEEA	Low Energy Electron Analyzer (PEACE component)
MCP	Micro-Channel Plate
MHD	MagnetoHidroDynamic
MIAOW	MIrror And slOW waves
MM	Magnetic Mirror
OVT	Orbit Visualization Tool
PEACE	Plasma Electron And Current Experiment (Cluster)
RAPID	Research with Adaptive Particle Imaging Detectors (Cluster)
STAFF	Spatio-Temporal Analysis of Field Fluctuation experiment (Cluster)
UT	Universal Time
VIT	Virtual Interference Techniques
WBD	Wide Band Data experiment (Cluster)
WHISPER	Waves of HIgh frequency and Sounder for Probing of Electron density by Relaxation (Cluster)

A.2 Array output for vector signals

Suppose that the sensor at position $\boldsymbol{r}_s$ measures a vector field. We can even combine measurements from two or more sensors at same position, e.g. magnetic and electric field into one vector: $\boldsymbol{X}_s(\boldsymbol{Q},t) = \boldsymbol{X}(\boldsymbol{Q},\boldsymbol{r}_s,t) = \left(X_s^1,\ldots,X_s^L\right)^\mathsf{T}$.

We can express the measurements in terms of the pattern functions in the same way as we did in Section (3.2):

$$\boldsymbol{X}_s(\boldsymbol{Q},t) = \sum_{n=1}^{N} \boldsymbol{c}_n w(\boldsymbol{q}_n,\boldsymbol{r}_s,t)$$

where $\boldsymbol{c}_n$ is a constant vector with the same dimension as $\boldsymbol{X}_s$. The array output can be written as:

$$\boldsymbol{X}_A(\boldsymbol{q}) = \langle \mathcal{W}(\boldsymbol{q},\boldsymbol{r},t) | \boldsymbol{X}(\boldsymbol{Q},\boldsymbol{r},t) \rangle_{\boldsymbol{r},t} = \sum_{n=1}^{N} \boldsymbol{c}_n \delta(\boldsymbol{q}_n - \boldsymbol{q})$$

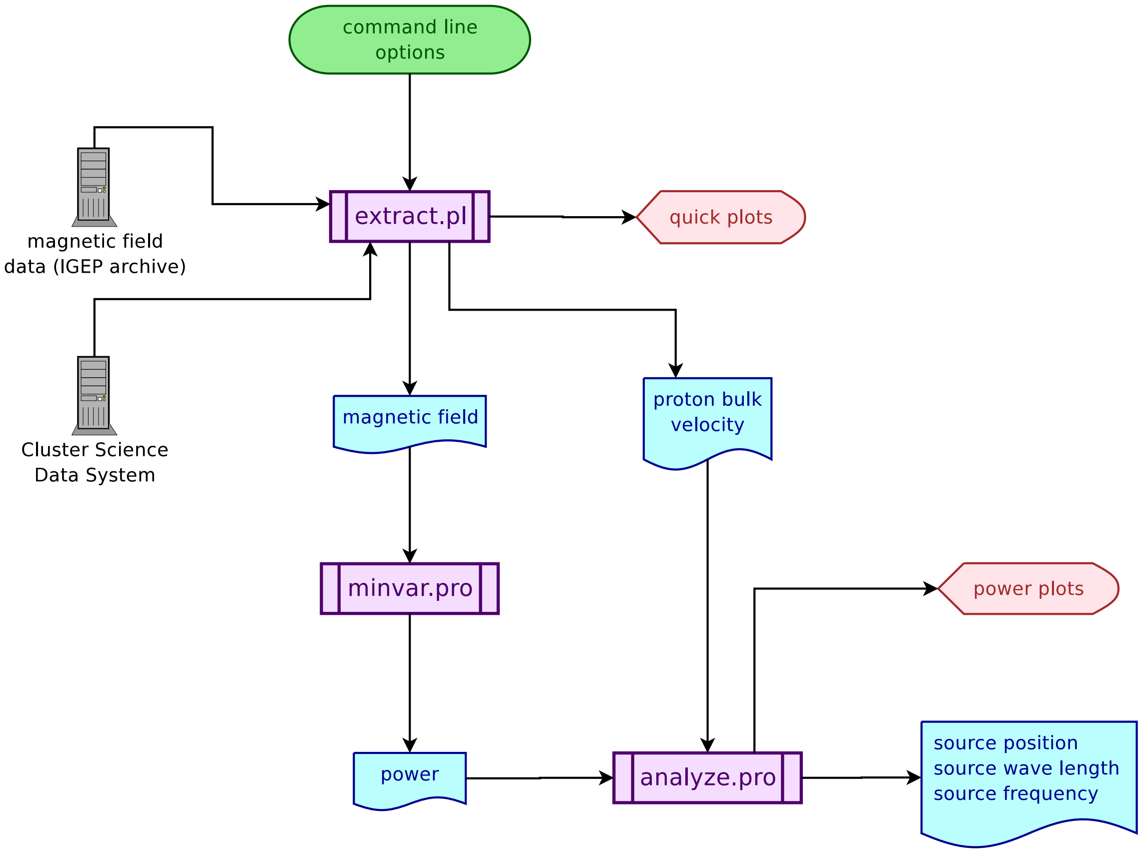
command line options
magnetic field data (IGEP archive)
extract.pl
quick plots
Cluster Science Data System
magnetic field
proton bulk velocity
minvar.pro
power plots
power
analyze.pro
source position
source wave length
source frequency

Figure A.1: Flowchart for the source locator. The Perl script extract.pl prepares the data for the main program, minvar.pro which produces the array power. Finally this is processed by analyze.pro in order to obtain the source parameters and to visualize the results.

where we have defined the $L \times L$ matrix $\mathcal{W}$ as the unity matrix multiplied by the pattern function: $|\mathcal{W}(\boldsymbol{q}, \boldsymbol{r}, t)\rangle = \mathcal{I}\,|w(\boldsymbol{q}, \boldsymbol{r}, t)\rangle$. The power is defined now as

$$P(\boldsymbol{q}) = \operatorname{trace}\big(\boldsymbol{X}_A(\boldsymbol{q})\boldsymbol{X}^{\dagger}_A(\boldsymbol{q})\big) = \sum_{n=1}^{N} \|\boldsymbol{c}_n\|^2 \delta(\boldsymbol{q}_n - \boldsymbol{q})$$

When we take into consideration the finite number of sensors, $\mathcal{W}$ becomes a $LS \times L$ matrix and $\boldsymbol{X}$ a LS dimension vector

$$\mathcal{W}(\boldsymbol{q}, t) = \big(\mathcal{W}_1(\boldsymbol{q}, t), \ldots, \mathcal{W}_S(\boldsymbol{q}, t)\big)^{\mathsf{T}}$$
$$\mathbf{X}(\boldsymbol{Q}, t) = \big(\mathbf{X}_1^{\mathsf{T}}(\boldsymbol{Q}, t), \ldots, \mathbf{X}_S^{\mathsf{T}}(\boldsymbol{Q}, t)\big)^{\mathsf{T}}$$

Using vector signals have the advantage of increasing the resolution for the same number of sensors by using more information about the detected wave field.

A.3 Source locator numerical implementation

To apply the source locator technique to Cluster magnetic field data we use a three step approach shown in figure (A.1). This modular structure allows us to take advantage of the strengths of different programming languages for different tasks. It also separates the lengthy process of computing the power from the mere analysis of the power and visualization of the results.

First, the desired time interval is supplied via command line to the *Perl* script `extract.pl` which fetches the magnetic field data from the IGeP data archive, checks it for gaps, prepares and saves it locally. The script then connects to the *Cluster Science Data System* (CSDS), acquires and saves the plasma flow velocity data locally. The “quick plots” – general views of the magnetospheric conditions and and of the orbit – provided as gif files by CSDS are displayed for the user.

The next step is the proper computing of the array power. This is done by the IDL code `minvar.pro`. The flowchart of this code is given in figure (A.2). First the magnetic field data previously prepared by `extract.pl` is presented to the user. Typically this comprises of one to two hours of 1 s resolution magnetic field data. A smaller window of user defined length (typically 512 or 1024 data points – 9 to 16 minutes) can be interactively slided through the data to select the desired subinterval. At all times the contents of the sliding window is enlarged for inspection. After the user selects the data subinterval a *Fast Fourier Transform* (FFT) is applied to the data and the next interactive stage is reached. The Fourier spectrum is shown to the user and the first local maximum is marked. The user can browse through local peaks automatically identified by the code or can input an arbitrary choice. Once the choice is made, the code moves to its main task, computing the array power.

As discussed in section (3.4.1) the array output matrix $\mathcal{M}$ is singular. To regularise it we perform an average both in time and in frequency. The average in time is done by the loop at line 158 and consists in computing the average over 16 half-length equally distributed intervals. The inside loop at line 160 performs the average over neighbored frequencies.

With the $\mathcal{M}$ matrix computed, between lines 172 and 195 the code computes the power at each point of the grid defined at lines 80 – 87 and saves it to a file.

The last step is the processing of the array power by `analyze.pro`. This identifies the maximum of the four dimensional power and saves the corresponding source parameters to a file. It also produces the plots representing slices through the array power shown in the previous chapters.

A.3.1 Code listings

minvar.pro:

```
1 forward_function max_pow_four, weight, select_index, myfft
  compile_opt idl2
3
  pro minvar ;        >>>> MAIN CODE <<<<<
5
  npct=30        ; number of points in one dim of the scan domain
7 bkt=2          ; frequency braketing
  fn='Sensor_'   ; file name
9 s=4            ; number of sensors
  ndata=512      ; number of data points
```

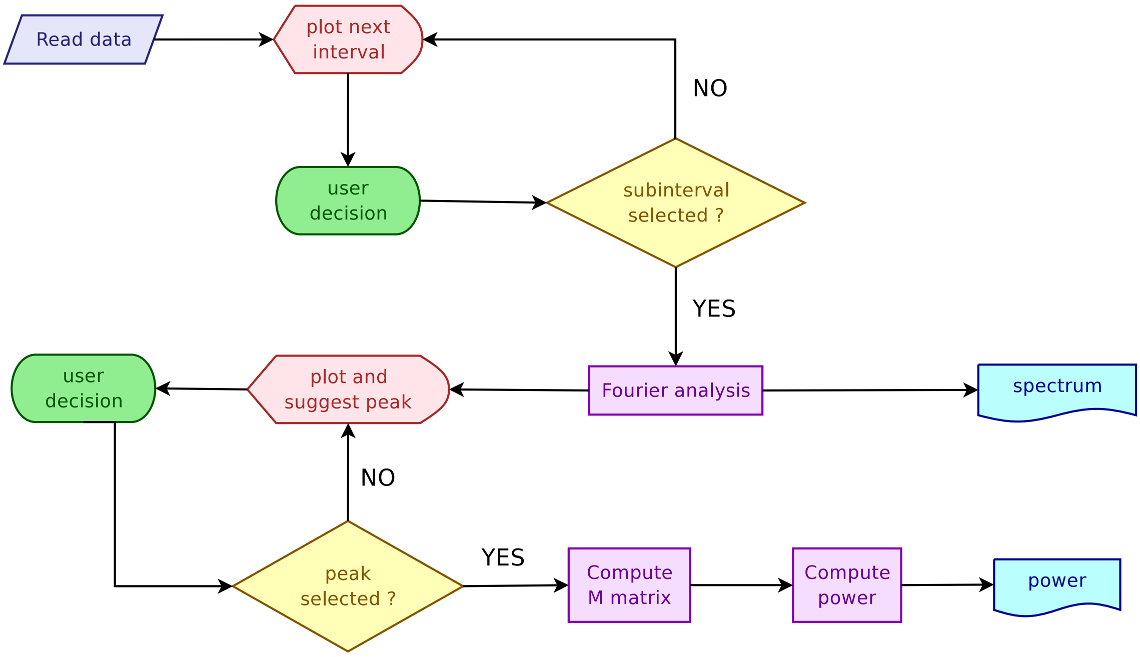
Read data
plot next interval
user decision
subinterval selected ?
NO
YES
Fourier analysis
spectrum
plot and suggest peak
user decision
NO
peak selected ?
YES
Compute M matrix
Compute power
power

Figure A.2: Flowchart of the main IDL code used for the source locator. The user first selects the data subinterval to be processed, then the frequency of interest. The output is the array power over the given grid.

```
constrain=1    ; impose divergence-free condition
start=0        ; shift of first subinterval

; determine the number and the dimension of data points
spawn,'wc␣'+fn+'0.dat',wc_out
wc_arr=strsplit(wc_out,/extract)
nlines=long(wc_arr[0])  ; number of lines to be read from each data file
nwords=long(wc_arr[1]) & dim=nwords/nlines-4 ; 1 for module data, 3 for vector

loadct,39,/silent

; read data
bmodule_=dblarr(s,nlines)
t_=dblarr(s,nlines) & b_=dblarr(s*dim,nlines) & r_=dblarr(3,s,nlines)
tbr=dblarr(4+dim,nlines)
for n=0,s-1 do begin
  filename=fn+strcompress(string(n),/remove_all)+'.dat'
  openr,1,filename
    readf,1,tbr
  close,1
  t_[n,*]=tbr[0,*]
  b_[n*dim:n*dim+dim-1,*]=tbr[1:dim,*]
  r_[*,n,*]=tbr[dim+1:dim+3,*]
  bmodule_[n,*]=sqrt(total(tbr[1:dim,*]^2,1))
endfor

t=dblarr(s,ndata) & b=dblarr(s*dim,ndata) & r=dblarr(3,s)
```

```
bmodule=dblarr(s,ndata)
b1_max=max(bmodule_[0,*])

; interactive set of the data subinterval
answer=''
!p.multi=[0,1,s+1]
while (answer ne 'y') do begin
  if (stregex(answer,'[0-9]',/boolean)) then start=long(answer)
  t=t_[*,start:start+ndata-1]/1000 & b=b_[*,start:start+ndata-1]
  r=total(r_[*,*,start:start+ndata-1],3)/ndata
  bmodule=dblarr(s,ndata)
  sensor=0
  for n=0,s*dim-1 do begin
    xxx=dblarr(ndata) & yyy=dblarr(ndata)
    xxx[*]=t[sensor,*] & yyy[*]=b[n,*]
    tmp=svdfit(xxx,yyy,3,yfit=fit,status=svdstatus)
    b[n,*]-=fit
    bmodule[sensor,*]+=b[n,*]^2
    if (~((n+1) mod dim)) then begin ; trigers on the last component
      bmodule[sensor,*]+=b[n,*]^2
      bmodule=sqrt(bmodule)
      plot,bmodule[sensor,*],xstyle=1,ystyle=1
      sensor++
    endif
  endfor
  plot,bmodule_[0,*],xstyle=1,ystyle=1
  oplot,[start,start],[0,b1_max], thick=2, color=150
  oplot,[start+ndata-1,start+ndata-1],[0,b1_max], thick=2, color=150
  tstr=timp2(t_[0,start])
  read,answer, $
  prompt=strcompress(tstr.s+string(start, " [ ", nlines-ndata," ] : "))
  tstart=t_[0,start] & tstop=t_[0,start+ndata-1]
  start+=100
  if (answer eq "q") then stop
  if (start+ndata ge nlines) then start=0
endwhile

dmax=max(reldist(r))
d=min(reldist(r)+unit(s)*dmax)    ; minimum distance between sensors

knyq=!dpi/dmax

kmin=knyq/1.d5   &  kmax=knyq                          ;
rmin=0.1d0*d     &  rmax=30.d0*d                       ;
lnmin=-180.d0    &  lnmax=180.d0                       ;
ltmin=-90.d0     &  ltmax=90.d0                        ; scan
distance=dindgen(npct)/(npct-1)*(rmax-rmin)+rmin       ; domain
longitude=dindgen(npct)/(npct-1)*(lnmax-lnmin)+lnmin   ;
latitude=dindgen(npct)/(npct-1)*(ltmax-ltmin)+ltmin    ;
k=dindgen(npct)/(npct-1)*(kmax-kmin)+kmin              ;

dt=total(t[*,ndata-1]-t[*,0])/s/(ndata-1)        ; average time step
omegavec=dindgen(ndata/2+1)/(ndata*dt)*2*!dpi

; Fourier spectrum
```

```
ft=myfft(b,navg=8, /time)
ftmax=max(2*abs(ft))

openw,2,'four.dat'
  tmp=dindgen(s*dim+1,ndata/2+1)
  tmp[0,*]=omegavec
  tmp[1:s*dim,*]=abs(ft[*,0:ndata/2])
  fmt=strcompress('('+string(s*dim+1)+'d)')
  printf,2,format=fmt,tmp
close,2


; interactive set of the frequency
omega=0
skip=bkt
answer=''
fscale='lin'
wnd=20
omax=!dpi/dt-2*!dpi*(wnd+bkt)/ndata/dt
xrng=[omegavec[2],omegavec[n_elements(omegavec)-1]]
while (answer ne 'y') do begin
  omega=0
  bf=max_pow_four(b,dt,omega,bkt,skip,wnd)   ; find peak frequecy
  if (stregex(answer,'^[0-9]',/boolean)) then begin
    omega=double(answer)*2*!pi/1000 < omax
    skip=round(omega*ndata*dt/2/!dpi)
  endif
  omidx=round(omega*ndata*dt/2/!dpi)
  sensor=-1
  for n=0,s*dim-1 do begin
    if (~(n mod dim)) then begin ; trigers on the first component
      if (fscale eq "lin") then $
        plot,omegavec, 2*abs(ft[n,0:ndata/2]),xstyle=1,ystyle=1, $
        xrange=xrng/(2*!pi)*1000,yrange=[ftmax/1000,ftmax] $
      else $
        plot,omegavec, 2*abs(ft[n,0:ndata/2]),xstyle=1,ystyle=1, $
        xrange=xrng/(2*!pi)*1000, yrange=[ftmax/1000,ftmax],/ylog,/xlog
      sensor++
    endif
    oplot,omegavec/(2*!pi)*1000, 2*abs(ft[n,0:ndata/2])
    oplot,[omegavec[omidx-bkt], omegavec[omidx-bkt]]/(2*!pi)*1000, $
          [ftmax/1000,2*ftmax], color=150, thick=2
    oplot,[omegavec[omidx+bkt], omegavec[omidx+bkt]]/(2*!pi)*1000, $
          [ftmax/1000,2*ftmax], color=150, thick=2
  endfor
  plot,sin(t[0,*]*omega),xstyle=1, ystyle=1, yrange=[-1.5,1.5]
  read,answer,prompt= $
  strcompress(string(fix(omega/(2*!pi)*1000),"␣[␣", $
              fix(omax/(2*!pi)*1000),"␣]␣(mHz)␣:␣"))
  if (answer eq "q") then stop
  if (stregex(answer,'z[0-9]',/boolean)) then begin ; zoom
    skip-=10
    xrng[1]=omegavec[n_elements(omegavec) -1]/fix(strmid(answer,1))
  endif
  if (stregex(answer,'(lin)|(log)',/boolean)) then begin
```

```
    skip-=10
    fscale=answer
  endif
  skip+=10
  if (skip ge ndata/2-wnd-bkt) then skip=bkt
endwhile

; scan the data interval (using subwindow twice smaller)
; in 16 overlaping steps and find M matrix
Mb=dcomplexarr(s*dim,s*dim)
for p=0,ndata/2,ndata/32 do begin
  B_fourier=max_pow_four(b[*,p:p+ndata/2-1], dt,omega,bkt,skip,wnd)
  for q=0,2*bkt do begin    ; frequency loop
     Mb+=B_fourier[*,q]##conj(B_fourier[*,q])/16/(2*bkt+1)
  endfor
endfor
M_inv=la_invert(Mb)

rt=sens_syst(r)  ; translation vector and rotation matrix
r_new=r-rt.t     ; translate to center of mass

; compute the Capon power for all scan domain
print, ""
pc=dblarr(npct,npct,npct,npct)
for m=0,npct-1 do begin
  rh=distance[m]
  for n=0,npct-1 do begin
    lng=longitude[n]
    pbar, m,npct,n
    for p=0,npct-1 do begin
      ltd=latitude[p]
      for q=0,npct-1 do begin
        w=weight(rho(r_new,[lng,ltd,rh]),k[q],s,dim)
        tmp=(transpose(conj(w))##transpose(M_inv)##w)
        if constrain then begin
          nk=cv_coord(from_sphere=[lng,ltd,1.d0], /to_rect, /degrees)
          V=unit(3)+nk#nk
          tmp=transpose(V)#tmp#V
        endif
        if n_elements(tmp) gt 1 then begin
          pc[m,n,p,q]=abs(trace(la_invert(tmp)))
        endif else begin
          pc[m,n,p,q]=abs(1/tmp)
        endelse
      endfor
    endfor
  endfor
endfor

print, "" & print, ""

openw, 1, 'power.dat'
writeu,1,npct,pc,distance,longitude,latitude,
   r_new,k,omega,rt,tstart,tstop
close,1
```

```
spawn, "beep␣-r␣3␣-f␣5000␣-l␣10"

end           ; >>>>>> END OF MAIN CODE  <<<<<<

;------------------------------------------------------------------

; return Fourier coefficients range of local dominant frq or of given frq
function max_pow_four, field, dt, omega, bkt,skip,wnd
  b=field
  s=n_elements(b[*,0]) & i=n_elements(b[0,*])
  df=1/dt/i   ; frequency step
  ft=myfft(b,navg=8, /time)
  ; corresponding frequencies for even i:
  ; [0,1,2,...,(i/2-1),  i/2,  -(i/2-1),...,-2,-1]/(i*dt)
  ; i/2+1 positive and i/2-1 negative
  if omega eq 0 then begin       ; find dominant frequency
    pow=2*abs(ft[*,0:i/2])       ; keep only positive frequencies
    index=0
    index=select_index(pow,bkt,skip,wnd)
    omega=index*df*2*!dpi
  endif else begin
    index=round(omega/df/2/!dpi)   ; corresponding index to given frequency
  endelse
  fmax=ft[*,index-bkt:index+bkt]
  return,fmax
end

;------------------------------------------------------------------

; local maximum
function select_index, pow,bkt,skip,wnd
  pp=pow
  pp[*,0:skip]=0 & pp[*,skip+wnd:*]=0
  ppp=total(pp,1)
  pmax=max(ppp,index)
  index=index < (n_elements(pow[0,*])-bkt)
  return, index
end

;------------------------------------------------------------------

; weights for computing the power
function weight, rh, k, s, dim
  c=1/norm(1/rh)
  i=dcomplex(0,1)
  w=c*exp(i*k*rh)/rh
  wm=dcomplexarr(dim,s*dim)
  for j=0,s-1 do begin
    wm[*,j*dim:j*dim+dim-1]=unit(dim)*w[j]
  endfor
  return,wm
end
```

```

;------------------------------------------------------------------------

; Fourier transformation
function myfft, dat, navg=n, time=time, frequency=frq, fwindow=fwnd
  b=dat
  if n_elements(b[0,*]) eq 1 then b=transpose(b)
  s=n_elements(b[*,0]) & i=n_elements(b[0,*])
  ft=dcomplexarr(s,i)

  if keyword_set(time) then begin ; time averaging
    ;n=16 ; nr of intervals for averaging (4, 8, 16, ... < i/2)
    for p=0,i/2,i/(2*n) do begin
      bb=dblarr(s,i)
      for q=0,s-1 do begin                                   ;
        tmp=linfit(dindgen(i/2),b[q,p:p+i/2-1],yfit=fit)     ; detrend
        bb[q,p:p+i/2-1]=b[q,p:p+i/2-1]-fit                   ;
      endfor                                                 ;
      wnd=dblarr(s,i)
      wnd[*,p:p+i/2-1] = (dblarr(s)+1)#HANNING(i/2,/DOUBLE)
      ft+=fft(wnd*bb,dimension=2)/n
    endfor
    ft[*,0:1]=1.d-64   ;we have no info about these freq (zero-padding)
  endif else begin
    if keyword_set(frq) then begin ; frequency averaging
      ; n=1 ; number of points on each side for averaging
      if keyword_set(fwnd) then begin ; tapering
        case strcompress(fwnd,/remove_all) of
          'wide':     begin
                        ramp=(1-cos(dindgen(i/4)/(i/4-1)*!dpi))/2
                        wnd=dblarr(i)+1
                        wnd[0:i/4-1]=ramp & wnd[3*i/4:i-1]=1-ramp
                        wnd=(dblarr(s)+1)#wnd*4/3
                      end
          'hanning':  wnd = (dblarr(s)+1)#HANNING(i,/DOUBLE)
        endcase
      endif else begin
        wnd=1
      endelse
      ft=fft(wnd*b,dimension=2)
      tmp=dblarr(s,i+2*n)                                  ;
      for p=-n,n do tmp[*,n+p:n+p+i-1]+=abs(ft)/(2*n+1)    ; smoothing average
      ft=tmp[*,n:n+i-1]*(ft/(abs(ft)))                     ;
    endif
  endelse

  return,ft
end
```

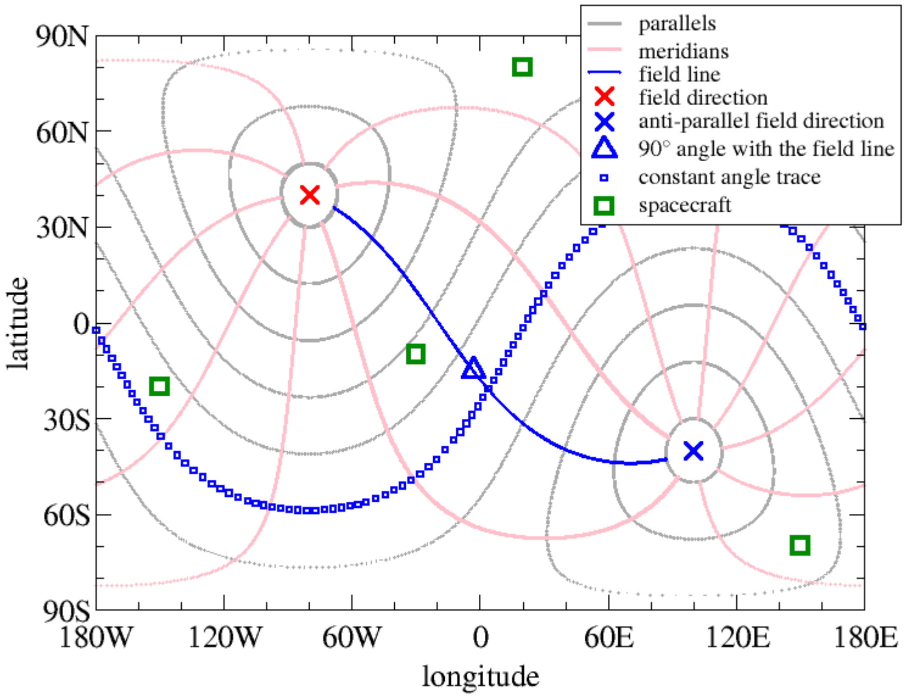

Figure A.3: Sketch of a typical longitude – latitude representation of the array power. For Cluster data the direction to the Sun is in the center of the map. A set of parallel and meridian lines associated with the magnetic field direction is shown for reference. The magnetic field line going through the wave source follows a meridian line. The directions making the same angle with the magnetic field as the detected wave gather along a parallel line.

A.4 Equirectangular projection

The array power computed by the wave telescope or by the source locator is visualized throughout this work as bi-dimensional slices. Many times the shape of the power maximum in the longitude – latitude slice reflects important properties of the wave field. This slice is a *equirectangular projection* (i.e. the spherical angular coordinates are linearly mapped to the carthesian bi-dimensional representation) and is important to recall some of its properties.

We should be aware that this projection does not preserve neither shape nor length, the distortion being stronger close to the poles (latitude $= \pm 90°$). In particular this means that the representation of a straight line is generally not a straight line.

A given direction is represented on the map by a point of coordinates (φ_0, θ_0). For instance the red cross in figure (A.3). The opposite direction is given by $(\varphi_0 + \pi, -\theta_0)$ – the blue cross in figure (A.3). Any line parallel with this direction is represented by a *meridian line* (pink in figure (A.3)) on the longitude – latitude map. The directions in space having a specified angle with our given direction are represented on the map by the *parallel lines*, drawn in gray in figure (A.3).

The figure (A.3) shows most of the elements which are present on the foreground of a longitude – latitude map of the array power. The magnetic field line (and sometimes the flow line) going through the identified power maximum follows a meridian line on the map. The direction of the magnetic field is represented by the red cross, and the point where the field or flow line is closest to the origin is marked by the triangle.

The position of the wave source on the magnetic field line projection gives the propagation angle α relative to the magnetic field. If the source is close to the triangle then the propagation is nearly orthogonal, if it is close to one of the crosses then the wave propagation is nearly parallel or anti-parallel. All directions making the same angle α with the magnetic field line are represented by the string of squares.

Acknowledgements

This thesis would not have been possible without the careful guidance of my supervisor, Karl-Heinz Glaßmeier. I am grateful to him not only for his role in my formation as a scientist, but also for his help and understanding in personal matters. Dinners at his home together with his family made me feel welcomed from the beginning of my stay in Germany.

I never ceased to be amazed by the profound knowledge of Rudolf Treumann. Enlightening discussions with him helped me to find the answer to many difficult questions. He encouraged and supported me in difficult moments.

I wish to thank Uwe Motschmann for his interest in my work and for his constructive suggestions.

I express here my gratitude to Dieter Schmitt for his unselfish efforts to coordinate the International Max Planck Research School in Lindau. His devotion helped me and countless fellow PhD students to expand our horizons and to find our way in science. The retreats and seminars organized by him provided invaluable opportunities not only to get acquainted with different fields of space science but also to relax and spend wonderful time together with the colleagues and friends in the School.

A large part of my thesis relies on magnetic field data calibrated and kindly provided by Karl-Heinz Fornaçon.

I am grateful to Edita Georgescu for her disinterested help. She trusted me and introduced me to the space science community.

I wish to express my special thanks to Gerhard Haerendel, who guided my first steps in magnetospheric physics and provided financial support for several fruitful stages at MPE Garching. These visits resulted into the magnetic mirror model, which is part of this work.

I owe a lot to my colleagues at the Institute for Space Science in Bucharest. To Horia Comişel for his sincere and open nature which always have been a comfort for me. To Octav Marghitu for his time and energy devoted to the interests of the research group at ISS. To Marius Echim for deep philosophical discussions over a glass of wine. To Adrian Blăgău, alias Nae, for teaching me what determination means. All of them offered me support and friendship.

My colleagues at TU-Braunschweig always assisted me both scientifically and on a personal level. My thanks extend to all of them: Andrea, Anja, Gero, Ingo, Ingo, Jan, Jean-Mathias, Jenz, Kai, Karl-Heinz, Lars, Michael, Reiner, Sebastian, Tilman, Torsten, Uli, and Yasuhito.

The relaxing time spent with my friends Yasuhito and Maki as guest in their home, enjoying piano music and delicious food, was definitely a major aid in the development of this work.

I would never have been able to manage the paperwork and the bureaucracy without the help of Sabine Filbrandt.

I wish to thank my Rumanian friends in Braunschweig, Irina, Vali, Delia, and Alex for making me feel at home, and for never complain about the many times I have woke them up early Sunday mornings.

Even if they are away in Romania I always felt close to my friends Filip, Sorin, Matei, Cătălina, Ovidiu, and Carmen Ţ. Their unconditioned trust helped to complete this work.

My father, my brother Vlad, and Viorica offered me more credit than I deserved. Their confidence was a great comfort for me during these years.

I am grateful to my mother who made me realize the mysteries of this world and inspired me with curiosity and with the wish to understand them. Her love gave me strength to follow the path I have chosen.

Most importantly, I am grateful for the love, patience and understanding of my fiancée, Carmen.

Bibliography

Abramowitz, M., and I. A. Stegun, Error function and fresnel integrals, in *Handbook of Mathematical Functions with Formulas, Graphs, and Mathematical Tables*, 9th ed., pp. 297–309, New York: Dover, 1972.

Acuña, M. H., Space-based magnetometers, *Review of Scientific Instruments*, *73*, 3717–3736, 2002.

Aschenbrenner, H., and G. Goubau, Eine Anordnung zur Registrierung rascher magnetischer Stoerungen, *Hochfreq Tech. Elektroakust.*, *47*, 178, 1936.

Balikhin, M. A., T. D. de Wit, H. S. C. K. Alleyne, L. J. C. Woolliscroft, S. N. Walker, V. Krasnoselśkikh, W. A. C. Mier-Jedrzejeowicz, and W. Baumjohann, Experimental determination of the dispersion of waves observed upstream of a quasi-perpendicular shock, *Geophys. Res. Lett.*, *24*, 787–790, 1997.

Balogh, A., et al., The Cluster Magnetic Field Investigation, *Space Science Reviews*, *79*, 65–91, 1997.

Barton, C. E., Geomagnetic secular variation, in *The Encyclopedia of Solid Earth Geophysics*, edited by D. E. James, pp. 560–577, Van Nostrand Reinhold, New York, 1989.

Baumjohann, W., and R. A. Treumann, *Basic space plasma physics*, London: Imperial College Press, —c1996, 1996.

Baumjohann, W., R. A. Treumann, E. Georgescu, G. Haerendel, K.-H. Fornaçon, and U. Auster, Waveform and packet structure of lion roars, *Annales Geophysicae*, *17*, 1528–1534, 1999.

Biermann, L., Kometenschweife und solare Korpuskularstrahlung, *Zeitschrift für Astrophysik*, *29*, 274–+, 1951.

Booth, N. O., and G. L. Mohnkern, Signal-to-noise gain from adaptive matched-field beamforming of multidimensional acoustic arrays, *Tech. Rep. 1661*, Space and Naval Warfare Systems Center, San Diego, CA 92152-5001, 1994.

Braginsky, S. I., Kinematic Models of the Earth's Hydromagnetic Dynamo, *Geomagnetizm i Aeronomiia*, *4*, 572–583, 1964.

Brown, W. L., W. N. Hess, and J. A. Van Allen, Introduction to "Collected papers on the artificial radiation belt from the July 9, 1962, nuclear detonation", *J. Geophys. Res.*, *68*, 605–606, 1963.

Buechner, J., and L. M. Zelenyi, Regular and chaotic charged particle motion in magnetotaillike field reversals. I - Basic theory of trapped motion, *J. Geophys. Res.*, *94*, 11,821–11,842, 1989.

Capon, J., High Resolution Frequency-Wavenumber Spectrum Analysis, in *Proc. IEEE, Volume 57*, pp. 1408–1418, 1969.

Capon, J., R. J. Greenfield, and R. J. Kloker, Multidimensional maximum-likehood processing of a large aperture seismic array, in *Proc. IEEE, Volume 55*, pp. 192–213, 1967.

Carlson, C. W., D. W. Curtis, G. Paschmann, and W. Michel, An instrument for rapidly measuring plasma distribution functions with high resolution, *Advances in Space Research*, *2*, 67–70, 1982.

Chapman, S., and V. Ferraro, A new theory of magnetic storms, I, the initial phase, *Terrest. Magnetism and Atmospheric Elec.*, *36*, 171–186, 1931.

Chapman, S., and V. Ferraro, A new theory of magnetic storms, I, the initial phase (continued), *Terrest. Magnetism and Atmospheric Elec.*, *37*, 147–156, 1932.

Chapman, S., and V. Ferraro, A new theory of magnetic storms, II, the main phase, *Terrest. Magnetism and Atmospheric Elec.*, *38*, 79–96, 1933.

Chisham, G., D. Burgess, and M. W. Schwartz, S. J. andDunlop, Observations of electron distributions in magnetosheath mirror mode waves, *J. Geophys. Res.*, *103*, 26,765–26,774, 1998.

Constantinescu, O. D., Floquet Theory for Quantum Systems with a Finite Number of Freedom Degrees in Interaction with Laser Fields, Bachelor's thesis, Bucharest University, Faculty of Physics, 1996.

Constantinescu, O. D., Study of a 1-D Electron Interacting with a Short-Range Potential and a Bichromatic Laser Field with Commensurate Frequencies, Master's thesis, Bucharest University, Faculty of Physics, 1997.

Constantinescu, O. D., Self-consistent model for mirror structures, *J. Atmos. Sol. Terr. Phys*, *64*, 645–649, 2002.

Constantinescu, O. D., Location of Wave Sources Using Cluster as a Sensor Array, 2006, invited Talk, *EGU General Assembly*, Vienna, Austria.

Constantinescu, O. D., K.-H. Glassmeier, R. Treumann, and K.-H. Fornaçon, Magnetic mirror structures observed by Cluster in the magnetosheath, *Geophys. Res. Lett.*, *30*, 4–1, 2003.

Constantinescu, O. D., K.-H. Glassmeier, P. M. E. Décréau, M. Fränz, and K.-H. Fornaçon, Low frequency wave sources in the outer magnetosphere, magnetosheath, and near Earth solar wind, 2006a, Submitted to Annales Geophysicae.

Constantinescu, O. D., K.-H. Glassmeier, U. Motschmann, R. A. Treumann, and M. Fränz, Plasma Wave Source Location Using CLUSTER as a Spherical Wave Telescope, *J. Geophys. Res.*, *111*, 2006b.

Constantinescu, O. D., K.-H. Glassmeier, S. Schaefer, M. Fränz, and P. M. E. Décréau, Location of low frequency waves sources in the outer magnetosphere, magnetosheath, and near Earth solar wind, 2006, invited Talk, University of Alberta, Edmonton, Canada.

Constantinescu, O. D., K.-H. Glassmeier, R. Treumann, U. Motschmann, and K.-H. Fornaçon, Wave sources locations in the bowshock and adjacent regions, in *Proceedings of the Cluster and Double Star symposium 5th Anniversary of Cluster in Space*, ESA, 2006.

Cornilleau-Wehrlin, N., et al., The Cluster Spatio-Temporal Analysis of Field Fluctuations (STAFF) Experiment, *Space Science Reviews*, *79*, 107–136, 1997.

Crooker, N. U., and G. L. Siscoe, A mechanism for pressure anisotropy and mirror instability in the dayside magnetosheath, *J. Geophys. Res.*, *82*, 185–+, 1977.

Décréau, P. M. E., et al., Whisper, a Resonance Sounder and Wave Analyser: Performances and Perspectives for the Cluster Mission, *Space Science Reviews*, *79*, 157–193, 1997.

DeSerio, R., Spherical sector electrostatic analyzers for measurements of energy and angular distributions, *Review of Scientific Instruments*, *60*, 381–388, 1989.

Dungey, J. W., The Length of the Magnetospheric Tail, *J. Geophys. Res.*, *70*, 1753–+, 1965.

Escoubet, C. P., R. Schmidt, and M. L. Goldstein, Cluster: Science and Mission Overview, *Space Sci. Rev.*, *79*, 11–32, 1997.

Fränz, M., T. S. Horbury, V. Génot, O. Moullard, H. Rème, I. Dandouras, A. N. Fazakerley, A. Korth, and F. Frutis-Alfaro, Solitary waves observed by cluster in the solar wind, in *Solar Wind Ten: Proceedings of the Tenth International Solar Wind Conference*, edited by M. Velli, R. Bruno, and F. Malara, pp. 562–565, American Institute of Physics, 2003.

Gilbert, W., *De magnete, magneticisque corporibus, et de magno magnete tellure; Physiologia noua, plurimis & argumentis, & experimentis demonstrata*, Londini, Excudebat Petrus Short, 1600.

Glassmeier, K.-H., and U. Motschmann, Comments on Time-Series Analysis, in *ESA SP-371: Proceedings of the Cluster Workshops, Data Analysis Tools and Physical Measurements and Mission-Oriented Theory*, edited by K.-H. Glassmeier, U. Motschmann, and R. Schmidt, pp. 7–14, 1995.

Glassmeier, K.-H., U. Motschmann, C. Mazelle, F. M. Neubauer, K. Sauer, S. A. Fuselier, and M. H. Acuña, Mirror modes and fast magnetoacoustic waves near the magnetic pileup boundary of comet Halley, *J. Geophys. Res.*, *98*, 20,955–+, 1993.

Glassmeier, K.-H., et al., Cluster as a wave telescope - first results from the fluxgate magnetometer, *Annales Geophysicae*, *19*, 1439–1447, 2001, correction, Annales Geophysicae, 21, 1071, 2003.

Gurnett, D. A., R. L. Huff, and D. L. Kirchner, The Wide-Band Plasma Wave Investigation, *Space Science Reviews*, *79*, 195–208, 1997.

Hasegawa, A., Drift mirror instability in the magnetosphere, *Phys. Fluids*, *12*, 2642, 1969.

Hess, W. N., *The radiation belt and magnetosphere*, Waltham, Mass.: Blaisdell, 1968, 1968.

Hubert, D., C. Lacombe, C. C. Harvey, M. Moncuquet, C. T. Russell, and M. F. Thomsen, Nature, properties, and origin of low-frequency waves from an oblique shock to the inner magnetosheath, *J. Geophys. Res.*, *103*, 26,783–26,798, 1998.

Huddleston, D. E., R. J. Strangeway, X. Blanco-Cano, C. T. Russell, M. G. Kivelson, and K. K. Khurana, Mirror-mode structures at the Galileo-Io flyby: Instability criterion and dispersion analysis, *J. Geophys. Res.*, *104*, 17,479–17,490, 1999.

Johnstone, A. D., et al., Peace: a Plasma Electron and Current Experiment, *Space Science Reviews*, *79*, 351–398, 1997.

Kasaba, Y., H. Matsumoto, Y. Omura, R. R. Anderson, T. Mukai, Y. Saito, T. Yamamoto, and S. Kokubun, Statistical studies of plasma waves and backstreaming electrons in the terrestrial electron foreshock observed by Geotail, *J. Geophys. Res.*, *105*, 79–104, 2000.

Kivelson, M. G., and C. T. Russell (Eds.), *Introduction to Space Physics*, Cambridge University Press, 40 West 20^{th} Street, New York, 1995.

Kivelson, M. G., and D. J. Southwood, Mirror instability. II - The mechanism of nonlinear saturation, *J. Geophys. Res.*, *101*, 17,365–17,371, 1996.

Lee, L. C., C. S. Wu, and C. P. Price, On the generation of magnetosheath lion roars, *J. Geophys. Res.*, *92*, 2343–2348, 1987.

Lions, J. L., ARIANE 5 Flight 501 Failure Report by the Inquiry Board, *Tech. rep.*, ESA, 1996.

Lucek, E. A., M. W. Dunlop, A. Balogh, P. Cargill, W. Baumjohann, E. Georgescu, G. Haerendel, and F. K. H., Identification of magnetosheath mirror modes in equator-s magnetic field data, *Ann. Geophysicae*, *17*, 1560–1573, 1999.

Lucek, E. A., D. Constantinescu, M. L. Goldstein, J. Pickett, J. L. Pinçon, F. Sahraoui, R. A. Treumann, and S. N. Walker, The Magnetosheath, in *Outer Magnetospheric Boundaries: Cluster Results*, edited by G. Paschmann, S. J. Schwartz, C. P. Escoubet, and S. Haaland, Space Sciences Series of ISSI, pp. 95–152, Springer, 2005a.

Lucek, E. A., D. Constantinescu, M. L. Goldstein, J. Pickett, J. L. Pinçon, F. Sahraoui, R. A. Treumann, and S. N. Walker, The Magnetosheath, *Space Science Reviews*, *118*, 95–152, 2005b.

Lucek, E. A., et al., Cluster magnetic field observations in the magnetosheath: four-point measurements of mirror structures, *Annales Geophysicae*, *19*, 1421–1428, 2001.

Lühr, H., MAGNETSRODE: Eine Einrichtung für magnetische Kalibrierungen und Testmessungen, *Tech. Rep. GAMMA 42*, Technical University of Braunschweig, 1984.

Möbius, E., et al., The time-of-flight spectrometer SULEICA for ions of the energy range 5-270 keV/charge on AMPTE IRM, *IEEE Transactions on Geoscience and Remote Sensing*, *23*, 274–279, 1985.

Motschmann, U., T. I. Woodward, K.-H. Glassmeier, and M. W. Dunlop, Array Signal Processing Techniques, in *Proc. CLUSTER Workshop on Data Analysis Tools*, edited by K.-H. Glassmeier, U. Motschmann, and R. Schmidt, pp. 79–86, ESA, 1995.

Motschmann, U., K. H. Glassmeier, and J. Pinçon, Multi-Spacecraft Filtering: Plasma Mode Recognition, in *Analysis methods for multi-spacecraft data*, edited by G. Paschmann and P. Daly, ISSI Sci. Rep. SR-001, pp. 79–87, ISSI, Bern, 1998.

Narita, Y., and K.-H. Glassmeier, Dispersion analysis of low-frequency waves through the terrestrial bow shock, *Journal of Geophysical Research (Space Physics)*, *110*, 12,215–+, 2005.

Narita, Y., K.-H. Glassmeier, S. Schäfer, U. Motschmann, K. Sauer, I. Dandouras, K.-H. Fornaçon, E. Georgescu, and H. Rème, Dispersion analysis of ULF waves in the foreshock using cluster data and the wave telescope technique, *Geophys. Res. Lett.*, *30*, 43–1, 2003.

Nettleton, H. R., and F. H. Llewellyn, A sensitive rotating-coil magnetometer, *Proceedings of the Physical Society*, *42*, 501–520, 1930.

Neubauer, F. M., and K. H. Glassmeier, Use of an array of satellite as a wave telescope, *J. Geophys. Res.*, *95*, 19,115–19,122, 1990.

Parker, E. N., Dynamics of the Interplanetary Gas and Magnetic Fields., *Astrophysical Journal*, *128*, 664–+, 1958.

Parker, E. N., Dynamical Theory of the Solar Wind, *Space Science Reviews*, *4*, 666–+, 1965.

Paschmann, G., et al., The Electron Drift Instrument for Cluster, *Space Science Reviews*, *79*, 233–269, 1997.

Pedersen, A., et al., The Wave Experiment Consortium (wec), *Space Science Reviews*, *79*, 93–106, 1997.

Pinçon, J. L., and F. Lefeuvre, The application of the generalized Capon method to the analysis of a turbulent field in space plasma - Experimental constraints, *Journal of Atmospheric and Terrestrial Physics*, *54*, 1237–1247, 1992.

Pinçon, J., and U. Motschmann, Multi-Spacecraft Filtering: General Framework, in *Analysis methods for multi-spacecraft data*, edited by G. Paschmann and P. Daly, ISSI Sci. Rep. SR-001, pp. 65–78, ISSI, Bern, 1998.

Pokhotelov, O. A., M. A. Balikhin, R. A. Treumann, and V. P. Pavlenko, Drift mirror instability revisited: 1. Cold electron temperature limit, *J. Geophys. Res.*, *106*, 8455–8464, 2001a.

Pokhotelov, O. A., O. G. Onishchenko, M. A. Balikhin, R. A. Treumann, and V. P. Pavlenko, Drift mirror instability in space plasmas: 2. Nonzero electron temperature effects, *J. Geophys. Res.*, *106*, 13,237–13,246, 2001b.

Pokhotelov, O. A., I. Sandberg, R. Z. Sagdeev, R. A. Treumann, O. G. Onishchenko, M. A. Balikhin, and V. P. Pavlenko, Slow drift mirror modes in finite electron-temperature plasma: Hydrodynamic and kinetic drift mirror instabilities, *J. Geophys. Res.*, pp. 1–1, 2003.

Pokhotelov, O. A., R. Z. Sagdeev, M. A. Balikhin, and R. A. Treumann, Mirror instability at finite ion-Larmor radius wavelengths, *Journal of Geophysical Research (Space Physics)*, *109*, 9213–+, 2004.

Press, W. H., S. A. Teukolsky, W. T. Vetterling, and B. P. Flannery, *Numerical Recipes in C The Art of Scientific Computing*, second ed., Cambridge University Press, 32 East 57^{th} Street, New York, NY 10022, 2002.

Primdahl, F., The fluxgate magnetometer, *Journal of Physics E: Scientific Instruments*, *12*, 241–253, 1979.

Rème, H., et al., The Cluster Ion Spectrometry (CIS) Experiment, *Space Science Reviews*, *79*, 303–350, 1997.

Rème, H., et al., First multispacecraft ion measurements in and near the Earth's magnetosphere with the identical Cluster ion spectrometry (CIS) experiment, *Annales Geophysicae*, *19*, 1303–1354, 2001.

Riedler, W., et al., Active Spacecraft Potential Control, *Space Science Reviews*, *79*, 271–302, 1997.

Robert, P., A. Roux, C. C. Harvey, M. W. Dunlop, P. W. Daly, and K.-H. Glassmeier, Tetrahedron geometric factors, in *Analysis methods for multi-spacecraft data*, pp. 323–348, Int. Space Sci. Inst., Bern, Switzerland, 1998.

Russell, C. T., et al., Mirror-mode structures at the Galileo-Io flyby: Observations, *J. Geophys. Res.*, *104*, 17,471–17,478, 1999.

Sablik, M. J., D. Golimowski, J. R. Sharber, and J. D. Winningham, Computer simulation of a 360° field-of-view "top-hat" electrostatic analyzer, *Review of Scientific Instruments*, *59*, 146–155, 1988.

Sahraoui, F., G. Belmont, J. Pinçon, L. Rezeau, A. Balogh, P. Robert, and N. Cornilleau-Wehrlin, Magnetic turbulent spectra in the magnetosheath: new insights, *Annales Geophysicae*, *22*, 2283–2288, 2004.

Sahraoui, F., et al., ULF wave identification in the magnetosheath: The k-filtering technique applied to Cluster II data, *J. Geophys. Res.*, *108(A9)*, 1335, 2003.

Schwartz, S. J., D. Burgess, and J. J. Moses, Low-frequency waves in the Earth's magnetosheath: present status, *Annales Geophysicae*, *14*, 1134–1150, 1996.

Séran, H. C., and P. Fergeau, An optimized low-frequency three-axis search coil magnetometer for space research, *Review of Scientific Instruments*, *76*, 4502–+, 2005.

Song, P., C. T. Russell, J. T. Gosling, M. Thomsen, and R. C. Elphic, Observations of the density profile in the magnetosheath near the stagnation streamline, *Geophys. Res. Lett.*, *17*, 2035–2038, 1990.

Song, P., C. T. Russell, and M. F. Thomsen, Slow mode transition in the frontside magnetosheath, *J. Geophys. Res.*, *97*, 8295–8305, 1992a.

Song, P., C. T. Russell, and M. F. Thomsen, Waves in the inner magnetosheath - A case study, *Geophys. Res. Lett.*, *19*, 2191–2194, 1992b.

Southwood, D. J., and M. G. Kivelson, Mirror instability. I - Physical mechanism of linear instability, *J. Geophys. Res.*, *98*, 9181–9187, 1993.

Stern, D. P., A brief history of magnetospheric physics during the space age, *Reviews of Geophysics*, *34*, 1–32, 1996.

Stone, E. C., A. C. Cummings, F. B. McDonald, B. C. Heikkila, N. Lal, and W. R. Webber, Voyager 1 Explores the Termination Shock Region and the Heliosheath Beyond, *Science*, *309*, 2017–2020, 2005.

Stone, R. G., and B. T. Tsurutani, Collisionless shocks in the heliosphere: A tutorial review, *Washington DC American Geophysical Union Geophysical Monograph Series*, *34*, 1985.

Tjulin, A., J.-L. Pinçon, F. Sahraoui, M. André, and N. Cornilleau-Wehrlin, The k-filtering technique applied to wave electric and magnetic field measurements from the Cluster satellites, *Journal of Geophysical Research (Space Physics)*, *110*, 11,224–+, 2005.

Treumann, R. A., and W. Baumjohann, *Advanced space plasma physics*, London : Imperial College Press, 1997., 1997.

Treumann, R. A., N. Sckopke, L. Brostrom, and J. Labelle, The plasma wave signature of a 'magnetic hole' in the vicinity of the magnetopause, *J. Geophys. Res.*, *95*, 19,099–19,114, 1990.

Treumann, R. A., C. H. Jaroschek, O. D. Constantinescu, R. Nakamura, O. A. Pokhotelov, and E. Georgescu, The strange physics of low frequency mirror mode turbulence in the high temperature plasma of the magnetosheath, *Nonlinear Processes in Geophysics*, *11*, 647–657, 2004.

Tsurutani, B. T., and P. Rodriguez, Upstream waves and particles: An overview of ISEE results, *J. Geophys. Res.*, *86*, 4319–4324, 1981.

Tsurutani, B. T., and R. G. Stone, Collisionless shocks in the heliosphere: Reviews of current research, *Washington DC American Geophysical Union Geophysical Monograph Series*, *35*, 1985.

Tsurutani, B. T., E. J. Smith, R. R. Anderson, K. W. Ogilvie, J. D. Scudder, D. N. Baker, and S. J. Bame, Lion roars and nonoscillatory drift mirror waves in the magnetosheth, *J. Geophys. Res.*, *87*, 6060–6072, 1982.

Tsurutani, B. T., G. S. Lakhina, E. J. Smith, B. Buti, S. L. Moses, F. V. Coroniti, A. L. Brinca, J. A. Slavin, and R. D. Zwickl, Mirror mode structures and ELF plasma waves in the Giacobini-Zinner magnetosheath, *Nonlinear Processes in Geophysics*, *6*, 229–234, 1999.

Van Allen, J. A., G. H. Ludwig, E. C. Ray, and C. E. McIlwain, Observation of High Intensity Radiation by Satellites 1958 Alpha and Gamma, *Tech. Rep. 28*, Jet Propulsion, 1958.

Van Allen, J. A., C. E. McIlwain, and G. H. Ludwig, Radiation Observations with Satellite 1958-ϵ, *J. Geophys. Res.*, *64*, 271–286, 1959.

Villante, U., An overview by Pioneers observations of the distant geomagnetic tail, *Space Science Reviews*, *20*, 123–143, 1977.

von Stein, R., K.-H. Glassmeier, and Dunlop, M., A Configuration Parameter for the CLUSTER Satellites, *Tech. Rep. 2*, Imperial College, London, 1992.

von Stein, R., K.-H. Glassmeier, and U. Motschmann, Cluster as a wave telescope and a mode filter, in *Proceedings of the Spatio-Temporal Analysis for Resolving Plasma Turbulence*, ESA, 1993.

Walker, S., F. Sahraoui, M. Balikhin, G. Belmont, J. Pinçon, L. Rezeau, H. Alleyne, N. Cornilleau-Wehrlin, and M. André, A comparison of wave mode identification techniques, *Annales Geophysicae*, *22*, 3021–3032, 2004.

Wilken, B., et al., RAPID - The Imaging Energetic Particle Spectrometer on Cluster, *Space Science Reviews*, *79*, 399–473, 1997.

Winterhalter, D., M. Neugebauer, B. Goldstein, and E. J. Smith, Ulysses field and plasma observations of magnetic holes in the solar wind and their relation to mirror-mode structures, *J. Geophys. Res.*, *99*, 23,371–23,381, 1994.

Woolliscroft, L. J. C., et al., The Digital Wave-Processing Experiment on Cluster, *Space Science Reviews*, *79*, 209–231, 1997.

Young, D. T., S. J. Bame, M. F. Thomsen, and R. H. Martin, 2-π-radian field-of-view toroidal electrostatic analyzer, *Review of Scientific Instruments*, *59*, 743–751, 1988.

Curriculum Vitae

Name: Ovidiu Dragoş Constantinescu
Birth place: Bucharest, Romania
Birth date: December 22 1970
Nationality: Rumanian

Education:

2002 - 2007

- Student of the *International Max Planck Research School on Physical Processes in the Solar System and Beyond at the Universities of Göttingen and Braunschweig*
- PhD Student at Technische Universität Carolo-Wilhelmina zu Braunschweig. Thesis title: *Wave sources and magnetic structures in the terrestrial magnetosphere*

1996 - 1997

University of Bucharest, Faculty of Physics, Theoretical Department: Master's Degree in Physics. Thesis prepared at Université Libre Bruxelles. Thesis title: *Study of a 1-D Electron Interacting with a Short-Range Potential and a Bichromatic Laser Field with Commensurate Frequencies*

1991 - 1996

University of Bucharest, Faculty of Physics: Bachelor of Physics. Thesis title: *Floquet Theory for Quantum Systems with a Finite Number of Freedom Degrees in Interaction with Laser Fields*

Positions:

2002 - 2007

Research Scientist at the Institut für Geophysik und extraterrestrische Physik, Braunschweig, Germany

2000 - 2001

Research Scientist at the Space Sciences Institute, Bucharest, Romania

1997 - 2000

Research Assistant at the Space Sciences Institute, Bucharest, Romania

Publications:

1. Constantinescu, O. D., K.-H. Glassmeier, P. M. E. Décréau, M. Fränz, and K.-H. Fornaçon, Low frequency wave sources in the outer magnetosphere, magnetosheath, and near Earth solar wind, 2006a, Submitted to Annales Geophysicae
2. Constantinescu, O. D., K.-H. Glassmeier, U. Motschmann, R. A. Treumann, and M. Fränz, Plasma Wave Source Location Using CLUSTER as a Spherical Wave Telescope, *J. Geophys. Res.*, *111*, 2006b
3. Lucek, E. A., D. Constantinescu, M. L. Goldstein, J. Pickett, J. L. Pinçon, F. Sahraoui, R. A. Treumann, and S. N. Walker, The Magnetosheath, in *Outer Magnetospheric Boundaries: Cluster Results*, edited by G. Paschmann, S. J. Schwartz, C. P. Escoubet, and S. Haaland, Space Sciences Series of ISSI, pp. 95–152, Springer, 2005a
4. Lucek, E. A., D. Constantinescu, M. L. Goldstein, J. Pickett, J. L. Pinçon, F. Sahraoui, R. A. Treumann, and S. N. Walker, The Magnetosheath, *Space Science Reviews*, *118*, 95–152, 2005b
5. Constantinescu, O. D., K.-H. Glassmeier, R. Treumann, U. Motschmann, and K.-H. Fornaçon, Wave sources locations in the bowshock and adjacent regions, in *Proceedings of the Cluster and Double Star symposium 5th Anniversary of Cluster in Space*, ESA, 2006
6. Treumann, R. A., C. H. Jaroschek, O. D. Constantinescu, R. Nakamura, O. A. Pokhotelov, and E. Georgescu, The strange physics of low frequency mirror mode turbulence in the high temperature plasma of the magnetosheath, *Nonlinear Processes in Geophysics*, *11*, 647–657, 2004
7. Constantinescu, O. D., K.-H. Glassmeier, R. Treumann, and K.-H. Fornaçon, Magnetic mirror structures observed by Cluster in the magnetosheath, *Geophys. Res. Lett.*, *30*, 4–1, 2003
8. Constantinescu, O. D., Self-consistent model for mirror structures, *J. Atmos. Sol. Terr. Phys*, *64*, 645–649, 2002
9. Constantinescu, O. D., Study of a 1-D Electron Interacting with a Short-Range Potential and a Bichromatic Laser Field with Commensurate Frequencies, Master's thesis, Bucharest University, Faculty of Physics, 1997
10. Constantinescu, O. D., Floquet Theory for Quantum Systems with a Finite Number of Freedom Degrees in Interaction with Laser Fields, Bachelor's thesis, Bucharest University, Faculty of Physics, 1996

Invited talks:

1. Constantinescu, O. D., Location of Wave Sources Using Cluster as a Sensor Array, 2006, invited Talk, *EGU General Assembly*, Vienna, Austria

2. Constantinescu, O. D., K.-H. Glassmeier, S. Schaefer, M. Fränz, and P. M. E. Décréau, Location of low frequency waves sources in the outer magnetosphere, magnetosheath, and near Earth solar wind, 2006, invited Talk, University of Alberta, Edmonton, Canada

Index

acoustic wave, 25
active
  potential control, 16
  region, 87, 92
adiabatic motion, *see* regular motion
AIC, 79, 92
Alfvén
  mode, 79
  shock, 9
aliasing, 30
Ampère law, 104
anisotropy
  magnetosheath, 10
  measured, 88
  model, 98
  simulation, 114
anti-correlation, *see* correlation
Archimedean spiral, 6
Ariane, 15
arrival time, 60
artificial data, *see* synthetic data
ASPOC, 16
aurora, 5, 10, 12

Baikonur, 15
barometric formula, 5
beamformer, 29
Bessel equation, 100
Birkeland, Kristian, 5
bowshock, 8, 92

calibration, 19
Capon technique, 36
chaotic motion, 109
Chapman-Ferraro current, 10
characteristic
  source distance, 91
  tetrahedron size, 15
CIS, 16, 19
close source, 78, 85, 87–90
Cluster, 15
CODIF, 16, 19
coherent waves, 37
composition, 19
corona, 5
correlation
  measured, 88
  simulation, 115
cube configuration, 35, 40
cusp, 10, 81, 87, 90

dipole, 11
discontinuity, 8
distant source, *see* remote source
distribution
  function, *see* velocity distribution
  of wave sources, 90
Doppler effect, 58, 77
drift current, 11, 105
DWP, 15
dynamo, 10

EDI, 15
EFW, 15
electrostatic analyzer, 19
elementary wave, 26
escaping particles, 108, 118

fast
  mode, 88, 90, 92
  shock, 9
fast Fourier transform, *see* FFT
FFT, 28, 139
FGM, 15, 17
firehose instability, 101
fit, 121
fluxgate magnetometer, *see* FGM
foreshock, 9, 81
  electron, 9, 81, 85, 88

  ion, 9, 81, 84, 85, 88, 90
Fregat, 16

ghost, 59, 70
Gilbert, Sir William, 5
gradient-curvature drift, 11, 105, 108
gyrotropic wave field, 87

heliopause, 7
HIA, 16, 19
de Hoffman - Teller frame, 8
Huygens principle, 72

IGeP, 19
IMF, 6, 10
information horizon, 8
interplanetary magnetic field, *see* IMF
interstellar pressure, 7
invertibility, 37
ion-cyclotron wave, 9, 79, 88–90
irregular motion, *see* chaotic motion

k-filtering, 44
kinetic
  effect, 116
  temperature, 113
Kourou, 15

Langmuir
  probe, 15
  waves, 9, 81
lion roars, 97
local source, *see* close source

Mach
  cone, 60
  number, 60
magnetic
  bottle, *see* magnetic mirror
  mirror, 97
  needle, 5
  reversal, 11
  storm, 11
  substorm, 12
magnetic moment
  charged particle, 98, 110
  Earth, 11
magnetohydrostatic equilibrium, 98
magnetometer, 17
magnetopause, 9
magnetosheath, 9, 86, 90
magnetosonic wave, 92
magnetosphere, 5
Magnetsrode, 19
MIAOW, 84
minimization, *see* fit
mirror
  mode, 79–80, 83–84, 92
  structure, *see* magnetic mirror
model
  magnetic mirror, 97
  propagation, 126
  wave, *see* synthetic data
moving
  sensor, 58
  source, 59
multipol, 10

noise, 39, 81
northward IMF, 10
Nyquist theorem, 30

orbit
  charged particle, 107
  Cluster, 15, 76, 80
orthogonal
  shock, 9
  system, 26
  temperature, 99, 113
  wave propagation, 85, 90

parallel
  shock, 9
  temperature, 99, 113
  wave propagation, 86
Parker spiral, 6
particle trajectory, *see* orbit
PEACE, 16
plane waves representation, 29
plasma
  depletion, 10, 115
  flow, 59, 78
plasmasheet, 6
plasmasphere, 12
pressure equilibrium, 98

quality index, 75

radiation belt, 11
Rankine - Hugoniot relations, 9
RAPID, 16
reconnection, 10
regular
    motion, 107
    tetrahedron, 34, 39–45, 64–73
regularization, 37
remote source, 77, 84–87
ring current, *see* drift current

sensor array, 25
shock, 8
singular matrix, 37
slow
    mode, 79, 92
    shock, 9
source locator, 55
southward IMF, 10
Soyuz, 15
spherical waves representation, 55
STAFF, 15, 17
standoff distance, 8
Starfish, 11
statistical study, 87
subsonic flow, 60, 70
supersonic flow, 61, 71
synthetic data, 31, 38–39, 47, 65

tail lobes, 12
termination shock, 7
trapped particles, 108, 117

validity domain, 45
Van Allen belt, *see* radiation belt
velocity distribution
    bi-Maxwellian, 98
    measuring, 19
    simulated, 112
virtual interference, 25
Voyager, 7

wave
    advanced, 61
    front, 57
    retarded, 61
wave telescope, 44
WBD, 15
WEC, 15
WHISPER, 15
witness spacecraft, 126